Y 3.At 7:
36/13-3

1970
Quarterly
Technical
Progress
Review
Volume 13—3

A publication of the
Division of Technical Information
U.S. Atomic Energy Commission
Prepared in Cooperation
with
The American Nuclear Society.

REACTOR TECHNOLOGY

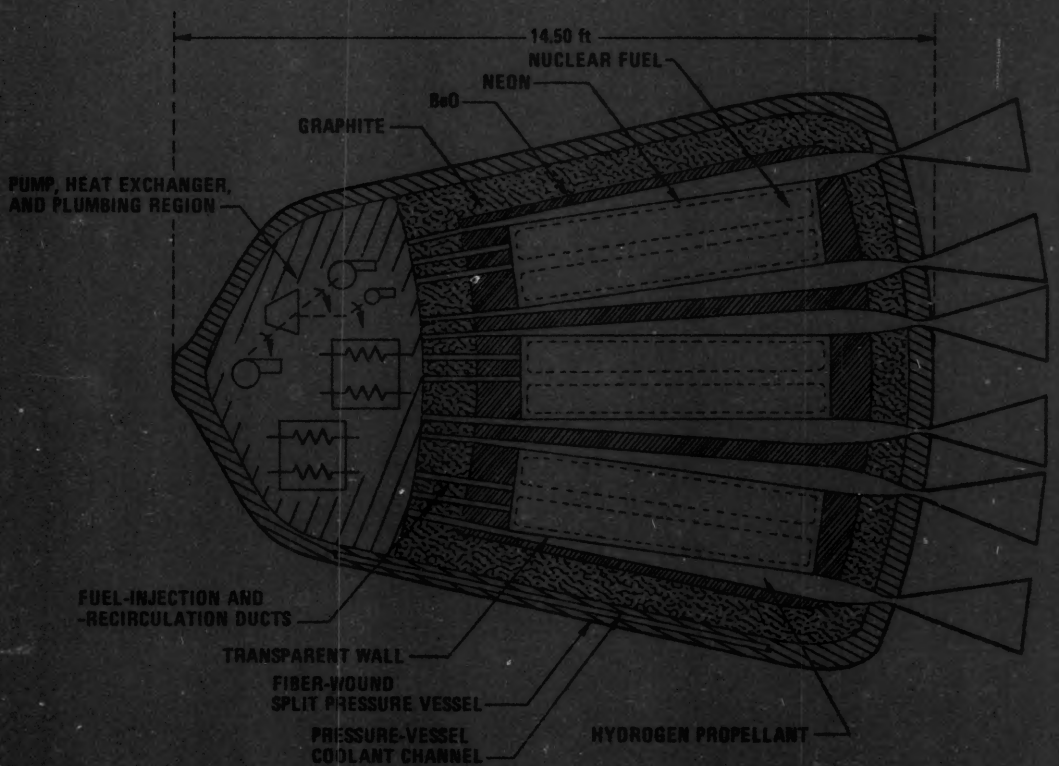

GAS-CORE NUCLEAR LIGHT-BULB ENGINE (SCHEMATIC)—See Page 228

TECHNICAL PROGRESS REVIEWS

The United States Atomic Energy Commission publishes the Technical Progress Reviews to meet the needs of industry and government for concise summaries of current nuclear developments. Each journal digests and evaluates the latest findings in a specific area of nuclear technology and science. *Nuclear Safety* is a bimonthly journal; the other two are quarterly journals.

Isotopes and Radiation Technology
P. S. Baker, A. F. Rupp, and associates
Isotopes Information Center, Oak Ridge National Laboratory

Nuclear Safety
Wm. B. Cottrell, W. H. Jordan, J. P. Blakely, and associates
Nuclear Safety Information Center, Oak Ridge National Laboratory

Reactor Technology
Prepared in cooperation with the American Nuclear Society

All are available from the U. S. Government Printing Office. See the back cover for ordering instructions.

NOTICE

This journal was prepared under the sponsorship of the U. S. Atomic Energy Commission. Neither the United States nor the U. S. Atomic Energy Commission, or any of their employees, contractors, subcontractors, or their employees, makes any warranty, express or implied, or assumes any legal liability or responsibility for the accuracy, completeness, or usefulness of any information, apparatus, product, or process disclosed, or represents that its use would not infringe privately owned rights.

Availability of Reports Cited in This Review

United States Atomic Energy Commission (USAEC) reports are available at certain libraries that maintain collections of these reports. They are also sold by the following governmental and international organizations: (1) Clearinghouse for Federal Scientific and Technical Information (CFSTI), U. S. Department of Commerce, Springfield, Va. 22151 ($3.00 for printed copy and $0.65 for microfiche); (2) International Atomic Energy Agency (IAEA), Vienna, Austria; and (3) National Lending Library, Boston Spa, England.

Other U. S. Government agency reports identified in this journal are generally available from CFSTI.

Reports from other countries are available at some libraries in the United States and from IAEA and the originating country. **United Kingdom Atomic Energy Authority (UKAEA)** reports are sold by Her Majesty's Stationery Office, London. **Atomic Energy of Canada Limited (AECL)** reports are sold by the Scientific Document Distribution Office, Atomic Energy of Canada Limited, Chalk River, Ontario, Canada. UKAEA and AECL reports issued after March 1, 1967, are sold by CFSTI to purchasers in the United States and its territories.

Private-organization reports should be requested from the originator.

The views expressed in this publication do not necessarily represent those of the United States Atomic Energy Commission, its divisions or offices, or of any Commission advisory committee or contractor.

Y3 AE7
36-13-3

REACTOR TECHNOLOGY

Vol. 13, No. 3 Summer 1970

Contents

CURRENT AWARENESS REVIEWS

(Prepared by Myrna L. Steele of AEC's Division of Technical Information Extension)

SODIUM-COOLED REACTORS:
Physics Aspects of the Enrico Fermi Fast Breeder Reactor 191
EBR-II Physics Aspects (Runs 35 to 40) 214
Plant-Systems Operations 222

AMERICAN NUCLEAR SOCIETY—CRITICAL REVIEWS

INTRODUCTION 225

GAS-CORE REACTOR TECHNOLOGY
J. D. Clement and J. R. Williams
Georgia Institute of Technology 226

XENON-INDUCED SPATIAL POWER OSCILLATIONS
Weston M. Stacey, Jr., Argonne National Laboratory 252

EMERGENCY CORE-COOLING PROBLEM IN LMFBR's
Ira Charak, Argonne National Laboratory 280

INTERGRANULAR CORROSION CRACKING OF TYPE 304 STAINLESS STEEL IN WATER-COOLED REACTORS
C. F. Cheng, Argonne National Laboratory 310

ILLINOIS STATE LIBRARY
OCT 21 1970
U. S. Dept. of Documents Deposit

Superintendent of Documents, U. S. Government Printing Office, Washington, D. C. 20402, $3.00 per year.

REACTOR TECHNOLOGY

is a quarterly review of progress and developments in the reactor field including the following subject areas:

Economics	Fuel Cycles
Physics	Fluid and Thermal Technology
Mechanics	Fuel Processing
Construction	Components
Fuel Elements	Operating Performance

Prepared for reactor physicists, operators, designers, fuel-cycle specialists, administrators, and others interested in the field, this journal reviews, summarizes, critically evaluates, and interprets the state of the art as reflected in the current literature.

The many reports and publications referenced merit further study, and readers are urged to consult them for additional details.

Qualified authors are invited to contribute review articles for consideration for publication.

U. S. Atomic Energy Commission
Division of Technical Information
Washington, D. C. 20545

Issued quarterly by the U. S. Atomic Energy Commission. Use of funds for printing this publication approved by the Director of the Bureau of the Budget on May 12, 1969.

Sodium-Cooled Reactors: Physics Aspects of the Enrico Fermi Fast Breeder Reactor

By Myrna L. Steele*

The Enrico Fermi Fast Breeder Reactor, located at Lagoona Beach, Mich., was designed with a 430-MW(t) capability; however, the maximum reactor power achievable with the first core loading, Core A, is 200 MW(t). The core and blanket, located in the lower reactor vessel, consist of square subassemblies containing enriched-uranium fuel pins and depleted-uranium blanket rods arranged to approximate a cylinder about 80 in. in diameter and 70 in. high. The core approximates a right cylinder 31 in. in diameter and 31 in. high; it is axially and radially surrounded by breeder blankets. The reactor cross section, shown in Fig. 1, indicates the placement of individual components within the reactor vessel. There is a total of 149 central lattice positions occupied by the core and inner-radial-blanket (IRB) subassemblies, the neutron source, and the 10 operating control- and safety-rod channels. All these positions are supplied with sodium coolant flowing upward from a high-pressure plenum connected to the discharge lines of the three primary sodium pumps. The cross section of the core and IRB regions is shown in Fig. 2. The coordinate system used to designate the location of subassemblies in the Fermi reactor can be understood by the use of this figure. Basically the designation is two position numbers that are the X and Y coordinates, respectively, of a conventional $X-Y$ coordinate system. The letter prefix attached to each position number designates the positive or negative sign in the conventional coordinate system: P for positive and N for negative. The core center position is P00–P00.

*U. S. Atomic Energy Commission, Division of Technical Information Extension, Oak Ridge, Tenn. 37830.

The reactor is designed to be controlled by two operating control rods; provisions have been made for eight safety rods, although as few as six have been used. All these rods are of the poison type, containing boron carbide (B_4C) in which the boron is enriched in ^{10}B. One operating control rod is for regulating, and the other is for shimming. The positions for the eight safety rods are uniformly spaced around the center of the core. During most of the operation to date, only seven rods have been installed, the eighth position being occupied by a rotating oscillator rod.

The reactor was first made critical on Aug. 23, 1963. Physics measurements were made while the reactor was operated at powers of less than 1 MW(t) from the date of first criticality until late 1965. Permission was given by the AEC on Dec. 17, 1965, for operation at powers up to 200 MW(t), and further physics testing was conducted. This work was terminated by the fuel-melting incident of Oct. 5, 1966. After an extensive investigation of the cause of the incident and a modification of the reactor to prevent that type of incident, approval was granted by the AEC early in 1970 to restart the reactor in accordance with a program submitted by Power Reactor Development Company, the reactor operator. When it is restarted, further testing will be done. Plans are for subsequent operation with a mixed-oxide core at powers up to 430 MW(t). This oxide core will have a volume of more than 800 liters, a central flux of 8×10^{15} neutrons/(cm^2)(sec), and sodium inlet and outlet temperatures of 600 and 900°F, respectively.

The results of physics tests on the initial core from August 1963 to October 1966 are discussed in this article. The tests are divided into two types for this

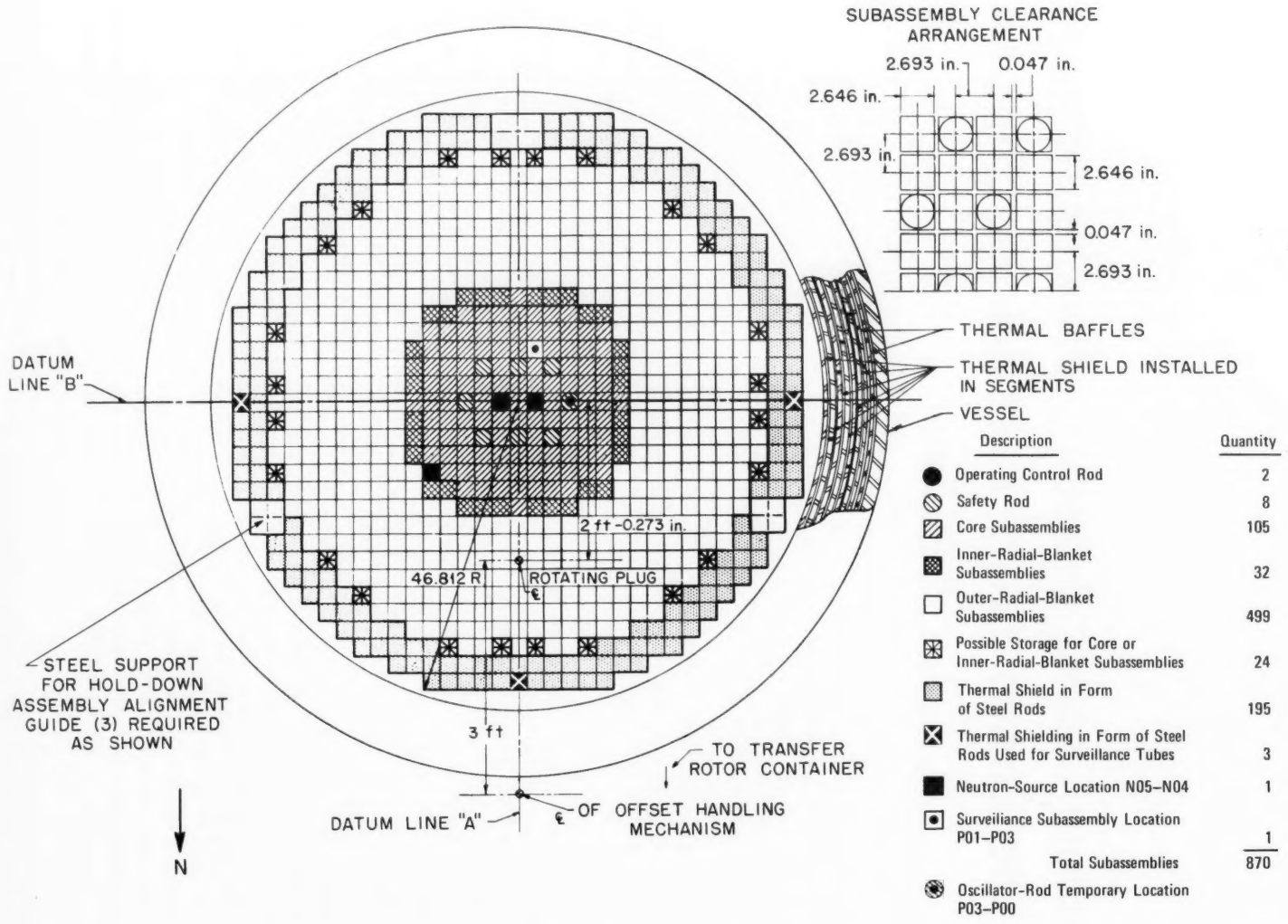

Fig. 1 Fermi reactor cross section.

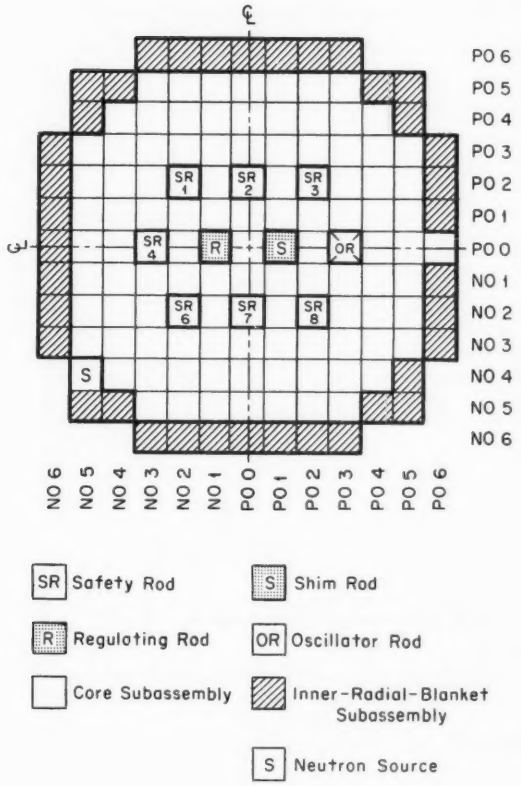

Fig. 2 Core and inner-radial-blanket cross section.

discussion: (1) basic physics (neutronics) characteristics and (2) integral physics parameters pertinent to reactor operation. The first type includes ^{235}U and ^{238}U worths, sodium worth, and fission and capture distributions; the second type includes isothermal temperature coefficient of reactivity, power coefficient of reactivity, reactor transfer function, and calibrations of control and safety rods.

NEUTRONICS CHARACTERISTICS

Worth Measurements of ^{235}U and ^{238}U in Core and Blanket Subassemblies

Reactivity worths[1] of the ^{235}U and ^{238}U in the core and blanket subassemblies were measured in 1964 from February 18 to April 1. Specially constructed subassemblies were used. Interchanging a subassembly in the core with a subassembly in the blanket permitted measurement of reactivity-worth differences between them as a function of position in the inner radial blanket and as a function of radial position in the core.

The worths in the core were measured by noting changes in reactivity following sequential substitutions of a shim subassembly for a normal fuel subassembly. Columnar reactivity worths of ^{238}U-for-sodium replacement were determined as a function of core position by noting reactivity differences between a proof-test subassembly and a dummy subassembly in identical core positions. Figure 3 shows a comparison between these ^{235}U vs. ^{238}U measured, calculated, and mockup-predicted reactivity values. The results of reactivity measurements are reported in units of inhours/kg. (To convert these results to dollars and cents units, use the Fermi reactor value of 0.0066 for the effective delayed-neutron fraction (β_{eff}) and the conversion factor of 319 inhours for 1 dollar.) Table 1 is a summary of the experimentally determined ^{235}U vs. ^{238}U columnar worths and the measured ^{238}U vs. void worths. Figure 4 shows the adjusted columnar reactivity worths of ^{235}U vs. void and ^{238}U vs. void. The probable errors associated with all measurements are based on statistical analyses of data scatter.

Comparisons of measured and calculated reactivity changes after interchanges of fuel and inner-radial-blanket subassemblies are given in Table 2.

Reactivity Worth of Sodium in a Core Subassembly

The reactivity worth[2] of sodium in a core subassembly was measured as a function of subassembly radial position in the core lattice. The results (in cents/kg) may be summarized as

Minimum, near core center	+1.82
Maximum, near core edge	+2.19
Average over core	+2.01

with a quoted probable error of less than ±5%. Table 3 shows the final results of the sodium-worth measurements as a function of core radial position.

^{235}U and ^{238}U Fission Distributions and ^{238}U Capture Distributions in Core and Blanket Regions

Enriched and depleted uranium foils[3] were irradiated in special core and radial-blanket subassemblies on July 22, 1964, Aug. 26 to Sept. 8, 1964, and May 27 to June 18, 1965, to obtain ^{235}U and ^{238}U fission-rate distributions and ^{238}U neutron capture-rate distributions. The enriched foils were 0.08 in. in diameter by 0.75 in. long and were made of Al–18 wt.% U

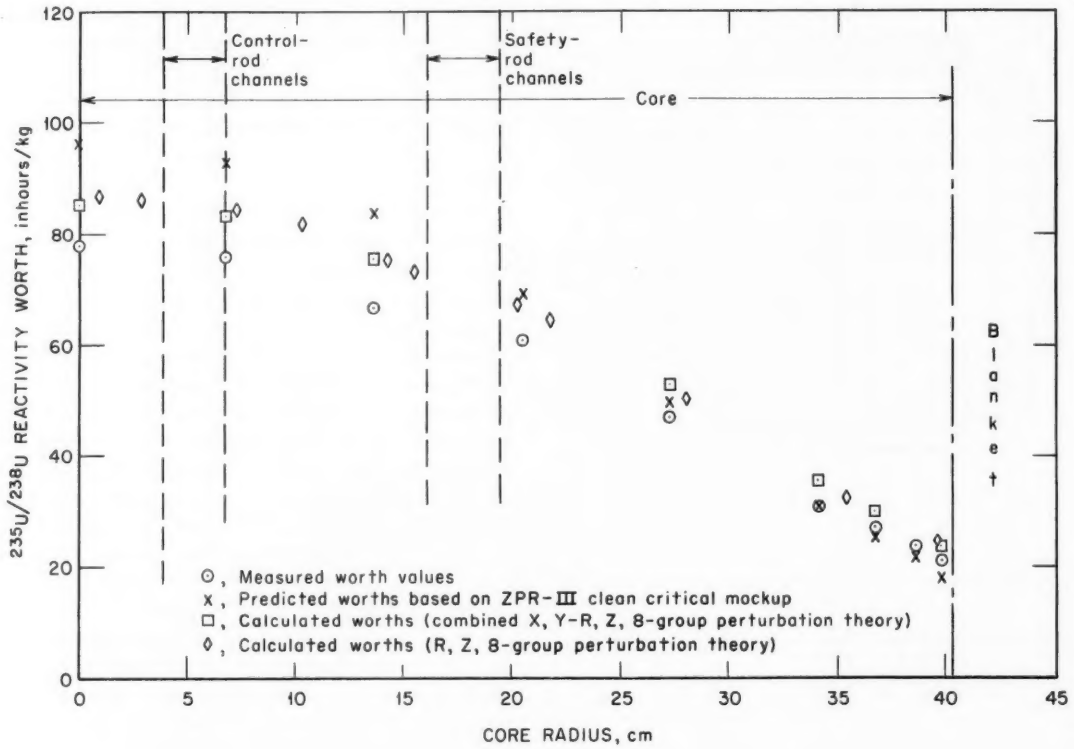
Control-rod channels
Safety-rod channels
Core
Blanket
$^{235}U/^{238}U$ REACTIVITY WORTH, inhours/kg
CORE RADIUS, cm
⊙, Measured worth values
x, Predicted worths based on ZPR-III clean critical mockup
□, Calculated worths (combined X, Y-R, Z, 8-group perturbation theory)
◊, Calculated worths (R, Z, 8-group perturbation theory)

Fig. 3 Columnar reactivity worths of ^{235}U vs. ^{238}U in the core.[1]

Table 1 Reactivity Worth of ^{235}U Relative to Void[1]

Measurement position		Measured and adjusted reactivity worths, inhours/kg		
Subassembly coordinate	Core radius, cm	Measured ^{235}U-for-^{238}U replacement worth	Measured* ^{238}U vs. void worth	Adjusted ^{235}U vs. void worth
P00–P00	0	78.0 ± 0.2	−2.6 ± 0.1	75.4 ± 0.4
N02–P00	13.69	66.4 ± 0.2	−2.1 ± 0.1	64.3 ± 0.4
P00–P01	6.84	75.8 ± 0.2	−2.5 ± 0.1	73.3 ± 0.5
P00–P03	20.52	60.5 ± 0.2	−1.5 ± 0.2	59.0 ± 0.5
P00–P04	27.36	46.7 ± 0.3	−0.7 ± 0.1	46.0 ± 0.5
P00–P05	34.19	30.9 ± 0.5	+0.1 ± 0.1	31.0 ± 0.6
N02–P05	36.83	26.7 ± 0.3	+0.4 ± 0.1	27.1 ± 0.4
N03–P05	39.88	21.2 ± 0.3	+0.5 ± 0.1	21.7 ± 0.4
N04–P04	38.66	23.6 ± 0.3	+0.5 ± 0.1	24.1 ± 0.4

*Measured ^{238}U values depended upon minor components calculated by means of perturbation theory.

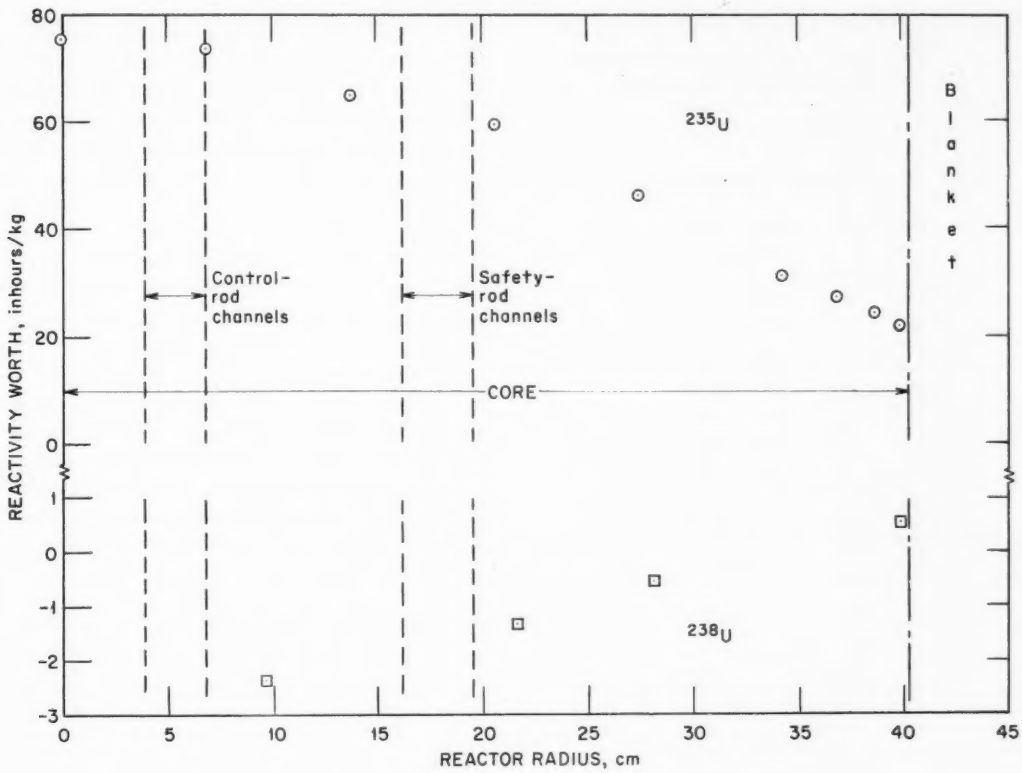

Fig. 4 Corrected columnar reactivity worths of ^{235}U vs. void and ^{238}U vs. void.[1]

Table 2 Measured and Calculated Reactivity Changes[1] Due to Interchanges of Fuel and Inner-Radial-Blanket Subassemblies

Measurement No.	IRB position	Average radius, cm	Measured reactivity change, inhours	Predicted reactivity change, inhours	
				ZPR-III critical experiment data*	Perturbation-theory calculation†
2	N05–P05	48.37	46.46 ± 0.77	37	52.1
3	N03–P06	45.88	57.31 ± 0.87	52	65.3
4	N04–P05	43.80	72.96 ± 0.79	66	81.0
5	N01–P06	41.61	87.21 ± 0.77	81	95.5
7	N02–P06	43.26	75.40 ± 0.76	69	82.8
8	P00–P06	41.04	92.80 ± 0.76	86	99.9
9	N01–P06	41.61	85.90 ± 0.74	80	94.4
10 and 12	N03–P05	39.88	102.12 ± 0.67	93	110.6
11	P00–P06	41.04	186.09 ± 0.41		

*Predictions based upon radially extrapolated ^{238}U worth data from ZPR-III critical-assembly mockup.

†Cylindrical (R, Z) model results synthesized with (X, Y) model results; differences in axial-blanket-zone compositions were ignored.

alloy, with the uranium enriched to about 93%. The depleted foils were made of uranium metal depleted to 0.22% ^{235}U; they were 0.080 in. in diameter and 1.0 in. long.

Table 3 Determination of Sodium Worth[2]

Radius, cm	Sodium worth, cents/kg*
39.9	2.05 ± 0.04
34.2	2.20 ± 0.06
15.3	1.99 ± 0.08
9.7	1.80 ± 0.04
29.1	1.92 ± 0.08
21.6	1.94 ± 0.04
38.7	2.16 ± 0.05
33.9	2.11 ± 0.06

*Determined on the basis of 6.76 kg of Na in four subassemblies and 3.19 inhours/cent.

In the counting technique used, foil activities were determined for two energy regions (band A and band B). The higher-energy region (band B) included, in addition to activities of the depleted foils and the enriched foils, fission-product-decay gamma radiation and the natural radioactivity of uranium. Activities in the lower-energy region (band A) were measured for depleted foils only. A lower limit for band B was set at 0.600 MeV, with no upper limit. The band A lower and upper limits were 87 and 125 keV, respectively. Further details, including count-rate data and normalization factors and procedures, are in Ref. 3.

A comparison[3] of results of measured and calculated values for fission and capture rates is shown in Figs. 5 to 8. Figure 5 shows the ^{235}U axial fission-rate distributions. The ^{238}U axial fission-rate distributions for the core and radial-blanket subassemblies are shown in Figs. 6 and 7, respectively. Figure 8 shows the ^{238}U axial capture-rate distributions for the core.

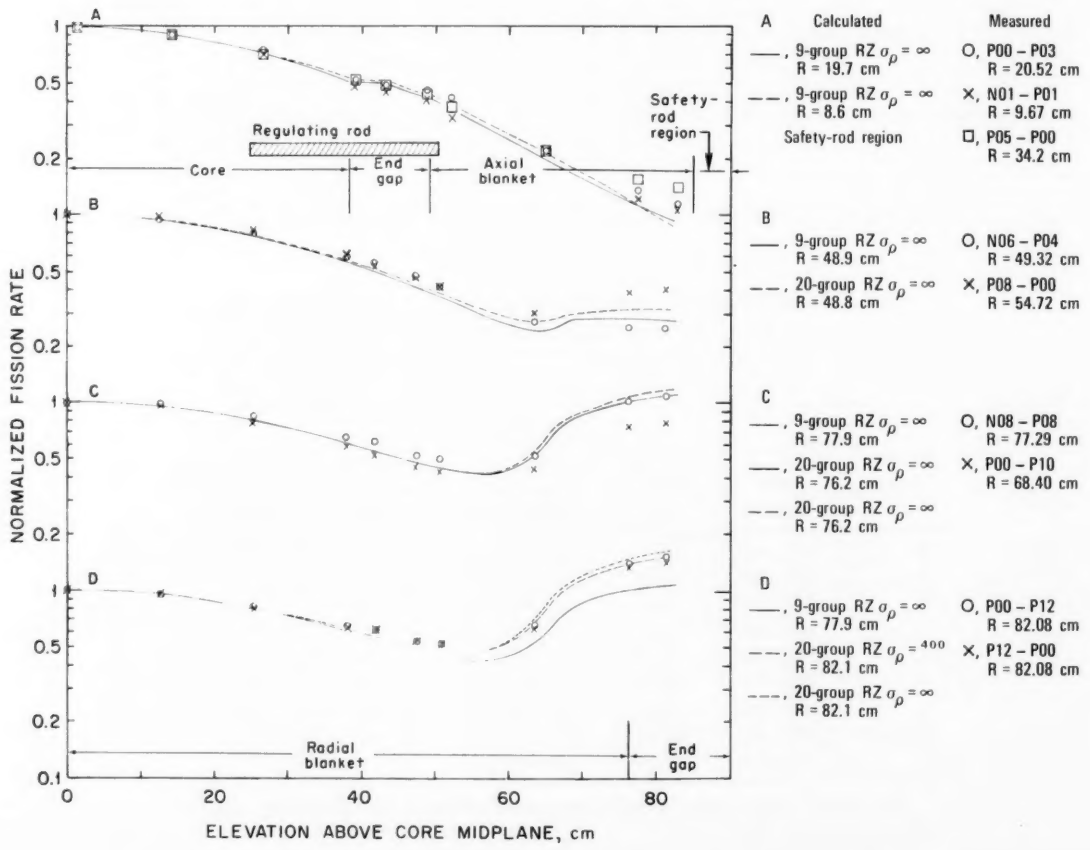
NORMALIZED FISSION RATE
ELEVATION ABOVE CORE MIDPLANE, cm
A
B
C
D
Regulating rod
Core
End gap
Axial blanket
Safety-rod region
Radial blanket
End gap
A Calculated
—, 9-group RZ $\sigma_\rho = \infty$ R = 19.7 cm
– –, 9-group RZ $\sigma_\rho = \infty$ R = 8.6 cm
Safety-rod region
Measured
O, P00 – P03 R = 20.52 cm
×, N01 – P01 R = 9.67 cm
□, P05 – P00 R = 34.2 cm
B
—, 9-group RZ $\sigma_\rho = \infty$ R = 48.9 cm
– –, 20-group RZ $\sigma_\rho = \infty$ R = 48.8 cm
O, N06 – P04 R = 49.32 cm
×, P08 – P00 R = 54.72 cm
C
—, 9-group RZ $\sigma_\rho = \infty$ R = 77.9 cm
—, 20-group RZ $\sigma_\rho = \infty$ R = 76.2 cm
– –, 20-group RZ $\sigma_\rho = \infty$ R = 76.2 cm
O, N08 – P08 R = 77.29 cm
×, P00 – P10 R = 68.40 cm
D
—, 9-group RZ $\sigma_\rho = \infty$ R = 77.9 cm
– –, 20-group RZ $\sigma_\rho = 400$ R = 82.1 cm
– – –, 20-group RZ $\sigma_\rho = \infty$ R = 82.1 cm
O, P00 – P12 R = 82.08 cm
×, P12 – P00 R = 82.08 cm

Fig. 5 Axial distributions of the ^{235}U fission rate.[3]

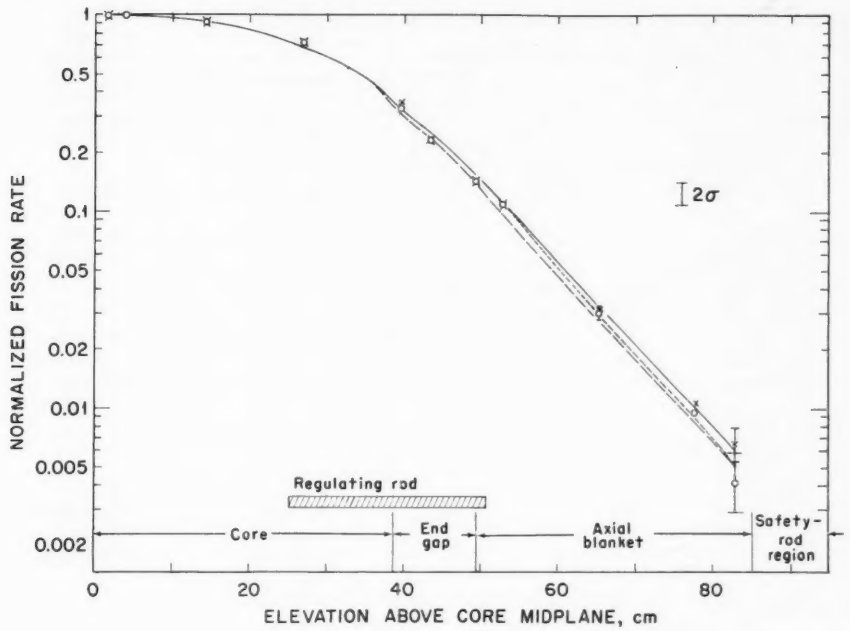
NORMALIZED FISSION RATE
ELEVATION ABOVE CORE MIDPLANE, cm
Regulating rod
Core
End gap
Axial blanket
Safety-rod region
2σ
Calculated
—, 9-group RZ R = 8.6 cm safety-rod region
– –, 9-group RZ R = 19.7 cm
– – –, 9-group RZ threshold R = 10.2 cm
Measured
O, P00 – P03 R = 20.52 cm
×, N01 – P01 R = 9.67 cm

Fig. 6 Axial distributions of the ^{238}U fission rate in the core subassemblies.[3]

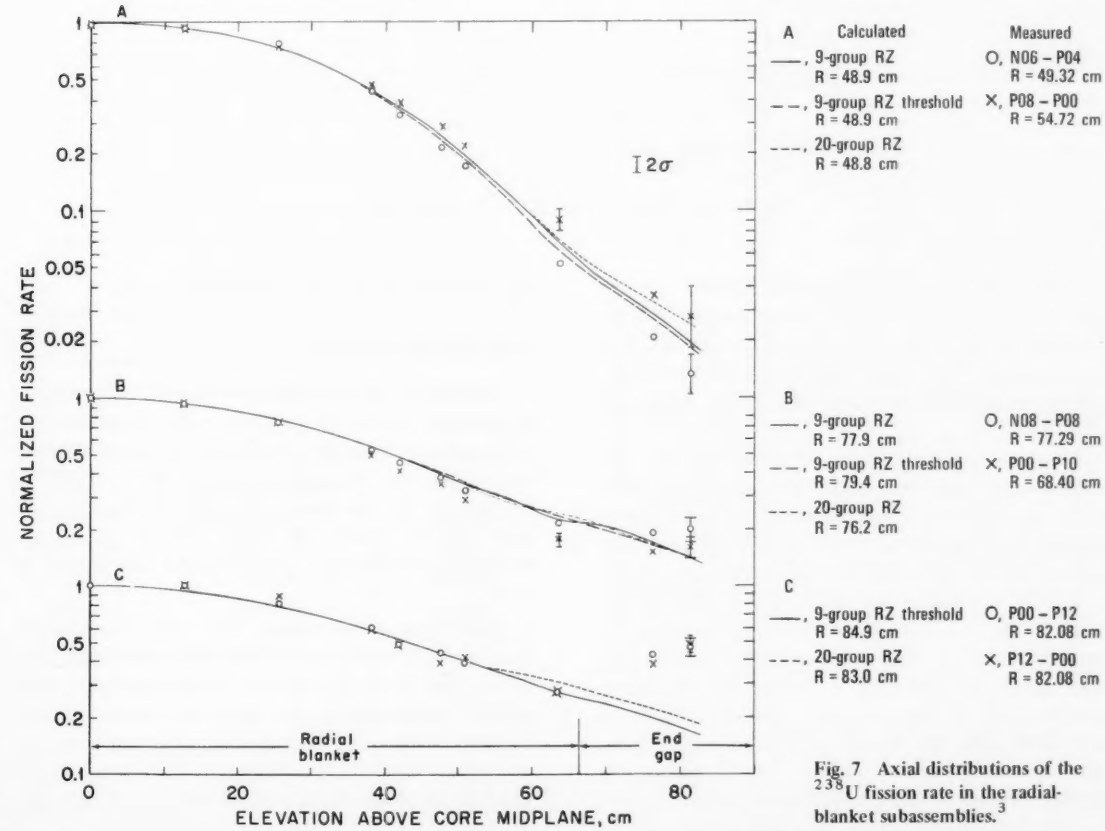
A
B
C
NORMALIZED FISSION RATE
ELEVATION ABOVE CORE MIDPLANE, cm
Radial blanket
End gap
2σ
A Calculated
—, 9-group RZ R = 48.9 cm
– –, 9-group RZ threshold R = 48.9 cm
– – –, 20-group RZ R = 48.8 cm
Measured
O, N06 – P04 R = 49.32 cm
×, P08 – P00 R = 54.72 cm
B
—, 9-group RZ R = 77.9 cm
– –, 9-group RZ threshold R = 79.4 cm
– – –, 20-group RZ R = 76.2 cm
O, N08 – P08 R = 77.29 cm
×, P00 – P10 R = 68.40 cm
C
—, 9-group RZ threshold R = 84.9 cm
– – –, 20-group RZ R = 83.0 cm
O, P00 – P12 R = 82.08 cm
×, P12 – P00 R = 82.08 cm

Fig. 7 Axial distributions of the ^{238}U fission rate in the radial-blanket subassemblies.[3]

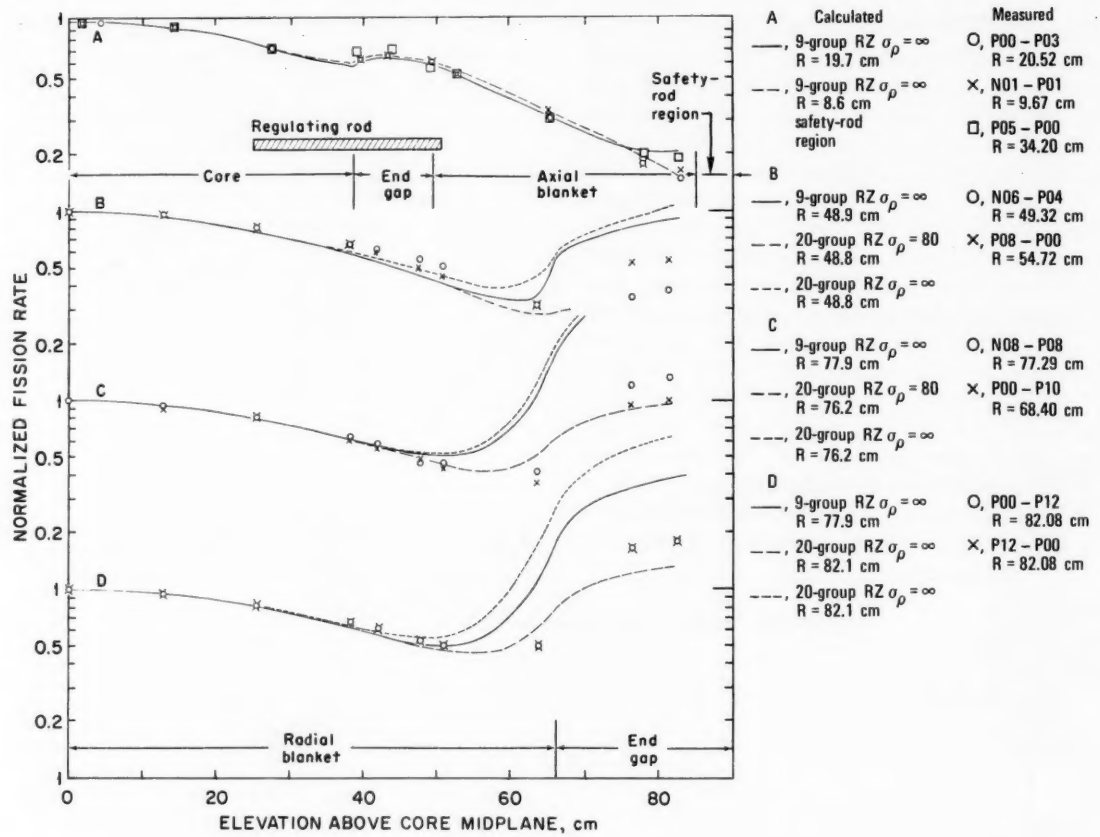
NORMALIZED FISSION RATE
ELEVATION ABOVE CORE MIDPLANE, cm
Regulating rod
Safety-rod region
Core
End gap
Axial blanket
Radial blanket
End gap
A
B
C
D
A Calculated
—, 9-group RZ $\sigma_\rho = \infty$ R = 19.7 cm
– –, 9-group RZ $\sigma_\rho = \infty$ R = 8.6 cm safety-rod region
Measured
O, P00 – P03 R = 20.52 cm
×, N01 – P01 R = 9.67 cm
□, P05 – P00 R = 34.20 cm
B
—, 9-group RZ $\sigma_\rho = \infty$ R = 48.9 cm
– –, 20-group RZ $\sigma_\rho = 80$ R = 48.8 cm
– – –, 20-group RZ $\sigma_\rho = \infty$ R = 48.8 cm
O, N06 – P04 R = 49.32 cm
×, P08 – P00 R = 54.72 cm
C
—, 9-group RZ $\sigma_\rho = \infty$ R = 77.9 cm
– –, 20-group RZ $\sigma_\rho = 80$ R = 76.2 cm
– – –, 20-group RZ $\sigma_\rho = \infty$ R = 76.2 cm
O, N08 – P08 R = 77.29 cm
×, P00 – P10 R = 68.40 cm
D
—, 9-group RZ $\sigma_\rho = \infty$ R = 77.9 cm
– –, 20-group RZ $\sigma_\rho = \infty$ R = 82.1 cm
– – –, 20-group RZ $\sigma_\rho = \infty$ R = 82.1 cm
O, P00 – P12 R = 82.08 cm
×, P12 – P00 R = 82.08 cm

Fig. 8 Axial distributions of the ^{238}U capture rate.[3]

Calculated and measured reaction rates are given in Table 4 for the core midplane. These data summarize the results of the neutron fission and capture distributions shown in Figs. 5 to 8 and provide an immediate quantitative comparison of measured and calculated values.

Power-level normalization between runs was accomplished by locating a depleted foil and an enriched foil in the temporary instrument thimble during each irradiation. Three curves were constructed from the standard-foil data after each irradiation. One curve gave the activity as a function of decay time of the enriched standard foil, and another curve gave the activity as a function of decay time of the depleted standard foil; these curves included count-rate data for all gamma radiation with an energy greater than 0.600 MeV. A third curve gave the activity as a function of decay time of the depleted standard for all gamma-ray energies between 87 and 125 keV.

INTEGRAL PHYSICS PARAMETERS

Reactivity Measurements

Isothermal Temperature Coefficient.[4] At the beginning of the nuclear test program, measurements of the isothermal temperature coefficient of reactivity were made over the temperature range 400 to 600°F. Critical-rod and positive-period data can be obtained from Ref. 4; results of both sets of isothermal-temperature-coefficient measurements are shown in Table 5.

Estimated uncertainties for the temperature-coefficient determinations from the critical-rod data are quoted as ±1.42 inhours; errors associated with period measurements are given as ±1.44 inhours. Figure 9 shows the results of measurements of the isothermal temperature coefficient of reactivity as a function of temperature over the 400 to 600°F range.

Table 4 Calculated and Measured Midplane[3] Reaction Rates in Core Subassemblies*

(8-Group X,Y; CRAM No. 011067)

	^{235}U fission			^{238}U fission			^{238}U capture		
	Calculated	Measured	Difference, †%	Calculated	Measured	Difference, †%	Calculated	Measured	Difference, †%
P00–P00	10.16	10.47	3.0	10.52	10.43	−0.9	10.11	9.95	−1.6
P00–P01	10.04	10.18	1.4	10.53	10.78	2.4	9.96	9.77	−1.9
N01–P01	9.99	9.86	−1.3	10.24	10.51	2.6	9.90	9.21	−7.0
P02–P00	9.50	9.47	−0.3	9.85	9.75	−1.0	9.44	9.54	1.1
P00–P03	9.04	9.44	4.4	9.69	9.72	0.3	8.89	8.89	0
P04–P00	7.98	7.64	−4.3	8.46	8.18	−3.3	7.89	7.76	−1.6
N03–P03	7.63	7.80	2.2	8.20	8.32	1.5	7.51	7.74	3.1
P00–P05‡	6.40	6.75	5.5	6.17	5.92	−4.1	6.41	6.38	−0.5
P05–P00	6.57	6.57	0	6.70	6.50	−3.0	6.53	6.43	−1.5
N04–P04	5.52	5.40	−2.2	5.04	5.17	2.6	5.56	5.92	6.5
N04–N04	6.24	5.83	−6.6	5.45	5.45	0	6.48	6.64	2.5
N05–N03	5.87	5.82	−0.9	4.91	5.10	3.9	6.15	6.39	3.9
P06–P00	5.05	4.77	−5.5	4.24	4.18	−1.4	5.17	5.37	3.9

*Each reaction-rate type is normalized so that the total for all subassemblies is 100.
†Percentage by which the measured value exceeds the calculated value.
‡This is the only core portion for which the integrated-count method was used to normalize the power.

Table 5 Values of Isothermal Temperature Coefficients from Positive-Period and Critical-Rod-Position Measurements*

Nominal temperature range, °F	Temperature coefficient (positive-period method), inhours/°F	Temperature coefficient (critical-rod-position method), inhours/°F
400–440	−0.8436 ± 0.0127	−0.8451
440–480	−0.8453 ± 0.0179	−0.8473
480–520	−0.8492 ± 0.0179	−0.8580
500–520	−0.8498 ± 0.0414	−0.8081
500–540	−0.8326 ± 0.0253	−0.8100
520–540	−0.8388 ± 0.0414	−0.8119
520–560	−0.8474 ± 0.0104	−0.8730
560–600	−0.8665 ± 0.0090	−0.8672

*Taken from data in Ref. 4.

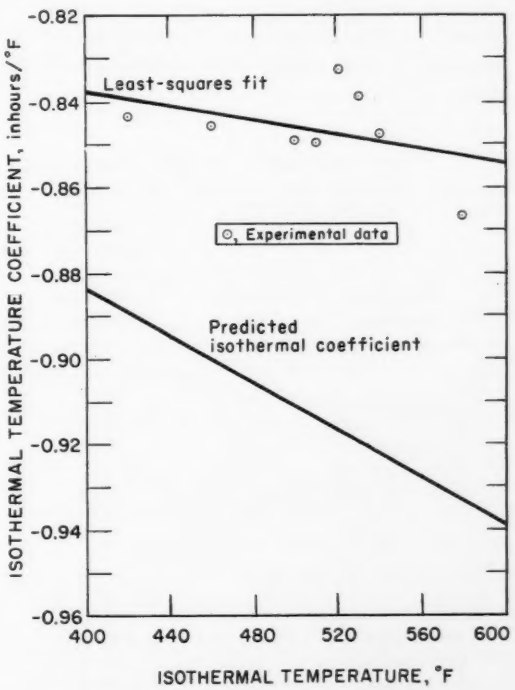

Fig. 9 Isothermal temperature coefficient vs. temperature.[4]

Power Coefficient. Power-coefficient measurements[5] were made at four different times during the nuclear test program at increasing power levels between 13 and 100 MW(t) (nominal) from Jan. 13 to July 12, 1966. These measurements were made during both power ascent and descent as a check for possible hysteresis effects like those observed in the EBR-II. Results are given in Tables 6 and 7 and Figs. 10 to 13. These data were corrected for only the inlet temperature to obtain reactivity loss as a function of operating power. However, as shown in Table 8, the metered-flow and -power values were corrected by the appropriate calibration factors to obtain the flow-dependent power coefficients. Power-coefficient values for all four sets of measurements are summarized in Table 8.

The components of the total temperature and power coefficients of reactivity for the Fermi reactor are the Doppler coefficient and the expansion-temperature coefficients. The total reactivity coefficient is the sum of these components. The best predicted value for the power coefficient, based on the product of an at-power temperature coefficient and the derivative of a selected average base temperature with respect to power, is −0.1864 cent/MW(t); the corresponding measured value is −0.174 cent/MW(t). The at-power temperature coefficients are defined with respect to the average base temperature and are dependent on the isothermal-temperature-coefficient values.

Transfer-Function Measurements

Reactor transfer-function measurements[6] were made using oscillator and reactivity-pulse tests. The oscillator tests were effected by means of two oscillator rods, one for low-power transfer-function measurements and the other for high-power transfer-function measurements. The rotating oscillator-rod assembly contained a B_4C poison cartridge mounted eccentrically to the axis of rotation. Rotation of this poison section induced a sinusoidal reactivity perturbation of known amplitude and phase angle. The amplitude and phase angle of the flux perturbation were measured relative to the reactivity perturbation and were then used to compute the transfer functions of the reactor. Transfer-function measurements were also made by generating reactivity pulses by a single, trapezoidal movement of the regulating rod. The perturbations in power and temperature which were induced by this regulating-rod motion were measured, and the data were reduced by Fourier analyses of their time derivatives.

The dynamic behavior of the reactor under various operating conditions can be determined from analysis of the transfer functions.

Oscillator Tests. The sinusoidal reactivity perturbation produced by the oscillator rod caused a power perturbation that was used as input for the transfer-

Table 6 Power-Coefficient Data Analyses: First and Second Measurements[5]

Operating conditions	Keithley power, MW(t)	Change in critical-rod position relative to first data point, in.	Loss in excess reactivity relative to first data point, inhours	Change in core inlet temperature relative to first data point, °F	Inlet-temperature reactivity correction, inhours	Net excess-reactivity loss relative to first data point	
						Inhours	Cents
			First Measurement				
13.3 MW(t) maximum power; two-loop operation; total metered flow of 5.63×10^6 lb/hr	0.492	0	0	0	0	0	0
	6.80	0.12	1.20	−5.62	4.62	5.82	1.82
	13.13	0.62	6.20	−7.12	5.84	12.04	3.78
	13.13	0.56	5.60	−5.92	4.84	10.44	3.28
	13.11	0.52	5.20	−6.97	5.72	10.92	3.42
	6.45	0.19	1.90	−4.27	3.50	5.40	1.69
	0.483	−0.29	−2.90	−4.12	3.37	0.47	0.15
			Second Measurement				
20.0 MW(t) maximum power; three-loop operation; total metered flow of 8.95×10^6 lb/hr	0.489	0	0	0	0	0	0
	10.15	0.62	6.20	0.10	−0.08	6.12	1.92
	19.85	1.28	12.80	0.40	−0.33	12.47	3.91
	9.85	0.70	7.00	0.70	−0.57	6.43	2.02
	0.487	0.08	0.80	0.80	−0.65	0.15	0.05

Table 7 Power-Coefficient Data Analyses: Third and Fourth Measurements[5]

Operating conditions	Keithley power, MW(t)	Change in critical-rod position relative to first data point, in.	Loss in excess reactivity relative to first data point, inhours	Inlet-temperature change relative to first data point, °F		Inlet-temperature reactivity correction, inhours		Integrated power relative to first data point, MWd	Burnup reactivity correction inhours	Net excess-reactivity loss relative to first data point			
										Core inlet temperature corrected		Reactor inlet temperature corrected	
				Core	Reactor	Core	Reactor			Inhours	Cents	Inhours	Cents
Third Measurement													
66.7 MW(t) maximum	0.496	0	0	0	0	0	0	0	0	0	0	0	0
power; two-loop	39.40	4.76	48.8	15.1	16.2	−12.4	−13.3	2.21	−0.11	36.24	11.36	35.28	11.06
operation; total	65.70	8.86	82.3	28.1	28.6	−23.0	−23.4	8.74	−0.45	58.73	18.41	58.41	18.31
metered flow of	40.0	5.03	51.4	16.4	18.5	−13.4	−15.2	13.16	−0.67	37.29	11.69	35.54	11.14
5.42×10^6 lb/hr	13.27	2.43	24.3	13.2	14.7	−10.8	−12.1	14.66	−0.75	12.76	4.00	11.52	3.61
	0.970	0.15	1.5	−1.8	−0.2	+1.5	+0.16	14.98	−0.76	2.23	0.70	0.93	0.29
Fourth Measurement													
100 MW(t) maximum	0.249	0	0	0	0	0	0	0	0	0	0	0	0
power; three-loop	19.98	1.33	13.80	4.3	4.4	−3.52	−3.61	0.69	−0.04	10.42	3.28	10.33	3.24
operation; total	40.30	2.84	29.50	9.4	10.9	−7.71	−8.94	1.52	−0.08	21.76	6.82	20.53	6.43
metered flow of	59.40	4.47	44.80	15.9	16.4	−13.04	−13.44	3.36	−0.17	31.59	9.92	31.19	9.78
9.61×10^6 lb/hr	80.40	6.26	59.60	20.5	20.7	−16.80	−17.0	9.61	−0.50	42.30	13.25	42.10	13.20
	99.35	8.35	73.00	20.5	25.5	−16.80	−20.90	16.18	−0.83	55.37	17.30	51.27	16.08
	109.40	10.16	81.80	22.9	29.1	−18.80	−23.80	20.55	−1.05	61.95	19.40	56.95	17.82
	109.40	9.91	80.70	20.7	27.3	−16.98	−22.40	25.87	−1.32	62.40	19.55	56.98	17.85
	99.35	8.25	72.70	16.9	21.9	−13.88	−17.98	28.42	−1.45	57.37	17.97	53.27	16.69
	79.20	6.00	57.50	12.3	17.8	−10.10	−14.60	32.16	−1.64	45.76	14.35	41.26	12.93
	59.70	4.40	44.30	7.5	13.1	−6.15	−10.72	35.08	−1.79	36.36	11.39	31.79	9.97
	40.0	2.87	29.60	1.8	7.6	−1.48	−6.24	36.12	−1.84	26.28	8.25	21.52	6.74
	19.69	1.76	18.10	2.6	5.2	−2.13	−4.26	36.85	−1.88	14.09	4.22	11.96	3.75
	0.770	0.23	2.30	−7.1	−0.9	+5.82	+0.74	37.14	−1.89	6.23	1.95	1.15	0.36

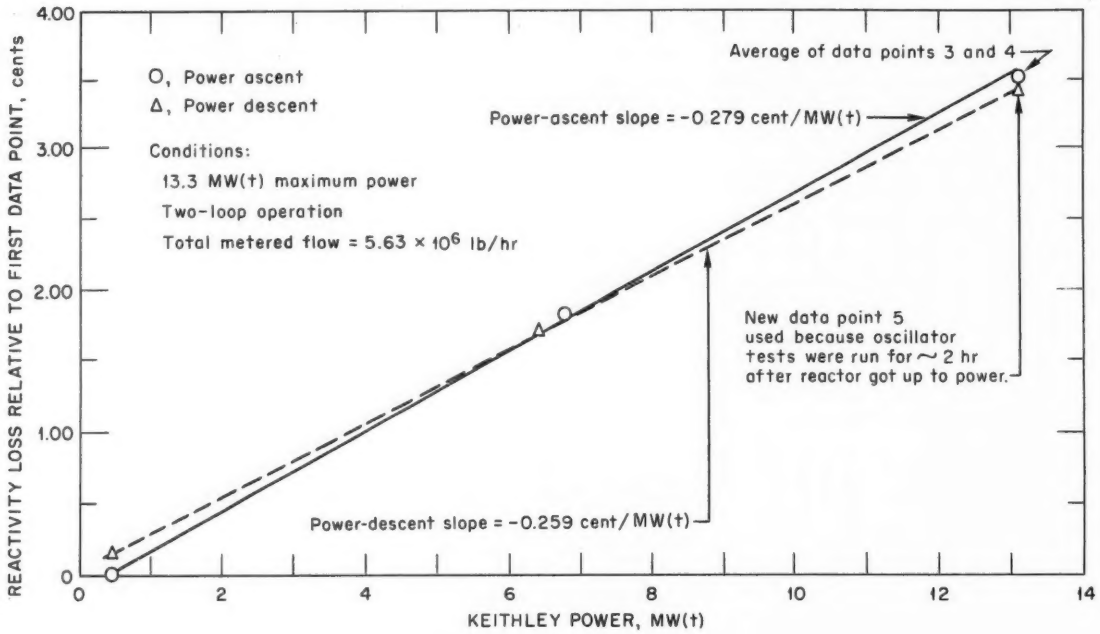

Fig. 10 Power-coefficient measurement corrected for core inlet temperature.[5]

function analyzer. The output of this analyzer was, in turn, the in-phase (real) and quadrature (imaginary) components of the reactor power oscillations.

Transfer-function measurements at essentially "zero" power covered the frequency spectrum of 0.005 to 5.0 Hz. The actual power range was 0.340 to 2.0 MW(t) and was chosen because it had no detectable reactivity feedback. Results of these measurements of the amplitude and phase-angle components of the transfer function are shown in Figs. 14 and 15.

At-power transfer-function measurements were made at 67 and 111 MW(t). These measurements were then combined with the zero-power transfer-function measurements to obtain the reactivity-feedback transfer function.

The amplitude and phase-angle components of the reactivity-feedback transfer function as corrected for fission-product feedback are shown in Figs. 16 and 17 for the reactor in the manual-control mode.

Transfer-function measurements were also made with the reactor in the automatic control mode. Two feedback effects occur when the reactor is in this automatic mode. One effect is attributed to the reactor system as a whole and is analytically represented by the feedback transfer function for the reactor system. The automatic control system contributes the second feedback effect; this feedback must be measured and extracted from the reactor transfer function that is measured while the reactor is in the automatic control mode. The amplitude and phase-angle components[6] of the automatic-control-system feedback transfer function are shown in Figs. 18 and 19.

Reactivity-Pulse Tests. An analog-computer-generated velocity-demand signal to the regulating rod was used to provide step-reactivity insertions as another method for obtaining reactor transfer functions. The velocity-demand signal automatically withdrew the regulating rod from its critical position a specified increment, held this new position for a given period of time, and then returned the rod to its initial position. Although the analog circuit is capable of producing either positive or negative reactivity pulses, only positive pulses were used for the Fermi transfer-function tests. The data, which were recorded on magnetic tape for Fourier analysis, were taken at 0.05, 56, and 88 MW(t). Figures 20 to 22 show the amplitude and phase-angle components of the transfer functions measured at these power levels.

Transfer-function data measured by pulse and oscillator techniques are compared in Table 9.

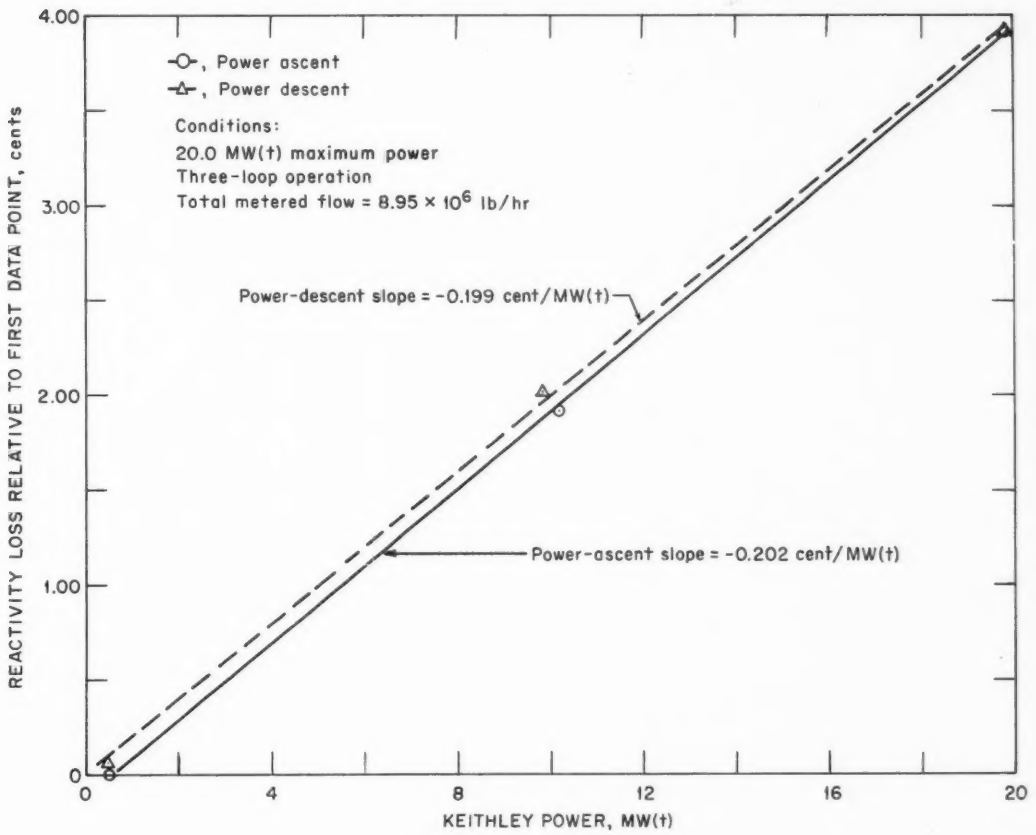

Fig. 11 Power-coefficient measurement corrected for core inlet temperature.[5]

Control- and Safety-Rod Calibrations

Detailed calibration measurements of the control and safety rods[8] were made during low-power testing in October and November 1963.

Regulating Rods and Shim Rods. Calibration of the regulating rod was achieved by positive- and negative-period measurements. Count-rate data from BF_3 counters and a Keithley micromicroammeter were plotted on semilog paper to obtain reactor periods; the period data were averaged and were then converted to reactivity by using the inhour relation. The calibration values thus obtained are listed in Table 10. Figure 23 compares measured and predicted (from ZPR-III critical-mockup data) calibration values for the rod fully unshadowed and fully shadowed.

Shim-rod calibrations were effected by subcritical count-rate reactivity measurements. Results of these calibrations are shown in Fig. 24.

Safety Rods. Subcritical count-rate reactivity measurements were also used in safety-rod calibrations. Table 11 shows the results for the fully shadowed and fully unshadowed safety rods, and Fig. 25, for the ganged safety rods.

SUMMARY

The results of physics tests on Core A as summarized here should permit (1) a generalized assessment of reactor characteristics and behavior and (2) a comparison with future core loadings, such as the oxide one planned for Core B. As results of testing subsequent to reactor restart are made publicly available, this summary will be updated.

Readers who need more detailed information on Fermi than that given in this article and in the

(Text continues on page 212.)

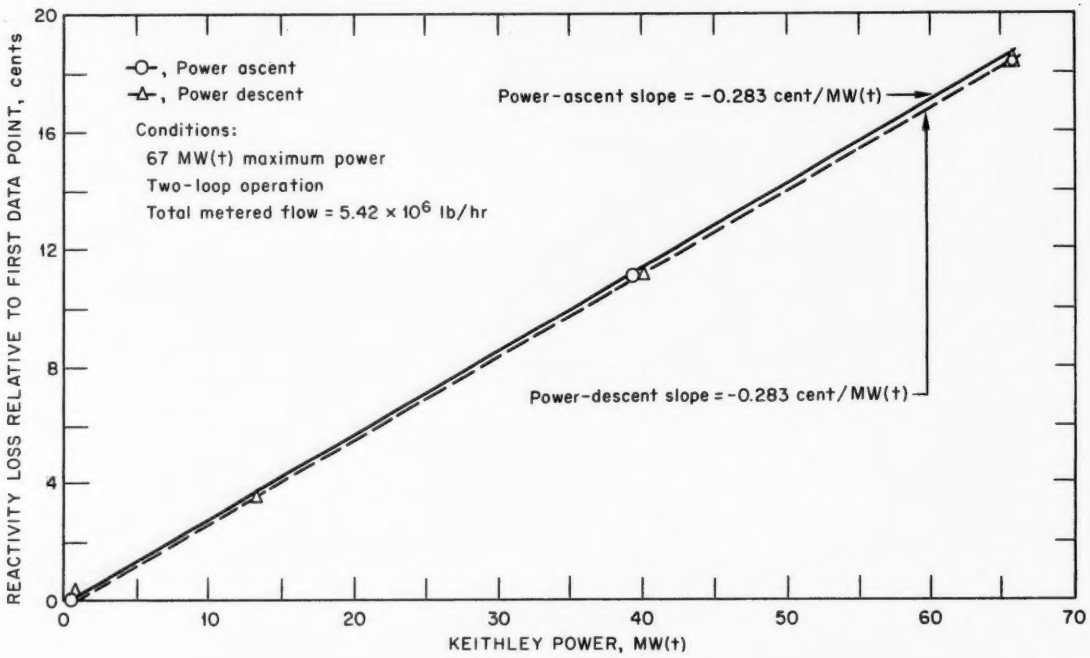

Fig. 12 Power-coefficient measurement corrected for reactor inlet temperature.[5]

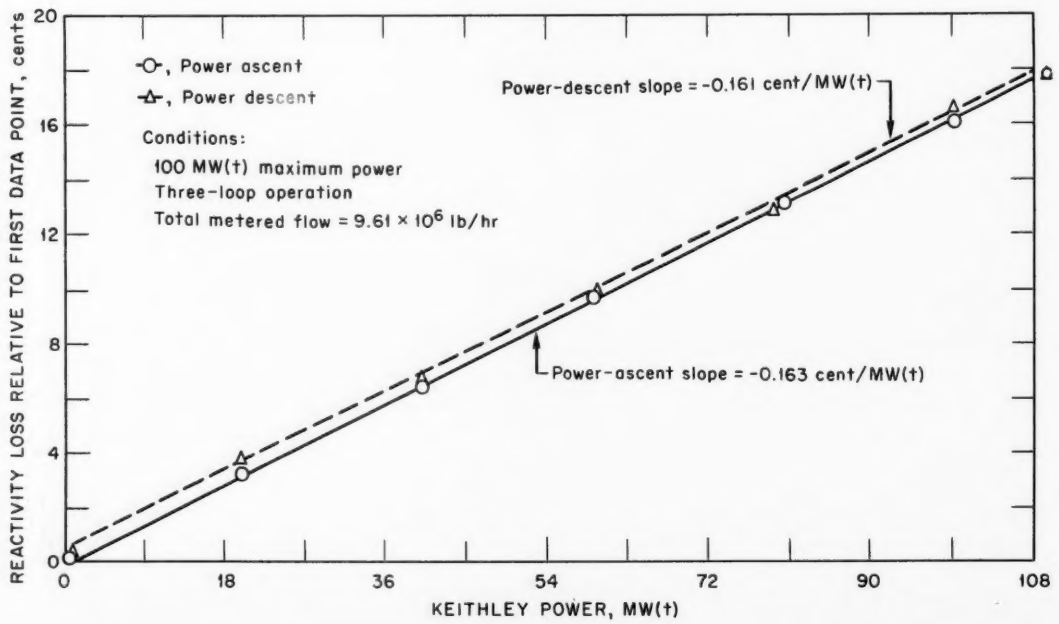

Fig. 13 Power-coefficient measurement corrected for reactor inlet temperature.[5]

Table 8 Power-Coefficient Data Corrected for Power and Flow[5]

Test description	Loop No.	Sum of 14- and 6-in.-line flows, 10^6 lb/hr: Meter	Correction factor	Actual	Desired programmed flow	Initial power coefficient, cents/MW(t)	Power-calibration correction factor	Initial power coefficient corrected for power, cents/MW(t)	Flow correction, cents/MW(t)	Final corrected power coefficient, cents/MW(t)	Extrapolated power coefficient,* cents/MW(t)
Measurement 1, at 13 MW(t) with two loops operating	1	3.04	0.889	2.70	2.95						
	2	−0.20	0.913	−0.18	0	−0.269 (±25%)	1.12	−0.301 (±23%)	+0.054	−0.247 (±13%)	−0.167 (Three loops)
	3	2.79	0.845	2.36	2.95						
	Total	5.63	–	4.88	5.90						
Measurement 2, at 20 MW(t) with three loops operating	1	3.00	0.889	2.67	2.95						
	2	3.00	0.913	2.74	2.95	−0.200 (±25%)	1.12	−0.224 (±23%)	+0.020	−0.204 (±13%)	−0.302 (Two loops)
	3	2.95	0.845	2.49	2.95						
	Total	8.95	–	7.90	8.85						
Measurement 3, at 67 MW(t) with two loops operating	1	2.75	0.889	2.44	2.95						
	2	2.83	0.913	2.58	2.95	−0.283 (±23%)	1.12	−0.317 (±20%)	+0.054	−0.263 (±7½%)	−0.178 (Three loops)
	3	−0.16	0.845	−0.14	0						
	Total	5.42	–	4.88	5.90						
Measurement 4, at 100 MW(t) with three loops operating	1	3.12	0.889	2.77	2.95						
	2	3.17	0.913	2.89	2.95	−0.162 (±23%)	1.12	−0.181 (±20%)	+0.007	−0.174 (±7½%)	−0.258 (Two loops)
	3	3.32	0.845	2.81	2.95						
	Total	9.61	–	8.47	8.85						

*Two-loop to three-loop or three-loop to two-loop.

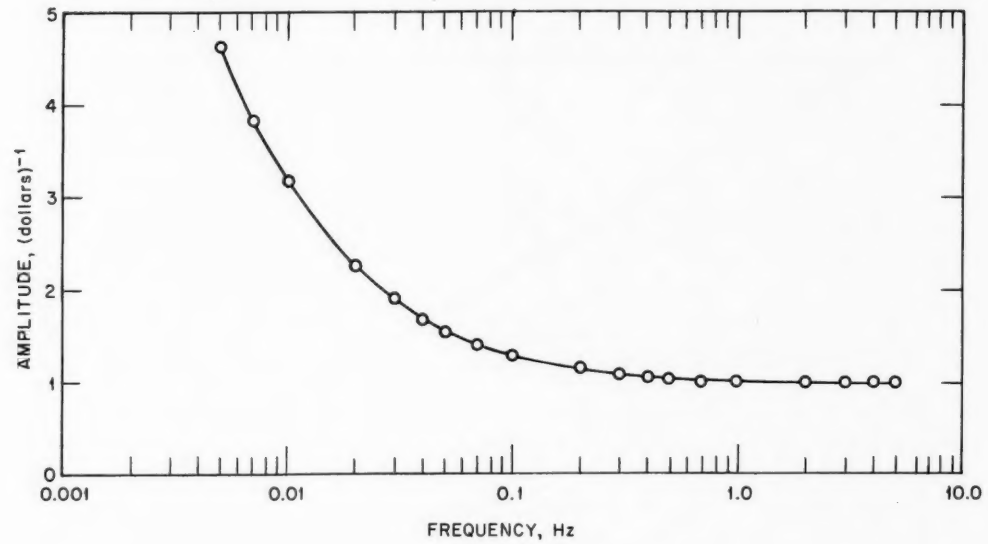

Fig. 14 Amplitude component of the transfer function in oscillator tests at zero power.[6]

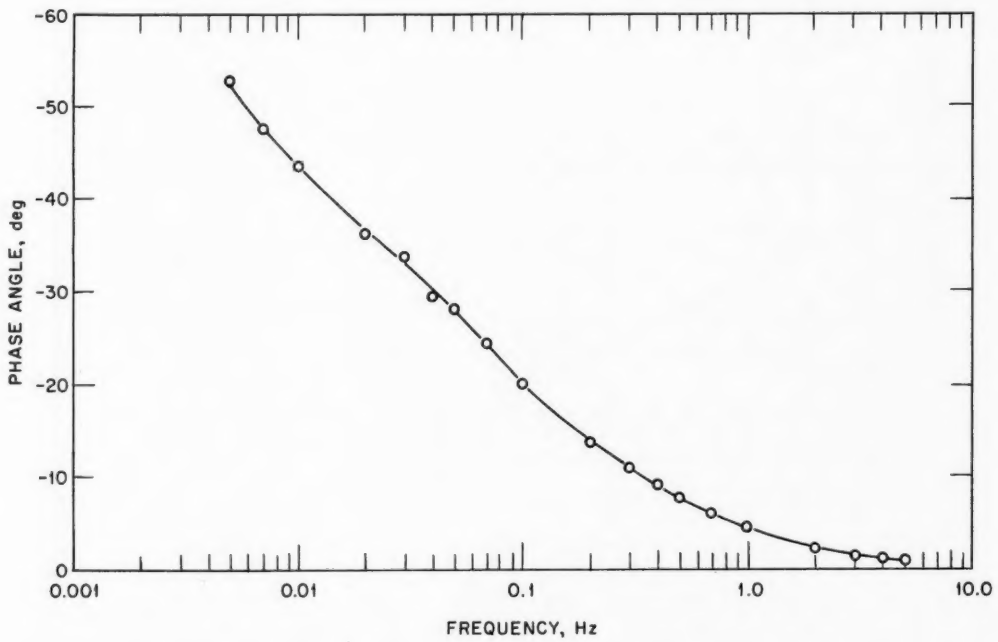

Fig. 15 Phase-angle component of the transfer function in oscillator tests at zero power.[6]

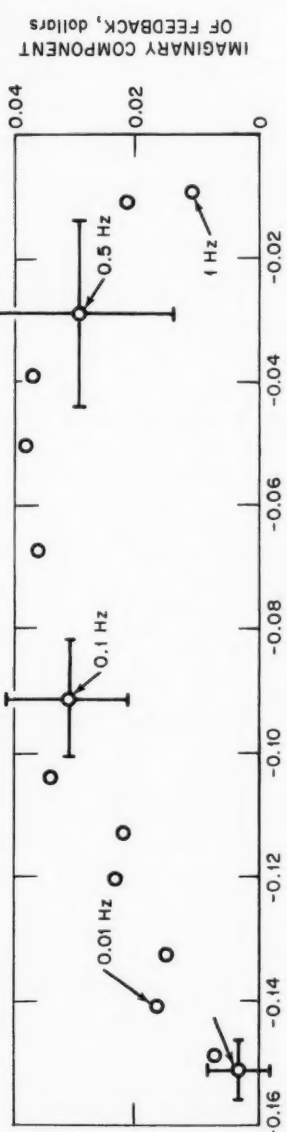

Fig. 16 Feedback transfer function at the 67-MW(t) power level with the reactor on manual control.[6] —, estimated uncertainty, real component. I, estimated uncertainty, imaginary component.

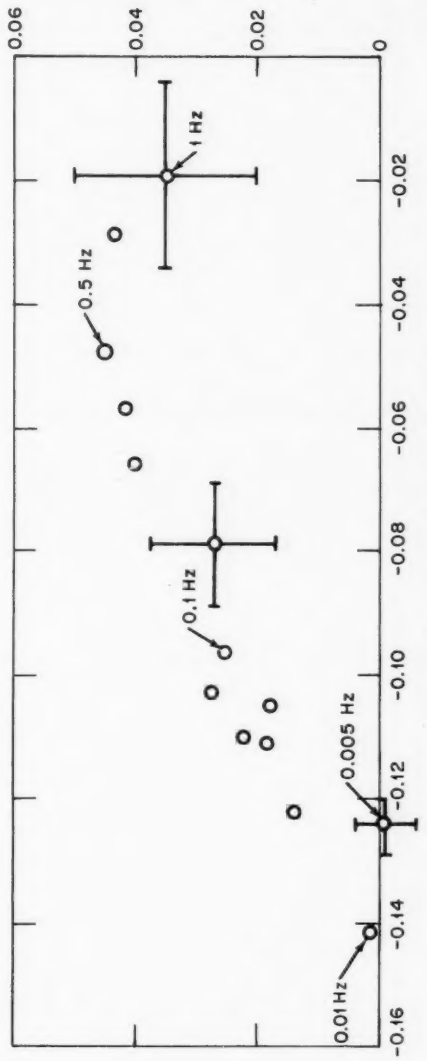

Fig. 17 Feedback transfer function at the 111-MW(t) power level with the reactor on manual control.[6] —, estimated uncertainty, real component. I, estimated uncertainty, imaginary component.

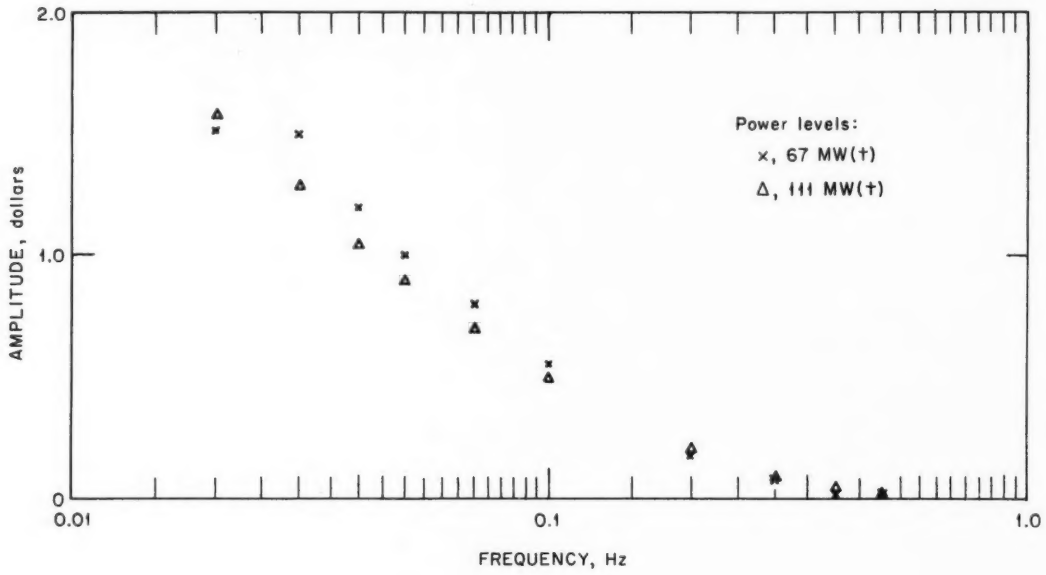

Fig. 18 Amplitude component of the transfer function for automatic control.[6]

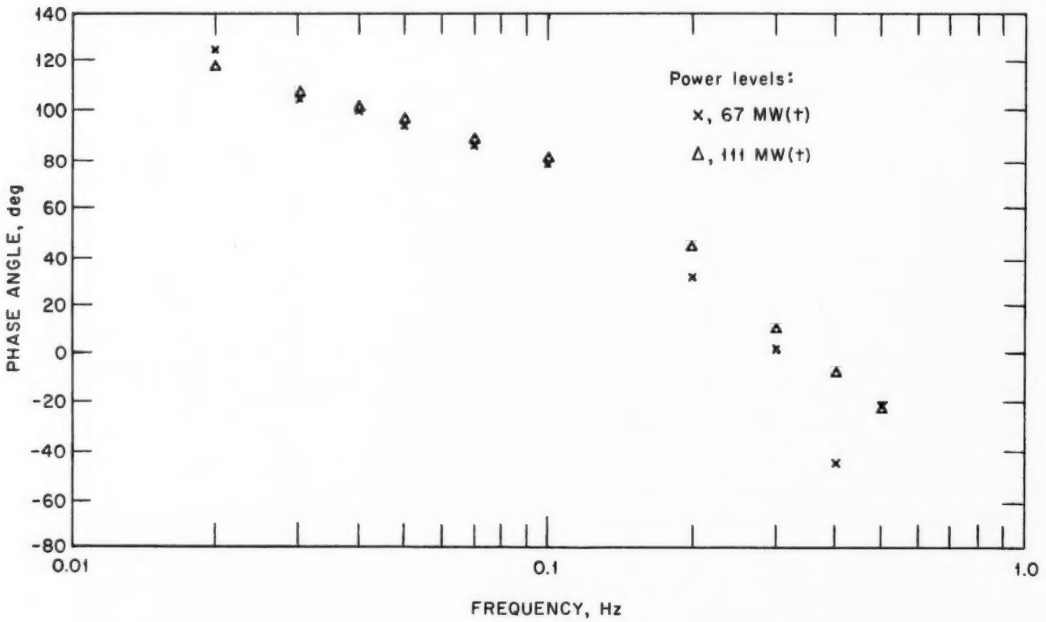

Fig. 19 Phase-angle component of the transfer function for automatic control.[6]

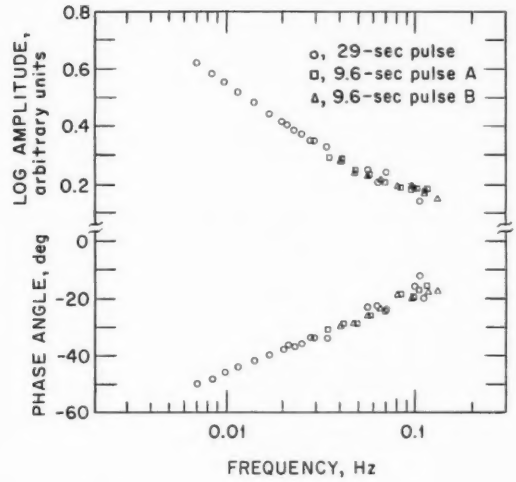

Fig. 20 Amplitude and phase-angle components of the reactivity-to-power transfer function as measured at the 0.05-MW(t) power level.[7]

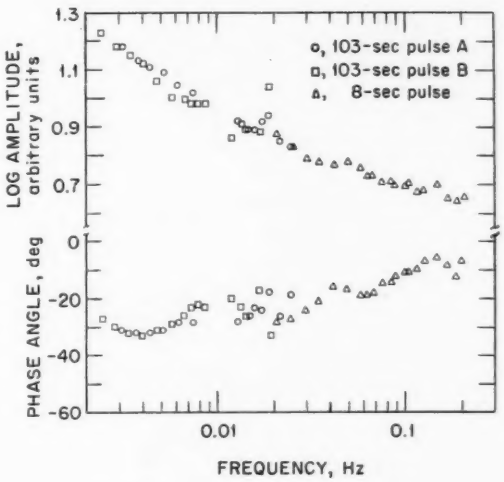

Fig. 22 Amplitude and phase-angle components of the reactivity-to-power transfer function as measured at the 88-MW(t) power level.[7]

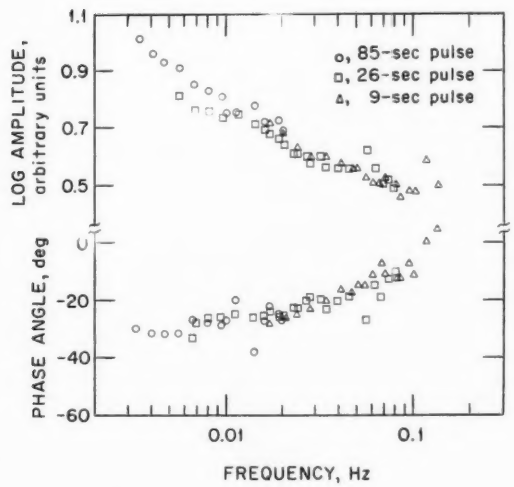

Fig. 21 Amplitude and phase-angle components of the reactivity-to-power transfer function as measured at the 56-MW(t) power level.[7]

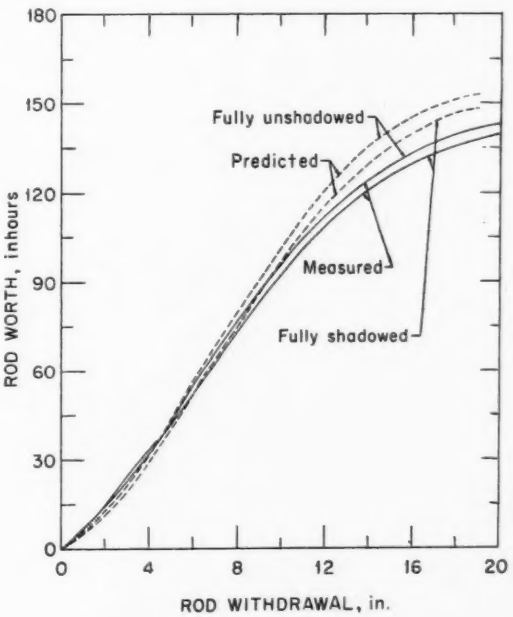

Fig. 23 Regulating-rod calibration curves.[8]

Table 9 Comparison of Reactivity-to-Power Transfer Functions as Measured by Pulse and Oscillator Techniques[7]

Transfer-function parameter	Measurement technique	Units	Frequency, Hz									
			0.005	0.007	0.01	0.02	0.03	0.04	0.05	0.07	0.1	0.2
0.05-MW(t) Reactor Power Level with Three Loops Operating												
Amplitude	Pulse	None		4.15	3.52	2.54	2.14	1.90	1.75	1.60	1.50	
	Oscillator	$(\text{Dollars})^{-1}$	4.63	3.82	3.21	2.28	1.93	1.70	1.58	1.42	1.32	1.17
	Pulse ÷ osc.	*		0.95	0.96	0.98	0.98	0.98	0.97	0.99	1.00	
	Theoretical	$(\text{Dollars})^{-1}$	4.19	3.50	2.95	2.16	1.80	1.60	1.49	1.38	1.28	1.12
	Pulse ÷ theory	*		1.01	1.02	1.00	1.01	1.01	1.00	0.99	1.00	
Phase	Pulse	Degrees		50	46	38	33	30	28	24	20	
	Oscillator	Degrees	53	48	44	37	34	30	28	24	20	14
	Pulse–osc.	Degrees		2	2	1	−1	0	0	0	0	
56-MW(t) Reactor Power Level with Two Loops Operating												
Amplitude	Pulse	None	8.30	7.00	5.90	4.38	3.92	3.73	3.55	3.24	2.92	
	Oscillator	$(\text{Dollars})^{-1}$	3.00	2.63	2.37	1.83	1.63	1.47	1.36	1.27	1.19	1.09
	Pulse ÷ osc.	*	1.13	1.09	1.02	0.98	0.98	1.04	1.07	1.04	1.00	
Phase	Pulse	Degrees	32	30	27	26	22	19	16	12	8	
	Oscillator	Degrees	30	29	28	27	25	24	22	19	16	10
	Pulse–osc.	Degrees	2	1	−1	−1	−3	−5	−6	−7	−8	
88-MW(t) Reactor Power Level with Three Loops Operating												
Amplitude	Pulse	None	12.8	10.4	9.10	7.23	6.47	6.00	5.75	5.33	5.00	
	Oscillator	$(\text{Dollars})^{-1}$	3.17	2.73	2.33	1.86	1.64	1.48	1.38	1.26	1.18	1.08
	Pulse ÷ osc.	*	0.95	0.90	0.92	0.92	0.93	0.96	0.98	1.00	1.00	
Phase	Pulse	Degrees	31	26	24	22	21	20	19	16	11	
	Oscillator	Degrees	35	33	30	28	26	24	22	19	16	11
	Pulse–osc.	Degrees	−4	−7	−6	−6	−5	−4	−3	−3	−5	

*Normalized to 1.00 at 0.1 Hz.

Table 10 Regulating-Rod Calibration*

Regulating-rod withdrawal, in.	Worth with shim rod withdrawn 20 in., inhours
2.0	14.27
4.0	32.02
6.0	54.48
8.0	76.21
12.0	111.50
14.0	124.13
16.0	132.95
18.0	138.65
20.0	142.98

*Taken from data in Table 2 of Ref. 8.

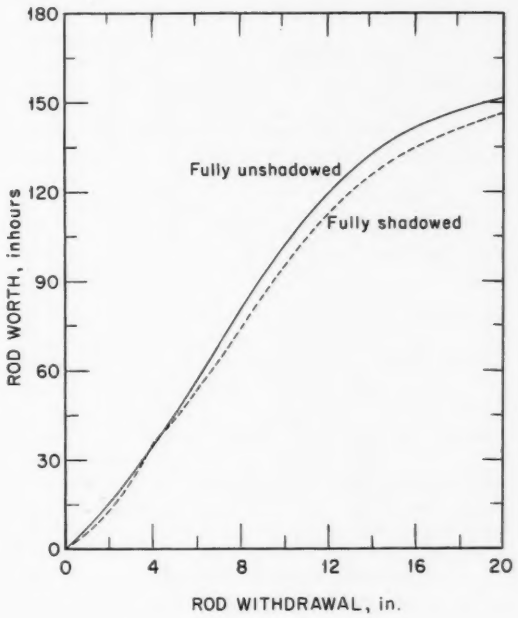

Fig. 24 Shim-rod calibration curves.[8]

Table 11 Safety-Rod Calibrations[8,9]

Safety rod No.	Predicted worth from critical experiment			Measured worth from rod-drop tests			Measured worth (this test)		
	Unshadowed, dollars	Shadowed, dollars	Reduction, %	Unshadowed, dollars	Shadowed, dollars	Reduction, %	Unshadowed, dollars	Shadowed, dollars	Reduction, %
1	1.45	1.13	22	1.28	1.02	20	1.26	1.10	13
2	1.65	1.29	22	1.46	1.14	22	1.48	1.35	9
3	1.45	1.13	22	1.19	1.04)	(12½)			
4	1.34	1.05	22	1.20	1.01	16	1.22	0.98	20
5	1.34	1.05	22	TIT	TIT	TIT	RS	RS	RS
6	1.45	1.13	22	1.25	1.00	20			
7	1.65	1.29	22	1.38	1.08	22			
8	1.45	1.13	22	1.16	(1.02)	(12½)			
Seven-rod-bank worth					8.00		9.45	9.85	

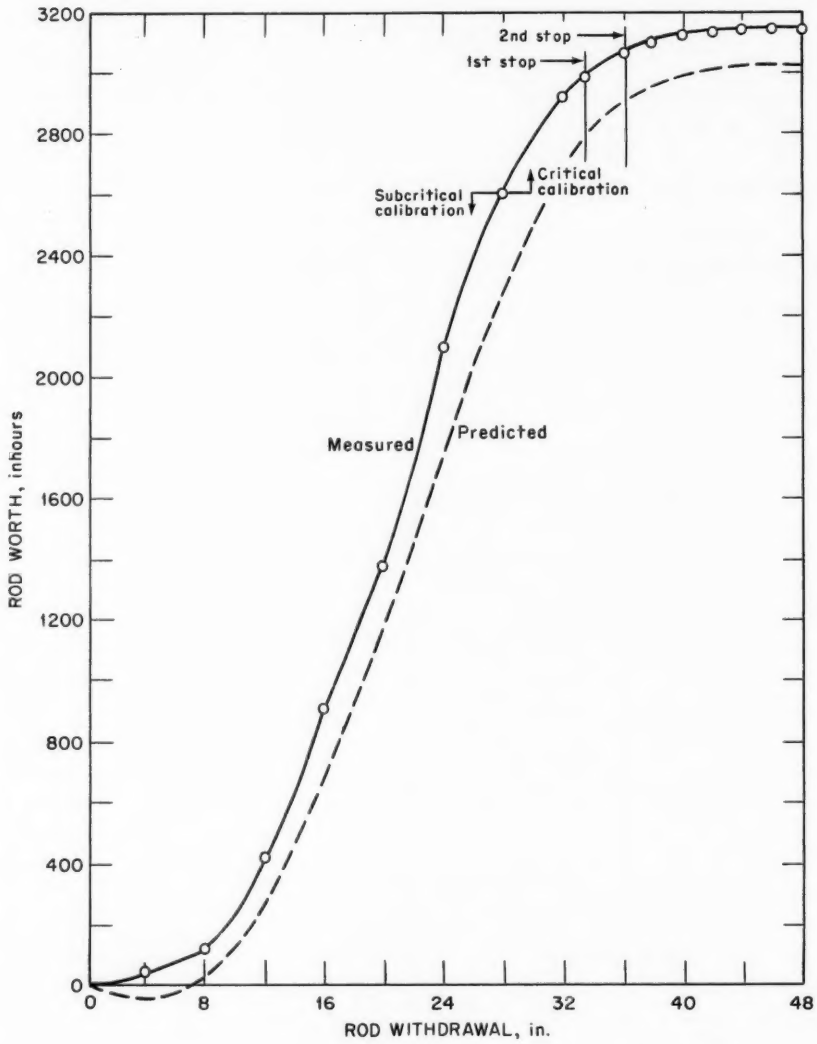

Fig. 25 Ganged-safety-rod calibration curves (seven rods).[8]

references should ask personnel of either Power Reactor Development Company (the reactor operator) or Atomic Power Development Associates, Inc. (the design and test group).

ACKNOWLEDGMENTS

I would like to express my sincere appreciation to A. E. Klickman of Atomic Power Development Associates for his detailed reviews of both preliminary and final manuscripts and for his many helpful suggestions and contributions.

REFERENCES

1. G. L. Ball, D. A. Daavettila, and R. E. Horne, Worth Measurements of Core and Blanket Subassembly Materials in the Enrico Fermi Reactor, Report APDA-NTS-6, Atomic Power Development Associates, Inc., September 1965.
2. B. M. Segal and R. E. Horne, Measurement of Sodium Worth in the Enrico Fermi Reactor, Report APDA-NTS-7, Atomic Power Development Associates, Inc., September 1966.
3. E. M. Page, R. E. Horne, R. J. Beaudry, and J. C. Montfort, Measurement and Calculation of the ^{235}U and ^{238}U Fission Distributions and ^{238}U Capture Distributions for the Enrico Fermi Fast Breeder Reactor, Report APDA-NTS-10, October 1967.

4. H. A. Wilber, E. A. Fischer, and R. E. Mueller, Measurement of the Isothermal Temperature Coefficient of Reactivity of the Enrico Fermi Reactor, Report APDA-NTS-5, Atomic Power Development Associates, Inc., June 1965.
5. R. E. Mueller and H. A. Wilber, Power Coefficient Measurements for the Enrico Fermi Reactor, Report APDA-NTS-9, Atomic Power Development Associates, Inc., November 1967.
6. A. E. Klickman, R. E. Horne, and H. A. Wilber, Oscillator Tests in the Enrico Fermi Reactor, Report APDA-NTS-11, August 1967.
7. M. L. Batch and A. E. Klickman, Transfer Functions from Reactivity Pulses Generated by the Regulating Rod: Enrico Fermi Reactor, Report APDA-NTS-14, Atomic Power Development Associates, Inc., December 1967.
8. R. E. Mueller and C. E. Branyan, Calibration Measurements of Control and Safety Rods in the Enrico Fermi Reactor, Report APDA-NTS-18, Atomic Power Development Associates, Inc., April 1968.
9. R. E. Horne and A. E. Klickman, Determination of the Safety Rod Drop Time in the Enrico Fermi Reactor, Report APDA-NTS-3, Atomic Power Development Associates, Inc., January 1965.

SUGGESTED READING LIST

R. E. Mueller, C. E. Branyan, and J. B. Nims, Initial Loading to Criticality of the Enrico Fermi Reactor, Report APDA-NTS-1, Atomic Power Development Associates, Inc., May 1964.

R. E. Mueller and H. A. Wilber, Determination of Control Rod Float in the Enrico Fermi Reactor, Report APDA-NTS-2, Atomic Power Development Associates, Inc., November 1964.

R. E. Mueller and H. A. Wilber, Investigation of Core Reproducibility of the Enrico Fermi Reactor, Report APDA-NTS-4, Atomic Power Development Associates, Inc., April 1965.

R. B. Nicholson, The Doppler Effect in Fast Neutron Reactors, Report APDA-139, Atomic Power Development Associates, Inc., June 1960.

E. M. Page and R. E. Horne, Flux Mapping Measurements to Determine the Location of the Permanent Detectors in the Enrico Fermi Reactor, Report APDA-NTS-8, Atomic Power Development Associates, Inc., September 1966.

R. E. Horne and E. M. Page, Measured and Calculated Fission Distribution in the Fermi Reactor, *Trans. Amer. Nucl. Soc.*, 7(2): (November 1964).

E. A. Fischer, Calculation of the Doppler Coefficient for Plutonium Oxide Fueled Fast Reactors, Report APDA-157, Atomic Power Development Associates, Inc., November 1963.

W. G. Davey and R. N. Curran, An Experimental Investigation of Some Sources of Errors in the Measurement of Absolute Fission Ratios in Fast Reactors, USAEC Report ANL-6468, Argonne National Laboratory, November 1961.

C. E. Branyan, Core A Critical Studies for the Enrico Fermi Atomic Power Plant on ZPR-III, USAEC Report ANL-6629, Argonne National Laboratory, October 1962.

A. E. Klickman et al., Reactor Dynamics Measurements on the Enrico Fermi Reactor, in Proceedings of the International Conference on Fast Critical Experiments and Their Analysis, October 10–13, 1966, USAEC Report ANL-7320, pp. 629-652, Argonne National Laboratory, 1967.

H. A. Bethe, Reactor Safety and Oscillator Tests, Report APDA-117, Atomic Power Development Associates, Inc., October 1956.

C. K. Sanathanan and Judith Koerner, Transfer Function Synthesis as a Ratio of Two Complex Polynomials, USAEC Report ANL-6716, Argonne National Laboratory, May 1963.

J. B. Nims et al., Physics Measurements in U. S. Fast Power Reactors, in Seminar on Physics Measurements in Operating Power Reactors, Rome, May 9–13, 1966.

Sodium-Cooled Reactors: Current Status of EBR-II Physics Aspects (Runs 35 to 40)

By Myrna L. Steele*

REACTIVITY

Transfer-Function Measurements

Rod-drop experiments[1] were conducted at the beginning and end of Runs 35 and 36 to evaluate the possibility of changes in reactivity feedback during typical operating cycles. The results of the rod-calibration tests are listed in Table 1. The rod-worth values

Table 1 Rod-Calibration Tests[1] at 0.5 MW(t)

Time when tests were made	Rod worth, dollars
Beginning of Run 35	0.02003
End of Run 35	0.01978
Beginning of Run 36	0.02206
End of Run 36	0.02208

obtained were used to determine the feedback transfer function from the following time-dependent feedback model:

$$-H = \frac{0.18}{1+0.2s} + \frac{0.042}{1+0.4s} - \frac{0.055}{1+2.4s} + \frac{0.03e^{-8.0s}}{1+2.5s}$$

In this model the proper time constants and feedback amplitudes are given, and the convention of positive signs for negative feedback and negative signs for positive feedback is used. Results of the data fit to the above model are shown in Figs. 1 to 4.

Inspection of Figs. 2 and 4 reveals discrepancies between the predicted and measured feedback transfer functions[1] for the ends of Runs 35 and 36. Additional rod-drop measurements[2] at the beginning and end of Run 37 were conducted to investigate the possibility that the apparent discrepancies between Runs 35 and 36 were real. The data from Run 37 were fitted to the feedback model in the same manner as the data from Runs 35 and 36. The model, with the proper time constants and feedback amplitudes, is shown in Figs. 5 and 6.

Reactivity Effect of Plutonium

Effects of plutonium buildup[1] on fuel-burnup rate in the EBR-II were evaluated in terms of reactivity effects and reported in August 1969. A loss in reactivity as a function of burnup had been observed as 0.15 inhour/MWd at the start of a run and, then after about a week of operation, dropped off to about 0.12 inhour/MWd and stayed constant for the balance of the run. Calculations confirmed the change in burnup rate as a result of plutonium generation in the core and blanket. The plutonium is produced through the beta decay of ^{239}Np, which has a negligible worth compared to ^{239}Pu. Table 2 shows the results of calculations of plutonium buildup in the core, taking into account the neutron absorption in ^{239}Pu. During reactor shutdown the ^{239}Np decays, and, consequently, no plutonium is produced in the reactor during the first few days. After about 1 week of operation, the neptunium component reaches saturation and plutonium is formed at a constant rate. The calculated saturation value of the ^{239}Pu buildup is consistent with the 0.03 inhour/MWd which was inferred from experimental observations.

*U. S. Atomic Energy Commission, Division of Technical Information Extension, Oak Ridge, Tenn. 37830.

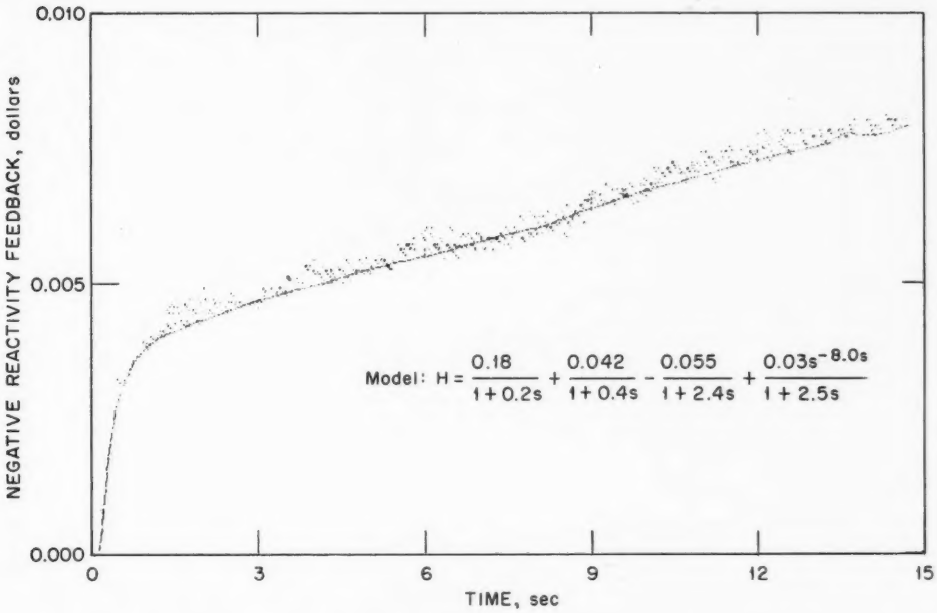

Fig. 1 Fit of rod-drop reactivity data[1] (from beginning of EBR-II Run 35) to Hyndman–Nicholson feedback model as presented in USAEC Report ANL-7476, July 1968.

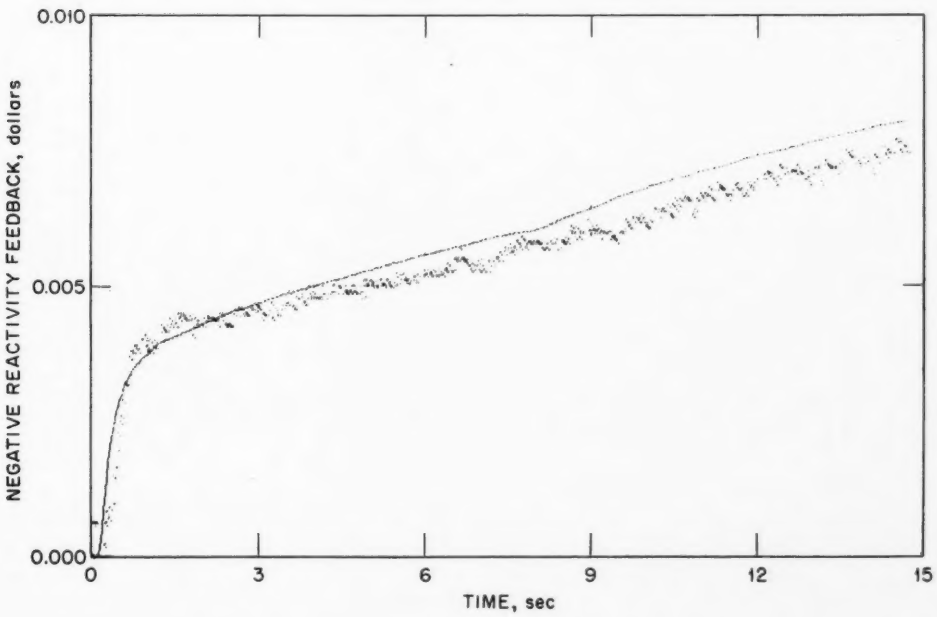

Fig. 2 Fit of rod-drop reactivity data[1] (from end of EBR-II Run 35) to Hyndman–Nicholson feedback model.

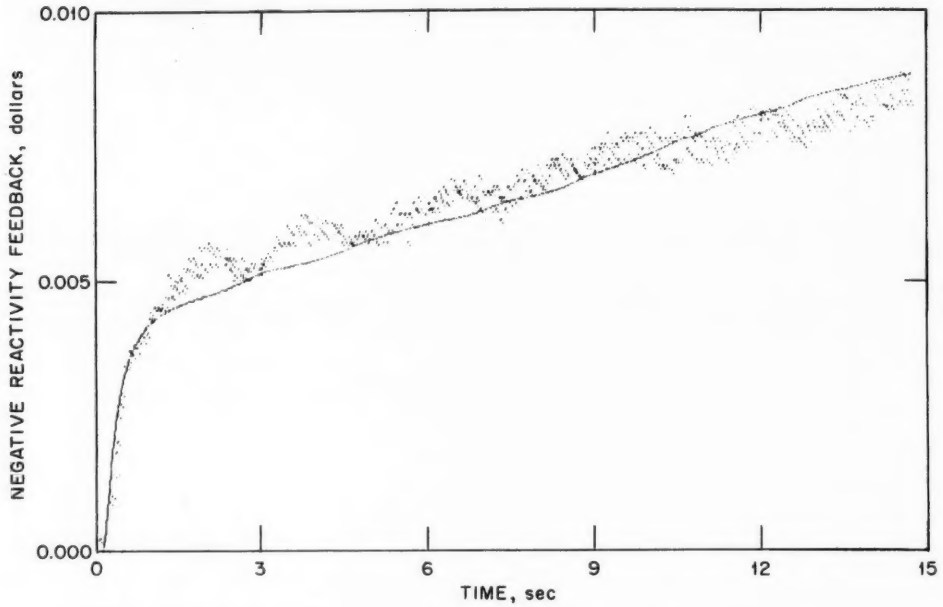

Fig. 3 Fit of rod-drop reactivity data[1] (from beginning of EBR-II Run 36) to Hyndman–Nicholson feedback model.

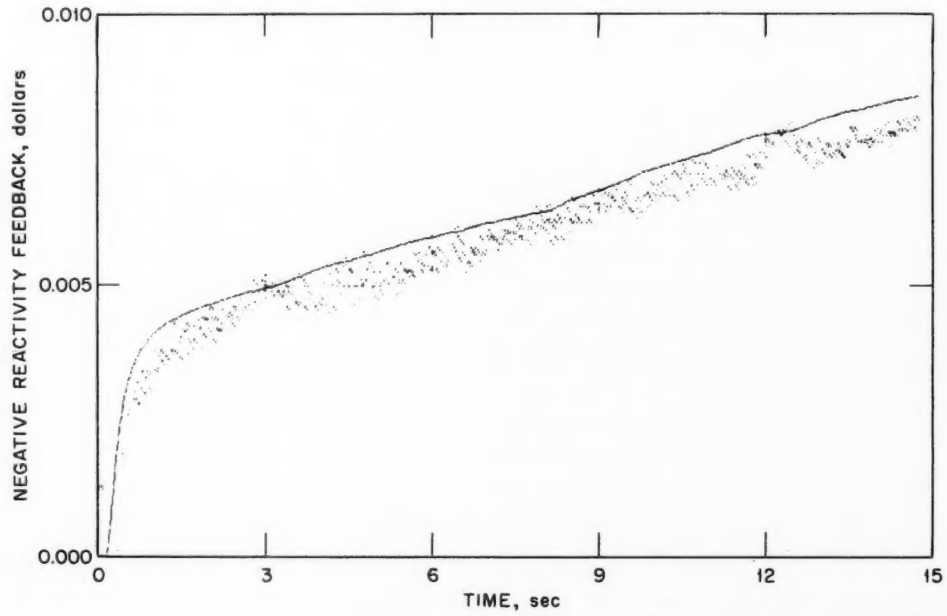

Fig. 4 Fit of rod-drop reactivity data[1] (from end of EBR-II Run 36) to Hyndman–Nicholson feedback model.

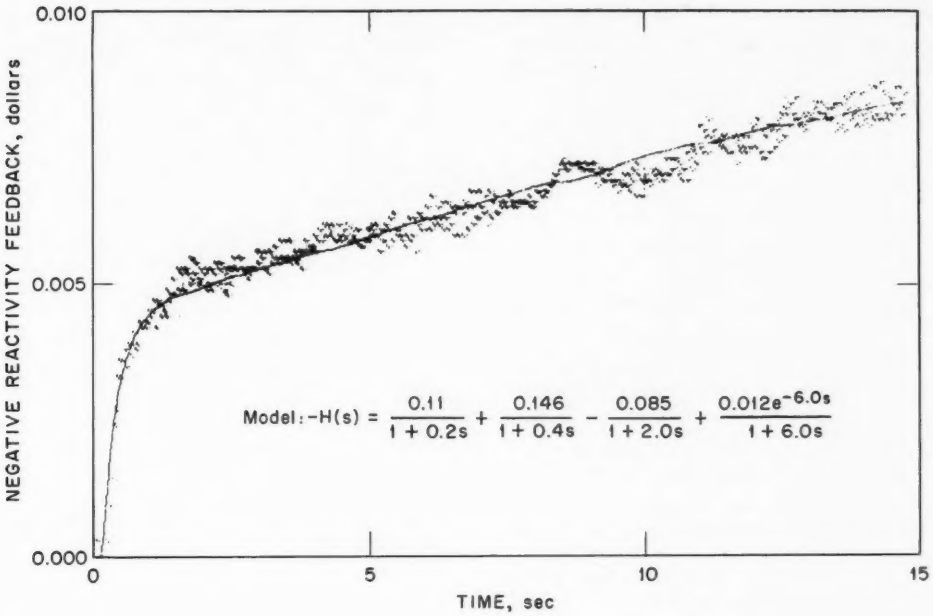

Fig. 5 Fit of rod-drop data from beginning[2] of Run 37 to time-dependent feedback model [50-MW(t)] power; 100% flow].

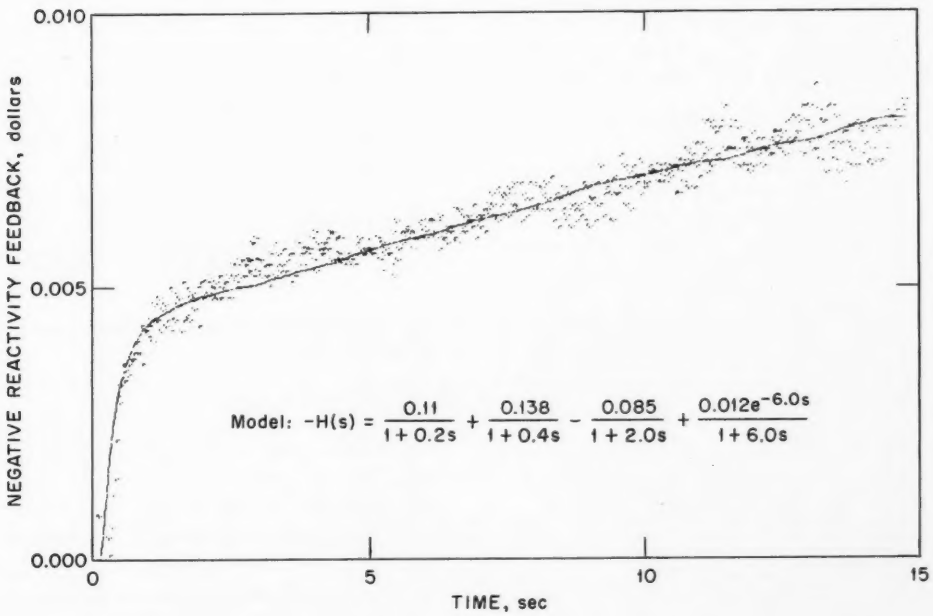

Fig. 6 Fit of rod-drop data from end[2] of Run 37 to time-dependent feedback model [50-MW(t) power; 100% flow].

Table 2 The Effect of Plutonium Buildup in Terms of Reactivity[1]

Time from start of run, hr	Plutonium buildup rate, inhour/MWd
0	0
24	0.0054
48	0.0135
72	0.0196
96	0.0241
120	0.0275
144	0.0299
168	0.0318
192	0.0331
216	0.0341
240	0.0349

Neutron-Flux and Power Distributions

Neutron-flux and power distributions are a function of core loading in any reactor. However, the variations in these distributions are particularly evident in a test reactor core where the in-core test positions can be occupied by different experiments from loading to loading.

In order to assess the degree of flux and power asymmetry[3] and other effects caused by irradiation experiments in the EBR-II, the DOT5 was used with the IBM 360/75 to numerically simulate core loadings and compute corresponding core-physics parameters.

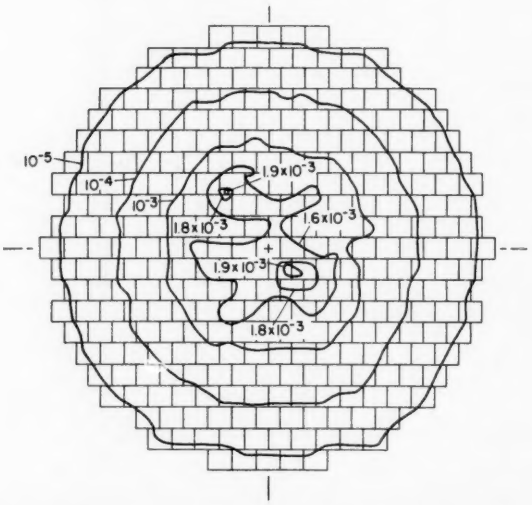

Fig. 7 Contour map of fast flux[4] in EBR-II Run 32B ($E > 2.23$ MeV).

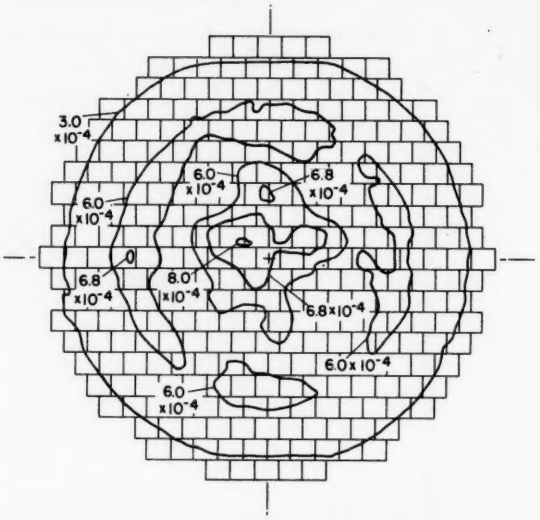

Fig. 8 Contour map of low-energy flux[4] in EBR-II Run 32B ($E < 40.9$ keV).

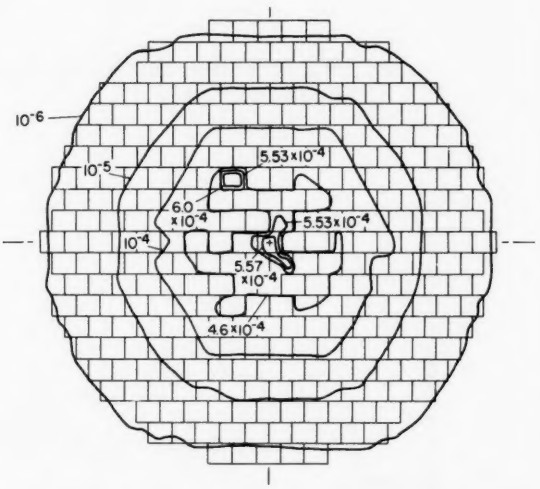

Fig. 9 Contour map of rate of fission-neutron emission[5] in EBR-II Run 42B.

Computed values[4,5] for flux and fission-rate distributions are shown on the EBR-II core-contour maps in Figs. 7 to 9. Figure 7 is a map of the fast flux ($E > 2.23$ MeV) for the Run 32B core loading; Fig. 8 is a low-energy-flux contour map and includes all neutrons with energies less than 40.9 keV; Fig. 9 shows that the contour map and power-distribution map are very nearly the same, differing only because the average number of neutrons released per thermal neutron fission is different for the various fissile isotopes.

Further checks[2] on the apparent power and flux asymmetries were carried out by DOT5 calculations of control-rod worths for the Run 32B core configuration. The computed and measured values are given in Table 3. The computed values (in $\% \Delta k$) were converted to inhours using the conversion factor of $1\% \Delta k = 430$ inhours.

Table 3 Control-Rod Worths[2] in Run 32B

Control-rod position	k_{ex}, inhours	
	Theoretical	Experimental
5A1	142	142
5A3	167	167
5B1	156	159
5B3	159	165
5C1	137	136
5C3	145	150
5D3	167	167
5E1	143	139
5E3	153	155
6E1	148	141
6E3	166	169

A correction factor of 0.88 was applied to the computed values to account for the fact that the control rods are withdrawn into the axial blanket and not totally removed from the system. The EBR-II personnel interpreted the agreement between measured and calculated values as confirmation of the observed flux tilt and asymmetric power distributions discussed above.[3-5]

The presence of experimental subassemblies in a reactor core produces local perturbations that are most easily described by a so-called flux- or fission-rate-depression factor. These depression factors are strongly dependent on the amount of fissile and fertile materials in an experimental subassembly relative to a normal driver subassembly.

Flux- and fission-rate-depression factors[5] were computed for some typical experimental subassemblies in EBR-II Run 38B by comparing the fluxes in each experimental subassembly with the fluxes that would be present in a driver subassembly located in the same position. Table 4 shows the results of these computations.

Often experimental subassemblies will produce localized flux peaking rather than flux depression. This flux enhancement is particularly evident in the vicinity of heavily loaded subassemblies because of the greater worth of the plutonium relative to the ^{235}U and because of the smaller amount of ^{238}U present in the normal driver subassemblies (both of these factors contribute to an average number of neutrons emitted per neutron absorbed). The environmental effects are illustrated most clearly by experimental subassembly X058 in Table 4. This subassembly was located on the edge of the core and adjacent to three blanket subassemblies. Subassembly X058, when compared with similarly loaded experimental subassemblies X054 and X040, also shows the position dependence of these depression factors. The flux- and fission-rate-depression factors given in Table 4 are average values that apply to each experimental subassembly as a whole.

Analysis of Run 38 Core-Physics Parameters

During Run 38A the power level was increased in two increments: one from 50 to 56 MW(t) and the other, 2 days later, from 56 to 62.5 MW(t). The core loading[6] for this run, which is shown in Fig. 10,

Table 4 Flux- and Fission-Rate-Depression Factors for EBR-II Run 38B

Type of subassembly	Subassembly No.	Fuel loading, g			Subassembly position	Environmental subassemblies*	^{235}U fission-rate-depression factor	Flux-depression factor					
								Lower energy of group, MeV					
		^{235}U	^{239}Pu	^{238}U				2.23	0.821	0.302	0.111	0.041	0
B7	X057	0	0	0	2B1	D, D, L, D, D, D	0.961	0.70	0.84	0.95	1.01	1.07	1.34
F37	X051	14	556	1966	3A2	L, D, C, D, D^2, D	0.972	0.83	0.87	0.93	1.02	1.08	1.23
A19	X050	737	203	80	4C2	D, D, D, L, C, D^2	0.995	0.92	0.94	0.96	1.02	1.06	1.19
A19	X064	939	311	108	4F2	D, D, L, D, C, D	1.001	0.94	0.95	0.96	1.03	1.07	1.21
F37A	X054	1747	553	213	4E1	D^1, D^2, D, C, D, L	1.013	1.03	0.98	0.97	1.03	1.05	1.13
F37	X058	1811	581	201	6F1	C, D, B, B, B, D	1.041	1.05	1.01	0.99	1.04	1.07	1.16
B37	X040	1918	581	180	5B2	D, D^1, C, D, D, C	1.019	1.04	0.99	0.97	1.03	1.06	1.15

*Six subassemblies surrounding the position of interest (clockwise starting with the subassembly nearest the center of the core: B = blanket; C = control rod; D = driver; D^1 = 66% enriched driver; D^2 = ½ driver fuel–½ stainless steel; H = heavily loaded fueled experimental subassembly; and L = lightly loaded fueled experiment or structural subassembly.

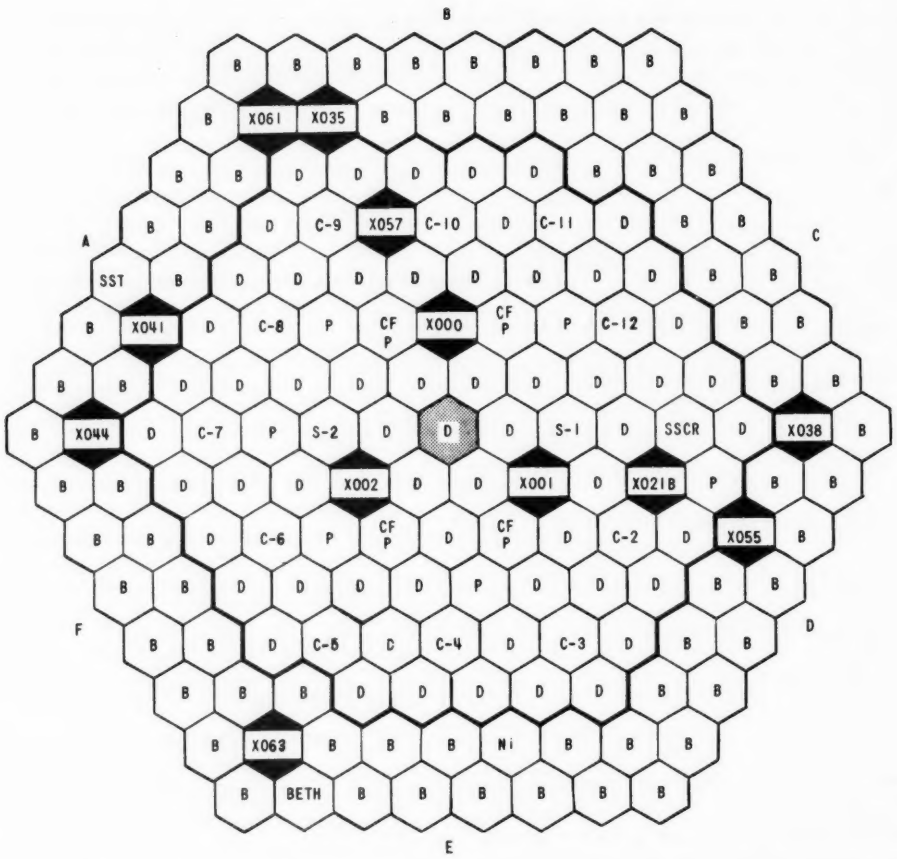

Fig. 10 Loading diagram[6] for EBR-II Run 38A. Code: B, depleted uranium; BETH, beryllium thimble; C, control rod; CF, controlled-flow subassembly; D, driver fuel; Ni, nickel-corrosion subassembly; P, ½ driver fuel – ½ stainless steel; S, safety rod; SSCR, stainless-steel control rod; SST, stainless-steel thimble; X, experimental subassembly.

utilized a depleted-uranium blanket and differed slightly from preceding loadings:

- Three structural-experiment-mockup subassemblies were located on row 3 flats, and the row 3 corner positions, which were not occupied by safety rods, contained half-worth subassemblies.
- Standard driver subassemblies were loaded into rows 1 and 2 as a part of a temperature-prediction program.
- All the reduced-flow subassemblies used in previous runs were removed from rows 2 and 3.
- Only two structural-irradiation experiments from previous runs were left in row 5.

Power-coefficient measurements with the revised core loading indicated an overall decrease in the power-reactivity decrement (PRD). These results are summarized in Fig. 11. The decrease in PRD was postulated to be the result of a decrease in negative, mechanically originated feedback effects caused by the removal of the reduced-flow subassemblies from the core.

Control-rod-worth measurements[6] for the Run 38 core loading showed a 6 to 8% decrease from those for the Run 37 configuration. Detailed analyses indicated that the increased stainless-steel content of row 3 in Run 38 had caused a change in radial fission-rate distribution and that a larger reactivity-burnup coefficient of about 0.02 inhour/MWd was noted as a result of central peaking in fission rate and the greater worth of the central subassemblies.

Temperatures indicated by all seven core-outlet thermocouples in rows 1 and 2 were consistent within 11°F. The temperature data were then related to power and coolant flow. All thermocouple readings increased linearly over the power range of 50 to 62.5 MW(t).

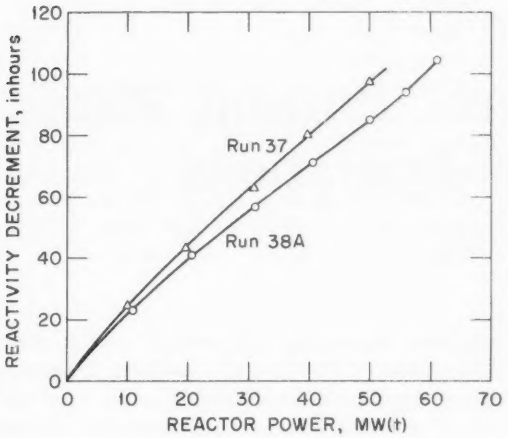

Fig. 11 Curves comparing initial power-reactivity decrement[6] in Runs 37 and 38A.

REFERENCES

1. Argonne National Laboratory, Reactor Development Program Progress Report, August 1969, USAEC Report ANL-7606, Sept. 26, 1969.
2. Argonne National Laboratory, Reactor Development Program Progress Report, October 1969, USAEC Report ANL-7632, Nov. 25, 1969.
3. Argonne National Laboratory, Reactor Development Program Progress Report, September 1969, USAEC Report ANL-7618, Oct. 27, 1969.
4. Argonne National Laboratory, Reactor Development Program Progress Report, December 1969, USAEC Report ANL-7655, Jan. 29, 1970.
5. Argonne National Laboratory, Reactor Development Program Progress Report, February 1970, USAEC Report ANL-7669, Mar. 30, 1970.
6. Argonne National Laboratory, Reactor Development Program Progress Report, January 1970, USAEC Report ANL-7661, Feb. 25, 1970.

Sodium-Cooled Reactors: Current Status of Plant-Systems Operations

By Myrna L. Steele

EBR-II

By the end of March 1970, Experimental Breeder Reactor II (EBR-II) had finished Run 41 for a cumulated total operation[3] of 33,498 MWd.

After fuel handling was completed at the beginning[1] of Run 39A, the seal trough of the small rotating plug was cleaned and filled and an approach-to-critical was begun. Subsequent to a shutdown for reactivity adjustments, the reactor was restarted, zero-power physics experiments were performed, and then the power level was increased to 50 MW(t).

Unscheduled Scrams

At the beginning of Run 40A, rod-drop experiments[2] were performed at 0.5 and 50 MW(t). After 9 days of operation, the reactor scrammed because of an indicated high rate of change of primary coolant flow. Since no actual flow rate occurred, the plug-in components in the rate-of-change amplifier were replaced, and reactor operation was resumed under the designation of Run 40B.

The reactor[3] was started up on March 5 for low-power physics tests, and 50-MW(t) operation was resumed the following day. On March 15 a scram was caused by a transient in the 138-kV station grid, but reactor power was soon returned to 50 MW(t).

Changes in Core Loading

In addition to the experimental subassemblies that were loaded[2] into the core at the beginning of Run 40, two vendor-supplied fuel surveillance subassemblies that were made from previously irradiated subassemblies were installed in the core. A 70% enriched subassembly, two controlled-flow subassemblies, a recycled-fuel surveillance subassembly, and an inner-radial-blanket (IRB) depleted-uranium surveillance subassembly were removed from the core.

Secondary Sodium System

During Run 39A the annunciator panel for the secondary sodium system registered a detection of smoke[1] in the sodium boiler plant. A small fire that appeared to be electrical in origin was discovered on the inlet piping of the surge tank. Further investigation revealed a leak at one of the sodium-vent valves on the side of the surge tank. The fire had apparently been caused by dripping sodium splashing on the lagging of the inlet line. The reactor was immediately shut down and the vent valve closed; an orderly cooldown of all systems to less than 400°F was effected, and the secondary sodium system was drained. The bellows on the vent valve was replaced, and leak detectors were installed in each of the five vent valves. The lagging and heaters were replaced, the secondary sodium system was refilled, all systems were heated to normal operating temperatures, and operation at 50 MW(t) was resumed.[1]

Power-Conversion System

At the beginning[1] of Run 39A, the capacity of the turbine-driven feedwater pump proved to be insufficient for 50-MW(t) operation and had to be overhauled after the run. During Run 39B the pump performed satisfactorily and was returned to service.

FERMI FAST BREEDER REACTOR

Preparations for reactor restart continued[4-6] through December with cold trapping of the primary

and secondary sodium loops occurring intermittently from October to December.

Sodium Systems

Cleaning of the primary sodium continued[4] through October, with a plugging temperature of 290°F being recorded for a 600°F system temperature. No cold trapping was required[5] during November since the primary-system temperature was maintained between 395 and 410°F with an indicated orifice plugging temperature of less than 265°F. During December the primary-system temperature was maintained[6] at 392 to 410°F with the cold trap operating for 17 hr at a maximum saturation temperature of 290°F.

The No. 1 secondary sodium loop was cold trapped for about 46 hr in October[1] to reduce the maximum saturation temperature from 350°F to 280°F. Cold trapping of the No. 1 secondary sodium loop was also required[5] for about 46 hr in November to reduce the saturation temperature from 370°F to less than 250°F. No cold trapping of the Nos. 2 and 3 secondary sodium loops was necessary[4,5] in October and November. In December the No. 1 secondary sodium loop was cold trapped[6] for 29 hr to reduce the saturation temperature from 300°F to less than 230°F; the No. 3 secondary sodium loop was cold trapped for 61 hr to reduce the saturation temperature from 275°F to less than 250°F. No cold trapping was required for the No. 2 secondary sodium loop.

On Nov. 5, 1969, the No. 3 secondary system was drained[5] to allow replacement of the steam manifold cover gasket in the No. 3 steam generator. The 24-in. vent-stack-rupture disk that had been leaking was also replaced at this time. The steam generator[6] was returned to standby on Dec. 9, 1969.

Offset Handling Mechanism

The probe survey that was completed in October[1] indicated that the flow-guarded IRB units would cause no handling problems for the offset handling mechanism (OHM). Consequently only minor modifications, which included resetting of elevation and latch controls and alteration of elevation-control wiring to include three up-limit switch positions, were made to the OHM.

Fuel Transport Facility

During the installation of a flow-guarded-length pot[5] into the transfer rotor, the pot dropped about 26 ft from the exit-port floor valve onto the transfer-rotor plate. Subsequent testing and elevation measurements showed that no change in torque was required for rotation and indicated that the rotor plate was not bent. When the pot was removed from the reactor vessel, it was observed to have a bent support flange and, consequently, was scrapped.

Metallurgical problems with the fuel pots were discovered when three of the pots of the fuel transport car had to be lengthened to accommodate the flow-guarded subassemblies. Ineffective heat-treatment during fabrication had caused the pots to become embrittled. These problems delayed the lengthening of the pots and necessitated fabrication to two temporary fuel-handling pots for transferring core and IRB subassemblies to the reactor. The temporary pots, which do not have fins, will be used to handle fuel that has not been appreciably irradiated.[5]

REFERENCES

1. Argonne National Laboratory, Reactor Development Program Progress Report, January 1970, USAEC Report ANL-7661, Feb. 25, 1970.
2. Argonne National Laboratory, Reactor Development Program Progress Report, February 1970, USAEC Report ANL-7669, Mar. 30, 1970.
3. Argonne National Laboratory, Reactor Development Program Progress Report, March 1970, USAEC Report ANL-7679, Apr. 27, 1970.
4. Power Reactor Development Company, Enrico Fermi Atomic Power Plant Report for October 1969, USAEC Report DOCKET-50016-31.
5. Power Reactor Development Company, Enrico Fermi Atomic Power Plant Report for November 1969, USAEC Report DOCKET-50016-33.
6. Power Reactor Development Company, Enrico Fermi Atomic Power Plant Report for December 1969, USAEC Report DOCKET-50016-34.

Suggested Reading List

John T. Madell and Richard E. Jarka, Analysis of the Linear Components of the Power-Reactivity Decrement in EBR-II, USAEC Report ANL-7539, Argonne National Laboratory, October 1969.

James B. Waldo, Mechanical Improvements of the EBR-II Fuel Unloading Machine, USAEC Report ANL-7585, Argonne National Laboratory, November 1969.

Charles C. Crothers, Investigation of Metallurgical Problems Associated with the EBR-II Fusible Seals, USAEC Report ANL-7589, Argonne National Laboratory, September 1969.

Martin W. Wamsganss, Jr., Evaluation of Potential Tube Vibration in EBR-II Steam Superheaters and Evaporators at Full Power, USAEC Report ANL-7600, Argonne National Laboratory, November 1969.

A. V. Campise, A Study of Dynamic Response of Various EBR-II Configurations to Hypothetical Malfunctions in Reactor Systems, USAEC Report ANL-7613, Argonne National Laboratory, November 1969.

V. G. Eschen, Surveillance of EBR-II Blanket Subassemblies, USAEC Report ANL-7597, Argonne National Laboratory, September 1969.

Larry P. Cooper, Bernard C. Cerutti, and Donald W. Cissel, Operating Experience with EBR-II Rotating Plug Freeze Seals, USAEC Report ANL-7617, Argonne National Laboratory, December 1969.

James B. Waldo and Lynn J. Christensen, System for Measuring Sodium Level in EBR-II, USAEC Report ANL-7623, Argonne National Laboratory, October 1969.

R. W. Hyndman, R. O. Haroldsen, and J. R. Karvinen, EBR-II: Digital Data Acquisition System Study, USAEC Report ANL-EBR-1, Argonne National Laboratory, May 1969.

R. R. Smith and D. L. Mitchell, Postirradiation Inspection of Subassemblies Discharged from Runs 25 and 26 in EBR-II, USAEC Report ANL-EBR-2, Argonne National Laboratory, March 1969.

C. C. Crothers, EBR-II Primary Sodium Storage Facility, USAEC Report ANL-EBR-3, Argonne National Laboratory, February 1969.

O. Seim, E. Hutter, T. Sullivan, R. Olp, J. Pardini, E. Filewicz, and R. Brubaker, Conceptual System Design Description of the EBR-II In-Core Instrument Test Facility, USAEC Report ANL-EBR-4, Argonne National Laboratory, June 1969.

H. Kacinskas, Study of Loading of EBR-II Electric Power System, USAEC Report ANL-EBR-5, Argonne National Laboratory, July 1969.

J. C. Case (Comp.), Core-Loading Diagrams for EBR-II Runs 4 Through 38, April 1965–Mid-December 1969, USAEC Report ANL-EBR-7, Argonne National Laboratory, December 1969.

AMERICAN NUCLEAR SOCIETY—CRITICAL REVIEWS

The Atomic Energy Commission has contracted with the American Nuclear Society to prepare for publication on a regular basis detailed Critical Review articles written by experts selected from the ANS membership and reviewed by an advisory committee of top leaders and scientists in the field. In this issue the articles are on pages 226–319.

Members of the Critical Review Advisory Committee are:

Sidney Siegel, *Chairman*	Atomics International
Jack Chernick	Brookhaven National Laboratory
William Chittenden	Sargent & Lundy Engineers
Paul Lottes	Argonne National Laboratory
Peter Murray	Westinghouse Electric Corporation
David Okrent	Argonne National Laboratory
Herbert Parker	Battelle–Northwest
Joseph Prestele	New York Consolidated Edison
W. C. Redman	Argonne National Laboratory
Charles Stevenson	Argonne National Laboratory
Bertram Wolfe	Battelle–Northwest

ANS Critical Review Editor, *Norman H. Jacobson*

ANS Officers:

President, *N. J. Palladino*

Vice President, *J. W. Landis*

Treasurer, *James R. Lilienthal*

Executive Secretary, *Octave J. Du Temple*

Comments on the articles should be communicated directly to the ANS Critical Review Committee or Editor, 244 E. Ogden Avenue, Hinsdale, Ill. 60521.

Gas-Core Reactor Technology

By J. D. Clement and J. R. Williams*

INTRODUCTION

Abstract: *A gas-core reactor consists of a cavity containing a fissionable gas surrounded by a moderator that is in a critical configuration. Fission neutrons from the core are thermalized in the reflector region and in part returned to the cavity. The primary motivation for developing high-temperature gas-core reactors has been for high-specific-impulse, high-thrust nuclear rocket propulsion. There has recently been increasing interest in also using the gas-core reactor for large, highly efficient, commercial power plants employing a magnetohydrodynamic (MHD) topping cycle.*

The two gas-core reactor concepts receiving the most attention are the coaxial-flow (open-cycle) reactor and the vortex-stabilized nuclear light-bulb (closed-cycle) reactor. The coaxial-flow reactor retains the fissile fuel in a critical configuration using a suitable flow scheme, whereas the light-bulb reactor contains the fuel in a regeneratively cooled transparent partition. To develop the technological base necessary for the construction of high-temperature gas-core reactors, investigators are currently carrying out extensive studies in the areas of nuclear analysis, heat-transfer and high-temperature-materials properties, fluid mechanics, and system dynamics, stability, and control of various gas-core reactor configurations. These studies indicate it may be technically feasible to carry out ground tests of full-scale high-temperature gas-core reactors in the near future.

WHY GAS-CORE REACTORS?

In recent years a sizable research effort has been devoted to developing a new type of nuclear reactor, called the gas-core or cavity reactor, that could heat a gaseous working fluid to much higher temperatures than current reactors using solid fuel elements. The primary motivation for developing a gas-core reactor has been for high-specific-impulse nuclear rocket propulsion. However, the recent development of MHD power plants of 20 MW and larger has generated interest in the application of gas-core reactors as a power source for large, highly efficient power plants using an MHD topping cycle. Since the Air Force has used rocket engines to power MHD plants, the gas-core nuclear rocket engine must now be considered as a potential power source in addition to being a propulsion device.

Economic studies have shown that the development of gas-core nuclear rockets would be a major step toward the commercial exploitation of the solar system.[1,2] The specific impulse of a gas-core rocket engine is expected to be in the range 1500 to 2500 sec, compared to about 830 sec for the NERVA and about 400 sec for the best chemical rockets. Since the size of a rocket vehicle is exponentially related to the inverse of its specific impulse, gas-core rockets could be much smaller than solid-core nuclear or chemical rockets required to perform a given mission. Gas-core rockets might also be used to substantially reduce trip times to the nearer planets.

Thus an effort is currently under way to develop the technological base required to construct a gas-core nuclear rocket engine. Whether, in the final analysis, this engine will be used primarily as a propulsion device or as a power source remains to be seen.

GAS-CORE REACTOR CONCEPTS AND APPLICATIONS

The fissile fuel in a gas-core reactor is contained in the reactor cavity, usually at a high temperature (12,000 to 50,000°K) in a gaseous or plasma state. The cavity containing this gaseous fissioning fuel is surrounded by the external moderator. The terms *plasma-core reactor* or *cavity reactor* are also applicable and have been used to refer to the gas-core reactor concept.

*School of Nuclear Engineering, Georgia Institute of Technology, Atlanta, Ga. 30332.

There is considerable interest in the two different approaches currently being pursued actively, both experimentally and analytically, toward developing a gas-core reactor. Much of this work is being sponsored by the AEC/NASA Space Nuclear Propulsion Office. The two concepts are: (1) the open-cycle concept, in which the fissioning fuel is exhausted from the reactor, and (2) the closed-cycle (nuclear light-bulb) concept, in which the fissioning fuel is physically contained within a thin radiation-transparent wall and recirculated. The

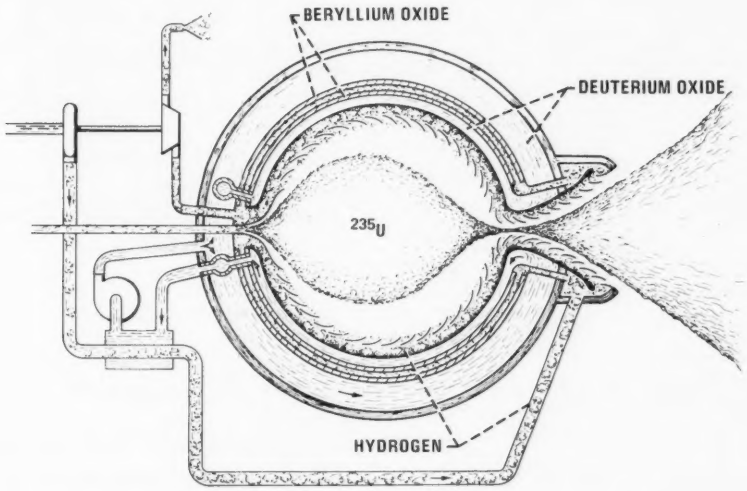

Fig. 1 Conceptual coaxial-flow gas-core nuclear rocket engine.[1]

open-cycle reactor concept can further be characterized by the flow scheme used to separate the fissioning fuel from the working fluid. The open-cycle concepts are the coaxial-flow reactor concept and the vortex-stabilized reactor concept.

The coaxial-flow reactor utilizes a slow-moving central stream of gaseous fissioning fuel to radiatively heat a more rapidly moving annular stream of particle-seeded gas which serves as the working fluid, or as the propellant in the case of a nuclear rocket engine. The flow scheme is relied on to minimize loss of fuel by mixing with the working fluid. Rom and Ragsdale[1] are directing a program of research aimed at developing the technology to construct a coaxial-flow gas-core rocket engine. Figure 1 is a diagram of a coaxial-flow reactor system being investigated by researchers at the NASA Lewis Research Center.

In the vortex-stabilized reactor, hydrogen is introduced tangentially into a cylindrical cavity. The resulting centrifugal force of the rotating vortex tends to confine the heavy fuel atoms near the wall of the cavity while the heat generated by the gaseous fuel is transferred to the working fluid passing through the fuel region. The two most important reasons for the use of vortex flow are: (1) the nuclear fuel is preferentially contained relative to the working fluid, and (2) the vortex flow appears to result in a laminar flow pattern that can be taken advantage of in the nuclear light-bulb concept to keep the gaseous nuclear fuel separated from the containing wall.[3] United Aircraft Corporation, under the direction of the Space Nuclear Propulsion Office, is studying the nuclear light-bulb concept.[3,4] Figure 2 illustrates the nuclear light-bulb vortex-stabilized reactor. Potential candidates for the material for the thin wall, which serves as a physical barrier to confine the core but is transparent to the thermal radiation, are fused silica of ~5 to 10 mils thickness and high-purity single-crystal beryllium oxide. A neon buffer is used between the fuel and the wall to keep the high-temperature fuel away from the transparent wall and to cool the wall.

Other schemes have also been proposed for gas-core reactors. Park and Love[5] have analyzed a scheme for fuel separation using MHD acceleration to produce a faster vortex than can be achieved by tangential fuel injection. The use of electromagnetic fields to increase fuel containment has also been investigated.[2] Evvard[6] has proposed a wheel-flow vortex concept in which the

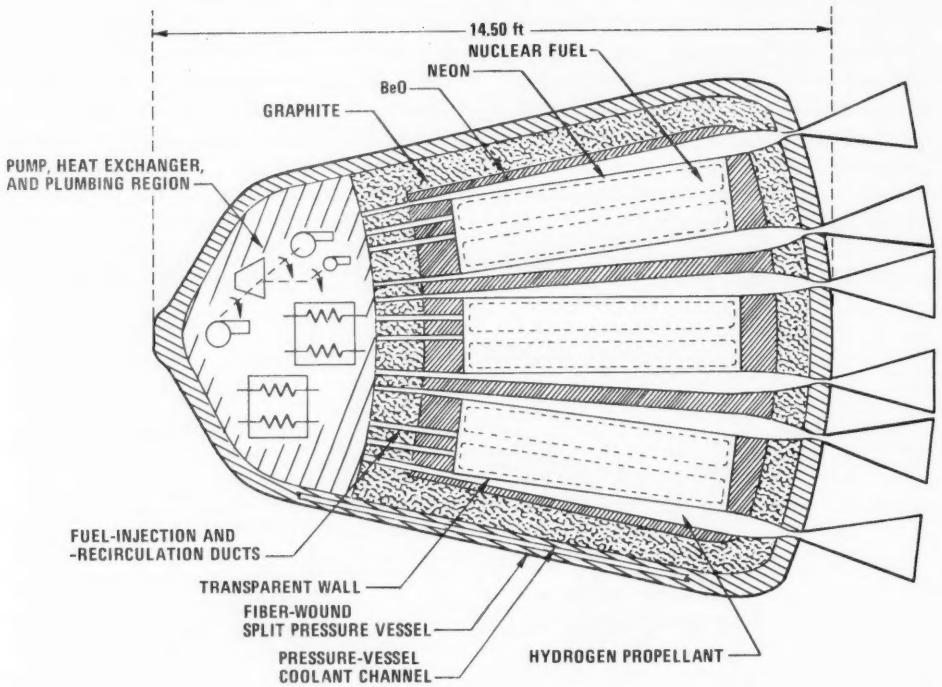

Fig. 2 Schematic diagram of a gas-core nuclear light-bulb engine.[53]

heated hydrogen propellant is removed tangentially from the cylindrical vortex cavity instead of through a nozzle at the end of the cavity.

Gritton and Pinkel[7] have recently published a conceptual design of a gas-core reactor for electric-power generation which would utilize pure uranium or plutonium gas. A thermionic topping cycle was used with a steam plant to provide an overall plant efficiency of about 40%. They concluded that attractive power levels in reactors of practical size can be obtained with gas pressures and wall temperatures within the potential capability of known structural materials. They estimated that an ~3-m-diameter spherical gas-core reactor would generate ~4000 MW(t) with a gas pressure of about 11 atm.

Major areas currently being investigated with respect to the various gas-core reactor concepts are: (1) nuclear analysis, (2) heat-transfer and high-temperature-materials properties, (3) fluid mechanics, and (4) system dynamics, stability, and control.

The nuclear problems are related to the large critical mass, reactivity coefficients that may lead to instabilities, and power distributions that affect heating rates. Also, in the case of the open-cycle concept for nuclear rocket propulsion, the escaping fuel presents an economic problem because of the high fuel cost. One heat-transfer problem, common to all these concepts, concerns the absorption of the thermal radiation from the core by the gaseous working fluid. Since hydrogen at temperatures below 7000°K is essentially transparent to the thermal-radiation emission of the uranium plasma core, an intermediate heat-transfer mechanism must be employed to heat the gas. This can be accomplished by seeding the gas with submicron-sized particles that have a high radiant-energy-absorption coefficient. The seeded gas is gray to the radiant energy, and the energy absorbed by the seed particles is transferred to the gas by conduction and convection. In the case of the nuclear light-bulb reactor, cooling the transparent wall presents a significant problem. In addition, the transparent partition must be very thin, and, unless the pressure difference can be made small and controlled, it must be quite strong. The fluid-mechanics problem of containing the plasma core and minimizing instabilities, and minimizing fuel loss in the case of open-cycle concepts, has received considerable attention for both the coaxial-flow and vortex-stabilized concepts. In connection with the system

stability, it is necessary to construct a model that simultaneously solves the overall systems' equations, including neutronics, heat balance, and flow patterns, to predict the response to startup and perturbations at full-power operation.

Gas-Core Reactors for Nuclear Rocket Propulsion

The basic purpose of a rocket engine is to produce thrust by accelerating gases from rest with respect to the rocket to an exhaust velocity v_e with respect to the rocket. This acceleration is usually achieved by heating the gases to a high temperature inside the engine and then allowing them to escape through a nozzle. In chemical rockets, this heating is accomplished by burning the fuel in the combustion chamber, and then the combustion products become the ejected gases. The nuclear rocket heats the gases with a nuclear reactor instead of by combustion.

The performance of a rocket engine is primarily measured by two criteria: the specific impulse and the thrust-to-weight ratio. The specific impulse is defined by

$$I_{sp} = \frac{\text{Engine thrust}}{\dot{m} g_c} \quad \text{sec} \tag{1}$$

where $\dot{m}$ is the mass flow rate of the propellant and g_c is a constant equal to the acceleration of gravity at sea level. The thrust-to-weight ratio is the thrust of the propulsion system divided by the total vehicle weight. The thrust-to-weight ratio for a space propulsion system should be as large as possible so a given mission can be accomplished with a minimum fuel expenditure and in a minimum time period. Also, some missions cannot be accomplished at all with low-thrust propulsion systems. The specific impulse, which is a measure of the effective exhaust velocity of the propellant, and the thrust-to-weight ratio are the primary factors determining the mission capability of a propulsion system.

Letting M_i and M_f be the initial and final masses of a rocket that has executed a mission equivalent to a velocity change Δv in free space, the mass ratio M_i/M_f is then related to Δv by

$$\frac{M_i}{M_f} = \exp\left(\Delta v / v_e\right) \tag{2}$$

where v_e is the effective exhaust velocity. Since the thrust is given by $\dot{m} v_e$, the specific impulse may also be written

$$I_{sp} = \frac{v_e}{g_c} \tag{3}$$

so I_{sp} is actually a measure of the effective exhaust velocity. Equation 2 may now be written

$$\frac{M_i}{M_f} = \exp\left(\Delta v / g_c I_{sp}\right) \tag{4}$$

Since the relation between the mass ratio and the specific impulse is exponential, a small change in the specific impulse may produce a very large change in the corresponding mass ratio. This means that, for a given payload and mission requirement, the size of the rocket vehicle may decrease considerably when the specific impulse of the propulsion system is increased.

Economical space travel will require a rocket propulsion system that has both a high specific impulse and a thrust-to-weight ratio of the order of unity or greater. Today's chemical boosters have an adequate thrust-to-weight ratio, but their specific impulse is limited to about 500 sec. The solid-core nuclear rocket is expected eventually[2] to develop a specific impulse of about 1000 sec. But for practical, economical space transportation, a rocket engine capable of a specific impulse of several thousand seconds, which also produces a thrust-to-weight ratio of unity or greater, is needed.

Nuclear electric rockets (ion propulsion) have the required specific impulse, but they have extremely low thrust-to-weight ratios and, therefore, would not be suitable for many space missions.

To increase the specific impulse of a propulsion system, one must increase the effective exhaust velocity v_e. For propulsion systems that obtain thrust by exhausting a hot gas through a nozzle, v_e is increased by increasing the average velocity of the gas molecules inside the engine. The root-mean-square velocity of the gas molecules may be found from

$$E = \frac{1}{2} m v^2 = \frac{3}{2} k T \tag{5}$$

where m is the molecular weight, T is the absolute temperature of the gas, and k is the Boltzmann constant. Thus

$$v^2 = \frac{3kT}{m} \tag{6}$$

and

$$v = \sqrt{\frac{3kT}{m}} = (\text{a constant}) \cdot \sqrt{\frac{T}{m}} \qquad (7)$$

Hence the exhaust velocity v_e, which is proportional to v, is given by

$$v_e = (\text{a constant}) \cdot \sqrt{\frac{T}{m}} \qquad (8)$$

The greater specific impulse of graphite-core nuclear rockets results not from an increase in the propellant temperature (actually T is lower than in the O–H engine) but from a considerable decrease in m. In the O–H rocket, the exhaust gas is mostly water with an average molecular mass considerably larger than that of molecular hydrogen, the exhaust gas of the nuclear rocket; so the specific impulse of the nuclear rocket is considerably greater, even at a slightly lower propellant temperature. Further increases in the specific impulse can be obtained only by increasing T. The solid-core nuclear rocket is limited to a specific impulse of about 1000 sec, because raising the temperature further would cause the core to melt.

Three approaches have been proposed which, in principle, might lead to an engine with the desired thrust-to-weight ratio and a specific impulse of several thousand seconds or greater. These are the Orion concept (in which thrust would be obtained from nuclear explosions behind the spacecraft), the gas-core nuclear rocket, and the thermonuclear fusion rocket. The Orion concept, or the nuclear pulse rocket, originated at Los Alamos shortly after World War II, and the first report on the project was written in 1955. The General Atomic Division of General Dynamics Corp. (now Gulf General Atomic Incorporated) developed a design weighing 2500 tons, which would have a specific impulse on the order of 4000 sec. However, according to Ulam,[8] the actual cost of building such a vehicle would be about a billion dollars or more. At present, nuclear pulse rockets are not considered practical because of their size and cost. Fusion propulsion may eventually be developed after fusion becomes practical as an energy source. The gas-core reactor concept, in which the propellant is heated by fission energy produced in a cavity reactor having its nuclear fuel in gaseous form, appears closest to becoming a reality.

One of the early analytical studies of the gas-core nuclear rocket was carried out by Meghreblian and his coworkers[9] at the Jet Propulsion Laboratory. They considered a vortex concept and concluded that, if regenerative cooling is the only mechanism for removing the nuclear radiation heat deposited in the solid parts of the engine, the specific impulse would be limited to about 2500 sec. They also studied the effect of the cavity diameter and void fraction on the critical mass and conducted a parametric survey of this type of engine for various mission requirements. Reactor cavity diameters varied from 2 to 3 m, reactor weights varied from 5000 to 50,000 kg, and the reactor power varied from 15,000 to 30,000 MW.

Duke and Houghton[10] reported an Aerojet-General design of an open-cycle engine based on the assumption of satisfactory hydrodynamic containment of the uranium core. They considered a cavity diameter and length of 5 ft, a hydrogen cavity temperature of 12,000°R, a hydrogen flow rate of 200 lb/sec, and a chamber pressure of 10,000 psia. Using regenerative and transpiration cooling of the nozzle with a particle-seeded boundary layer to absorb thermal radiation, they arrived at a nozzle temperature of 4000°R. A rather detailed engine design was arrived at which included the characteristics of the pumps, reflector region, and nozzle. On the basis of the assumptions of this study, the resulting engine had a specific impulse of 1730 sec, a thrust of 405,000 lb, and a weight of 92,000 lb.

Rom[11] obtained a patent on the coaxial-flow gas-core rocket engine, which was estimated at that time to have a specific impulse as high as 3000 sec. The patent describes some of the operating characteristics and problems associated with this concept. Ragsdale[12] presented a parametric study of open-cycle gas-core reactors showing the effect of the reactor pressure and volume fraction of fuel in the cavity on the critical mass of uranium and showed that the fuel-volume fraction must be >0.20. He also studied the effect of the fuel temperature and reactor pressure on the thrust produced by this type of engine. For a thrust of 1,000,000 lb, the average fuel temperature varied from 28,000°K at 100 atm pressure to 40,000°K at 1000 atm pressure. A more recent study by Ragsdale[13] related the amount of uranium that would be contained in such an engine to the cavity diameter, which was varied from 8 to 16 ft; the reactor pressure, which was varied from 100 to 1000 atm; the engine thrust, which was varied from 10^5 to 10^6 lb; the specific impulse; and the separation ratio (ratio of hydrogen mass flow rate to fuel mass flow rate), which was varied from 10 to 200.

McLafferty[14] obtained the first patent on the light-bulb concept. He and his coworkers at United

Aircraft Corporation have carried on an extensive research program related to this concept during the past decade.[3] They have recently reported an analysis of the light-bulb engine,[4] which arrived at a critical mass of 11.4 kg, a reactor power level of 4600 MW, a thrust of 91,000 lb, a specific impulse of 1890 sec, a reactor pressure of 500 atm, and a fuel-volume fraction of 0.25. Unlike the open-cycle concepts, this engine design utilized seven unit cavities in a graphite/beryllium oxide moderator.

Gas-Core Reactors for MHD Power Systems

In recent years much has been said about the thermal effects produced by large electric power plants. There is increasing concern today about all forms of pollution and the relation between man and his environment. The fear has been expressed repeatedly that the electric utilities may not be able to meet the increasing demand for power in the 1970's and 1980's, because of strong local opposition to the construction of new generating plants, and that as our power reserves shrink below zero, blackouts and brownouts will become common and rationing of power may be necessary. Much of the opposition to these new plants is based on their thermal effects, and local governments are being forced to require that these plants adhere to strict limits as to the permissible amount of waste heat.

The demand for electric power is doubling about every 10 years. If this power is not provided, our economy may be crippled. To provide this power without vastly increasing the already objectionable amount of thermal pollution may require the construction of more efficient power plants. The amount of heat rejected per unit power output can be expressed as $(1-\eta)/\eta$, where η is the efficiency of the plant. Increasing the efficiency from 35 to 70% reduces the waste heat from 1.86 to 0.43/MW(e), a factor of 4.3. Since an electric power plant is essentially a heat engine operating between two temperature extremes to produce electric power, the maximum possible efficiency of such a plant is increased by increasing the temperature of the heat source or by lowering the temperature of the heat sink. The minimum heat-rejection temperature is fixed by the environment, so the only approach to increasing the maximum possible efficiency is by increasing the temperature of the heat source.

Unfortunately most energy-conversion devices, such as turbines and thermoelectric elements, cannot operate with source temperatures above ~2500°K. However, there is one energy-conversion device that can extract energy from a working fluid at much higher temperatures; in the MHD generator, power is extracted from the volume of a fluid moving in a duct where the fluid can be much hotter than the walls of the duct. The rocket engine is an ideal short-term source for such a fluid. Currently, operating MHD power plants use such a heat source. A 20-MW rocket-driven MHD power plant has been built by AVCO for the Air Force in Tullahoma, Tenn.; they have also built a 32-MW generator.[15] These generators, however, can operate for only a few minutes because of fuel consumption. The 20-MW plant is used for powering a hypersonic wind tunnel. The first large fossil-fuel-fired MHD power plant designed for continuous commercial operation is now under construction on the outskirts of Moscow.[16]

The performance of an MHD generator increases with size because of the increasing volume-to-surface area ratio; the specific weight of the magnet decreases with size and power. There should be no insurmountable difficulties in building high-performance MHD devices as large as 10,000 MW. The construction of such a device awaits the development of a power source that can supply this energy in the form of an extremely hot, rapidly moving gas.

Heat sources for MHD generators, which have received essentially all the attention thus far, have been either combustion devices or solid-core nuclear reactors. The maximum temperatures for combustion devices are ~3000°K and are even lower for solid-core nuclear reactors. Even when the working fluid is seeded with an easily ionized gas (i.e., cesium or potassium), if the electron temperature is equal to the gas temperature, the electrical conductivity of the fluid is low,[17,18] particularly after accelerating the gas through a nozzle. This low electrical conductivity was the initial obstacle to actual operation of an MHD device,[19] and the low conductivity is now the major barrier to the realization of the high efficiencies and power densities of which the MHD generator is theoretically capable.[17] A solution to the low-electrical-conductivity problem was thought to be imminent in the early 1960's, when nonequilibrium ionization was first investigated for MHD devices. Heating the electrons to a higher temperature than the gas can increase the electrical conductivity by a factor of 10 or more. The proposed method of preferentially heating the electrons is by use of the magnetically induced electric field.

This work on nonequilibrium ionization has been directed toward solid-core nuclear-reactor heat sources

using noble gases, such as argon, in a closed cycle. Nonequilibrium ionization in combustion devices is not feasible because the very large electron-atom and electron-molecule collision cross sections in combustion products make it virtually impossible to obtain a condition of unequal electron and gas temperatures. The energy transfer from the higher-temperature electrons to the gas is much too high.

However, even for the solid-core nuclear reactor using a closed cycle, Brogan[17] states, "Indeed, almost the total research effort in generator working fluids for use with a nuclear reactor heat source has been given to the single topic of nonequilibrium ionization. It has proven to be an elusive quarry." Magnetically induced nonequilibrium ionization may still hold the solution to the low electrical-conductivity problem, but the most optimistic experimental results have failed thus far to produce evidence that the desired values of electrical conductivity (~100 mho/cm) can be produced by this method. Brogan also discusses both basic and practical reasons for the difficulty in attaining useful nonequilibrium ionization.

A heat source capable of higher temperatures than the 2500°K available from the solid-core nuclear reactor[2] appears to be very desirable and perhaps even essential. The use of a new heat source for MHD generators in the form of a gas-core nuclear reactor seems to offer two solutions to the low electrical-conductivity problem that would remove the major obstacle in achieving the high efficiency and power density of which an MHD generator is potentially capable. The first is the very high working-fluid temperature (5000 to 7000°K) that may be produced with gaseous reactors, and the second is the very high radiation flux available in the vicinity of such a reactor. This radiation flux may be extremely effective in ionizing the gas and preferentially heating the electrons. It could overcome many of the difficulties encountered with magnetically induced nonequilibrium plasmas. The feasibility of increasing the electrical conductivity by different types of radiation has been analyzed[20] with some encouraging results.

Submicron-sized particles in the gas-core reactor could also enhance the electrical conductivity of the fluid by supplying additional electrons by thermionic emission. In fact, this phenomenon has been suggested and studied briefly as a possible substitute for potassium or cesium seeding.[21,22] The combination of solid-particle seeding and potassium seeding could be a fruitful approach in MHD generators driven by devices other than a gas-core reactor.

The fundamental advantage of combining an MHD generator with a gas-core reactor is a more or less complete removal of any constraint on the top temperature of the thermodynamic cycle. This is particularly important for space power systems that require a high radiator temperature. The gas-core reactor MHD generator may also serve as a topping cycle for large ground-based power plants to improve their efficiency. As indicated by Rosa,[23] the gas-core reactor may very well prevent MHD technology from becoming obsolete. It appears to be the best heat source capable of allowing the MHD generator to realize its true inherent advantages.

The only significant difference between the gas-core rocket reactor and the gas-core reactor for MHD power would be the use of argon instead of hydrogen as the working fluid. Since the neutron-absorption cross section of an argon atom is slightly less than that of a hydrogen molecule, the operating characteristics would probably be enhanced by the substitution of argon for hydrogen. Also, the use of argon should improve uranium containment in the open-cycle systems.

Several preliminary design studies (Fig. 3) of gas core reactor/MHD power plants and propulsion systems have been reported.[23-26] One recent analysis[26] concluded that large commercial power plants using a gas-core nuclear-rocket-type reactor could have thermal efficiencies in excess of 70%. In summary, the advantages of the gas core reactor/MHD power plant are as follows:

1. High thermal efficiencies of the order of 70%.
2. Thermal pollution per electrical megawatt reduced a factor of 3 to 5 over today's plants.
3. Very high fuel economy due to the high efficiency and high fuel burnup achieved by recirculating the fissile fuel.
4. The possibility of continuous fuel reprocessing.
5. The continuous removal of xenon and other fission-product poisons from the reactor.
6. The absence of fuel elements which may rupture and have to be replaced.
7. A basically simpler reactor than today's power reactors.

It may be said that the gas-core reactor and the MHD generator are relatively new concepts, each with its own problems, and that there are twice as many problems if the two are brought together. However, that is not the case for the gas core reactor/MHD concept. Today's big problem with MHD power generation is achieving high electrical conductivities; however,

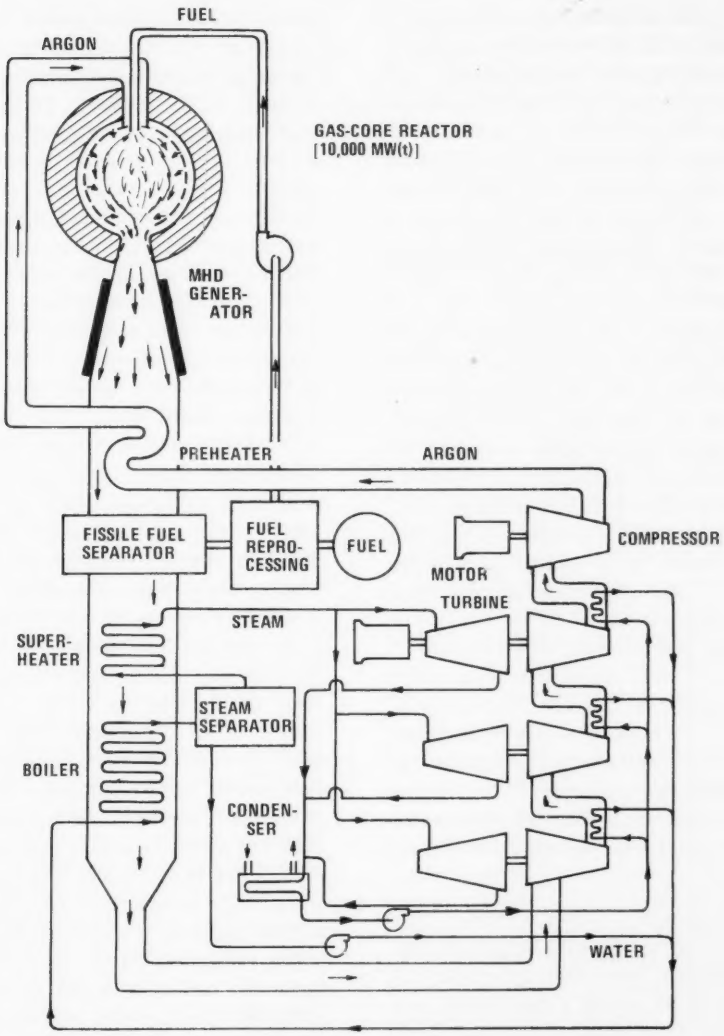

Fig. 3 Preliminary design of a gas core reactor/MHD power plant.[26]

the gas-core reactor essentially solves that problem by providing an extremely hot working fluid. Also, the major problems attributed to the gas-core reactor stem from its use for high-specific-impulse nuclear rocket propulsion; i.e., the requirement of a high separation ratio, a very hot exhaust, and the use of hydrogen as a working fluid. The constraints on a gas-core reactor for MHD power are much less severe. Thus combining the gas-core reactor and the MHD generator should help solve the problems of both. Of course, there are a number of technical problems that must be solved. These include the high-temperature-materials problems associated with both the reactor and MHD generator and the control and safety problems of the system.

NUCLEAR ANALYSIS AND EXPERIMENTS

The work by Bell[27] is one of the earlier analytical studies of a gas-core reactor. He used age and diffusion theories to analyze a spherical gaseous cavity surrounded by a moderator–reflector. Age theory was used to describe neutron slowing down in the moderator (no slowing down or fast absorption was per-

mitted in the fuel), and diffusion theory was used to describe thermal-neutron diffusion into the cavity and the resulting fissions in the fuel. In this analysis, the gas-core reactor was considered to be strictly a thermal reactor. Calculations were made for a UF_6 gas core and for various thicknesses of D_2O, beryllium, and carbon moderators. At approximately the same time, Safonov[28,29] also performed a similar study of a spherical model using diffusion and age theories. Since this early work by Bell and Safonov, there have been a variety of nuclear analyses.

In the United States, the first cavity-reactor experiments were performed at the Los Alamos Scientific Laboratory[30-32] using a 40- by 40-in.-cylindrical cavity surrounded by a D_2O reflector 20 in. thick. In the first experiments uranium was added in the form of metallic foil and placed on the periphery of the cavity; in later experiments graphite rods containing enriched uranium were used. The Russians have also reported the successful operation of a zero-power gas-core reactor experiment.[33] Experiments were performed for the National Aeronautics and Space Administration (NASA) by the Case Institute of Technology[34] using BF_3 to simulate a neutron-absorbing gas and a Pu–Be source to supply the neutrons. A wealth of experimental data has been provided as a result of the cavity-reactor critical experiments performed by Pincock, Kunze, and their colleagues.[35-42] In this section the neutronics analysis is reviewed, followed by a summary of some of the results of the cavity-reactor experiments.

Mills[32] analyzed experiments done as early as 1953 on externally moderated reactors with simple spherical and cylindrical geometries. These studies were made to establish the accuracy of transport calculations and showed fair agreement between theory and experimental data. Mills made an analytical study of gaseous ^{235}U reactors with D_2O, carbon, and beryllium moderators using spherical and cylindrical geometries. Critical masses varied from 0.5 to 30 kg, depending on the configurations and moderators used. Mills' results were relatively close to those of Safonov. It will be noted that, from this point on, the models used for the analyses became increasingly more sophisticated.

In 1961 Ragsdale and Hyland[43] reported nuclear calculations for cylindrical and spherical gas-core reactors using gaseous ^{235}U as the fuel and D_2O as the reflector. A parametric study was made with variations in moderator thickness, fuel-region radius for a given cavity radius, the effect of the cavity liner (structural material), and the moderator temperature. The spherical cavity was analyzed using a one-dimensional diffusion program with six neutron groups, including one thermal group, with the temperature of the D_2O being varied from 70 to 180°F. Since the thermal-neutron source was supplied by the moderator–reflector, it was assumed that the reflector temperature governed the neutron energy. Thermal cross sections were obtained for this temperature regardless of region. The criteria for the validity of diffusion theory as established by Safonov were used in this analysis and were a function of the "cavity grayness." The cylindrical reactor was analyzed in a similar manner using a two-dimensional neutron calculation with four neutron-energy groups. In both geometries the propellant region (hydrogen) was assumed to have a constant density, with absorption and slowing down in this region disregarded.

In 1963, Hyland, Ragsdale, and Gunn[44] extended their work. Although the earlier analyses were concerned primarily with spherical models, this later work was devoted solely to cylindrical reactors using a four neutron-energy group, two-dimensional diffusion code as before. Uranium-235 and ^{239}Pu were considered as fuels, and D_2O (at 300°F) and graphite (at 300 and 3200°F) were investigated as moderator materials. The study was conducted in two parts: The first part considered the effect on critical mass of a variable fuel-region radius in a fixed-size cavity; the second part pertained to specific effects for one particular configuration. In this analysis the reflector–moderator thickness was maintained at a constant 100-cm thickness since it had been concluded earlier that this would be about the optimum for reducing the critical mass without incurring an excessive weight penalty. The fuel region was centered in the cylindrical cavity and extended the entire length of the cavity with end reflection. On the basis of hydrodynamic, economic, heat transfer, and structural considerations, assumptions were made regarding relative flow rates, pressures, temperature ratios, etc. With these constraints a cavity radius of 150 cm was chosen as a representative value; later, a cavity radius of 40 cm was considered. The thermal cross sections used were computed at the moderator temperature, and the effect of Doppler broadening was considered due to the elevated fuel temperature. A Maxwellian flux shape was used in numerically evaluating the mean cross section.

Kaufman et al.[45] performed gas-core reactor calculations in 1965 using transport codes with a two-dimensional cylindrical geometry over a wide range of engine parameters. The study included

1. The effect of the pressure vessel on the critical mass.

2. Temperature effects on fuel requirements with D_2O, BeO, and carbon reflectors.

3. Comparison of reflectors and possible composite reflectors.

4. Geometry effects, such as length-to-diameter ratio.

Neutron transport codes developed by Los Alamos were adapted for this study. One-dimensional calculations were used initially to evaluate the effectiveness of various reflectors for a wide range of cavity dimensions and moderator temperatures. Also studied were composite reflectors and pressure-vessel effects. Using the two-dimensional version of the transport code in cylindrical coordinates, the effects of geometric variables on critical mass were evaluated. Varying the cavity radius gave the length-to-diameter ratio and the fuel-radius critical-mass data for cylindrical reactor configurations. One-dimensional calculations using spheres with the same surface-to-volume ratio and reflector thickness as the cylinder were used to select the reflector compositions and to provide first guesses for the two-dimensional calculations. An attempt was made to collapse the number of energy groups to reduce computing time. In going from 24 to 3 groups, machine time was reduced by a factor of 12. After a number of comparisons had been made between calculations using 24, 15, 13, and 3 groups, it was concluded that, in many cases, a single three-group set was quite adequate to yield the critical mass, total fluxes, absorptions, and leakages over the three important energy ranges. This was possible only by using the previously obtained multigroup results for a related problem. The full-group theory usually required a large amount of machine time. The report concluded that a large reduction in the critical mass of plutonium could be achieved by adding a small thickness of D_2O to the carbon reflector to make a composite reflector, thus indicating that such a combination may be desirable from a cost and weight standpoint.

Some useful and interesting transport calculations were reported by Plunkett[46] in March 1967. In the initial stages of his investigation, there was considerable concern about the applicability of diffusion theory to the process of neutron birth in the cavity, thermalization in the moderator, and the diffusion of thermal neutrons back into the cavity. Owing to this concern and to the work by Mills,[32] a multigroup S_N ($N = 8$) method was chosen as the basic calculational procedure to describe the angular distribution. A 16-group cross-section library was used for fast and epithermal groups. Thermal cross sections were calculated by averaging over a Maxwellian neutron distribution at the temperature of the moderator. The thermal cutoff was taken at 5 kT. Depending on the temperature of the moderator, 16, 15, or 14 energy groups were used. As the moderator temperature increased, some of the lower energy groups in the standard group data were overlapped by the increased energy of the thermal group. A mesh spacing of 4 cm was selected after comparison with runs using finer mesh spacings. The effect of Doppler broadening was considered in the calculations, due to the elevated fuel temperature, and found to be small in all cases. In the multigroup transport calculations, a rather common problem developed, namely, that of lengthy machine time. This caused a retreat from transport to diffusion theory with appropriate comparisons made over a wide range of parameters. As a result of this work, diffusion theory was considered to be adequate. Critical loadings never differed by more than 0.6% from the S_N results, and the flux distributions were in remarkably good agreement. This resulted in a change from transport to diffusion theory as the basic calculational tool, which proved to be desirable due to the many two-dimensional calculations made. It is interesting to note here that, although diffusion theory was considered adequate, a few-group treatment was inadequate.

As a further check on the diffusion theory, a comparison was made between the theory and critical experiments performed by Jarvis and Beyers[47] at Los Alamos using a cavity reactor with a 40-in.-diameter cavity containing fully enriched-uranium-loaded graphite rods surrounded by a 20-in. D_2O reflector. The maximum discrepancy between the calculated and experimental results was 3% in reactivity, indicating a higher reactivity eigenvalue. A parametric study was made in a spherical geometry using one-dimensional multigroup diffusion calculations to evaluate the effects of core size, reflector composition, fuel composition, reflector thickness, and temperature. Also, a study was undertaken to evaluate the effects on criticality of configurational changes that might be encountered in a rocket engine. The effects of temperature changes, fuel-radius variations, changes in the reflector voids, etc., were studied. These measurements were made in a cylindrical geometry.

A Rand report[48] published in 1963 showed that upscattering of thermal neutrons by the hot hydrogen is an important consideration. This suggests that a multi-thermal-group approach is essential to appropriately describe the thermal-neutron spectrum over the reactor. Most of the earlier work used only a single thermal group.

A significant contribution to this area was presented by Herwig and Latham[49] in May 1967. Their calculations were the first to include the detailed effects of hot hydrogen scattering on the low-energy neutrons returning into the cavity from various reflector–moderator configurations. This analysis was undertaken to provide information on the basic interactions between various nuclear reactor parameters that influence the reactivity and other nuclear characteristics of large reflector-moderated gas-core cavity reactors. This study was aimed at evaluating reactor characteristics rather than the critical mass, so a rather simple model was chosen using a spherical geometry. One-dimensional diffusion calculations were made with an 18 neutron-energy-group set, and 12 of these groups were in the thermal region. Scattering was permitted from any group within the 12 to any other group. The use of the two configurations demonstrated the differences in the nuclear characteristics of cavity reactors due to changes in reflector–moderator parameters such as temperature, slowing-down power, $(n,2n)$ neutron production, and thermal-neutron-scattering and thermal-neutron-absorption cross sections. The D_2O and carbon reflector–moderator, which provided a very effective fast-neutron scatterer adjacent to the cavity, gave rise to a relatively low-temperature neutron-energy spectrum (300°K) and produced large spatial changes in neutron-energy spectra. On the other hand, the BeO reflector–moderator provided a relatively less effective fast-neutron scatterer adjacent to the cavity, giving rise to a harder neutron-energy spectrum (2200°K) entering the cavity, and included a large contribution to the reactivity due to the Be$(n,2n)$ reaction cross section.

Latham has conducted a series of extensive calculations for the nuclear light-bulb model.[50–54] Some of Latham's methods and results from Refs. 52 and 53 are summarized below. The objectives of Latham's work were

1. To evaluate the effects of variations in engine design on the ^{233}U critical mass.
2. To compare critical-mass requirements using ^{233}U to those for ^{235}U and ^{239}Pu.
3. To evaluate various factors affecting engine dynamics.

The reference-engine configuration used seven reactor cavities, as illustrated by Fig. 2. Each cavity is 6 ft long by 2.3 ft in diameter. Beryllium oxide is used between the unit cavities, and layers of beryllium oxide and graphite surround the seven units to provide neutron reflection. Latham used the S_4 approximation and 24 neutron-energy groups for his one-dimensional calculations.

Latham used several thermal-neutron-energy groups in the 0- to 1.125-eV range to calculate the neutron absorptions and spectra accurately for adjacent regions in the moderator at quite different temperatures. The effects of neutron upscattering by the presence of hydrogen and hot neon in the 1200 to 7000°K temperature range inside the transparent partition were calculated by adding several thermal-neutron-energy groups in the 1- to 29-eV range. The basic set of 24 neutron-energy groups was chosen with 14 of the groups covering the 0- to 29-eV range and the remaining groups covering the 29- to 10^7-eV range. Fast-neutron cross sections were calculated[55] using GAM-I, with the slowing-down spectra determined for the various local moderator materials. The slowing-down spectrum in the cavity regions was assumed to be that corresponding to the beryllium oxide moderator, which was the material in largest quantity adjacent to the cavities. Thermal-neutron-absorption cross sections were calculated using TEMPEST,[56] with the spectra again chosen for the temperatures and materials of the local moderator regions. Up- and downscattering probabilities within the thermal-neutron-energy groups were calculated[57] using SOPHIST-I. SOPHIST-I includes in the up- and downscattering probabilities the enhancement of reaction rates due to the relative velocity between the neutron and the nucleus, so this effect was included in the calculation of the transport cross sections for the various materials. Two-dimensional configurations were analyzed economically by using the 24-group cross sections from the one-dimensional infinite-cylinder calculations to generate volume- and flux-weighted four-group cross sections. The boundary between groups 3 and 4 in the four-group set was at 8.32 eV, and some upscattering of neutrons from group 4 to group 3 did occur. Upscattering probabilities were eliminated from the two-dimensional problems by using the option in ANISN[58] to create a four-group cross-section set that had only downscattering. That option subtracts the upscattering from the downscattering and thereby maintains the balance of transfer of neutrons between adjacent groups. Two-dimensional calculations (Fig. 4) were made based on diffusion theory (EXTERMINATOR)[59] and also the S_4 transport approximation using DOT.[60]

Some of Latham's important results were:

1. On the basis of the two-dimensional diffusion calculations, a ^{233}U critical mass of 15.5 kg was obtained as compared with a value of 14.0 kg (11% less) using the two-dimensional transport program.

Figure 5 is a graph of the results that illustrate the effect of the moderator-volume fraction on critical mass.

2. Uranium-235 and ^{239}U critical masses based on the one-dimensional calculations were 22.8 and 20.8 kg, respectively.

3. Positive reactivity coefficients resulted from increases in operating pressure and temperature. Values of computed reactivity coefficients are listed in the System Dynamics, Stability, and Control section (page 245).

4. An increase in the amount of tungsten used as a particle seed in the propellant resulted in a reactivity decrease. The effect of the tungsten seeding on the critical mass was small.

5. The prompt-neutron lifetime was 0.516 msec.

6. A reactivity decrease resulted from an increase in fuel radius with the chamber pressure and ^{233}U mass held constant.

7. Figure 5 shows a comparison of the flux distributions calculated using diffusion and transport codes.

A series of critical experiments was performed by Pincock et al.[35-42] to study the ability of various calculational procedures so as to evaluate criticality and other reactor parameters accurately for a configuration closely resembling that of the coaxial-flow gas-core reactor and to provide experimental values for the parameters of interest. A large number of critical experiments were performed in a mockup in which the fuel was dispersed as small foils in various patterns representing fuel distributions in a gas-core reactor. An actual gaseous UF_6 core configuration was made critical in May 1967. The gaseous fuel was contained inside an aluminum tank with a diameter of 122 cm and a length of 109 cm. The surrounding moderator–reflector tank was a cylinder having a diameter and length, inside, of 183 and 122 cm, respectively, and, outside, of 366 and 305 cm, respectively. The tank was filled with D_2O to a nominal thickness of 89 cm and contained a 10.2-cm-thick beryllium slab in the D_2O spaced 6.7 cm from the cavity wall. For the cavity experiments using fuel foils, the cavity-reactor assembly consisted of a cavity region 182.9 cm in diameter by 121.9 cm long, surrounded by an average thickness of 88.9 cm of D_2O. The experiments described include measurements of a large number of reactor-physics parameters such as the effects of core size, fuel worth, structural material worth, hydrogen propellant worth, neutron generation time, and flux distributions.

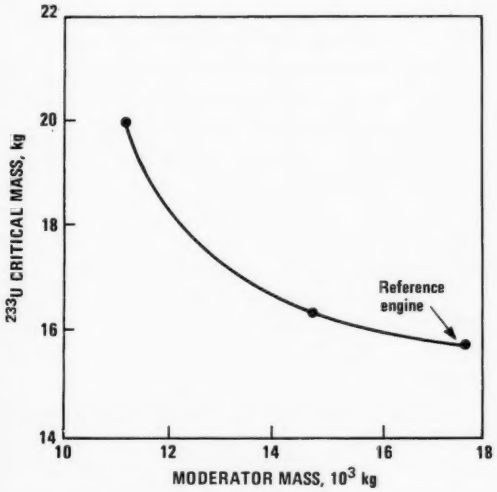

Fig. 4 Effect of total moderator mass on the ^{233}U critical mass for the nuclear light-bulb engine.[53]

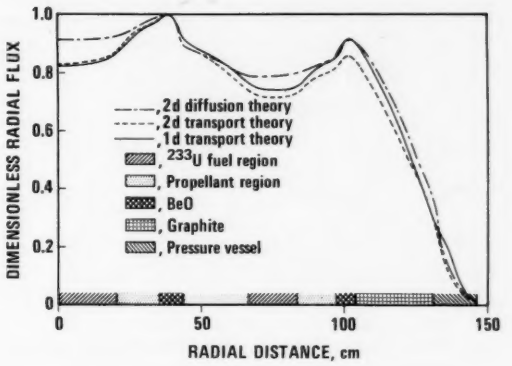

Fig. 5 Comparison of thermal-radial-flux plots for one- and two-dimensional neutron-diffusion-theory and neutron-transport-theory calculations for the nuclear light-bulb engine.[53]

Figure 6, taken from Ref. 42, is a representative measured radial thermal-flux distribution for the complete coaxial-flow mockup showing the peaking of the thermal flux in the reflector. The calculations analyzing the Idaho cavity-reactor experiments were made using (1) a 19 energy-group diffusion theory and S_4 and S_8 transport theory and (2) 4- and 7-group two-dimensional diffusion theory. Some results of the study were (1) the difference between the results of S_4 and S_8 calculations is small; (2) use of a single thermal group is not adequate, resulting in 2.5% greater reactivity than for 7 thermal subgroups; (3) the critical mass in the complete mockup was 44.9 kg of uranium;

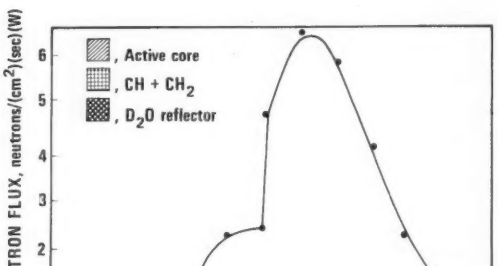

Fig. 6 Radial thermal-flux distribution for the coaxial-core mockup of the Idaho cavity-reactor experiments.[42]

(4) the average fuel worth was 0.250% Δk; and (5) the worth of the exhaust nozzle mockup was 0.46% Δk or equivalent to 1.8 kg of fuel in the cavity.

The NASA Lewis Research Center studied the application of Monte Carlo methods to analyze the gas-core experiments, but, according to R. E. Hyland, they found that the statistical nature of the results led to uncertainties that could only be reduced by unacceptable computer costs.

HEAT TRANSFER

Whenever the working fluid in a high-temperature gas-core reactor is different from the fissile fuel, a mechanism must be provided for the transfer of heat from the hot fissioning gaseous core to the working fluid. The gas-core reactor concepts currently under investigation for nuclear rocket propulsion require not only that the heat be transferred from the fissioning core to the hydrogen propellant but also that this process occur with little or no mixing between the gaseous fuel and the propellant. Thus radiant heating of the propellant by intense thermal radiation from the core must be employed as the primary means of heat transfer. Since hydrogen at temperatures below about 7000°K is transparent to this thermal radiation, it must be seeded with a material that has a high absorption coefficient over the wavelength range corresponding to the thermal-radiation emission spectrum of the fissioning core.

The absorption coefficients of possible gaseous seed materials exhibit a strong dependence on wavelength, since gases tend to absorb in lines or bands, whereas the absorption coefficients of particle clouds are smooth and relatively slowly varying functions of wavelength. The best material for seeding the hydrogen in a gas-core nuclear rocket engine appears to be dispersed submicron-sized particles of refractory metals. Aerosols of such particles are highly absorbing over the wavelength range of interest for gas-core reactors at temperatures up to the vaporization temperature of the particles.

Thus the treatment of heat transfer in a gas-core reactor can be broken down into two processes: (1) the transport of heat that is generated by fission through the hot core of gaseous fissioning fuel to the surface where it leaves the core, primarily as thermal radiation, and (2) the absorption of this thermal radiation in the seeded working fluid. To permit an evaluation of these processes for gas core reactors, various investigators have calculated, and others have measured, the heat-transfer parameters of uranium plasma, hydrogen, and clouds of refractory particles.

In 1966, Gurvich and Yugman[61] reported calculations of the thermodynamic functions of gaseous uranium at temperatures up to 20,000°K. Keston and Krascella[62] used a semiempirical model for uranium to calculate the opacity of uranium plasma and the heat-transfer characteristics of the uranium core. The more recent calculation of Parks et al.[63] uses methods closer to first principles. They assumed a modified Thomas–Fermi potential that was calibrated against one-electron binding energies, which had been calculated at Los Alamos using a relativistic, self-consistent field approach. Their results for the composition, thermodynamic functions, and optical parameters of uranium from 5000 to 110,000°K over the pressure range 100 to 1000 atm are probably the most accurate available. They showed that the spectrum-averaged opacity of gaseous uranium increases with temperature to a maximum of about 50,000 cm^2/g at about 12,000°K and decreases at higher temperatures. These results indicate that, if the average temperature of the uranium core of a gas-core reactor is about 40,000°K and the reactor pressure is 500 atm, the mean opacity of the uranium core would then average about 30,000 cm^2/g. Since the average density of such a core would be about 0.0044 g/cm^3, the mean free path of a photon in the core would be of the order of 0.004 cm, or 40 μ. This means that the uranium core is optically black to its own thermal radiation, and the radiant energy leaving the core will be emitted from very near the core surface.

The results of these theoretical calculations are compared in Ref. 63 with experimental values, inferred

from measurements by Meggers et al.,[64,65] of the intensity of line emission from an arc containing uranium. The theoretical and experimental values, compared at 5100°K and a pressure of 3.58×10^{-4} atm, agree well within an order of magnitude even though there are large uncertainties in both the experimental and theoretical results.

Measurements of the absorption coefficient of uranium plasma over the wavelength range from 2800 to 8800 Å are being made by Miller, Wilkerson, and Koopman[66,67] using a shock tube. Uranium plasma temperatures from 7500 to 12,000°K and partial pressures from 0.02 to 0.2 atm are being investigated. Their measured values of the absorption coefficient agree well with those calculated by Parks et al.[63] for wavelengths between 4000 and 8800 Å; however, the observed values decrease rapidly as the wavelength is decreased below 4000 Å, whereas the theory predicts a rapid increase at shorter wavelengths (Fig. 7). The wavelength range below 4000 Å is very important in the core region of the reactor. Thus, if the uranium-absorption coefficient is, in fact, much lower than predicted in the ultraviolet, the mean free path of these photons may be much longer and the core more transparent than had been thought. This would reduce the average core temperature due to the enhanced heat transfer through the core and would also enhance the ultraviolet thermal-radiation emission from the fuel region of the reactor.

The thermal emission spectrum from hot gaseous uranium has been investigated both experimentally and theoretically. Krascella[68] has reported theoretical investigations of the radiant emission spectrum from the fuel region of a gas-core reactor and concluded that the spectral distribution of the thermal radiation differs appreciably from that of a black body and is shifted into the shorter wavelength region. He also concludes that the thermal-radiation spectrum emitted from the fuel region is controlled by a very thin layer of fuel near the surface of the fuel region because of the highly opaque nature of the nuclear fuel. Schneider et al.[69] measured the emission spectrum of a uranium arc and showed that the emission was much stronger in the ultraviolet than in the visible. Measurements of the thermal emission from uranium in U–Ar plasmas, which have been made by Marteney, Mensing, and Krascella,[70] have also demonstrated enhanced emission in the ultraviolet. Some of the results of these measurements are illustrated by Fig. 8.

The closed-cycle gas-core reactor concept requires that thermal radiation emitted by the fuel region be transmitted through an internally cooled transparent

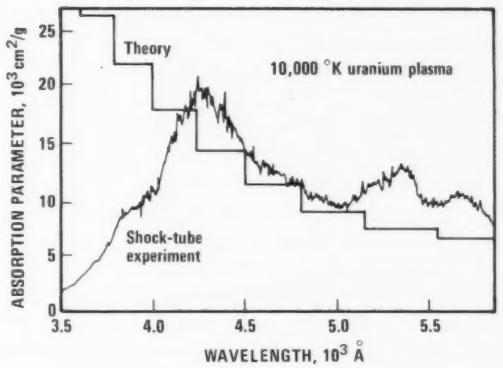

Fig. 7 Optical absorption coefficient of uranium plasma.[94]

partition into the working fluid. The United Aircraft Corporation, Research Laboratories, studying the closed-cycle concept, have carried on a research program investigating the properties of various possible materials for the construction of the transparent partition. At present, fused silica and beryllium oxide are considered the most likely candidates for the partitions; however, since fused silica is cheaper and much easier to fabricate, most of the experimental work to date has involved fused silica.

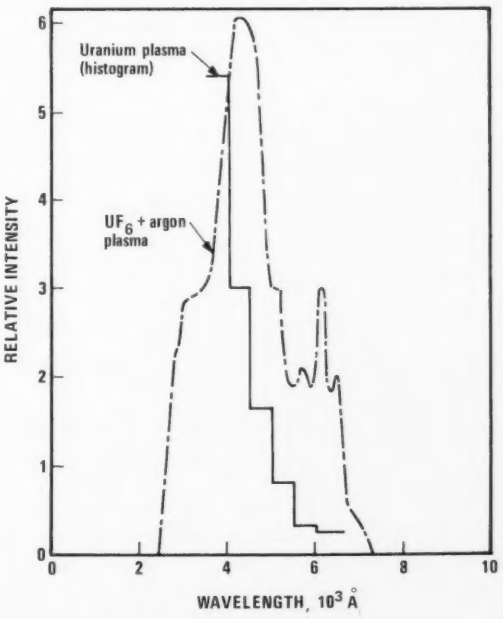

Fig. 8 Thermal-radiation emission spectra of uranium plasma.[69,70]

Palma and Gagosz[71] have recently reported measurements of the optical absorption of fused silica during neutron and electron irradiation at elevated temperatures and showed that, for a fast-neutron ($E > 0.75$ MeV) dose rate of 2×10^4 rads/sec, the radiation-induced absorption coefficient at 2150 Å dropped from 0.276 cm^{-1} at 550°K to 0.022 cm^{-1} at 1190°K. Absorption induced by 1.5-MeV electron irradiation at dose rates as high as 1.6×10^7 rads/sec was found to decrease as the temperature was raised. The results of these studies indicate that, if the fused-silica partition is maintained at a temperature of about 1200°K or higher, the effects of the intense nuclear radiation, which would otherwise increase the absorption coefficient of the partition, tend to anneal out. These absorption measurements were made for a wavelength of 2150 Å because this is the center of the most prominent irradiation-induced absorption band in the Corning Grade 7940 fused silica that was used. Since fused silica is highly absorbing for wavelengths below 1800 Å, radiant energy in this wavelength range which is emitted from the core will be absorbed either in the transparent partition or in the neon buffer region between the fuel region and the partition. There has been some consideration to seeding the neon buffer region with a gas such as oxygen to absorb this energy before it reaches the partition. Whether or not this will be necessary depends on the amount of thermal radiation emitted from the fuel region in the wavelength range over which the partition is significantly absorbing.

Just about all the radiant energy emitted from the fissioning fuel must be absorbed in the working fluid flowing around the core to provide for maximum heating of the working fluid, and, at the same time, reduce the heat flux to the moderator to an acceptable level. The addition of an absorbing seed material to the working fluid is necessary to permit radiant heating of the working fluid over the temperature range where it would otherwise be transparent. It will be necessary to develop techniques for providing this particle seeding on a large scale.

Submicron-sized refractory-metal particles appear to be the best seed material because they are highly absorbing over a broad wavelength range in the ultraviolet, visible, and near infrared regions of the spectrum, and they can withstand high temperatures without vaporizing. Also, such particles have remained essentially in thermal equilibrium with the working-fluid gas, since the particles are heated by the thermal radiation and the gas is heated by conduction from the particles. One study of radiant heating of a seeded gas in a coaxial-flow gas-core reactor geometry which was carried out by Masser[72] has concluded that the difference between the particle and bulk-gas temperature would be <300°K and would be much less over most of the propellant region. Also, flash-heating experiments[73] demonstrated that, when particles dispersed in hydrogen were heated several thousand degrees Kelvin in less than a millisecond, the gas temperature followed the particle temperature with a time lag of about 1 msec.

To accurately predict the temperature distribution in the propellant region of a gas-core reactor, one must know the thermal-emission spectrum from the fuel region, the absorptive properties of the working fluid as a function of temperature at the reactor operating pressure, and the absorption and scattering characteristics of the seed particles suspended in the working fluid. Krascella[74] and Patch[75,76] have calculated the composition, optical parameters, and thermodynamic properties of hydrogen over a range of temperatures to 50,000°K and pressures to 1000 atm. These calculations indicate that hydrogen at several hundred atmospheres pressure would become opaque to the thermal radiation from the core at about 7000°K (Fig. 9). Thus the seed particles are no longer needed above about

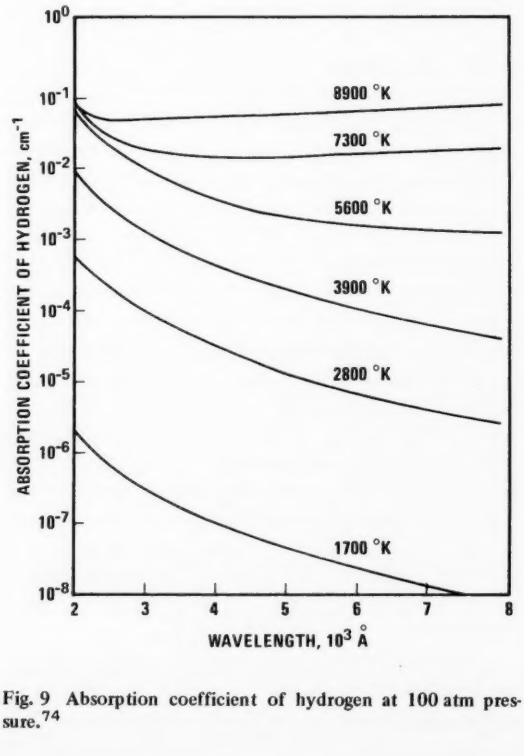

Fig. 9 Absorption coefficient of hydrogen at 100 atm pressure.[74]

7000°K. The purpose of the seed material, then, is to permit the propellant to be heated up to this temperature. Masser[77] extrapolated existing vapor-pressure data to 1000 atm for 13 materials with atmospheric boiling points over 3000°K and thermal-neutron-absorption cross sections <5b. He concluded that tungsten would have a boiling point of about 9340°K and several carbide materials would have boiling points of the order of 8000°K.

At temperatures well below 7000°K, hydrogen is essentially transparent. The equation for steady-state thermal-radiation transport through a transparent gas seeded with particles may be written

$$\frac{1}{\rho}\frac{dI(\lambda,\Omega)}{ds} = -\mu_e(\lambda)I(\lambda,\Omega) + j(\lambda) + \mu_s(\lambda)\int_0^{4\pi} I(\lambda,\Omega')p(\lambda,\cos\theta)\frac{d\Omega'}{4\pi} \quad (9)$$

where I = the intensity of radiant energy in a unit wavelength interval at λ traveling in direction Ω
s = distance
Ω = solid angle
j = emission coefficient
p = scattering amplitude function
θ = angle of scattering

It is seen from this equation that the four important parameters one must know to evaluate radiant heat transfer through particle-seeded gases are:

$\mu_e(\lambda)$, the extinction parameter
$\mu_s(\lambda)$, the scattering parameter
$p(\lambda, \cos\theta)$, the scattering amplitude function
$j(\lambda)$, the emission coefficient

These parameters must be known over the applicable temperature and wavelength range. In addition, $p(\lambda, \cos\theta)$ must be known for scattering angles of from 0 to 180°.

A rigorous solution to Maxwell's equations for the absorption and scattering of radiant energy by homogeneous spherical particles of any composition suspended in a homogeneous nonmagnetic transparent medium was published in 1908 by Mie[78] and is now commonly known as the Mie theory. Krascella[79] applied a transformation procedure developed by Aden[80] to the Mie equations to calculate the effects of particle size, wavelength, and particle temperature on particle opacity in those regions of the ultraviolet, visible, and infrared spectra for which complex refractive-index data were available. Shenoy[81] used Krascella's program to extend these calculations to other types of particles and to a broader wavelength range. At present, there is no theory to accurately predict the absorption and scattering characteristics of irregularly shaped particles. The Mie theory predicts that $\mu_a(\lambda)$ is a maximum when the particle radius is of the order of the wavelength λ divided by 2π. Thus, for a given particle-seed density ρ, the absorption of thermal radiation in the near infrared, visible, and ultraviolet regions of the spectrum is greatest for submicron-sized particles of diameters in the range 0.05 to 0.50 μ. Submicron-sized particles of refractory materials are generally highly irregular in shape, so the Mie theory can be used only as an approximation to the absorption and scattering characteristics of these particles.

Various groups have experimentally investigated the absorption and scattering parameters of gases seeded with refractory particles. Lanzo and Ragsdale[82] measured the absorption of thermal radiation by suspended particles as a function of material, size, and concentration. This experiment involved radiating energy from an electric arc to air that contained submicron-sized refractory particles. Seeded air was introduced into an annular heat exchanger. The arc was initiated, and the unseeded air temperature in the annulus reached 556°K. When carbon particles were added to the air stream, they absorbed radiant energy and caused the outlet temperature to increase to 667°K. This behavior shows that particle-seeded air will absorb radiant energy from the electric arc. Keng and Orr[83] reported theoretical and experimental studies of radiant heat transfer from a heated tungsten cylindrical enclosure to a particle cloud within it. A transparent gas, helium, was passed through the tube, and the tube dimensions and helium flow rate were selected to give a low thermal efficiency for forced-convection heating. The addition of tungsten or carbon particles to render the gas opaque caused a significant increase in heat absorption.

Marteney[84] studied techniques of producing dispersions of submicron-sized solid particles in a carrier gas and investigated the optical parameters of these particles for several wavelengths. Tests were conducted with carbon and tungsten particles having nominal radii of 0.0045 and 0.01 μ dispersed in helium and nitrogen. These studies showed that the application of aerodynamic shear forces to a carbon aerosol resulted in an increase by a factor of 5 in the absorption parameter. This increase is believed to be caused by a reduction in the size of particle agglomerates since, theoretically, a decrease in the average agglomerate size should result in an increase in the value of the extinction parameter.

The first experimental work involving particle-seeded gases at very high temperatures was reported by Burkig.[85] In this experiment a cloud of particles in a gas was injected into a transparent quartz tube and exposed to the flash of a xenon flashtube. The temperature rise of the gas was inferred from the pressure rise measured with a fast-response pressure transducer. The bulk of the work was with micron-sized particles of carbon, iron, and tantalum carbide. In general, initial pressures of 2 and 5 atm were investigated for both helium and hydrogen. During the flash, as indicated by the pressure transducer, the temperature of the carbon aerosol rose to about 2500°K or more for ~1 msec. Shenoy, Williams, and Clement[86] measured the extinction parameters of submicron-sized particles of carbon, tungsten, and silicon at various temperatures up to 2200°K over a wavelength range of 1600 to 6000 Å (Fig. 10). Their experimental values showed good agreement with the Mie theory at those temperatures and wavelengths for which the availability of complex refractive-index data made Mie calculations possible.

The scattering amplitude function and the extinction parameter of micron-sized aluminum oxide particles were reported by Love[87] for wavelengths in the infrared region between 4 and 16 μ. Marteney[84] showed that light scattering from submicron-sized carbon and tungsten particles is highly forward. Williams and Jacobs[88] have measured the scattering amplitude functions of submicron-sized particles of tungsten, carbon, silicon, tungsten carbide, and silicon carbide from 1 to 179°.

Now that data on the heat-transfer parameters of clouds of submicron refractory particles are becoming available, one should be able to calculate the temperature distribution in the propellant region more accurately than previously. A few years ago Kascak[89] assumed a fairly opaque core and a gray propellant and calculated the temperature distribution throughout the propellant region of a coaxial-flow reactor. He also investigated the effect of a seed–hydrogen opacity window, which might exist if the seed vaporizes at a lower temperature than that required for the hydrogen to become highly absorbing, and showed that such a window would serve to make the temperature distribution in the propellant region more uniform. Kascak[90] has also calculated the temperature distribution in the fuel region of a coaxial-flow gas-core reactor. Estimated average fuel temperatures varied from a low of 30,500°K at 100 atm pressure and 10^5 lb of thrust to a high of 61,100°K at 1000 atm pressure and 10^6 lb of thrust. Keston and Krascella[91] calculated the temperature profile in a cylindrical fuel region of a gas-core reactor and arrived at average fuel temperatures of from ~35,000 to ~50,000°K.

McLafferty[92,93] has reported analytical studies of the absorption of thermal radiation in the transparent wall of a nuclear light-bulb engine and the temperature distribution in the propellant region. He showed that the addition of a small amount of oxygen to the neon buffer region will result in the absorption of much of the ultraviolet energy that would otherwise be absorbed in the transparent wall. For fused silica the maximum permissible wall thickness decreases from 15 mils for a 6000°K effective black-body fuel radiating temperature to ~0.1 mil at 15,000°K. The maximum wall thickness is increased by a factor of ~5 if a beryllium oxide wall is used instead of fused silica. Thus the major problem with the light bulb is to arrive at a transparent partition which is thin enough to transmit the thermal radiation without overheating but which is of sufficient thickness to provide the necessary structural strength to survive in the environment of a rocket engine. A 5-mil wall thickness was chosen for the reference-engine design. The propellant inlet temperature would be ~2300°K and the exit temperature ~6000°K for the light-bulb engine.

A comprehensive review of the present status of research regarding the optical parameters of uranium plasma, hydrogen, and various particle seeds recently presented by Patch[94] brings together opacity information needed for heat-transfer calculations for gas-core reactors. He concludes that calculations and measurements of radiant heat transfer, where scattering is treated as a function of angle, are needed and that the effect of thermionic emission from the hot particles should be taken into account. He also points out the need for more information on absorption by the vapor or reaction products of the seed materials.

FLUID MECHANICS

Mixing of coaxial jets finds many physical applications and has been investigated since 1925. Kulik, Leithem, and Weinstein[95] present a brief discussion of some of the earlier background. Clark et al.[96] have presented a comprehensive summary of gaseous nuclear rocket fluid-mechanics work up to 1967. McLafferty[3] and Clark et al.[96] have also discussed the more recent work at United Aircraft. Chang, Chi, and Chen[97] carried out a series of vortex experiments which demonstrated a high separation ratio could be achieved for very small fuel-volume fractions.

EXTINCTION PARAMETER, cm^2/g

EXTINCTION PARAMETER, cm^2/g

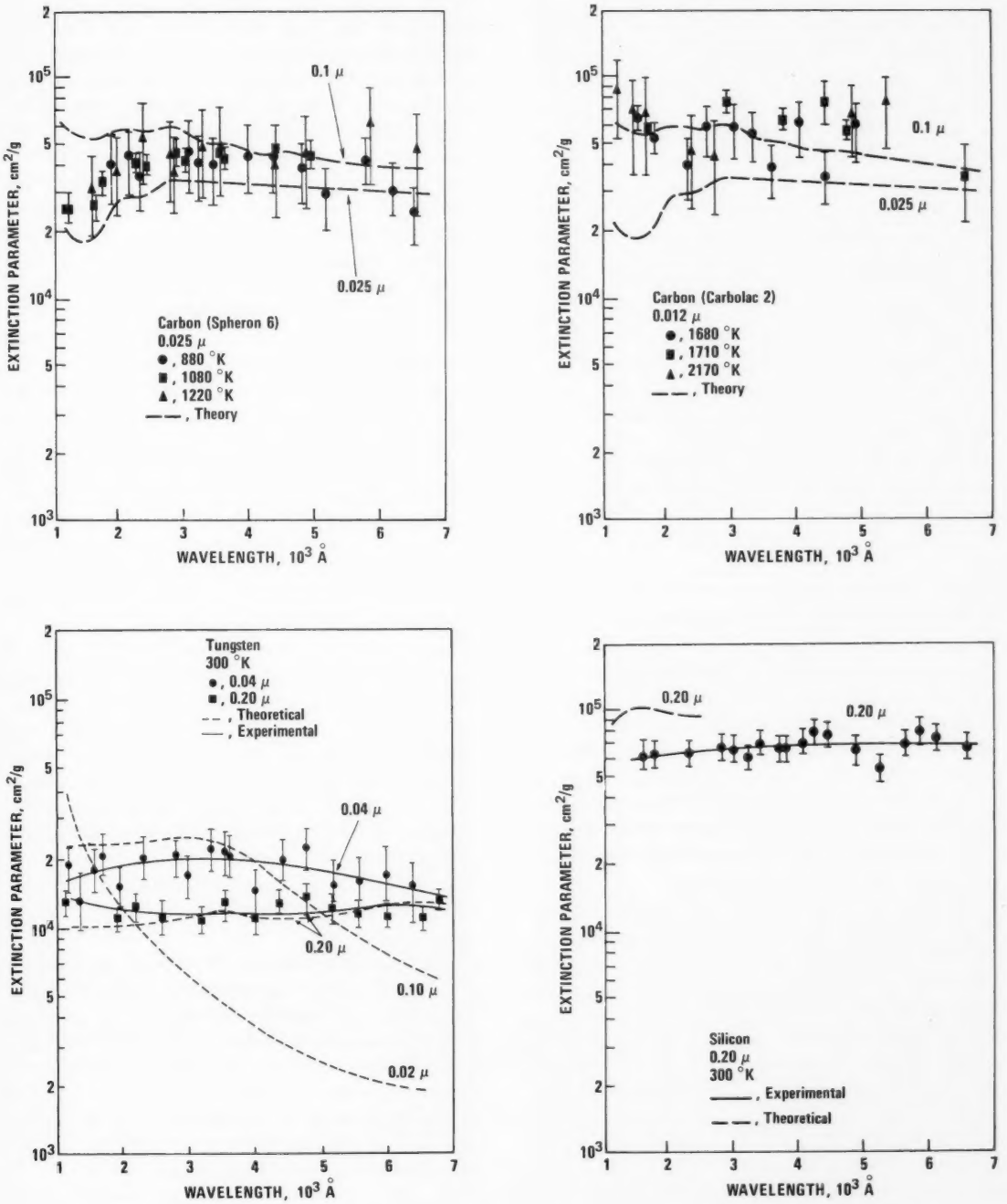

Fig. 10 Extinction parameters of submicron carbon, tungsten, and silicon particles suspended in hydrogen.[86]

For the gas-core nuclear rocket engine, the separation ratio is defined as the ratio of the mass flow rate of hydrogen propellant to the mass flow of fissile fuel. High separation ratios are desirable for nuclear rocket reactors because of the cost of fissile fuel and the undesirable effect of the fuel atoms on the specific impulse. A separation ratio of at least 30 is considered essential for practical gas-core nuclear rocket engines, with a separation of 50 to 100 or higher to be desired. The primary purpose of the various flow schemes being investigated is to maximize the separation ratio. The light-bulb concept is an attempt to solve this problem by putting the fissioning gas in a container.

The earliest work on the gas-core reactor was directed primarily toward the vortex concept because it was thought the centrifugal acceleration of the vortex would confine the heavier uranium gas close to the walls of the cylindrical cavity while the hydrogen diffused through the uranium, became heated, and was exhausted through the nozzle. Tangential fluid injection and MHD acceleration were considered as possible approaches to maintaining the vortex flow. The results of an extensive series of flow tests carried out by NASA and others showed that the separation ratio achieved was far too low for a practical vortex-stabilized open-cycle gas-core nuclear rocket engine.[96]

Two other approaches have since been taken to solve the problem of fuel containment. One approach was to adopt a different flow scheme, the coaxial-flow reactor, and try to make it work. Theoretically, by giving the central stream of fissile fuel a small velocity relative to the outer annular fast-moving region of hydrogen, the separation ratio could be made large. The other approach was to retain the vortex concept but to confine the uranium vortex in a transparent container. This is the light-bulb concept.

Most of the work on the coaxial-flow concept during the 1960's was directed by Ragsdale and Rom.[13,98] Ragsdale[13] has recently completed a study of the relation between the separation ratio and other engine parameters for open-cycle reactors. Most of the fluid-dynamics experiments related to the coaxial-flow concept involved measurements of coaxial flows in cylindrical pipes or ducts. The results were not encouraging because the large fuel-volume fraction, necessary because of criticality considerations, made high separation ratios impossible. Masser and Taylor[99] have recently achieved an improvement of this type of flow for low velocity ratios by inserting a Mylar honeycomb section into the injection region. Perhaps the most promising breakthrough to date for the coaxial-flow concept (Fig. 1) was achieved recently by Lanzo.[100] The geometry tested was made up of a curved porous wall, through which the clean air (propellant) was introduced. Smoky air (fuel) was injected into the cavity opposite the exhaust port. The flow pattern was analyzed photographically. It was shown that a relatively large, stagnant fuel volume forms in the cavity for separation ratios as high as 100. Although this experiment did not properly mock up some important engine parameters and conditions, such as heat generation, density ratios, and Reynolds numbers, the concept appears very promising.

The first indications of laminar vortex flow were[101] found in water vortex tests in 1964. Results of two-component gas tests showed that a favorable radial gradient of density (increasing density with increasing radius) tended to stabilize vortex flow.[3,96] These tests were carried out with air injected near the outer periphery of the vortex to drive the vortex and with mixtures of different simulated fuel gases injected near the center line to simulate a fuel cloud. Helium dyed with iodine injected near the vortex center line showed a steep radial gradient in gas concentration near the outer region of the cloud. A major difficulty with the cold vortex-flow test was that injection of substantial quantities of simulated fuel into the central region led to high levels of turbulence.

Recently a number of studies have been directed toward investigating fuel confinement by more closely simulating the core at high temperatures using radio-frequency (r-f) heating in two-component systems.[3,102-104] Recent research[102] has indicated that heating of the central fissioning plasma in the coaxial-flow system may serve to significantly increase fuel containment. This series of experiments has demonstrated that there is very little mixing between the central heated flow and the surrounding unheated flow, whereas at room temperature, there is considerable mixing.

Roman, Klein, and Voyt[105,106] have reported the development of a high-intensity 1.2-MW r-f source. Radio-frequency energy was supplied to an argon plasma within a radial-inflow vortex. Tests were conducted up to 16 atm pressure with 216 kW deposited in the steady-state discharge. Klein[107] reports using an r-f induction heater to conduct experiments to simulate the absorption of thermal radiation in the propellant duct of a nuclear light-bulb reactor.

In spite of the vast amount of available experimental and analytical fluid-mechanics data, internal and surface stability of the fuel region in the gas-core reactor remains one of the most crucial unanswered questions.

SYSTEM DYNAMICS, STABILITY, AND CONTROL

Although there is extensive literature concerning dynamics and control of solid-core reactors for nuclear rocket applications, especially in connection with the Kiwi, NERVA, and Phoebus reactor programs, little information has been available on gas-core reactor-system dynamics until recently. The reason, of course, was the lack of knowledge of the pressure and density changes and core-radius changes that may introduce reactivity and neutron-density fluctuations. The most recent and comprehensive studies are the engine-dynamics analysis for the nuclear light-bulb reactor-engine system carried out by Latham[56] and the cavity-reactor critical experiments on waves and control methods reported by Pincock and Kunze.[41]

Latham's studies were based upon a vortex-stabilized nuclear light-bulb engine design (see Fig. 2) with the following characteristics:

1. Cavity configuration—seven separate cavities having a total overall volume of 170 ft^3, each having a length of 6 ft.
2. Cavity pressure—500 atm.
3. Specific impulse—1870 sec.
4. Total propellant flow (including seed and nozzle transpiration coolant flow)—49.3 lb/sec.
5. Thrust—92,000 lb.
6. Engine power—4600 MW.
7. Engine weight—70,000 lb.
8. Ratio of average density in fuel-containment region to neon density at edge of fuel—0.7.
9. Fuel radiating temperature—8200°R.
10. Propellant exit temperature—6700°R.
11. Average fuel residence time—20 sec.
12. Critical mass—13.7 kg.
13. Prompt-neutron lifetime—0.000516 sec.
14. Fuel radius—0.681 ft.
15. Average thermal-fission cross section—193 b.
16. Steady-state fuel-injection rate—1.5 lb/sec.
17. Reactivity-feedback coefficients—

    Fuel, $(\delta k/k)/(\Delta T_M/T_M) = +0.045$.

    Moderator temperature, $(\delta k/k)/(\Delta T_M/T_M) = +0.045$.

    Propellant density, $(\delta k/k)/(\Delta\rho_H/\rho_H)_{prop} = +0.0544$.

    Moderator coolant density, $(\delta k/k)/(\Delta\rho_H/\rho_H)_{mod} = +0.0315$.

    Fuel-region radius, $(\delta k/k)/(\Delta R_F/R_F) = -0.0413$.

Latham developed models simulating both engine-startup and full-power-generating conditions.

The startup steps Latham proposed were: (1) close nozzle (it was shown in Ref. 55 that a variable-throat-area nozzle would be necessary to limit the flow rate of the propellant during startup); (2) fill both the hydrogen ducts and the neon system from storage until the neon density is equal to the neon density at the edge of the fuel region at nominal full-power operation at a pressure of 20 atm at 600; (3) turn on neon-recirculation pump; (4) inject fuel until critical mass is reached; (5) increase power level and adjust flow rates and pressure to maintain criticality and the pressure balance throughout the system and to limit component temperatures to desirable levels; (6) inject propellant seeds at about 10% of full power (this occurs at an equivalent black-body radiating temperature of 8500°R); and (7) raise power to desired level. Making the studies tractable required the assumption that startup can be controlled so as to permit the power to be increased on a linear ramp from zero to full. The results of Latham's startup studies showed:

1. The critical mass of ^{233}U varies from 8.5 kg at zero-power conditions to 14.2 kg at full power (Fig. 11).
2. The sequence of events during startup is not strongly dependent upon the length of the startup ramp, primarily due to the large heat capacity for the beryllium oxide/graphite moderator.
3. In the initial stages of startup, more pumping power is needed than the turbine can supply, so an auxiliary power source will be needed at startup.
4. No serious thermal-stress problems were found during startup. Figures 11 and 12 from Ref. 54 show, respectively, the variations, during startup, of the ^{233}U critical mass and of the average fuel temperature.

Latham's model for the engine under full-power operating conditions involved solving a simultaneous set of equations describing the thermal and fluid dynamics and neutron kinetics behavior of the system. The reactivity-feedback coefficient included (1) a contribution to the excess reactivity needed to compensate for the loss of delayed neutrons from the fuel region, (2) a time-varying term used as an input driving function, (3) the reactivity feedback associated with changes in the fuel loading, average moderator temperature, propellant density, moderator coolant density, and fuel-region radius. Responses of the uncontrolled engine to various perturbations were calculated. The oscillations, which were usually damped but sometimes maintained at a constant amplitude, were driven primarily by the positive moderator temperature coefficient and the fuel-injection rate, which tended to

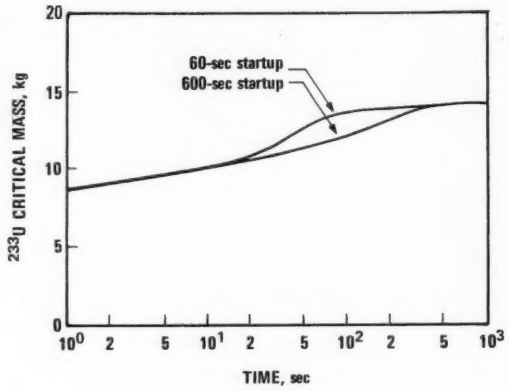

Fig. 11 Variation of ^{233}U critical mass during startup power ramps for the nuclear light-bulb engine.[54]

exceed the steady-state rate when the chamber pressure dropped to <500 atm. Figure 13, taken from Ref. 54, shows the response of the total reactivity and power level to a step increase in reactivity of 0.0017. The major conclusion was that engine control can be achieved by controlling the fuel-injection rate.

The possibility of fluid oscillations of an acoustic nature in the gaseous uranium fuel region, with feedback to the oscillations caused by reflection and diffusion of neutrons, was studied analytically by Becker.[108] He used a model of a uniform, infinitely long, stationary gas region bounded radially by a neutron reflector and heat sink. Becker found that the neutronic feedback had a stabilizing influence, with the degree of stabilization strongly dependent on the reflector material.

Podney and Smith[109] have also presented a theory that describes power-level variations in a gas-core reactor, produced by density changes in the gaseous fuel region.

The Idaho cavity-reactor critical experiments[41] were based on the coaxial-flow concept (Fig. 1). The objective was to evaluate the reactivity effect of a "wave," in which an undulation develops in the outer fuel boundary and moves through the cavity. These waves were simulated in the critical experiment within a 183-cm-diameter by 122-cm-long cavity. Of significance was the reactivity worth of the waves with respect to a smooth core boundary 122 cm in diameter. Two wave configurations and two amplitudes were considered:

1. Wave crest develops, giving a net fuel addition to the reactor.

7.3-cm crest height	$+0.7\%\Delta k$
22-cm crest height	$+6\%\Delta k$

2. Wave crest and trough develop, with no net fuel addition to the reactor.

7.3-cm amplitude	$+0.3\%\Delta k$
22-cm amplitude	$+2.8\%\Delta k$

As the wave progresses down the length of the core, the worth of the fuel in the wave does not substantially

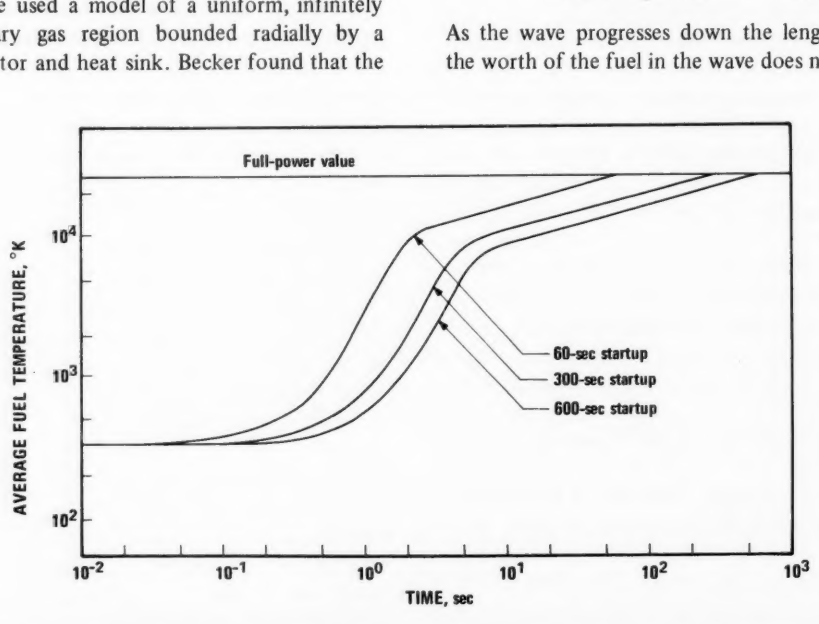

Fig. 12 Average fuel temperature during startup power ramps for the nuclear light-bulb engine.[54]

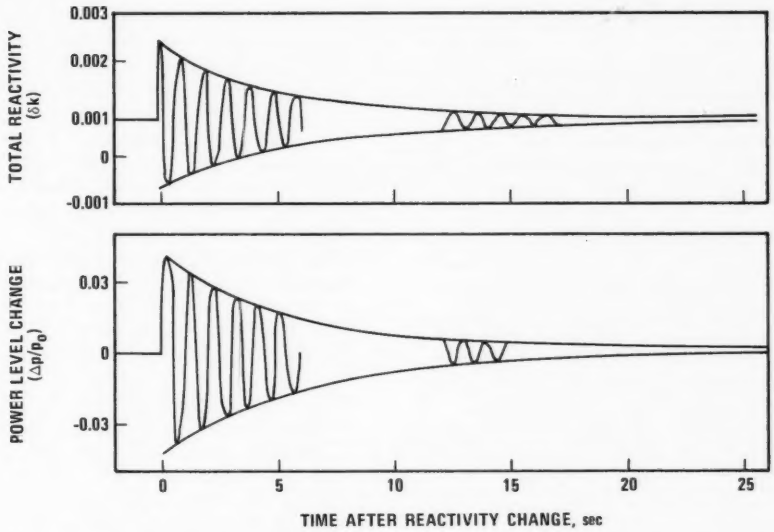

Fig. 13 Response of nuclear light-bulb engine to a positive step change in reactivity of 1 dollar.[54]

vary, according to the measurements. In addition to the occurrence of waves, the flowing-fuel shape in practice will not be the uniform cylinder that has generally been simulated in the critical experiments. The measured reactivity penalty for the loss of the "corners" was 5.5% Δk. Also, displacement of the fuel away from the end wall of the cavity will be required in practice so that the wall will not come into contact with the extremely high temperature fuel. A 7.5-cm space between the end wall and the core created an additional 2.8% Δk reactivity penalty. The waves may lead to rapid reactivity fluctuations that could occur during flowing-gas operation. The control system used to date in the Idaho cavity-reactor critical experiment has consisted of 20 to 30 1.7-cm-diameter boron carbide control rods in one of the end reflectors and have provided control worths of 4 to 6% Δk. Two other control schemes were evaluated. One of these was a cadmium sleeve to be moved longitudinally to encircle the core radially; the second scheme consisted in rotating control drums in the reflector. A complete control system of either type could incorporate at least 10% Δk in reactivity, and thus a more than adequate shutdown margin would be provided for any unexpected perturbations occurring in the cavity.

CONCLUSIONS

There is no clear-cut choice that can be made at present between the two candidate gas-core reactors that have been discussed. Schwenk and Franklin[110] have recently presented a detailed comparison of these two gas-core concepts. They discuss the problems related to these concepts, as well as the potentials for their solution.

Each system has attractive features, as well as limitations. The nuclear light-bulb reactor provides for complete fuel containment. However, the realization of this system depends on the survivability of the transparent partition in the reactor environment. The critical fuel loading for a seven-cavity light-bulb engine is significantly lower than that required for the coaxial-flow concept. The loss of fuel and fission products from the open-cycle engine is primarily a potential economic problem. Masser[111] has shown that the radiation dose to the vehicle from the backflow of fission products is negligible, and various other investigators have also shown that there is no pollution or radiation hazard produced by the release into space of all the fission products and unfissioned uranium from the coaxial-flow engine.[1] Demonstration of the fluid-dynamics stability of the fissioning core and satisfactory propellant heating under operating conditions is a requirement for both concepts. Suitable techniques for particle seeding and fuel injection must also be developed.

An extensive research program has been carried out in most problem areas. It now appears feasible to consider a demonstration of the principle by a full-scale experiment as proposed by Rom.[1]

REFERENCES

1. Frank E. Rom, Comments on the Feasibility of Developing Gas Core Nuclear Reactors, Report NASA-TM-X-52644, National Aeronautics and Space Administration, Lewis Research Center, October 1969.
2. R. W. Bussard and R. D. DeLauer, *Fundamentals of Nuclear Flight,* McGraw-Hill Book Company, Inc., New York, 1965.
3. G. A. McLafferty, Investigation of Gaseous Nuclear Rocket Technology, Summary Technical Report, Report H-9100093-46, United Aircraft Corporation, Research Laboratories, November 1969.
4. J. W. Clark, B. V. Johnson, J. L. Kendall, A. E. Mensing, and A. Travers, Open Cycle and Light Bulb Types of Vortex-Stabilized Gaseous Nuclear Rockets, *J. Spacecraft Rockets,* 5(8): 941 (August 1968).
5. C. P. Park and W. Love, Gas Core Nuclear Rocket Concept with Fuel Separation by MHD-Driven Rotation, in *Proceedings of the Symposium on Research on Uranium Plasmas and Their Technological Applications,* University of Florida, January 1970.
6. J. C. Evvard, Wheel-Flow Gaseous-Core Reactor Concept, Report NASA-TN-D-2951, National Aeronautics and Space Administration, Lewis Research Center, November 1965.
7. E. C. Gritton and B. Pinkel, A Gaseous-Core Reactor Concept for Electrical Power Generation, *Nucl. Appl. Technol.,* 8: 355 (April 1970).
8. S. Ulam, Nuclear Rocketry: The Orion Project, *Nucl. News,* 1(8): 25 (January 1965).
9. R. V. Meghreblian, Gaseous Reactors for Booster Propulsion, *Amer. Rocket Soc. J.,* 32: 13 (January 1962).
10. E. E. Duke and W. J. Houghton, Gas-Core Nuclear Rocket Engine, *J. Spacecraft Rockets,* 4(12): 1592 (December 1967).
11. F. E. Rom, Gaseous Nuclear Rocket, U. S. Patent No. 3,202,582, filed Aug. 28, 1961.
12. R. G. Ragsdale, Are Gas-Core Nuclear Rockets Attainable?, American Institute of Aeronautics and Astronautics, Paper No. 68-570, June 1968.
13. R. G. Ragsdale, Relationship Between Engine Parameters and the Fuel Mass Contained in an Open-Cycle Gas-Core Reactor, Report NASA-TM-X-52733, National Aeronautics and Space Administration, January 1970.
14. G. H. McLafferty, Gaseous Reactor Container, U. S. Patent No. 3,223,591, filed Aug. 27, 1962.
15. A. C. J. Matteson et al., Energetics 6: Magnetohydrodynamic Power, *Mech. Eng.,* pp. 38-41, November 1966.
16. R. K. Evans, 75-MW Power Plant Nears Completion, *Power,* pp. 66-67, (January 1969).
17. T. R. Brogan, The Plasma MHD Power Generator, *Advances in Plasma Physics,* Vol. 1, Interscience Publishers, a division of John Wiley & Sons, Inc., New York, 1968.
18. S. V. Shelton and W. O. Carlson, Variable Collision Cross Section Effects on Electrical Conductivity, *AIAA (Amer. Inst. Aeronaut. Astronaut) J.,* 4(9): 1776 (September 1966).
19. B. Karlovitz and D. Holasz, History of the K & H Generator and Conclusions Drawn from the Experimental Results, in *Proceedings of the Third Symposium on the Engineering Aspects of MHD,* Gordon and Breach, Science Publishers, Inc., New York, 1963.
20. R. Voshall and W. Emmerich, MHD Power Generation with Photoionization, *IEEE (Inst. Elec. Electron. Eng.) Trans. Aerospace Electron Syst.,* 2(2): 807 (April 1964).
21. A. T. Hooper, D. Newby, and A. H. Russell, Closed-Cycle Nuclear MHD Studies Using Dust Suspensions, in *Electricity from MHD,* Symposium Proceedings, Salzburg 1966, Preprint No. SM-74/73, International Atomic Energy Agency, Vienna, 1966 (STI/PUB/128).
22. B. Waldie and I. Fells, An Experimental Study of Gas Borne Suspensions of Thermionic Emitters as MHD Working Fluids, *Phil. Trans. Roy. Soc. (London), Ser. A,* 261: 490-495 (July 6, 1967).
23. R. J. Rosa, *Magnetohydrodynamic Energy Conversion,* McGraw-Hill Book Company, Inc., New York, 1968.
24. A. Sherman, Gaseous Fission Closed Loop MHD Generator, in *Proceedings of the Symposium on Research on Uranium Plasmas and Their Technological Applications,* University of Florida, January 1970.
25. R. J. Rosa, Propulsion System Using a Cavity Reactor and Magnetohydrodynamic Generator, *Amer. Rocket Soc. J.,* July 1961.
26. J. R. Williams and S. V. Shelton, Gas-Core Reactors for MHD Power Systems, in *Proceedings of the Symposium on Research on Uranium Plasmas and Their Technological Applications,* University of Florida, January 1970.
27. G. I. Bell, Calculation of the Critical Mass of UF_6 as a Gaseous Core, with Reflectors of D_2O, Be, and C, USAEC Report LA-1874, Los Alamos Scientific Laboratory, February 1955.
28. G. Safonov, The Criticality and Some Potentialities of Cavity Reactors, USAEC Report RM-1835, Rand Corporation, July 1955.
29. G. Safonov, Externally Moderated Reactors, in *Proceedings of the Second United Nations International Conference on the Peaceful Uses of Atomic Energy, Geneva, 1958,* Vol. 12, p. 705, United Nations, New York, 1958.
30. G. A. Jarvis, Cavity Reactor, in Proceedings of an Advanced Nuclear Propulsion Symposium, Report LA-3229-MS, p. 344, Los Alamos Scientific Laboratory, June 1965.
31. C. B. Mills, Criticality, in Proceedings of an Advanced Nuclear Propulsion Symposium, Report LA-3229-MS, p. 362, Los Alamos Scientific Laboratory, June 1965.
32. C. B. Mills, Reflector Moderated Reactors, *Nucl. Sci. Eng.,* 13(4): 301 (August 1962).
33. K. Kikoin et al., Experimental Reactor with Gaseous Fissionable Substance (UF_6), *Soviet J. At. Energy,* 5(3): 1167 (September 1958).
34. F. Miraldi, G. Nelson, G. Holmberg, and G. Skoff, Neutron Flux Distributions: (Experiments Vs. Theory) for a Water Reflected Spherical Cavity System, Report NASA-CR-72231, Case Institute of Technology, December 1966.
35. G. D. Pincock and J. F. Kunze, Cavity Reactor Critical Experiment, Vol. I, USAEC Report NASA-CR-72234, General Electric Company, Nuclear Materials and Propulsion Operation, September 1967.
36. G. D. Pincock, J. F. Kunze, R. E. Wood, and R. E. Hyland, Cavity Reactor Engineering Mockup Critical

Experiment, *Trans. Amer. Nucl. Soc.*, 11: 29 (1968); also Report NASA-CR-72409, June 1968.

37. G. D. Pincock and J. F. Kunze, Cavity Reactor Critical Experiment, Vol. II, Report NASA-CR-72415, May 1968.
38. G. D. Pincock and J. F. Kunze, Cavity Reactor Critical Experiments, Vol. III, Report NASA-CR-72384, November 1968.
39. W. B. Henderson and J. F. Kunze, Analysis of Cavity Reactor Experiments, Report NASA-CR-72484, January 1969.
40. J. F. Kunze, G. D. Pincock, and R. E. Hyland, Cavity Reactor Critical Experiments, *Nucl. Appl.*, 6: (February 1969).
41. G. D. Pincock and J. F. Kunze, Cavity Reactor Critical Experiment, Vol. IV, Report NASA-CR-72550, October 1969.
42. G. D. Pincock and P. L. Chase, Cavity Reactor Critical Experiment, Vol. V, Report NASA-CR-72577, November 1969.
43. R. G. Ragsdale and R. E. Hyland, Some Nuclear Calculations of $^{235}U-D_2O$ Gaseous-Core Cavity Reactors, Report NASA-TN-D-475, National Aeronautics and Space Administration, Lewis Research Center, October 1961.
44. R. E. Hyland, R. G. Ragsdale, and E. J. Gunn, Two-Dimensional Criticality Calculations of Gaseous-Core Cylindrical-Cavity Reactors, Report NASA-TN-D-1575, National Aeronautics and Space Administration, Lewis Research Center, March 1963.
45. R. M. Kaufman, W. F. Osborn, Jr., J. R. Simmons, and E. B. Roth, Reactor Physics Calculations for the Gaseous Core Cavity Reactor, *Allison Res. Eng.*, 8: 11-18 (1965).
46. T. F. Plunkett, Nuclear Analysis of Gaseous-Core Nuclear Rockets, *Nucl. Appl.*, 3: 178 (March 1967).
47. G. A. Jarvis and C. G. Beyers, Critical Mass Measurements for Various Fuel Configurations in the LASL D_2O Reflected Cavity Reactor, American Institute of Aeronautics and Astronautics, Paper No. 65-555, June 1965.
48. H. W. Hubbard, A. L. Latter, and E. A. Martinelli, Second Report on Propulsion by a Gaseous Fission Reactor, USAEC Report RM-3851-AEC, Rand Corporation, October 1963.
49. L. O. Herwig and T. W. Latham, Nuclear Characteristics of Large Reflector-Moderated Gaseous-Fueled Cavity Reactors Containing Hot Hydrogen, *AIAA (Amer. Inst. Aeronaut. Astronaut.) J.*, 5(5): 930 (May 1967).
50. T. S. Latham, Nuclear Criticality Study of a Specific Vortex-Stabilized Gaseous Nuclear Rocket Engine, Report E-910375-1, United Aircraft Corporation, Research Laboratories, October 1966.
51. T. S. Latham, Nuclear Criticality Studies of Specific Light Bulb and Open-Cycle Gaseous Nuclear Rocket System, Report F-910375-2, United Aircraft Corporation, September 1967.
52. T. S. Latham, Criticality Studies of a Nuclear Light Bulb Engine, American Institute of Aeronautics and Astronautics, Paper No. 68-571, June 1968.
53. T. S. Latham, Nuclear Studies of the Nuclear Light Bulb Rocket Engine, Report G-910375-3, United Aircraft Corporation, September 1968.
54. T. S. Latham, H. E. Bauer, and R. J. Rodgers, Studies of Nuclear Light Bulb Startup Conditions and Engine Dynamics, Report H-910375-4, United Aircraft Corporation, September 1969.
55. G. D. Joanou and J. S. Dudek, GAM-1, A Consistent P-1 Multigroup Code for the Calculation of Fast Neutron Spectra and Multigroup Constants, USAEC Report GA-1850, Gulf General Atomic Incorporated, June 1961.
56. R. H. Shudde and J. Dyer, TEMPEST-II, A Neutron Thermalization Code, USAEC Report TID-18284, Atomics International, June 1962.
57. E. H. Canfield, R. N. Stuart, R. P. Freis, and W. H. Collins, SOPHIST-I, An IBM 709/7090 Code Which Calculates Multigroup Transfer Coefficients for Gaseous Moderators, USAEC Report UCRL-5956, University of California, Lawrence Radiation Laboratory, October 1961.
58. W. W. Engle, A Users Manual for ANISN, A One Dimensional Discrete Ordinates Transport Code with Anisotropic Scattering, USAEC Report K-1693, Union Carbide Corporation, Nuclear Division, Mar. 30, 1967.
59. T. B. Fowler, M. L. Tobias, and D. R. Vondy, EXTERMINATOR-II: A Fortran IV Code for Solving Multigroup Neutron Diffusion Equations in Two Dimensions, USAEC Report ORNL-4078, Oak Ridge National Laboratory, April 1967.
60. F. R. Mynatt, A Users Manual for DOT, A Two Dimensional Discrete Ordinates Transport Code with Anisotropic Scattering, USAEC Report K-1964, Union Carbide Corporation, Nuclear Division.
61. L. V. Gurvich and V. S. Yugman, Calculation of the Thermodynamic Properties of Gaseous Uranium and Plutonium and Their Ions Up to 20,000°K, in *Thermodynamics with Emphasis on Nuclear Materials and Atomic Transport in Solids*, Vol. 2, p. 613, International Atomic Energy Agency, Vienna, 1966.
62. A. S. Keston and N. L. Krascella, Theoretical Investigation of Radiant Heat Transfer in the Fuel Region of a Gaseous Nuclear Rocket Engine, Report NASA-CR-695, United Aircraft Corporation, January 1967.
63. D. E. Parks, G. Lane, J. C. Stewart, and S. Peyton, Optical Constants of Uranium Plasma, Report GA-8244 (NASA-CR-72348), Gulf General Atomic Incorporated, February 1968.
64. W. F. Meggers, C. H. Corliss, and A. F. Scribner, *Tables of Spectral Line Intensities*, National Bureau of Standards, Monograph 32, Parts I and II, Superintendent of Documents, U. S. Government Printing Office, Washington, 1961.
65. C. H. Corliss and W. R. Bozman, *Experimental Transition Probabilities for Spectral Lines of Seventy Elements Derived from the NBS Tables of Spectral Line Intensities*, National Bureau of Standards, Monograph 53, Superintendent of Documents, U. S. Government Printing Office, Washington, 1962.
66. T. D. Wilkerson, D. W. Koopman, M. H. Miller, R. Bengtson, and G. Charatis, *Phys. Fluids*, 12: 22 (1969).
67. M. H. Miller, T. D. Wilkerson, and D. W. Koopman, Uranium Plasma Opacity Measurements, in *Proceedings of the Symposium on Research on Uranium Plasmas and Their Technological Applications*, University of Florida, January 1970.

68. N. L. Krascella, Theoretical Investigation of the Radiant Emission Spectrum from the Fuel Region of a Nuclear Light Bulb Engine, Report H-910092-12, United Aircraft Corporation, Research Laboratories, October 1969.
69. R. T. Schneider, A. G. Randol III, C. D. Kylstic, and M. J. Ohanian, Measurements of the Emission Coefficient of a Uranium Plasma, *Trans. Amer. Nucl. Soc.*, 12(2): 413 (December 1969).
70. P. J. Marteney, A. E. Mensing, and N. L. Krascella, Experimental Investigations of the Spectral Emission Characteristics of Argon–Tungsten and Argon–Uranium Induction Heated Plasmas, Report G-910092-11, United Aircraft Corporation, Research Laboratories, September 1968.
71. G. E. Palma and R. M. Gagosz, Optical Absorption in Fused Silica During Irradiation at High Temperature, Report H-930709-1, United Aircraft Corporation, Research Laboratories, November 1969.
72. C. C. Masser, Radiant Heating of a Seeded Gas in a Coaxial-Flow Gaseous Reactor, Report NASA-TN-D-3197, National Aeronautics and Space Administration, Lewis Research Center, January 1966.
73. D. E. Knapp, V. C. Burkig, and J. S. Cory, Flash Heating of Seeded Gases, American Institute of Aeronautics and Astronautics, Paper No. 67-501, July 1967.
74. N. L. Krascella, Tables of the Composition, Opacity and Thermodynamic Properties of Hydrogen at High Temperatures, Report B-910168-1, United Aircraft Corporation, Research Laboratories, September 1963.
75. R. W. Patch, Components of a Hydrogen Plasma Including Minor Species, Report NASA-TN-D-4993, January 1969.
76. R. W. Patch, Interior Absorption Coefficients and Opacities for a Hydrogen Plasma, Report NASA-TM-X-1902, October 1969.
77. C. C. Masser, Vapor-Pressure Data Extrapolated to 1000 Atmospheres for 13 Refractory Materials with Low Thermal Absorption Cross Sections, Report NASA-TN-D-4147, October 1967.
78. G. A. Mie, Beitrage zur Optik Truber Medien, Speziell Kolloidaler Metallosungen, *Ann. Phys. (Leipzig)*, 25: 377 (1908).
79. N. L. Krascella, Theoretical Investigations of the Absorption and Scattering Characteristics of Small Particles, Report C-910092-1, United Aircraft Corporation, Research Laboratories, September 1964.
80. A. L. Aden, Electromagnetic Scattering from Spheres with Sizes Comparable to the Wavelength, *J. Appl. Phys.*, 22(5): 601-605 (1951).
81. J. R. Williams, A. S. Shenoy, and J. D. Clement, Theoretical Calculations of Radiant Heat Transfer Properties of Particle-Seeded Gases, Report NASA-CR-1505, February 1970.
82. C. D. Lanzo and R. G. Ragsdale, Experimental Determination of Spectral and Total Transmissivities of Clouds of Small Particles, Report NASA-TN-D-1405, National Aeronautics and Space Administration, Lewis Research Center, September 1962.
83. E. Keng and C. Orr, Investigation of Radiant Heat Transfer to Particle-Seeded Gases for Application to Nuclear Rocket Engine Design, Report NASA-CR-953, November 1967.
84. P. J. Marteney, Experimental Investigation of the Opacity of Small Particles, Report C-910092-2, United Aircraft Corporation, Research Laboratories, September 1964.
85. V. C. Burkig, Thermal Absorption in Seeded Gases, Report DAC-59985, McDonnell-Douglas Aircraft Corp., January 1967.
86. A. S. Shenoy, J. R. Williams, and J. D. Clement, Measurements of the Extinction Parameters of Hot Seeded Hydrogen at One Atmosphere Pressure, Report NASA-CR-1504, February 1970.
87. T. J. Love, An Experimental Investigation of Infra-Red Scattering by Clouds of Particles, Report ARL-64-109, Aerospace Research Laboratories, June 1964.
88. J. R. Williams and W. R. Jacobs, Radiant Heat Absorption Parameters of Particle-Seeded Gases, in *Proceedings of the Sixth Annual Southeastern Seminar on Thermal Sciences*, North Carolina State of the University of North Carolina, Raleigh, April 1970.
89. A. F. Kascak, Coaxial Flow Radiation Heat Transfer Analysis, in Proceedings of an Advanced Nuclear Propulsion Symposium, Los Alamos, Report LA-3229-MS, Los Alamos Scientific Laboratory, p. 208, June 1965.
90. A. F. Kascak, Estimates of Local and Average Fuel Temperatures in a Gaseous Nuclear Rocket Engine, Report NASA-TN-D-4164, National Aeronautics and Space Administration, Lewis Research Center, September 1967.
91. A. S. Keston and N. L. Krascella, Theoretical Investigation of Radiant Heat Transfer in the Fuel Region of a Gaseous Nuclear Rocket Engine, Report NASA-CR-695, United Aircraft Corporation, January 1967.
92. G. H. McLafferty and W. G. Burwell, Theoretical Investigation of the Temperature Distribution in the Propellant Region of a Vortex Stabilized Gaseous Nuclear Rocket, Report C-910093-10, United Aircraft Corporation, September 1964.
93. G. H. McLafferty, Absorption of Thermal Radiation in the Transparent Wall of a Nuclear Light Bulb Rocket Engine, *J. Spacecraft Rockets*, 4: 758 (June 1967).
94. R. W. Patch, Status of Opacity Calculations for Application to Uranium-Fueled Gas-Core Reactors, Report NASA-TM-X-52722, January 1970.
95. R. A. Kulik, J. J. Leithem, and H. W. Weinstein, Effect of Free Stream Turbulence on Coaxial Mixing, Report NASA-CR-1336, May 1969.
96. J. Clark, B. Johnson, J. Kendall, A. Mensing, and A. Travers, Summary of Gaseous Nuclear Rocket Fluid Mechanics, American Institute of Aeronautics and Astronautics, Paper No. 67-500, July 1967.
97. C. C. Chang, S. W. Chi, and C. M. Chen, Gas-Core Nuclear Rocket Fluid Mechanics Experiments at the Catholic University of America, American Institute of Aeronautics and Astronautics, Paper No. 67-502, July 1967.
98. R. G. Ragsdale and F. E. Rom, Gas Core Reactor Work at NASA–Lewis, American Institute of Aeronautics and Astronautics, Paper No. 67-499, July 1967.
99. C. C. Masser and M. F. Taylor, Photographic Study of a Bromine Jet Flowing in a Coaxial Air Stream with Honeycomb at the Injection Plane, Report NASA-TM-X-1900, October 1969.
100. C. D. Lanzo, A Flow Experiment in a Curved Porous Wall Gas-Core Cavity Geometry, *Nucl. Appl. Technol.*, 8(1): 6 (January 1970).

101. R. Roback, Thermodynamic Properties of Coolant Fluids and Particle Seeds for Gaseous Nuclear Rockets, Report NASA-CR-279, United Aircraft Corporation, Research Laboratories, September 1964.
102. M. T. Thorpe, Induction Plasma Heating, System Performance, Hydrogen Operation and Gas Core Reactor Simulator Development, Report NASA-CR-1143, August 1968.
103. J. J. Keyes and W. K. Sartory, Exploratory Plasmadynamic Studies of Vortex and Coaxial Flow Geometries Employing Radio-Frequency Induction Heating, in *Proceedings of the Symposium on Research on Uranium Plasmas and Their Technological Applications,* University of Florida, January 1970.
104. A. E. Mensing and J. F. Jaminet, Experimental Investigations of Heavy Gas Containment in R-F Heated and Unheated Two-Component Vortices, Report H-910091-20, United Aircraft Corporation, Research Laboratories, September 1969.
105. W. C. Roman, Development of a High Intensity R-F Radiant Energy Source for Simulating the Thermal Environment of the Nuclear Light Bulb Reactor, in *Proceedings of the Symposium on Research on Uranium Plasmas and Their Technological Applications,* University of Florida, January 1970.
106. W. C. Roman, J. F. Klein, and P. G. Voyt, Experimental Investigations to Simulate the Thermal Environment, Transparent Walls and Propellant Heating in a Light Bulb Engine, Report H-910091-19, United Aircraft Corporation, Research Laboratories, September 1969.
107. J. F. Klein, Experiments for Simulating the Absorption of Thermal Radiation in the Propellant Duct of a Nuclear Light Bulb Reactor, in *Proceedings of the Symposium on Research on Uranium Plasmas and Their Technological Applications,* University of Florida, January 1970.
108. M. Becker, Coupled Fluid and Neutronic Oscillations in High Temperature Gaseous Uranium, in *Proceedings of the Symposium on Research on Uranium Plasmas and Their Technological Applications,* University of Florida, January 1970.
109. W. N. Podney and H. P. Smith, Jr., Neutron Kinetics of Cavity Reactors, in *Proceedings of the Symposium on Research on Uranium Plasmas and Their Technological Applications,* University of Florida, January 1970.
110. F. C. Schwenk and C. E. Franklin, A Comparison of Open and Closed Cycle Gaseous Core Reactor Systems, in *Proceedings of the Symposium on Research on Uranium Plasmas and Their Technological Applications,* University of Florida, January 1970.
111. C. C. Masser, Radiation Hazard from Backflow of Fission Fragments from the Plume of a Gas-Core Nuclear Rocket, Report NASA-TM-X-52743, January 1970.

Xenon-Induced Spatial Power Oscillations

By Weston M. Stacey, Jr.*

Spatial power oscillations induced by, and coupled to, oscillations in the spatial xenon distribution attracted considerable attention several years ago in relation to the large production reactors, the Shippingport pressurized-water reactor (PWR), and the Canadian heavy-water reactors (HWR's). However, it is only recently that this phenomenon has become a concern in the light-water reactors (LWR's) that dominate the U. S. power-reactor market, as economic considerations have dictated ever larger core sizes. In the absence of remedial control adjustments, some of these larger, future cores† may be intrinsically unstable with respect to xenon-induced spatial power oscillations. In this case, specific remedial control action will be required. Even if the cores are intrinsically stable, significant spatial power oscillations may be sustained during load following, in the absence of remedial control action.

Because of the time scale involved (a typical oscillation period is 25 to 35 hr), xenon-induced spatial power oscillations are not generally felt to be a safety problem, as such. However, they can effect adverse economic consequences.[1] The reactivity involved in control rods, which are specifically required to suppress oscillations, must be offset by increased fuel enrichment, which increases fuel-cycle costs. Increased thermal margin must be factored into the design to allow for spatial power oscillations, which may result in a larger core, thus increasing fuel-cycle and capital costs. The instrumentation required to detect spatial power oscillations, so that appropriate control action can be taken, may be costly. Designing a core to be intrinsically stable with respect to xenon-induced spatial power oscillations could require changes in the lattice metal-to-water ratio and fuel-element size which adversely affect fuel-cycle costs and pumping requirements. Thermal cycling associated with the spatial power oscillations could increase stress levels, thus requiring a thicker or stronger cladding for the fuel elements.

These economic considerations are stressed over safety considerations on the basis of assumptions that spatial power oscillations will be suppressed (by design for intrinsic stability or by detection and remedial control action) and that the core design will be sufficiently conservative to tolerate the damped oscillations that occur. In the event that either of these assumptions is invalid, then xenon-induced spatial power oscillations constitute a potentially serious problem, in that the spatial power tilting could lead to fuel failure and subsequent difficulties.

Early work[2-12] on xenon-induced spatial power oscillations was directed primarily toward obtaining a stability index that described the threshold for diverging oscillations, in an uncontrolled reactor, in terms of parameters that characterized the core. A linear analysis was normally employed, with the spatial dependence represented by a modal expansion or a nodal approximation. This work indicated that, in general, stability of the spatial power distribution with respect to xenon-induced oscillations decreases with: (1) increased core size, (2) reduced neutron migration length, (3) decreased magnitude of the negative power coefficient of reactivity, (4) increased neutron-flux level,‡ and (5) increased flatness of the thermal-neutron-flux distribution.

*Applied Physics Division, Argonne National Laboratory, Argonne, Ill. 60439.

†Currently operating cores, the Ginna and Beznau PWR's, may be unstable with respect to axial oscillations in the absence of remedial control action.

‡If the negative power coefficient is sufficiently large, and the neutron-flux level is sufficiently high, an increase in flux level is stabilizing.

Xenon-induced spatial power oscillations may be induced by changes in the core power level or spatial distribution, such as may be produced by changes in control-rod position, coolant density distribution, fuel-temperature distribution, or soluble-poison concentration. Such changes are associated with normal changes in the operating condition of the reactor (e.g., load following). Some evidence exists that random fluctuations in the neutron flux are capable of initiating xenon-induced spatial power oscillations.[13]

The recent resurgence of interest in xenon-induced spatial power oscillations has stimulated something of a renaissance in theoretical work on the subject. This article reviews recent work on: (1) stability analyses, (2) digital and analog computer simulation methods, (3) experiments, (4) verification of analytical methods, (5) analytical studies, and (6) methods and theory of control.

PHYSICAL MECHANISM

Xenon is produced in a reactor through a fission-product-decay chain such as that shown in Fig. 1. The

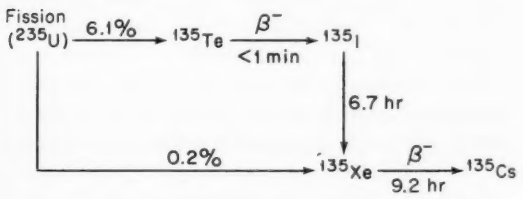

Fig. 1 Mass-135 fission-product chain.

production rate of xenon depends primarily on the concentration of iodine, which depends on the concentration of fissionable nuclei and on the neutron-flux history over the past 50 hr or so. The destruction rate of xenon depends on the instantaneous thermal-neutron flux (neutron capture) and the xenon concentration (radioactive decay). Thus, when the neutron-flux level changes, the xenon destruction rate changes immediately in the same direction, while the xenon production rate (primarily via iodine decay) initially remains essentially unchanged. Slowly the iodine concentration, and thus the xenon production rate, will change in the same direction as the change in neutron-flux level. Because of its large absorption cross section for thermal neutrons [$\sigma(^{135}\text{Xe}) \sim 3 \times 10^6$ b], a change in the xenon concentration can produce a significant change in k_∞, thus affecting the neutron-flux level. This delayed reaction of the xenon concentration to a change in neutron-flux level, and the subsequent response of the neutron flux to changes in the xenon concentration, is the mechanism by which xenon induces oscillations in the spatial power distribution.*

A simple, hypothetical example serves to illustrate how this mechanism functions to induce spatial power oscillations. Assume that a flux tilt is introduced in a uniform reactor that has been operating with a symmetric power distribution. In the high-flux region, the xenon concentration is reduced (increased destruction), increasing k_∞ in that region; in the low-flux region, the xenon concentration is increased (reduced destruction), decreasing k_∞ in that region. This enhances the flux tilt. Eventually the xenon production exceeds destruction in the high-flux region because of the iodine buildup and subsequent decay, and vice versa in the low-flux region. Subsequently the xenon concentration in the high-flux region exceeds that in the low-flux region, at which time the flux tilt reverses, etc. In this manner, the xenon concentration and the neutron flux in each region may oscillate out of phase with one another.

Any "negative feedback" mechanism that tends to reduce flux tilting generally will tend to suppress† xenon-induced spatial power oscillations. Moderator density‡ and Doppler feedback are good examples.

The time scale of the I–Xe dynamics is on the order of hours. Effects such as delayed neutrons, time lags associated with heat transfer from the fuel to the coolant, and coolant-loop circulation times are short-term relative to the I–Xe time scale and need not be represented explicitly in an analysis.[15,16] Fuel-depletion effects are sufficiently long-term to be neglected during a given xenon transient.

STABILITY ANALYSIS

If a perturbation is introduced into the spatial power distribution, will the delayed xenon feedback mechanism induce spatial power oscillations which

*In an uncontrolled reactor, this mechanism can also produce oscillations in the total power level.[14] However, the total power output of a reactor core can be readily regulated. The concern in this article is with oscillations in the spatial power distribution which occur while the total power is regulated to be constant or to have a desired variation in time.

†This is not always true, as will be discussed in a subsequent section.

‡Moderator density changes may not constitute a negative feedback mechanism if the moderator is sufficiently poisoned, or under certain other conditions.

grow, remain the same amplitude, or diminish in time? This is the question of stability, and the three possible answers correspond to instability (diverging oscillations), neutral stability (constant amplitude oscillations), and stability (converging or damped oscillations). The answer to this question depends on the properties of the reactor core (intrinsic stability properties), the control-system and operating procedure, and the nature of the initiating perturbation.

Most stability analyses deal only with the intrinsic stability characteristics of the reactor core, assuming that the effect of any control action is to maintain a constant total power and ignoring the nature of the perturbation. When the initiating perturbation is assumed to be small, the xenon, iodine, and neutron-flux spatial distributions may be expanded about their respective equilibrium distributions, and nonlinear terms may be discarded on the basis of the argument that small perturbations produce small deviations in the xenon and neutron-flux distributions and the product of these small deviations is negligible. An examination of the mathematical properties of these linearized equations then yields information about the stability of the spatial power distribution in a small region in phase space surrounding the equilibrium point.

In the most frequently encountered type of linear stability analysis, the spatial and temporal dependence of the neutron-flux, xenon, and iodine distributions is represented by a modal expansion in spatial eigenfunctions with expansion coefficients that have an exponential time dependence.* The exponents depend on the physical characteristics of the reactor core and the equilibrium state; it is the determination of this dependence that requires most of the effort involved in a linear stability analysis. The spatial power distribution is deemed to be stable, neutral, or unstable with respect to oscillations in a given spatial mode, depending on whether the real part of the corresponding exponent is negative, zero, or positive.

A variety of spatial eigenfunctions have been employed in linear stability analyses, and many methods of analysis have been used to determine the sign of the real part of the exponent. The natural, or p modes,[17-20] possess superior mathematical properties but are the most computationally intractable. These modes are the eigenfunctions of the system of equations that result from the assumption of exponential time dependence (or from Laplace transforming) in the linearized equations that describe the neutron-flux, xenon, and iodine distributions; the exponent (or transform variable) introduced by the time derivatives serves as the eigenvalue. As such, the p modes possess the property of finality,[17] which means that the exponents associated with any spatial mode can be calculated without considering other spatial modes, and thus the stability of the least-stable first harmonic mode can be determined without complicating the calculation with higher harmonics, when no other feedback mechanisms are present.

In general, the p modes are complex and satisfy a set of equations that look like the ordinary equations for the static neutron-flux distribution plus coupled equations for the iodine and xenon concentrations, with the eigenvalue appearing in the latter. Special codes are required to solve such equations,[21] and to date only slab geometry has been treated. Actual p-mode analyses have been limited to idealized models. The effect of temperature feedback on the p modes has been studied for the simple case of a uniform ring reactor.[22] When temperature feedback is explicitly accounted for, the eigenfunctions possessing the property of finality satisfy an even more complicated set of equations than do the p modes.[23]

The xenon and iodine equations in the p-mode formulation may be solved for the xenon concentration in terms of the neutron flux and the p eigenvalue and the result used to eliminate the xenon from the equation for the neutron flux. The neutron-flux equation then looks like the conventional equation for the neutron flux, but with an additional absorptionlike term with a complex spatially dependent "absorption cross section" involving the p eigenvalues. If this complex absorption cross section is assumed to be real, then the equation can be solved with standard neutron-diffusion codes only slightly modified. This general procedure is referred to as the "μ-mode approximation."[9,17-21] An approximation to the first harmonic p eigenvalue is obtained by iterating on p until the calculated eigenvalue equals the known first harmonic eigenvalue. Two variants of the μ-mode approximation are employed, the one discussed above in which the additional absorption cross section is spatially dependent and a similar procedure in which the additional absorption cross section is treated as spatially constant and is defined in terms of spatially averaged quantities. The latter is referred to as the "normal" μ-mode approximation, and the former is known as the "modified" μ-mode approximation.

*Note that Laplace transforming the time dependence of the linearized equations and then making a modal expansion of the spatial dependence have the same effect.

Linear stability analyses with the μ-mode approximation can be performed with standard neutron-diffusion codes after minor modification. A special code is available for μ-mode analyses in slab geometry.[24] This type of analysis has been applied extensively,[19,20] as will be discussed subsequently.

Although the ability of μ-mode stability analyses to predict relative stability trends has been established,[20] this type of analysis has the following shortcomings:

1. Nodal lines for the first harmonic mode must be known from symmetry considerations and must be compatible with the allowed boundary conditions of the neutron-diffusion codes used for the modal calculations.
2. Control feedback is not incorporated.
3. Temperature feedback is incorporated indirectly as a perturbation on the μ-mode result, and not directly in the calculation.[17,19,20]
4. Several flux solutions (usually four) must be performed in the iterative procedure of determining the p eigenvalue.
5. Slight modification to standard neutron-diffusion codes is required to compute the μ modes.

Perhaps the most computationally tractable method appropriate for the analysis of realistic reactor models utilizes a spatial expansion in λ modes, which are the eigenfunctions of the standard equation for the static neutron flux, with equilibrium xenon- and temperature-feedback effects implicit in the cross sections. This technique was one of the first introduced[2] and has been subsequently refined, both with respect to the methods employed to determine the p eigenvalues[17,25] and in a more rigorous definition of spatial averages.[25] Temperature feedback can be included directly in the calculation. When a single expansion mode (the first harmonic) is used, an explicit relation among the real part of the exponent (which determines the time dependence), an appropriately averaged thermal-neutron flux, and the subcriticality of the first harmonic mode can be obtained.[25] The λ modes can be calculated with standard neutron-diffusion codes without modification, provided that either the node lines of the harmonics can be identified or an iteration scheme capable of converging on higher harmonics (such as Wielandt) is available.

The ability of λ-mode stability analyses to predict relative stability trends has also been established.[26-28] This type analysis shares the first two shortcomings enumerated above the the μ-mode analysis, however, the third and fifth shortcomings are not inherent in the λ-mode analysis. In the λ-mode analysis,[25] it is necessary to perform a first harmonic mode adjoint calculation in addition to the first harmonic flux calculation, so the λ-mode analysis partly overcomes the fourth shortcoming enumerated above for the μ-mode analysis.

Modal expansions in eigenfunctions of the Helmholtz equation (trigonometric functions, Bessel functions, etc.) have been used in several studies which have contributed to an appreciation of modal interaction effects.[29-31] These eigenfunctions correspond to λ modes for bare homogeneous reactors. It was found that the influence of higher harmonics tends to be stabilizing at low-flux levels and for smaller core dimensions and tends to be destabilizing at high-flux levels and for larger reactors. Most LWR's of current interest appear to belong to the first category, so predictions based on a first harmonic mode analysis should be conservative.

Effects of nonlinearities on modal stability analyses have been examined by solving the modal equations on an analog computer, retaining the nonlinear terms.[32] For equilibrium states for which the linear analysis predicts converging oscillations (stability), the nonlinearities do not change the qualitative results. The principal effect of the nonlinearity is to reduce the amplitude of the flux tilt, relative to the prediction of the linear theory. For equilibrium states for which diverging oscillations are predicted by the linear analysis (unstable), the nonlinearities cause the transient response eventually to settle into a constant amplitude, limit-cycle-type oscillation.

A nonlinear stability criterion, based on the methods of Lyapunov, was proposed[33] recently but has not been applied. The method of comparison functions[34] could also likely be employed for nonlinear xenon-stability analyses, although no work has been done in this area.

Currently the major emphasis is not on the prediction of stability. Paramount, rather, are the questions of predicting transient spatial power distributions during a xenon-induced oscillation and of determining the appropriate remedial action to limit power tilting.

COMPUTER SIMULATION

To predict the transient response during a xenon-induced spatial power oscillation, accounting for temperature–density effects, the effects of control action, and the nature of the initiating perturbation, one must resort to a computer simulation. Early

analyses of this type were performed on analog computers,[12,35,36] as was one recent analysis,[19] by breaking up the spatial dependence into discrete nodes that were coupled neutronically and thermal–hydraulically. In general, only a relatively few spatial nodes could be accommodated (a 52-node model seems to be the largest reported in the literature[19]) and definition of neutronic coupling parameters posed a serious uncertainty.

In recent years, digital computers, with their greater capacity and accuracy, have become sufficiently fast that digital simulation now is the primary method of analysis employed for studying xenon-induced spatial power oscillations. Any neutron-diffusion code, with a finite-difference spatial representation, can, in principle, be readily adapted to simulate xenon-induced spatial power oscillations. Treatment of the I–Xe dynamics is similar to a standard depletion option. Several few-group, finite-difference, diffusion-depletion codes have been modified to enable simulation of xenon-induced spatial power oscillations with explicitly represented control-rod motion. Usually it is necessary to modify such codes to treat thermal–hydraulic feedback effects, which is relatively straightforward for PWR's but more complicated for boiling-water reactors (BWR's). Other codes have been developed specifically for xenon-induced spatial power-transient simulations. For example, multidimensional simulations that were performed with XENOSC,[37] TURBO,[38] PDQ-7,[39] and MAPLE SYRUP[40] have been reported. Typically a rather coarse mesh spacing is employed for multidimensional models.

For example, simulation of xenon-induced spatial power oscillations in an 800-MW(e) PWR has been performed with two- and three-dimensional two-group models.[41] The two-dimensional model employed 289 spatial mesh points, and the three-dimensional model employed 289 spatial mesh points in each of 18 planes for a total of 5202 mesh points. The typical computer time, on the CDC-6600, was 8 and 40 min per time step for the two- and three-dimensional calculations, respectively, when thermal feedback was treated. Thus a typical 30 time-step transient required 4 hr for the two-dimensional simulation and 20 hr for the three-dimensional simulation. In another study,[42] 14,000 spatial mesh points were used in a three-dimensional model.

Consequently multidimensional finite-difference simulations, even with considerably less detail than is customary in static design studies, appear to be time consuming enough to preclude their widespread use in the analysis of the multitude of conditions that must be considered in determining the appropriate operating and control procedures for a given reactor. Alternatives are to simulate in fewer dimensions or to simulate with a less-detailed representation. There is some evidence that xenon-induced spatial power oscillations may be nonseparable in the three spatial dimensions when leakage, control, coolant density (and void distribution), and fuel temperature effects are considered (this will be discussed subsequently). Thus three-dimensional simulations may be required under certain, if not all, conditions.

Pursuit of the second alternative, simulation with a less-detailed representation, has led to the development of one-group nodal codes in which the nuclear properties of the different core regions are characterized by k_∞ and M^2 (neutron migration area). The 3DXT code[43] represents a core with approximately 1000 nodes, incorporates xenon and coolant enthalpy feedback into k_∞ and M^2 on a nodal basis, simulates detector response, and automatically adjusts explicitly represented control rods to maintain criticality. The CEXE code[44,45] will accommodate a maximum of 3610 nodes (incorporating xenon, Doppler, and moderator feedback into k_∞ and M^2 on a nodal basis), will search for a critical soluble-poison concentration, or will more explicitly represent control rods in a predetermined manner. The XENOLUX code[46] represents a core with up to 3000 (BWR version) or 1600 (PWR version) nodes, incorporates moderator density and xenon feedback, and represents soluble poison and part- and full-length control rods. The FILE-6 code[47] represents a core with a maximum of 2000 nodes; incorporates xenon, Doppler, and coolant-void feedback; and represents control elements either uniformly or as discrete absorbers. The NODCOD code represents a core with up to 2650 nodes, accounts for moderator and Doppler feedbacks, and has options for poison and part- or full-length rod criticality searches.[48]

When the 3DXT, NODCOD, and CEXE codes are used, intranodal coupling coefficients are adjusted to ensure that the nodal calculation matches a reference and one or more perturbed planar and axial power distributions as calculated by detailed few-group, one- and two-dimensional, finite-difference codes. Experience[43,45,48] has indicated that it is possible to select coupling coefficients in this manner so that the nodal simulation of xenon-induced spatial power oscillations is in good agreement with simulations performed with few-group, detailed mesh finite-difference codes in one and two dimensions. The one-group treatment seems to be adequate, provided the effect of xenon on the

spectrum is accounted for in determining the Δk_∞ due to xenon changes.

A 3DXT calculation (777 nodes, coolant enthalpy and xenon feedback, control-rod criticality search) requires ~20 sec per flux solution, or 25 min (averaging three flux solutions per time step to find critical rod position) for a typical 25 time-step transient, on the CDC-6600.[43] A CEXE calculation (970 nodes, xenon feedback only, no-control search) requires 4 hr for a 25 time-step problem on the IBM 360/65.[45] A typical FILE-6 calculation (1008 nodes, coolant-void and Doppler feedback, no-control search) requires 1 min per time step, or 25 min for a 25 time-step problem, on the CDC-3600.[47] A typical BWR load-following study with the XENOLUX code requires 1 hr on the CDC-6600 for a 48 time-step calculation.[46] Calculations with the NODCOD code require ~1 min per time step on the CDC-6600.[48]

Synthesis methods[49,50] provide another possible alternative for a simple representation, although these methods do not appear to have been employed to any significant extent in the simulation of xenon-induced spatial power transients. The nonlinear xenon-flux interaction may present some difficulty to the selection of appropriate trial functions. A synthesis method using continuous Green's functions modes has been reported.[51] Green's functions modes are the solution to a source problem in the core in question with the fission cross section artificially set to zero everywhere; the source is taken as the equilibrium fission distribution in a portion of the reactor, the different modes corresponding to the different portions of the reactor being used for the source. The virtue of synthesis methods, if they can be shown to provide an accurate simulation, is that a large number of transients can be simulated very economically, once an appropriate set of trial functions has been generated.

In any digital simulation of xenon-induced spatial power oscillations, it is necessary to take finite-length time steps, and the longer the time step, the more economical is the calculation. However, the common assumption of a constant spatial flux distribution over the length of a time step can lead to significant error if the time step is too large. For the digital simulation of uncontrolled xenon-induced spatial power oscillations, a correction factor to account for the effect of finite time-step length on the calculated damping factor has been derived from a λ-mode analysis[27,52,53] and has been confirmed by reducing time-step size in the digital simulation.[27,54] Figure 2 illustrates trajectories of the true damping factors as a function of time-step size. The parameter ⟨A⟩ depends on the level and spatial distribution of the neutron flux and on the first harmonic λ-mode shape, and the expression used in Fig. 2 is an approximation in terms of the volume-averaged flux ($\bar{\phi}_0$) which has been found appropriate for PWR's. Digital simulations are seen to confirm the theoretical behavior predicted by the modal analysis.

In general, a core that is unstable to the first overtone will be predicted to be relatively more stable (i.e., the oscillations will diverge less rapidly) by a digital simulation with finite time steps. For highly stable cores (large negative damping factors), the digital simulation will predict less rapidly converging oscillations. Thus the possibility exists that a digital simulation may predict stability (negative damping factor) when a core is intrinsically unstable (positive damping factor).

The effect of finite time-step length on the magnitude of the power tilt, or the course of a transient when control action is taken, has not been studied theoretically. Such important questions in all likelihood will be answered only by reducing the time-step length in digital simulations and observing the result for individual cases.

Other numerical approximations associated with the digital simulation of xenon-induced spatial power oscillations were investigated for a finite-difference representation of a PWR.[27] When the spacing between mesh points was varied, separations up to 10.8 cm could be used without seriously impairing the solution. It was found that, in ordinary and extrapolated iteration schemes that use the most recent flux solution to obtain a first guess for the fission-source distribution, the flux at each point converges monotonically. If the power is increasing at a point, insufficient convergence of the solution underpredicts the increase in power. Similarly, if the power is decreasing at a point, insufficient convergence underpredicts the decrease in power. Thus insufficient convergence of the flux solution at each time step tends to artificially suppress an oscillation.

EXPERIMENTS

Spontaneous and operator-initiated xenon-induced spatial power oscillations have been observed in several operating reactor cores. Experimental data are available for PWR's, BWR's, and HWR's.

Shippingport PWR

The Shippingport PWR Core 1 (PWR-1) consisted of an annular seed region of highly enriched uranium with internal and external blankets of natural uranium

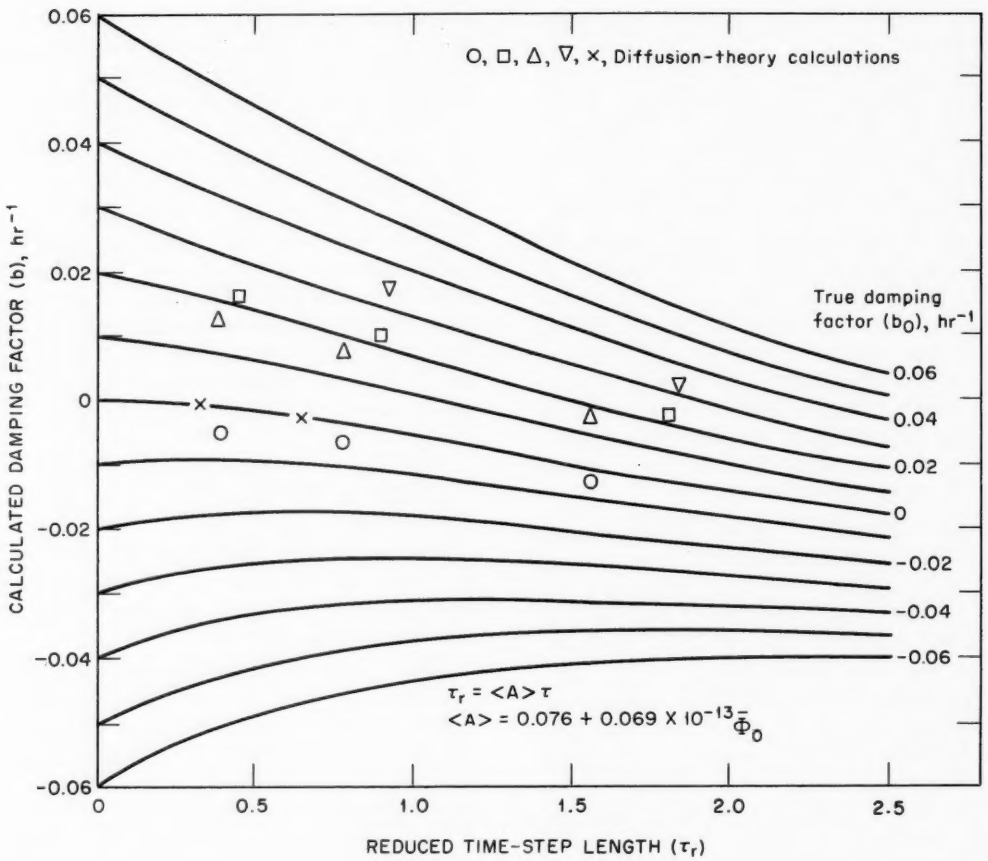

Fig. 2 Damping-factor dependence on time-step size.[27]

dioxide. Four groups of control rods were arrayed in the seed. At any time in life, only one group was controlling. Figure 3 is a schematic cross section of the core. Rated full power was 231 MW(t). Four seeds were depleted. Spontaneous and operator-induced planar[55] and axial[56] xenon-induced spatial power oscillations have been inferred from the reading of four external ion chambers located in instrument wells separated by 90° in azimuth. The operating history of PWR-1, with respect to xenon-induced spatial power transients, is given in Table 1. An example of the reduced experimental data is shown in Fig. 4, where a spatial power oscillation was intentionally initiated in Seed 4. Many of the data for planar oscillations in PWR-1 (Seeds 1 to 4) are collected in Ref. 20, where the following summary is made:

1. Instability existed only during Seeds 1 and 4, with Seed 1 being slightly more unstable than Seed 4.

2. Oscillation amplitudes were restricted to 6 to 8% of full power. It was possible to control the power level (fundamental mode) and each degenerate harmonic mode without affecting the other modes.

3. There was no evidence indicating a significant content of modes higher than the first harmonic.

4. In general, N–S and E–W oscillations were equally probable. However, the insertion of two highly reactive subassemblies in the inner blanket caused the E–W oscillations to become increasingly dominant during the course of an oscillation.

5. In all seeds, stability improved with seed depletion.

6. During unstable Seed 4, a 13% decrease in power level resulted in a 15.2-hr decrease in the time required for the oscillation amplitude to double.

7. The time required for the oscillation amplitude to double varied from −14 hr (80% power near end of

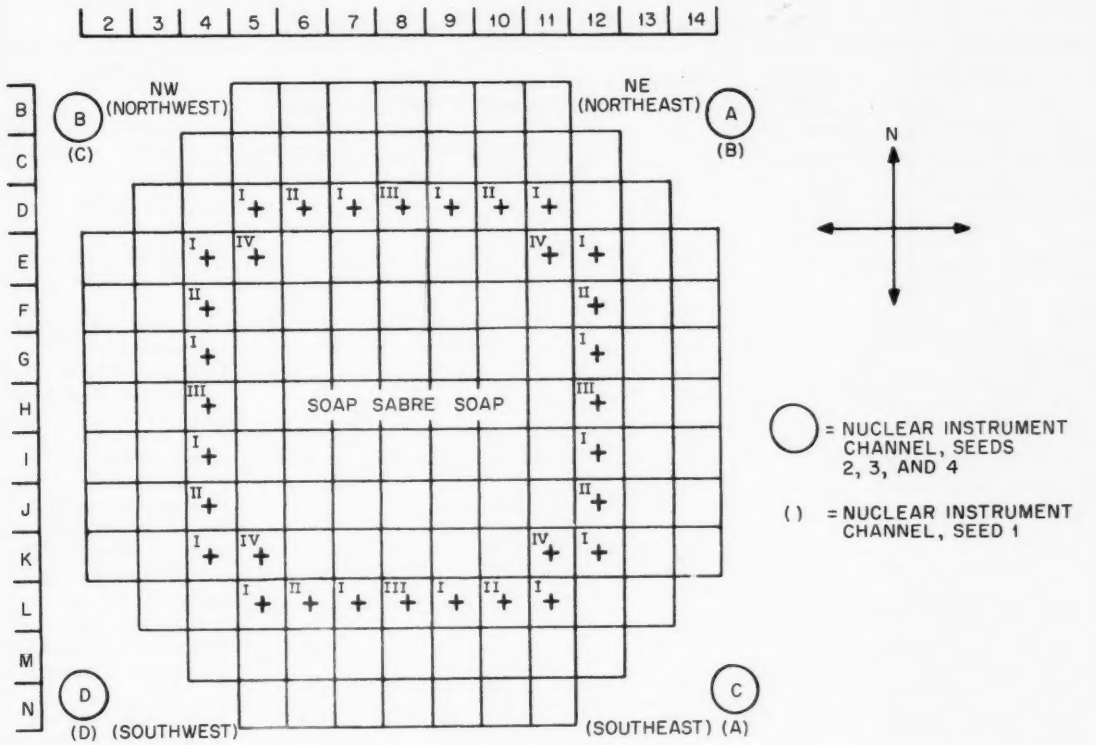
2 3 4 5 6 7 8 9 10 11 12 13 14
B C D E F G H I J K L M N
NW (NORTHWEST)
(C)
NE (NORTHEAST)
(B)
SOAP SABRE SOAP
N
= NUCLEAR INSTRUMENT CHANNEL, SEEDS 2, 3, AND 4
( ) = NUCLEAR INSTRUMENT CHANNEL, SEED 1
(D) (SOUTHWEST)
(SOUTHEAST) (A)

Fig. 3 Cross section of Shippingport reactor.[20] (Seed channels are indicated by +; Roman numerals refer to rod group.)

life for Seed 4) to +30 hr* (full power and temperature near beginning of life for Seed 1). Oscillation periods varied from 22 to 27 hr, with the longer periods generally associated with greater stability.

8. Temperature feedback had a large effect on stability. This was indicated by the return of instability during Seed 1 when the average temperature was decreased 25°F, thus reducing in magnitude the negative temperature coefficient.

9. The importance of the rod program, apart from the temperature feedback, was the largest factor affecting stability.

10. The buildup and subsequent depletion of ^{239}Pu in the blanket was primarily responsible for the increased stability of Seeds 2 and 3 and the eventual return of instability late in life for Seed 4.

*Negative number indicates the time required for the oscillation amplitude to be reduced by one-half. The most rapidly damped oscillation corresponds to −14 hr, and the most rapidly diverging oscillation corresponds to +30 hr; the others were intermediate (-14 hr $\geq \tau_{1/2} \geq +30$ hr).

Connecticut Yankee PWR

Two tests were performed to establish the feasibility of measuring a stability index for xenon-induced spatial power oscillations.[57] The first test consisted in moving the control rods over a 15-in. interval in a pseudo-random sequence and determining the frequency-response characteristics in the vicinity 1×10^{-5} Hz. This test was performed at equilibrium xenon at 490 MW(e). Soluble boron was used to compensate the rod motion and subsequent xenon redistribution to maintain constant total power. External ion chambers located midway of the top and bottom halves of the core were monitored at 5-min intervals for 124 hr. The measured frequency response was interpreted in terms of a spatially dependent transfer function, which can theoretically be expanded in the natural p modes of the reactor. This allows the real and imaginary parts of the p eigenvalue to be deduced from the measured transfer function.[58] This interpretation indicated the reactor was intrinsically stable and that the real part of the p eigenvalue was -0.26 hr^{-1}

Table 1 Summary of Observed PWR-1 Xenon Stability[20]

Seed	Control rod Group	Control rod Height, in.	Interval Dates	Interval EFPH	Power level, %	Avg. temp., °F	Oscil. period, hr	Doubling time, hr*	Nodal line direction	Comments
1	II	28	4/30 to 5/3	480	85	500	~24	+200	NE–SW	Induced, divergent. Three loops: 1A, 1D, and 1C. Insertion of symmetric Group 1 rods did not affect the oscillation.
1958	II	28(33)	7/1	682	100	525	22.3	+30.4 ± 1.3	NW–SE	Spontaneous, divergent. Most unstable case. Three loops: 1A, 1B, and 1C. Loop 1D replaced 1C on 7/13.
		(34)	to				22.3	+37.6 ± 5	E–W	A slight divergence continued to 8/3. Following this, oscillation amplitude slowly converged. Between 7/21 and 7/29, two diagonal oscillations, 90° out of phase, are indicated (possibly a slow precession toward an N–S node).
	II	41	8/14	1693						
	II	42(49)	9/23	1785	100	500	22.8	+116 ± 27	N–S	Spontaneous, divergent. Suppression of the NW–SE diagonal did not affect the NE–SW diagonal. Conditional convergence was evident from 10/15 to 10/23. The return of instability was probably initiated by the decrease in average temperature at 1700 EFPH, which resulted in a less-negative temperature coefficient. Four loops.
			to							
		64	11/3	2790						
2 1961	IV	63	7/7 to 7/12	7600	75	475	25.5	−15.9 ± 0.16	NE–SW	Induced, convergent. Data permitted an accurate analysis of the rapidly converging oscillation. Three loops: 1A, 1B, and 1C.
3 1962	II	57	5/4 to 5/9	3789 3876	75	495	27.25	−21.6 ± 0.9	NE–SW	Induced, convergent. As with Seed 2, the ion-current data were very good. Four loops.

Note: The four control-rod groups are sequential; the controlling group height (above core bottom) is a very approximate average during the time oscillations were observed. Average temperature was generally constant within ±1°F during a 24-hr period, and the average power level was constant within ±1%. The oscillation periods are accurate to ±½ hr. A negative doubling time indicates the amplitude half-life of a convergent oscillation.

*The uncertainty in doubling time is the root-mean-square channel deviation from the four-channel average. It is misleadingly large for the spontaneous oscillations during Seed 4 because the first overtone modes are nondegenerate.

Table 1 (Continued)

Seed	Control rod Group	Control rod Height, in.	Interval Dates	Interval EFPH	Power level, %	Av. temp., °F	Oscil. period, hr	Doubling time, hr	Nodal line direction	Comments
4 1963	II	27(28)	3/9	797	100	500	23.8	+40 ± 17†	N–S	Spontaneous, divergent.
		(29)					23.8	+158 ± 23	N–S	The average doubling
		(30)	to				23.8	+85 ± 15	N–S	time between 3/13 and
		(31)					23.5	+117 ± 53	N–S	3/17 was +66 ± 13.
		40	4/20	1800						The spontaneous oscillations were partially suppressed. The last suppression was very effective. Conditionally convergent oscillations continued through 4/20.
	II	51	6/4 to 6/9	2668 2786	92	495	26	−41 ± 2	E–W	Induced, convergent. These tests were performed to measure the stability dependence on power level.
	II	53	6/11 to 6/16	2824 2968	80	495	26	−26 ± 2	E–W	Induced, convergent. These tests were performed to measure the stability dependence on power level.
	IV	36	12/4 to 12/9	5559 5674	80	495	27	−14 ± 2	E–W	Induced, convergent. This test and the preceding tests were for the most stable mode.

†The N–S node is expected to be more unstable than the E–W node. There is a clear precession toward the N–S node. The mixture of these nodes accounts for the large uncertainties attached to their average values. The most unstable node appears to have a doubling time of 25 hr.

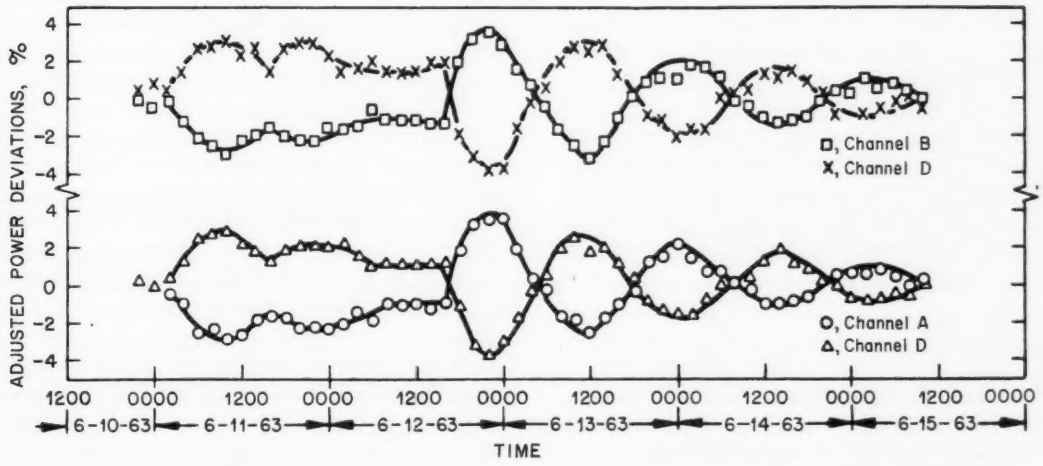

Fig. 4 Observed spatial power oscillations in Shippingport PWR-1, Seed 4 (Ref. 20).

The second test was performed to measure the impulse response. With the reactor at equilibrium xenon conditions at 600 MW(e), rods were inserted 8 in. for 4 hr, then withdrawn. Soluble-boron concentration was adjusted to maintain constant power. External ion-chamber responses were monitored for 56 hr. Interpretation of these data using the frequency-response method[58] yielded $-0.08\ hr^{-1}$ for the real part of the p eigenvalue, and standard impulse-response analysis yielded a result of $-0.05\ hr^{-1}$

Dresden BWR

Xenon-induced spatial power-oscillation effects have been measured in the Dresden 1 core (and other BWR's) as part of the normal load-following response.[1] In addition, several special tests have been carried out in Dresden 1 to examine both axial and azimuthal oscillations. Dresden 1 has a rated full power of 210 MW(e), an active core height of 9.1 ft, and a core diameter of 12 ft.

Oscillations in the spatial power distribution initiated by load following have exhibited stable behavior. All observed spatial power redistributions due to xenon have completely damped out in from 5 to 30 hr.

A special test was conducted in Dresden 1 by positioning control rods asymmetrically to cause a planar flux tilt and allowing the xenon to come to equilibrium with the tilted flux. Then the control rods were returned to symmetric positions. The azimuthal power shape followed the control-rod movement, and then there was a small transient that was completely damped in 15 hr.

Tests for stability with respect to axial oscillations have been conducted by reducing the reactor power for a short time. Spatial flux redistributions due to xenon are completely damped in 5 to 20 hr, depending upon whether the total power is held constant or allowed to vary. From these tests, and corresponding analyses for larger cores, it is concluded that an axial xenon-induced spatial power oscillation in a BWR will damp out in one cycle due to the nonuniform axial variation of the power coefficient, which makes it easier for the power to shift down than to shift up.

Other BWR's

Results of startup tests in the Gundremmingen (11 ft high), Oyster Creek, Nine Mile Point, and Tsuruga (12 ft high) reactors and of special spatial xenon tests in the Gundremmingen reactor indicate that these BWR's are very stable with respect to xenon-induced spatial power oscillations.[59,60] Inlet-flow control was used during all these tests.

Two special tests performed in the Gundremmingen reactor consisted in shifting the power distribution to skewed axial or radial shapes, maintaining the skewed shapes until equilibrium xenon was established, then repositioning the control rods to the symmetric positions associated with the normal operating state. The reactor was maintained at constant inlet temperature and pressure, but the power was allowed to vary. Two traversing in-core ion-chamber probes and heat-balance measurements were used to follow the transient axial power distribution.

In the axial test the power was initially skewed to the top of the core so that the peak was in the region of greatest steam voids. After equilibrium was established in the skewed condition, the rods were repositioned so that the power initially shifted down in the core. Subsequently the power shifted down a bit more, then returned monotonically to the new equilibrium shape. This is illustrated in Fig. 5.

Attempts to induce an azimuthal transient by skewing the power into one quadrant, establishing equilibrium xenon conditions, and then returning the rods to their symmetric positions were unsuccessful. No appreciable transients were observed, indicating a high degree of damping.

Savannah River HWR's

Spontaneous xenon-induced power oscillations have been a familiar phenomenon in the slightly enriched D_2O-moderated and -cooled production reactors.[28,61] These large reactors are intrinsically unstable to such oscillations. Both planar and axial oscillations have been observed, and in one case a combined axial–planar (quadrupole) oscillation occurred.[28]

Instrumentation for detecting gross tilts in the spatial power distribution is extensive. Fuel and effluent temperature, the pump-suction temperature in each of six radial sections, the response of gamma-heat sensors located at nine radial locations (each with seven axial levels), and the response of 10 external ion or compensated fission chambers are monitored frequently.

A series of seven axial and three radial experiments in which xenon-induced spatial power oscillations were intentionally initiated was performed recently.[62] These experiments were performed at constant reactor power in the C reactor, which approximates a cylinder 15 ft high and 15 ft in diameter. A summary[62] of

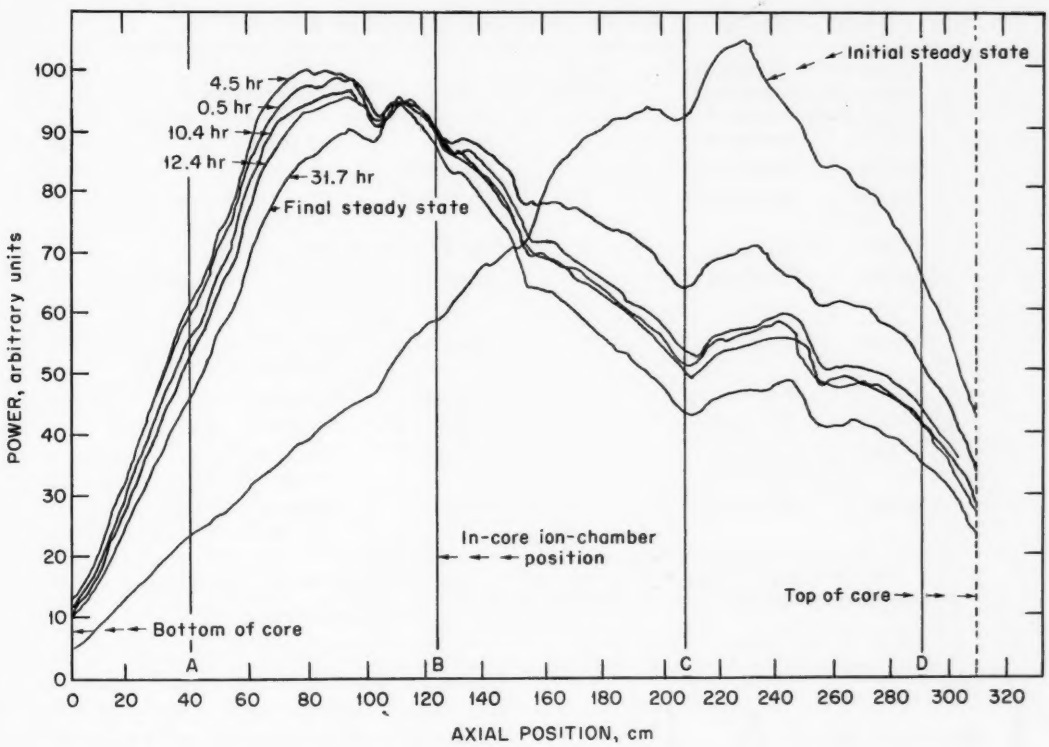

Fig. 5 Axial power distribution during xenon transient test in the Gundremmingen reactor.[59]

these experiments is given in Table 2. Figure 6 shows the relative flux variation at a point near the top of the core and near the axial center line for three different experiments. The time-dependent data obtained from these experiments include detailed axial flux shapes at nine interior locations, chamber currents at 10 external locations, power for each fuel assembly, distribution of coolant inlet and outlet temperatures and moderator temperatures, and rod configurations.

VERIFICATION OF METHODS

Some measure of confidence in the stability analyses and simulation methods has been obtained by intercomparison and by comparison with experimental data. Any such comparison is, in general, a joint test of the method and the modeling procedure used to represent the physical phenomena in a reactor core; the two usually are inseparable. This is true particularly of comparisons with experimental data.

An extensive study of the stability with respect to planar oscillations of the Shippingport Core 1 has been performed using a modified μ-mode analysis.[20] The μ modes were computed with few-group, two-dimensional, diffusion-theory codes based on core compositions obtained from depletion studies (thus some uncertainty existed as to the actual composition). Temperature-feedback effects were not included. These calculations indicated that the ordering of increasing degrees of seed stability for the four seeds used in PWR-1 is 1, 4, 3, 2. This is in qualitative agreement with the experimental data, although the quantitative agreement is poor because temperature feedback was not generally included in the calculations. In the one case for which temperature feedback was included in the calculation [Seed 1 at 2050 effective full-power-hours (EFPH)], the calculated time required for the oscillation amplitude to double was 153 hr, compared to the observed value of 115 ± 27 hr. The modified μ-mode calculations did not disagree with the variation in observed stability for the depleting seeds.

Quantitative calculations required a detailed description of geometry and material distribution, precluding the use of simple spatial averages to represent

Table 2 Summary of Xenon Experiments in Savannah River Reactor[62]

Expt. No.	Equilibrium flux shape	Power control*	Result	Other attributes
Axial 1	Symmetric	U	Stable	Low power
Axial 2	Peaked at top	U	Convergent	Low power
Axial 2A	Symmetric	S	Convergent	Low power; flux less flat than 1
Axial 4	Symmetric	S	Stable	Medium power
Axial 5	Symmetric	S	Stable	Medium power; started in Rx center only
Axial 6	Symmetric	S	Divergent	High power; less flat than 2A, 4
Axial 7	Peaked at top	S	Convergent	High power
Radial 1	Symmetric	U	Stable	High power
Radial 2	Symmetric	U	Convergent	High power; flux less flat than R1
Radial 3	Symmetric	U	Divergent	Medium power; flux flat like R1

*U, controlling rod tips were all at same (uniform) level in top of the reactor; S, controlling tips were staggered, with half in the top and half in the bottom.

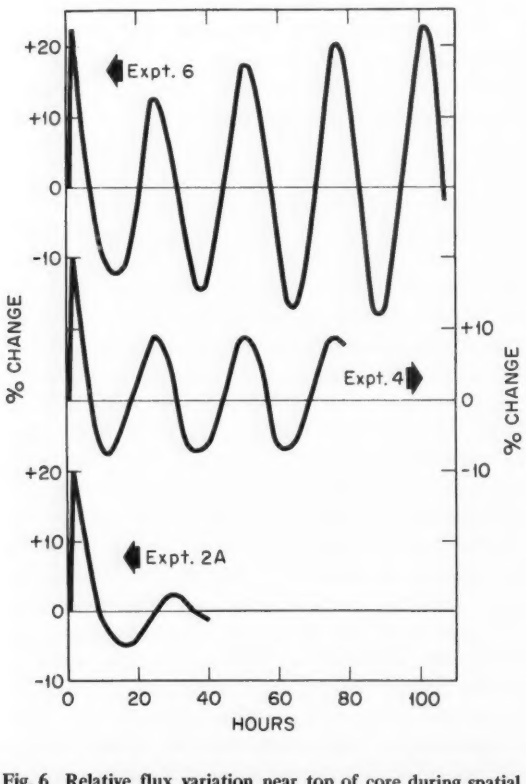

Fig. 6 Relative flux variation near top of core during spatial power oscillation experiments in a Savannah River reactor.[62]

parameters in the stability analysis. The predictions of the stability analysis were conservative when the stabilizing temperature feedback was not included.

Stability predictions based on a μ-mode analysis, using a few-group, finite-difference, two-dimensional model for calculation of the μ modes, have been compared with 52-node analog simulations for a large pressurized-water seed–blanket reactor.[19] The ratio of threshold-to-reference thermal-flux levels ($\bar{\eta}/\bar{\eta}_0$) at which neutral stability occurred (oscillations neither diverged or converged) was obtained empirically from the analog simulation and compared to the predictions from the μ-mode analysis as a function of a power-feedback coefficient (K). The results, shown in Fig. 7, indicate agreement to within 10%; the analog simulation becomes unstable at slightly lower power levels than predicted by the stability analysis. Differences in the reactor models used in the two calculations may partially account for this difference.

The λ-mode stability analysis has been applied to a wide variety of reactor types. The original Randall–St. John type analysis,[2] using a volume average flux and a flux-flattening parameter, correctly predicts qualitative stability trends observed in the heavy-water Savannah River production reactors.[28] However, it did poorly in predicting the recent experiments conducted in one of these reactors.[62,63] Predictions of this type are in qualitative agreement with digital simulation results for

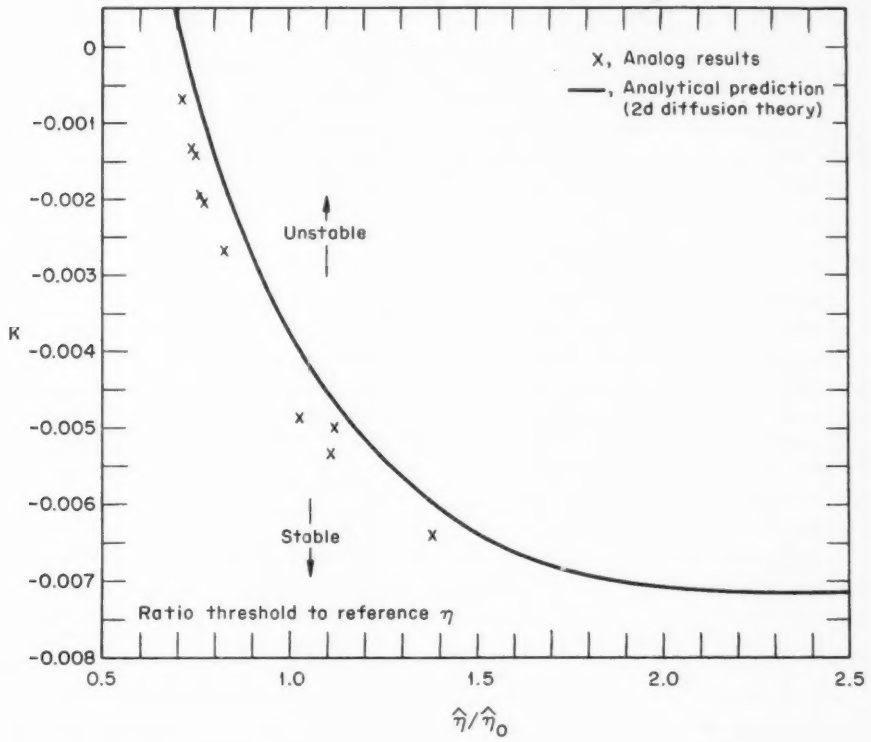

Fig. 7 Comparison of μ mode and analog stability predictions for LSBR.[19]

large BWR's[64] and PWR's.[27] However, it was found that a more rigorous spatial averaging could lead to significantly better quantitative agreement in PWR's.[27]

An improved λ-mode analysis,[18,25] in which appropriately defined spatial averages of the neutron flux are employed, has been applied to the analysis of the Shippingport Core 1 and has been compared with digital-simulation results for two-dimensional PWR models.[18,26] These results are depicted in Fig. 8, where the parameter Ω is related to the separation of the fundamental and first harmonic λ-mode eigenvalues and incorporates temperature feedback, and the parameter η is proportional to an appropriately averaged thermal-neutron flux. For the Seed 1 PWR result, an experimental value of Ω was inferred from the observed time required for the oscillation amplitude to double. For Seed 4, unstable oscillations were measured at 893 and 1397 EFPH, in qualitative agreement with the prediction. Digital simulations and λ-mode analyses were based on identical few-group models, so the agreement is considered a valid confirmation of the linear stability-analysis method. Subsequent calculations have also indicated agreement between this λ-mode analysis and digital simulations for PWR models.[54]

Relatively few direct comparisons of digital (or analog) simulations with experiments have been reported. Measurements of xenon-induced spatial transients in the Dresden 1 and Gundremmingen BWR's indicated strong damping and trends that are in reasonable agreement with theoretical predictions.[1] One-dimensional digital simulations of the axial oscillations in the Savannah River HWR were in poor agreement with measured data,[61,63] which may imply that multidimensional effects are important because it is known that the spatial flux distribution is nonseparable in the radial and axial dimensions.[63] Three-dimensional digital simulations, with the MAPLE SYRUP finite-difference code,[40] predict the amplitudes of the observed oscillations quite well. However, the calculated periods are systematically about 10% longer than observed. In addition, the detailed shape of the transient during the first half period is poorly calculated.[63]

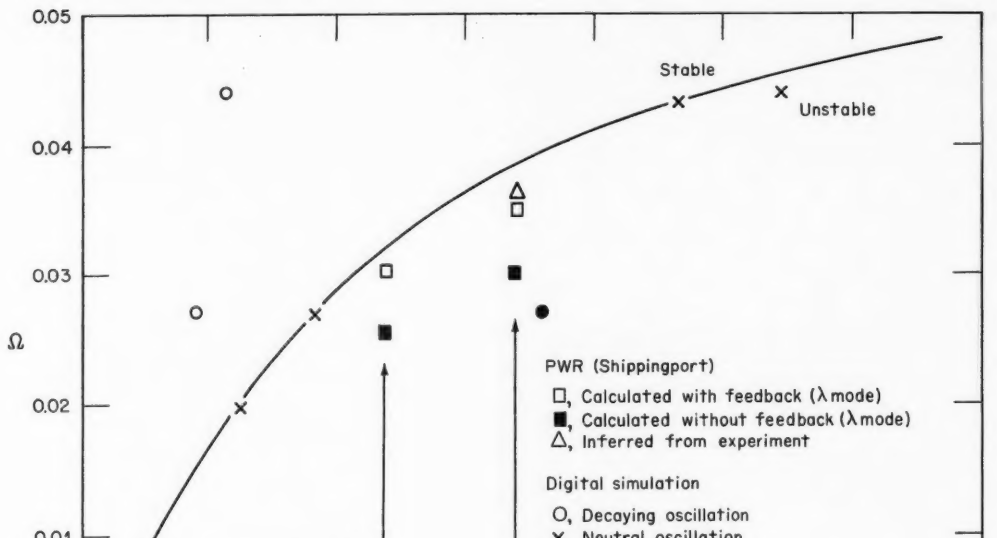

Fig. 8 Comparison of λ-mode stability prediction with experiment and digital simulation.[26] (Location of symbol denotes λ-mode prediction, type symbol indicates result.)

A different type of digital simulation has been employed in the analysis of the Connecticut Yankee PWR xenon-stability tests.[58] The space-dependent frequency response was computed with the SPARTA code[65] and compared with the observed results. Good agreement was obtained, as shown in Fig. 9, where the phase of the transfer function (γ) is plotted. Stability characteristics of the core with respect to xenon-induced spatial power oscillations can be inferred from this information by expanding the transfer function in p eigenfunctions.[58] Examination of the behavior of the transfer function in the vicinity of the natural frequency of a given p mode allows the p eigenvalues to be inferred.

Some comparisons of the less-detailed nodal and modal representations with detailed few-group finite-difference representations for the simulation of xenon-induced spatial power transients have been made. Comparison of 3DXT (one-group nodal) calculations with results from one- and two-dimensional, few-group, finite-difference codes indicates that 3DXT adequately predicts (1) static power shapes and shifts therein due to rod motion and changes in xenon or coolant

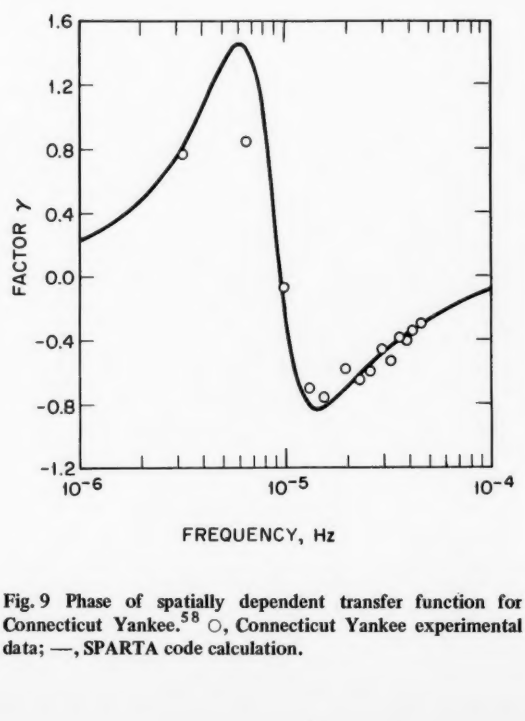

Fig. 9 Phase of spatially dependent transfer function for Connecticut Yankee.[58] ○, Connecticut Yankee experimental data; —, SPARTA code calculation.

enthalpy and (2) critical control-rod positions and power shapes during a xenon-induced spatial power transient.[43] Errors in nodal power fractions of 1 to 5% are the rule, although larger errors have been observed. CEXE (one-group nodal) calculations are in relatively good agreement with one- and two-dimensional, few-group, finite-difference calculations on the prediction of power shapes during an uncontrolled xenon-induced spatial power transient.[66] For both codes, it is necessary initially to adjust nodal coupling coefficients to obtain agreement with few-group finite-difference calculations of perturbed and unperturbed power shapes to ensure that the nodal model will tilt reasonably. Modal calculations with continuous Green's functions modes have been demonstrated to agree well with finite-difference calculations in one and two dimensions, provided: (1) enough modes are used—12 and 32 for the one- and two-dimensional problems discussed—and (2) the source regions used in generating the modes is no more than four neutron migration lengths in linear dimension.[51] It would seem that similar accuracy could be obtained with fewer modes, if the modes were chosen as extreme flux shapes that might be expected in the oscillation—a strategy which has been exploited successfully in other applications of synthesis methods.

ANALYTICAL STUDIES

A number of studies have been performed for the purposes of obtaining a better understanding of the interaction of the many physical phenomena that influence xenon-induced spatial power oscillations and of determining the effect of design parameters upon these phenomena, and consequently upon the oscillations. These studies have utilized stability-analysis or computer-simulation methods, or sometimes both, and have been devoted to specific reactor types. Although the same mechanisms are present in all water-moderated reactors, their relative influence varies greatly. Thus it is convenient to summarize these studies by reactor type.

Boiling-Water Reactors

The dominant feature of BWR's, with respect to xenon-induced spatial power oscillations, is the large negative power coefficient of reactivity due to coolant voids. This large negative power coefficient generally makes BWR's less susceptible to planar oscillations than a PWR of equivalent dimensions and power and makes BWR's less susceptible to planar than axial oscillations. Accordingly most studies of xenon-induced spatial power oscillations have been devoted to one-dimensional axial studies, many of which are summarized in Ref. 1.

Digital simulation of axial transients in reactors of the Dresden 2 [713 MW(e)] and Browns Ferry [1075 MW(e)] class exhibit a highly damped oscillatory response. In fact, BWR's as large as 3000 MW(e) and 24 ft high appear to be stable with respect to xenon-induced spatial power transients,[1] and well-damped spatial power transients are predicted for 5000-MW(e) reactors that are controlled by inlet flow.[60] However, dual-cycle BWR's may be somewhat less stable.

Axial nonuniformities in the coolant density cause variations in spectrum-averaged nuclear parameters by factors of 2 to 3 and produce an increasing magnitude of the negative power coefficient with height. This nonlinear coolant density distribution is very effective in damping axial oscillations.[1,67] At steady-state operation at rated power in the present BWR's, by General Electric Company, the power is peaked in the bottom of the core, and the iodine concentration has the same axial distribution. However, the xenon concentration is peaked toward the top of the core because of the smaller spectrum-averaged xenon cross section in the region of larger steam-void fraction. In a flow-controlled reactor, when the power is reduced with flow and shifts to the bottom of the core, the larger decay of iodine in the bottom tends, initially, to force the power upward. However, the larger negative power coefficient in the top of the core strongly inhibits the upward shift. This nonlinear bidirectional response of BWR's to an axial xenon redistribution causes large axial perturbations to damp in one xenon cycle (16 to 34 hr), almost independent of core length, for a flow-controlled reactor. The reduced stability of dual-cycle plants arises because, when the power is reduced by a reduction in subcooling, the power distribution shifts upward in response to movement of the boiling boundary. Thus the nonlinear damping mechanism is not brought into play as effectively. It is important to describe all nonlinear effects: the heat flux and flow dependence of subcooled boiling; Doppler; influence of steam voids on rod worths, Doppler, and microscopic xenon cross sections; and the effects of burnable poisons and fuel burnup.[60]

Design of BWR's at General Electric has been based* on making the negative power coefficient of

*Actually, design parameters chosen on an economic basis have resulted in a sufficiently negative coefficient, and no design changes have been required specifically to inhibit xenon-induced spatial power oscillations.[1]

reactivity large enough to keep the core inherently stable with respect to xenon-induced spatial power oscillations.[1,60] An increase in magnitude of the negative power coefficient can be obtained by decreasing the moderator-to-fuel ratio, decreasing the fuel-rod diameter, increasing the fuel enrichment, decreasing the fuel exposure, decreasing the soluble poison in the moderator, decreasing the ratio of exterior-to-interior water, increasing the cladding-to-fuel absorption ratio, decreasing the core size, increasing the void content, or increasing the ratio of shielded-to-unshielded control absorbers. Many of these changes obviously would be detrimental to economic considerations.

A three-dimensional study of xenon-induced spatial power oscillations, by digital simulation, in heavy-water-moderated, boiling light-water-cooled reactors (HWBLWR's) was performed to investigate the effect of void coefficient, core size, and void distribution on stability.[47] A HWBLWR differs from a BWR in that the void coefficient may be positive or negative, depending on the core design. When the void coefficient is negative, there is no qualitative difference in the power-reactivity feedback in a HWBLWR and a BWR.

The void coefficient of reactivity was found to have a stabilizing or destabilizing effect on planar oscillations, depending on whether it is negative or positive. When the first harmonic azimuthal mode was oscillating, higher harmonics were excited through the nonlinear feedback. In particular, a higher harmonic with an axial component was excited by oscillation of the first harmonic azimuthal mode through the nonlinear void feedback. The control required to maintain constant power also coupled different modes of oscillation. Clearly, planar and axial oscillations are nonseparable in this case.

A positive (negative) void coefficient was found to have a stabilizing or destabilizing effect on axial power oscillations, depending on the axial void distribution. If the boiling boundary is sufficiently low in the core, a positive (negative) void coefficient produces a positive (negative) component to the total power coefficient. In this case an increase in power lowers the boiling boundary, which shifts the power down (positive void coefficient) or up (negative void coefficient); a downward power shift further lowers the boiling boundary, which further shifts the power down, etc., for a positive void coefficient; an upward power shift raises the boiling boundary, which shifts the power down compensating the initial upward shift, for a negative void coefficient.

If, on the other hand, the boiling boundary is sufficiently high in the core, a positive (negative) void coefficient produces a negative (positive) contribution to the total power coefficient. In this case, an increase in power lowers the boiling boundary, which shifts the power up (positive power coefficient) or down (negative power coefficient): an upward power shift raises the boiling boundary, which shifts the power down compensating the initial upward shift, for a positive void coefficient; a downward power shift lowers the boiling boundary, which further shifts the power down, for a negative void coefficient. For a sufficiently large negative (positive) void coefficient, it is unlikely that the boiling boundary could be established sufficiently high (low) in the core that the void contribution to the power coefficient was positive (negative).

Pressurized-Water Reactors

A detailed study of the xenon spatial stability characteristics of the proposed Large Seed–Blanket Reactor (LSBR) was conducted using μ-mode linear stability analysis and a 52-node analog simulation.[19] The LSBR concept consists of 55 hexagonal seed–blanket modules cooled with pressurized H_2O. Each module contains an annular seed of ^{233}U or ^{235}U diluted with ^{232}Th or ^{238}U embedded in a blanket of ^{232}Th or ^{238}U. Typical dimensions of cores studied were 7.5 ft axially and 16.4 ft in radius, and a typical power level was 1800 MW(t).

Stability was found to decrease as the power distribution was flattened. Stability with respect to planar oscillations was increased by increasing the radius of the seed annuli, thus increasing the seed-to-seed coupling.

Doppler and moderator feedbacks were responsible for the observed stability; without these feedback effects the first azimuthal harmonic was unstable with respect to xenon-induced oscillations. The magnitude of the moderator temperature coefficient, which varied from -1.9 to -1.0×10^{-4} $\Delta k/°F$, had a strong influence on the planar stability. Stability could be significantly increased by isolating the coolant flow of the individual steam generators to different quadrants of the core. Axial stability was only slightly influenced by the moderator temperature coefficient, other than the effect it had on the equilibrium axial power distribution. For concepts in which fertile material was in the seed regions, the Doppler temperature feedback was as effective in stabilizing the axial mode as the azimuthal (planar) mode; when ^{232}Th was placed in the seed, the stabilizing effect of the Doppler feedback

was approximately 3.7 times as large as the effect of the moderator temperature feedback. In all concepts the Doppler feedback was more effective than the moderator temperature feedback in inhibiting xenon-induced spatial power oscillations.

Systems with ^{233}U–^{232}Th were more stable than equivalent ^{235}U–^{238}U systems because of the larger negative Doppler coefficient and the more advantageous xenon and iodine yields associated with the former. Not only is the total mass-135 chain yield smaller for ^{233}U than for ^{235}U but also the direct xenon yield is a greater fraction of the total for the former, thus further reducing the delayed reactivity effect.

It is interesting that the LSBR was found to be stable with respect to xenon-induced spatial power oscillations, whereas the Shippingport Core 1, with less than half the diameter of the LSBR, experienced spontaneous planar oscillations. The LSBR concept has a somewhat lower thermal-neutron-flux level, and larger stabilizing Doppler and moderator (primarily Doppler) feedbacks, than Shippingport Core 1.

One-dimensional digital simulations of uncontrolled axial transients in a model representative of a large, slightly enriched PWR indicated that cores up to 10 ft in height would be stable with respect to xenon-induced spatial power oscillations.[68] However, the stability was found to decrease with increasing core height and with increasing flux flattening. The Doppler feedback was the dominant stabilizing mechanism because the moderator coefficient was found to have relatively little influence on axial oscillations. Stability depended on the type of perturbation initiating the transient.

Three-dimensional digital simulations of a PWR core with axial and radial dimensions of 24 and 19 neutron migration lengths, respectively, were performed to study the effect of control-rod motion, temperature feedback, and initiating perturbation on axial oscillations.[18,43] Doppler feedback was treated indirectly, as a component of the moderator feedback on k_∞, in these calculations.

Control-rod motion dominated the transient response. Two transients were initiated by shutting down a reactor, which had been operating at a thermal-flux level of $\sim 2 \times 10^{13}$ n/(cm^2)(sec), for 12 hr and then returning it to power. In one case, control was effected by discrete rods, and in the other case a uniform poison was varied to maintain criticality. Power traces in the top (XX) and bottom (YY) of the core are shown in Fig. 10. These and similar results lead to the conclusions that (1) axial stability analyses that do not represent the control system explicitly can lead to unreliable results and (2) undesirable axial xenon oscillations are most readily altered by modifying the control-rod motion used to maintain criticality. When this transient was repeated, with control motion to maintain criticality, but with only 2 hr of shutdown instead of 12, and consequently with a smaller xenon buildup and redistribution to initiate an oscillation, the spatial power oscillations were highly damped.

Moderator feedback was found to influence axial oscillations via several interrelated phenomena. Negative (positive) feedback limits (enhances) local power peaking by decreasing (increasing) k_∞ and increasing (decreasing) leakage locally, which is stabilizing (destabilizing) during an oscillation. However, negative (positive) feedback tends to flatten (peak) the axial power distribution, which makes a core more (less) susceptible to oscillations; thus negative (positive) feedback is indirectly destabilizing (stabilizing).

When the axial power distribution shifts in response to a change in control-rod position, the associated change in axial coolant enthalpy distribution produces a net reactivity that must be compensated by a further change in rod position in a rod-controlled core. Depending upon whether the compensating rod motion tends to enhance or limit the original power shift, this effect can be destabilizing or stabilizing, respectively. When a downward rod motion causes the power to shift up, this effect of negative (positive) moderator feedback is destabilizing (stabilizing). However, this effect is stabilizing (destabilizing) for negative (positive) feedback when a downward rod motion causes the power to shift down. An example was depicted[18,43] in which negative moderator feedback led to diverging axial oscillations, whereas positive moderator feedback resulted in converging oscillations.

An extensive study of xenon-induced spatial power oscillations was conducted to investigate: (1) the effect of core parameters on planar stability, (2) methods of controlling planar oscillations, and (3) three-dimensional oscillation effects.[69] Modal stability analyses and one- and two-dimensional digital simulations were employed in the first phase, which is summarized in Ref. 27. The reactor core was typical of a PWR, with 2.6% enriched ^{235}U, a diameter of 11 ft, and a moderator temperature coefficient of -0.5×10^{-4} $\Delta k/°F$.

General conclusions of this study were in substantial agreement with earlier work, in that it was shown that planar stability increases with: (1) decreasing core diameter, (2) decreasing flux flatness, (3) increasing

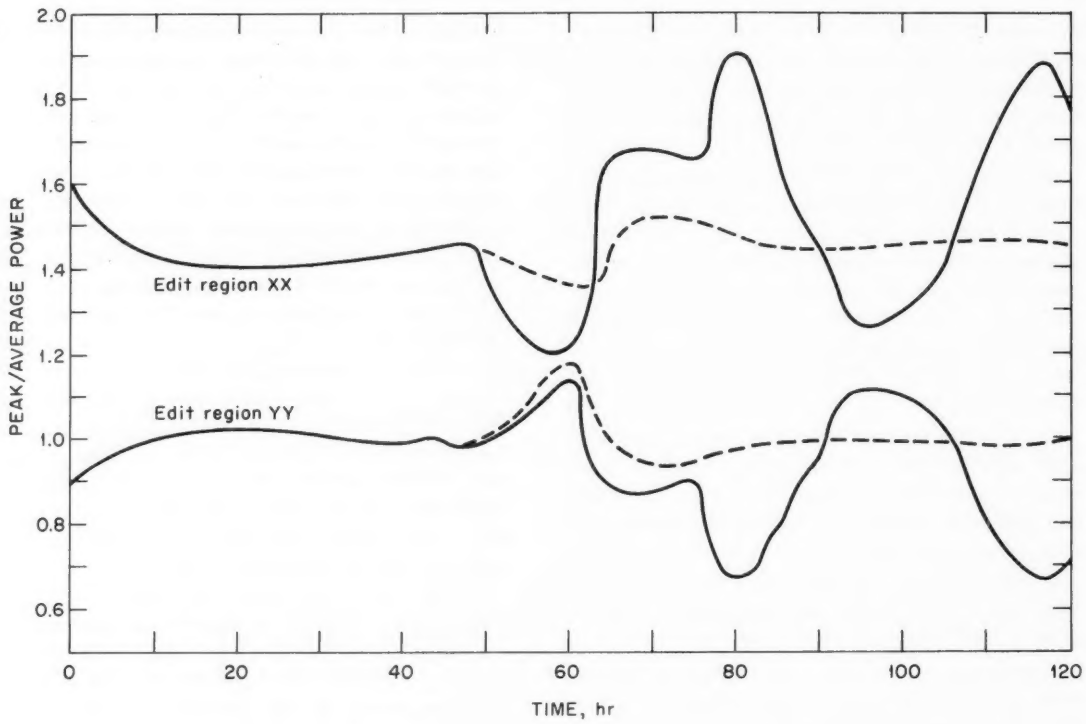

Fig. 10 Power oscillations during simulated xenon transient.[43] (—, control rods used; ---, soluble poison used.)

enrichment, for a fixed power coefficient, (4) increasing magnitude of the negative power coefficient, (5) decreasing iodine yield from fission, (6) increasing direct xenon yield from fission, (7) decreasing spectrum-averaged xenon cross section, and (8) decreasing power density for small negative power coefficients and increasing power density for large negative power coefficients. Sensitivity of stability to any other core parameter decreased as the negative power coefficient increased in magnitude. The Doppler coefficient was found to be quite important in suppressing xenon-induced spatial power oscillations. For small perturbations the characteristics of the digitally simulated response were independent of the perturbation. However, for large perturbations the stability of the response was sensitive to the magnitude and location of the perturbation. The effects of delayed neutrons and of the delay time required for heat to be transferred from fuel to coolant were investigated and found to be negligible. The oscillations were insensitive to the nonlinear characteristics of the Doppler feedback, but it was found that the nonlinear properties of the fuel-to-coolant heat transfer could be important.

One-, two-, and three-dimensional calculations have been performed[42] for a PWR with an active core height of 12 ft and a power density of 104.5 W/cm^3—typical of those presently being designed. The three-dimensional calculation was based on two-group diffusion theory (finite difference), with coolant density and fuel temperature feedback explicitly represented and with a sophisticated coolant-flow model that included interassembly mixing and subcooled voids. A perturbation representing the full insertion of one control rod for 1 hr was introduced, and the subsequent behavior of the power distribution (without further control) was simulated. This perturbation excited a converging planar oscillation and a diverging axial oscillation. Attempts to simulate the planar oscillation with a two-dimensional calculation for an average plane resulted in more rapidly converging oscillations than were observed in the three-dimensional simulation, reflecting the mode coupling between the unstable axial oscillation and the converging planar oscillation which could not be accounted for in the two-dimensional calculation. Shown in Fig. 11 are predictions of the transient power density at a location

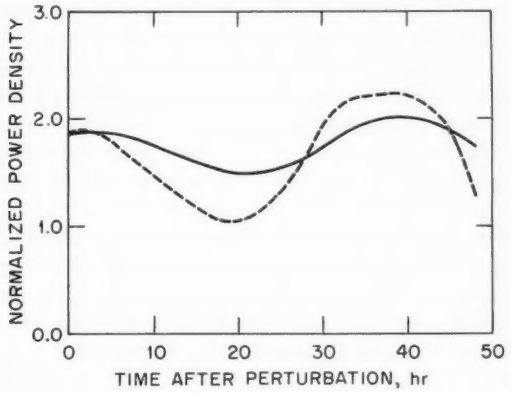

Fig. 11 Nonseparable multidimensional effects in a simulated xenon-induced spatial power transient.[42] —, three-dimensional calculation; ---, combined one- and two-dimensional calculation.

close to peak power in the unperturbed core, calculated directly with the three-dimensional model and combined from the one- and two-dimensional calculations. This further illustrates the importance of accounting for multidimensional nonseparability.

Another study[66] was made, based on the Pickering reactor, which is composed of 390 pressure-tube fuel channels containing natural UO_2 and is moderated and cooled by heavy water. The core is a right-circular cylinder with an active height of ~19.5 ft and a diameter of 20.8 ft. The rated power is 1630 MW(t). Two-dimensional digital simulations indicated that the reactor was unstable with respect to azimuthal xenon-induced spatial power oscillations, and one-dimensional digital simulations indicated that it was stable with respect to axial oscillations. A three-dimensional digital simulation predicted that both the axial and azimuthal oscillation modes were more stable than were predicted by the one- and two-dimensional simulations, respectively. However, unstable azimuthal oscillations were predicted by the three-dimensional simulation.

CONTROL

In some of the large light-water reactors now being designed and built, it will almost certainly be necessary to take some type of remedial control action specifically to limit xenon-induced spatial power oscillations, either to damp oscillations in an intrinsically unstable core or to reduce power peak during a converging oscillation in an intrinsically stable core. The type of control action that is appropriate for a given situation is not always obvious, because control that reduces a flux tilt at the present time may actually aggravate the conditions that cause flux tilting at a future time.

Control-rod motion has actually been found to induce axial oscillations in the Shippingport Core 1.[56] Analyses of this phenomenon[18,43,70,71] indicate that the reactivity effects associated with the redistribution of the axial power, xenon, and coolant temperature distributions caused by the initiating control action can interact in such a manner as to induce axial oscillations. An example is shown in Fig. 10, where the control-rod motion required to maintain criticality after a short shutdown induces axial oscillations in a core that would be stable if criticality were maintained with soluble-poison control. Another study[72] has shown that diverging planar oscillations can be induced by control-rod motion in an intrinsically stable core, and it has been found that an inappropriate control scheme can destabilize an otherwise stable core.[8]

The control system has an important effect on the predicted xenon-induced spatial power oscillations in BWR's,[1] and proper analytical representation of the control mechanism is essential.[60] Of three possible modes of control for load following (inlet flow, inlet temperature, and control rods), inlet-flow control appears to provide the best damping and least driving of axial xenon-induced spatial power oscillations. Both coolant control systems are preferable to the use of control rods in this respect, because the change in moderator boiling provides a distributed perturbation as opposed to the local perturbation produced by the motion of control rods. Current practice at GE for BWR's is to design the flow-control system so that a range of ~35% power can be controlled with flow during load following. Control-rod movement is used to regulate power swings outside this range and usually to follow slow xenon changes. This control scheme has been employed successfully on several large BWR's.[60]

A zonal control scheme has been investigated for a HWBLWR that is marginally stable with respect to planar oscillations.[72] The zonal control system was intended to maintain the average power in each zone of the reactor constant by periodically adjusting a control rod belonging to each zone. Two types of control schemes were investigated: (1) a single control action consisting in a single adjustment of each rod and (2) a single control action consisting in multiple adjustments of each rod until the average power level in each zone is sufficiently close to the desired zonal power level. Both schemes were found to completely suppress power oscillations within the first half-cycle, as long as the period of the control action was less than 1 hr.

With a period longer than 4 hr, both control schemes produced diverging planar xenon-induced power oscillations, even though the core was intrinsically stable.

Use of part-length control rods is the favored method of suppressing axial xenon-induced spatial power oscillations in PWR's.[46,68,73,74] The part-length rods are employed to "chase" the power peaks and are used over an axial range wherein their worth is relatively constant. Figure 12 indicates how part-length rods would be moved to damp out axial oscillations in an intrinsically unstable PWR. The core model was 12 ft in height and 12 ft in diameter, with a rated power of 800 MW(e). Temperature feedback was not included in the calculations. Eight part-length 3-ft rods were moved, as indicated by the shaded area. The control strategy involved moving the part-length rods at 2-hr intervals to maintain the power imbalance between the top and bottom of the core within ±10%. Such a power imbalance would be detected by external ion chambers in the upper and lower halves of the core.

The general strategy[74] on the use of part-length rods is to move these rods manually, as the need arises, to keep the axial power imbalance within preset limits. Should this procedure fail, the reactor protection system will trip the plant if the axial power imbalance exceeds a certain value, thus precluding core damage. The ability to infer axial power imbalances unambiguously from the responses of out-of-core detectors is an important and nontrivial factor in the success of such a strategy. The part-length rod control system is working in the Beznau and Ginna PWR's and is installed in the Robinson 2 and the Indian Point 2 PWR's, so that this strategy will be tested in the near future.

Control of planar xenon-induced power oscillations in PWR's has been studied for a square-annulus-type core approximately 11 ft in diameter.[69,75,76] Oscilla-

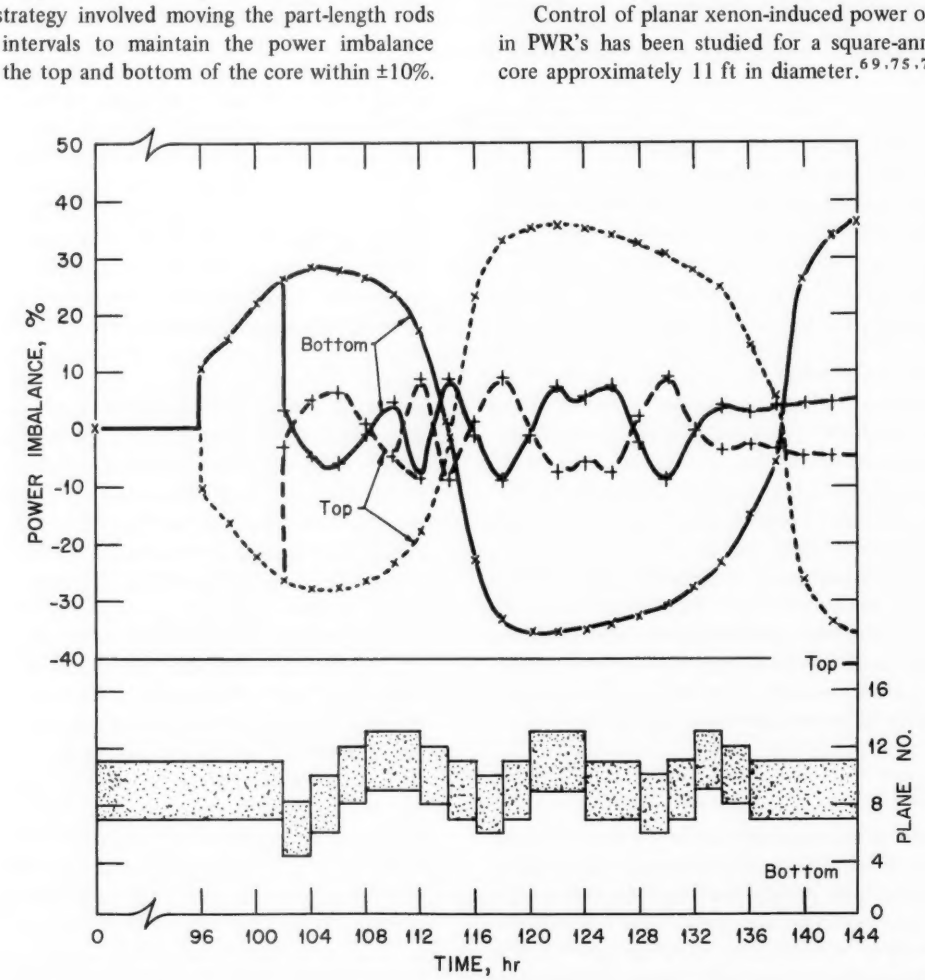

Fig. 12 Control of axial oscillations with part-length rods.[73] (Shaded region indicates location of rods.) +, with rod movement; X, without movement.

tions with node lines along the 45 and 90° diagonals were considered, and the former were found to be less stable. Eight rods, located every 45° on the major and minor diagonals, were used. Temperature feedback was suppressed in these calculations. Two types of control action (single insertion and repeated insertion) were examined. In the former, when the power in any quadrant exceeds the average of the four quadrants by a set amount, a single rod nearest the power peak is fully inserted. When the power tilt reverses and approaches the set limit in another quadrant, the rod is withdrawn. Figure 13 illustrates a case in which a 4-hr rod insertion sufficed to damp a diverging oscillation. When the corrective rod was withdrawn after 2 hr, the oscillation was only neutral, indicating that combinations of operating conditions and quadrant power-peaking limits may exist for which this single insertion control scheme does not work. A repeated insertion of the same rod, for 2 hr, initiated 2 hr after the first 2-hr rod insertion, resulted in a diverging oscillation. A second type of repeated insertion, commencing half an oscillation period later when the power had shifted to the diametrically opposite quadrant and using a rod in that quadrant, sufficed to damp the oscillation, as shown in Fig. 14. Detection of quadrant powers by external detectors on the corners was simulated.

A suggested means of determining remedial control action involves controlling the flux, through rod movement, to force the iodine and xenon distributions back to their equilibrium shapes and then returning the control rods to their equilibrium position, thus causing the neutron flux to return instantaneously to its equilibrium distribution.[77] This procedure depends on a prediction of the spatial distributions of xenon, iodine, and the neutron flux at all times during a xenon-induced spatial power oscillation and on the ability to predict the effect of a given control-rod adjustment on subsequent xenon and iodine spatial distributions. An expansion of the spatial dependence in natural p modes was used in a one-dimensional example.[77] The p modes can, at present, only be obtained for one-dimensional geometry, and the spatial xenon and iodine distributions can only be determined by calculation when the history of the neutron-flux spatial distribution is known.

The heavy-water-cooled and -moderated production reactors at the Savannah River Plant are intrinsically unstable and have experienced xenon-induced

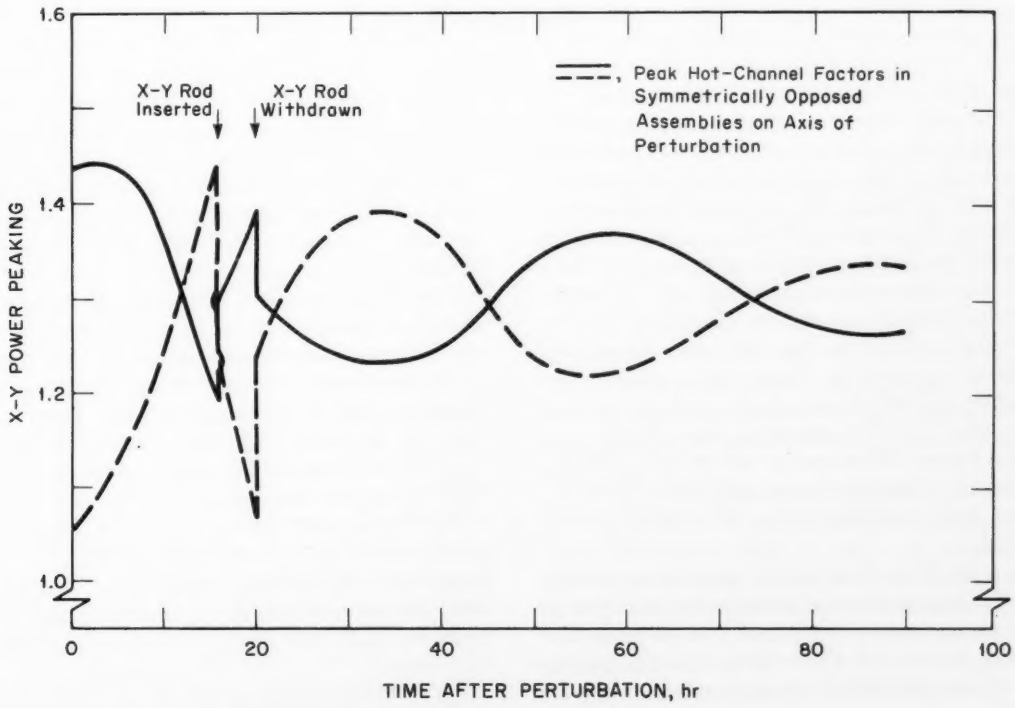

Fig. 13 Control of a planar xenon transient with a single rod insertion.[76]

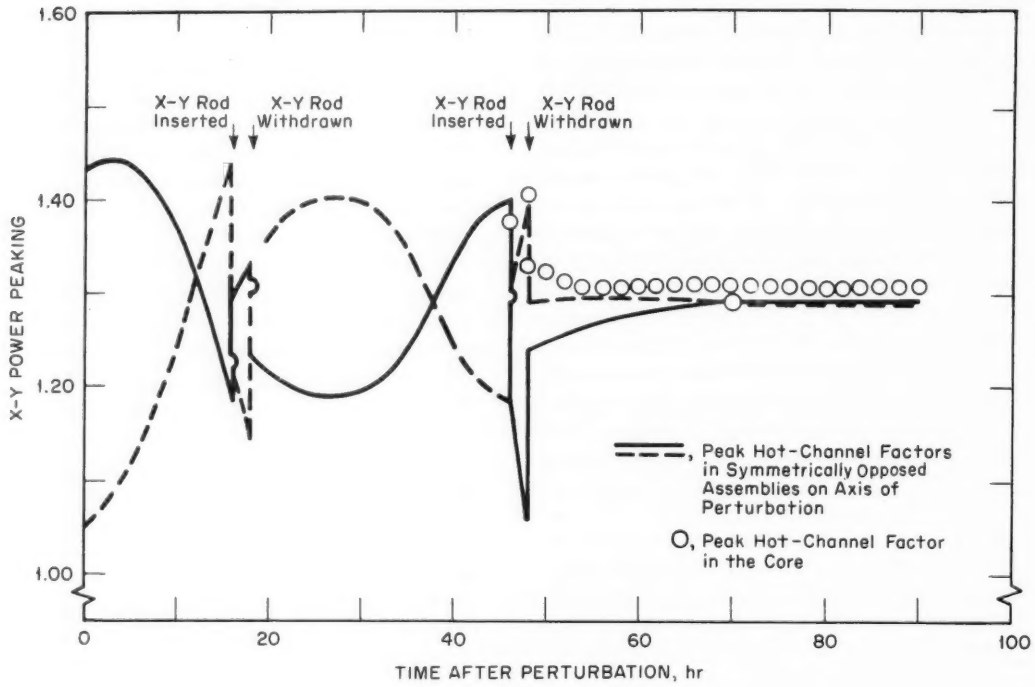

Fig. 14 Control of a planar xenon transient with repeated rod insertions.[76]

power oscillations for years.[28,61] Monitored are the local fuel and effluent temperatures, the pump-suction temperature in each of six radial sectors, the response of gamma-heat sensors located at nine radial locations (each with seven axial levels), and the response of 10 external ion or compensated fission chambers. On-line computers are used to assimilate and reduce these data. Full- and part-length control rods are frequently adjusted by small amounts to maintain a desired temperature distribution. No other normal operating procedures are used to control xenon effects. This procedure has worked well, in general. Problems have arisen when: (1) close control of power distributions was not maintained because of reduced power, (2) the control-rod configuration was unfavorable for xenon control, and (3) unfamiliar types of xenon effects have occurred.

In some of the xenon-induced spatial power oscillations that have grown large enough to be identified as such, the control system was used to force the power deviation to zero and hold it there. In other cases a more efficient procedure (requiring less control action) of anticipating the coming xenon action and counterbalancing it was used. In regions where the flux was high but beginning to decrease (indicating that xenon was being produced faster than it was being destroyed), the control system was altered to increase the flux and thus destroy the extra xenon. This empirically developed procedure has resulted in more rapid suppression of the oscillations with less total control-rod motion.[28,61]

The Pickering reactor, heavy-water moderated and cooled, is predicted to be unstable with respect to planar xenon-induced power oscillations in the absence of remedial control action.[66] Studies have been performed in which a single control action, taken at the time the initiating perturbation is introduced, was employed to eliminate the present power tilt.[66] This type of control was found to delay the ensuing oscillation somewhat but not to affect the amplitude growth or period. In another analytical study,[78] it was found that xenon-induced spatial power oscillations could be suppressed within one cycle by using a zone control system.* The zone control system consisted of

*In another study,[69,75,78] discussed above, the response was found to be sensitive to the duration of the single corrective control action.

14 absorbers distributed in the reactor, each with a nearby in-core flux detector. The function of the zone control system was to vary the strength of the control absorbers so that the deviation in the flux at the corresponding detectors, relative to the untilted value, was minimized.

Choice of the appropriate control action to suppress xenon-induced spatial power oscillations is obviously a matter of concern for large LWR's, possibly more so for the PWR's than for the BWR's with their inherent large negative power coefficient. Procedures used to date in studying control schemes have been of an empirical nature; a plausible control action was tried and improved on.

In principle, the problem of choosing the appropriate remedial control action is amenable to solution by the methodology of modern optimal control theory. At least two difficulties intervene, however. The rigorous control theory involves a sufficiently large number of calculations that its direct application is practical only for systems described by relatively few equations, whereas even a semirigorous description of the physical phenomena that must be accounted for in reactor analysis requires a very large set of equations. What is needed is a computationally tractable semioptimal control theory that can be applied to large sets of equations and, on the other hand, a less-detailed description of the physical phenomena in a reactor (i.e., a compromise). A second difficulty stems from the incomplete knowledge that always exists as to the physical state of an operating reactor.

Application of the methodology of modern control theory to xenon-induced spatial power-oscillation problems has been limited. The calculus of variations has been used to obtain equations for determining the optimal remedial control.[79-81] In one case[79,80] the equations were linearized, and the spatial dependence was expanded in natural p modes, which are difficult to obtain except in one-dimensional models. Another application[81] retained the nonlinear equations and represented the spatial dependence by a nodal approximation. Feasibility of the method was established in both cases by numerical calculations on simple models.

Dynamic programming has been employed to obtain a computing algorithm for the efficient determination of the appropriate control action from among a predetermined set of allowable control actions.[82] In this application, several decision intervals are defined and a given type of control action is used throughout a decision interval. (Many control actions of a given type occur in a decision interval.) Use of the dynamic programming algorithm minimizes the computations necessary to determine the sequence of control-action types in the different decision intervals and thus minimizes a performance index. This algorithm has been employed for three-dimensional calculations,[82] based on an adaptation of the 3DXT code,[43] and for two-dimensional calculations,[83] based on an adaptation of the XENOSC code.[37] In these applications the reactor models were sufficiently detailed to be realistic, and the shortcoming of the method resulted from the necessity of limiting the number of decision intervals and the number of allowable control-action types in each decision interval to obtain reasonable computation times.

SUMMARY

Xenon-induced spatial power oscillations must be considered in the design and operation of large light-water-moderated and -cooled nuclear reactors.[84] PWR's in the 1000-MW(e) class may be intrinsically unstable with respect to axial oscillations and require specific remedial control action to limit spatial power tilting and to suppress diverging power oscillations. BWR's of this size, although probably intrinsically stable because of their large negative power coefficient, may require remedial control action to limit spatial power tilting; however, inlet-flow control seems to result in a highly damped transient. Studies performed to date indicate that such remedial control action is feasible and that, by monitoring the power and/or temperature distribution within an operating reactor and taking appropriate control action, even intrinsically unstable reactors may be reliably operated. Such has been the experience with the large heavy-water moderated and -cooled production reactors. However, load-following requirements make the control of a reactor operating on a utility grid considerably more complicated than is the case for a production reactor. Also, the instrumentation employed to infer the neutron and xenon distributions is much more substantial for production reactors than is presently envisioned for PWR's.

Methods of analysis fall into two general categories—stability analyses and (digital or analog) simulation. Stability analyses, as the name implies, are concerned with the prediction of thresholds for diverging spatial power oscillations in terms of parameters related to the core size, composition, power level, and spatial power distribution. Linear stability analyses have been useful in predicting stability trends with changes in core parameters. When the analysis is based on a sufficiently detailed representation of the core

and when the parameters are computed from appropriate spatial averages or the spatial dependence is treated explicitly, linear stability analyses have yielded predictions in good quantitative agreement with digital simulations and with experiment. The major shortcoming of such analyses is the failure to appropriately represent the control action that would be employed in maintaining criticality. Although stability analyses provide useful information about the influence of design parameters on core stability, the designer must also have quantitative information about the nature of xenon-induced spatial power oscillations and about the influence of various remedial control actions on such oscillations. Digital or analog simulation is required for obtaining such information.

Simulations of xenon-induced spatial power oscillations must represent: (1) the neutron-flux distribution, (2) xenon and iodine distributions, (3) coolant density and void distributions, (4) control-rod location and movement, (5) soluble-poison concentration (if it changes), (6) material zoning, (7) fuel temperature, and (8) nonlinear effects such as the heat flux and flow dependence of subcooled boiling, the Doppler temperature dependence, and the steam-void dependence of the rod and Doppler worths and of the microscopic xenon cross section. Control action employed to maintain criticality during load following or to suppress spatial power oscillations (e.g., changes in rod location, coolant flow, or temperature) must be represented explicitly. Prompt-neutron dynamics, delayed neutrons, the time lag associated with heat transfer from fuel to coolant, and coolant-loop circulation delays all may be neglected because their time scales are much shorter than the time scale of the Xe–I dynamics. Fuel-burnup effects may be ignored during the course of a transient because of their much longer time scale, but simulations at different stages of burnup are necessary because of changes in composition, thermal-flux level, xenon cross section, xenon and iodine yields, power coefficient, etc.

Standard neutron-diffusion codes, employing a finite-difference few-group representation, have been modified to permit simulation of xenon-induced spatial power oscillations. Because of analytical and experimental evidence that control-rod motion and nonlinear feedback effects couple oscillations associated with different spatial dimensions, it appears that multidimensional simulations are required, at least in some cases. Computing times for two- and three-dimensional simulations are measured in hours and tens-of-hours, respectively, using the standard codes, even with a coarse spatial mesh description. Three-dimensional nodal models, which can be normalized to the standard codes, have been developed. These nodal codes are much faster than the standard codes and appear to be sufficiently accurate, when properly normalized. More work needs to be done on comparing the nodal codes with the standard codes and in comparing both with experiment. Also, more work is required to establish under what conditions it is permissible to assume spatial separability and perform simulations on lower dimensional models. Analog models are hard pressed to represent the core with enough spatial detail to allow an accurate simulation.

Relatively little quantitative comparison of analytical methods with experiment has been done, primarily because of the paucity of experimental results. Data are available on planar oscillations in the Shippingport PWR and on planar and axial oscillations in one of the Savannah River HWR's, although the difficulties associated with constructing an appropriate calculational model are nonnegligible. Confidence in calculational methods could be enhanced considerably if xenon-induced spatial power oscillation experiments were performed in future reactors, preferably early in life when the composition is well known.

Recent studies have confirmed and extended earlier results on stability trends and have accentuated the importance of accounting explicitly for the control system when analyzing the stability or transient behavior of a core. In general, stability is decreased by: (1) increasing the core size, (2) increasing the thermal-neutron-flux (hence power) level, (3) increasing the flatness of the thermal-neutron-flux distribution, (4) decreasing the magnitude of the negative power coefficient, (5) reducing the neutron-migration length, and (6) going to fuel mixtures with larger iodine yields and with a smaller Xe–I yield ratio. Increasing the magnitude of the negative power coefficient appears always to be stabilizing for planar oscillations but may be destabilizing for axial oscillations under certain conditions.

For sufficiently high thermal-neutron-flux levels and for sufficiently large negative power coefficients, increasing the power level could be stabilizing for planar oscillations, but the contrary will be true in most cases presently being considered. In BWR's the large negative power coefficient associated with coolant voids is the predominant stabilizing feedback mechanism, whereas Doppler feedback appears to be somewhat more important than the moderator feedback in inhibiting oscillations in PWR's. Cores that are intrinsically stable may sustain diverging xenon-induced spatial power oscillations, driven by the

control system employed to maintain criticality. Conversely, intrinsically unstable cores may be operated with only limited spatial power oscillations if the appropriate remedial control action is taken.

Studies have demonstrated that axial oscillations can be suppressed by chasing the power peak with part-length control rods, whereas planar oscillations can be controlled with full-length rods, if the gross core power distribution is known. This type control scheme, which seems to be favored for PWR's, is similar to that successfully employed in the heavy-water production reactors at Savannah River. Selecting a generally applicable control procedure which is not too complicated and does not involve adverse economic consequences requires more work. The essence of the problem is to be able to interpret the core power distribution unambiguously from detector responses and to predict the transient response to a given control action, under a variety of temperature, fuel cycle, and load-following conditions. This problem undoubtedly will receive increasing analytical and experimental attention in the future, particularly for PWR's, for which the problem is more important. When the ability to interpret detector responses and to simulate transient response has been adequately developed and verified, recent applications of optimal control theory may be extended to assist in the selection of the most satisfactory control procedure.

REFERENCES

1. R. L. Crowther, Xenon Considerations in the Design of Large Boiling Water Reactors, Report APED-5640, General Electric Company, Atomic Power Equipment Department, 1968.
2. D. Randall and D. S. St. John, Xenon Spatial Oscillations, *Nucleonics*, **16:** 82 (1958); also *Nucl. Sci. Eng.*, **14:** 204 (1962).
3. J. V. Wilson, Xenon Instabilities, *Nucl. Safety*, **5**(4): 345 (Summer 1964).
4. G. C. Fullmer, Xenon Instability in Graphite Reactors, USAEC Report HW-69084, Hanford Atomic Products Operation, 1961.
5. J. G. Tyror, Instability and Control in Large GCRS, *Nucl. Power*, **4**(38): (1959).
6. A. G. Ward, The Problem of Flux Instability in Large Power Reactors, Canadian Report AECL-345, 1956.
7. A. F. Henry and J. D. Germann, Oscillations in the Power Distribution Within a Reactor, *Nucl. Sci. Eng.*, **2:** 469 (1957).
8. R. M. Pearce, Xenon Oscillations in Finite Reactors, *Nucl. Sci. Eng.*, **16:** 336 (1963).
9. D. R. Harris and P. S. Lacy, A Simple Approximate Test for Spatial Xenon Stability, *Trans. Amer. Nucl. Soc.*, **3**(2): 437 (November 1960).
10. J. C. Stewart, A Generalized Criterion for Xenon Instability, USAEC Report KAPL-M-JS-4, Knolls Atomic Power Laboratory, 1958.
11. R. S. Wick, Space- and Time-Dependent Flux Oscillations (and Instability) in Thermal Reactors Due to Nonuniform Formation and Depletion of Xenon, USAEC Report WAPD-TM-138, Westinghouse Electric Corp., Bettis Atomic Power Laboratory, 1958.
12. R. M. Pearce, Method of Studying Xenon Spatial Instability with an Analog Computer, *Nucl. Sci. Eng.*, **11:** 328 (1961).
13. H. J. Kamack, Large Heavy-Water Moderated Power Reactors, USAEC Report DP-899, p. 80, Savannah River Laboratory, 1964.
14. J. Chernick, The Dynamics of a Xenon Controlled Reactor, *Nucl. Sci. Eng.*, **8:** 233-243 (1960).
15. J. Chernick, G. Lellouche, and W. Wollman, The Effect of Temperature on Xenon Instability, *Nucl. Sci. Eng.*, **10:** 120 (1961).
16. G. S. Lellouche, Control of Xenon Spatial Oscillations, USAEC Report BNL-6330, Brookhaven National Laboratory, 1962.
17. S. Kaplan, Modal Analysis of Xenon Stability, in Naval Reactors Physics Handbook, A. Radkowsky (Ed.), USAEC Report TID-7030, Vol. I, pp. 977-1010, Superintendent of Documents, U. S. Government Printing Office, Washington, 1964; see also The Property of Finality and the Analysis of Problems in Reactor Space–Time Kinetics by Various Modal Expansions, *Nucl. Sci. Eng.*, **9:** 357 (1961).
18. W. M. Stacey, Jr., *Space–Time Nuclear Reactor Kinetics*, Chap. 5, Academic Press Inc., New York, 1969.
19. T. R. England, G. L. Hartfield, and R. K. Deremer, Xenon Spatial Stability in Large Seed–Blanket Reactors, USAEC Report WAPD-TM-606, Westinghouse Electric Corp., Bettis Atomic Power Laboratory, 1967; see also *Trans. Amer. Nucl. Soc.*, **10**(1): 255 (June 1967).
20. T. R. England, Analysis of Xenon Power Oscillations in Shippingport PWR Core 1, USAEC Report WAPD-TM-605, Westinghouse Electric Corp., Bettis Atomic Power Laboratory, 1969; see also *Trans. Amer. Nucl. Soc.*, **7**(2): 220 (November 1964).
21. R. L. Ewen, Calculation of Complex Natural Modes for Spatial Xenon Oscillations and Comparison with a Simple Approximation, USAEC Report WAPD-T-1459, Westinghouse Electric Corp., Bettis Atomic Power Laboratory, 1962; see also *Trans. Amer. Nucl. Soc.*, **5**(1): 179 (June 1962).
22. S. Kaplan and J. B. Yasinsky, Natural Modes of the Xenon Problem with Flow Feedback—An Example, *Nucl. Sci. Eng.*, **25:** 430 (1966).
23. G. S. Lellouche, On the Location of Higher Spatial Harmonic Stability Criteria, USAEC Report BNL-13053, Brookhaven National Laboratory, 1968.
24. R. L. Ewen, MULE—A FORTRAN Program for the Calculation of Three Types of Overtone Modes, USAEC Report WAPD-TM-369, Westinghouse Electric Corp., Bettis Atomic Power Laboratory, 1963.
25. W. M. Stacey, Jr., Linear Analysis of Xenon Spatial Oscillations, *Nucl. Sci. Eng.*, **30:** 448 (1967).
26. R. J. Hooper, R. A. Rydin, and W. M. Stacey, Jr., Verification of a Xenon Spatial Stability Criterion, *Nucl. Sci. Eng.*, **34:** 344 (1968).

27. C. G. Poncelet and A. M. Christie, Xenon-Induced Spatial Instabilities in Large Pressurized Water Reactors, USAEC Report WCAP-3680-20, Westinghouse Electric Corp., Atomic Power Division, 1968; see also *Trans. Amer. Nucl. Soc.*, **10**(2): 571 (November 1967).
28. P. L. Roggenkamp, Xenon Control at Savannah River, USAEC Report DP-MS-68-27, Savannah River Laboratory, 1968.
29. G. S. Lellouche, Space-Dependent Xenon Oscillations, *Nucl. Sci. Eng.*, **12:** 482 (1962).
30. G. L. Gyorey, The Effect of Modal Interaction in the Xenon Stability Problem, *Nucl. Sci. Eng.*, **13:** 338 (1962).
31. J. Canosa and H. Brooks, Xenon-Induced Oscillations, *Nucl. Sci. Eng.*, **26:** 237 (1966).
32. S. G. Margolis and S. Kaplan, Nonlinear Effects on Spatial Power Distribution and Oscillations with Xenon Reactivity Feedback, USAEC Report WAPD-BT-21, Westinghouse Electric Corp., Bettis Atomic Power Laboratory, 1961; see also *Trans. Amer. Nucl. Soc.*, **3**(2): 183 (November 1960); see also Naval Reactors Physics Handbook, USAEC Report TID-7030, Vol. I, p. 1001, Superintendent of Documents, U. S. Government Printing Office, Washington, 1964.
33. W. M. Stacey, Jr., A Nonlinear Xenon Stability Criterion for a Spatially Dependent Reactor Model, *Nucl. Sci. Eng.*, **35:** 395 (1969).
34. W. E. Kastenberg, A Stability Criterion for Space-Dependent Nuclear-Reactor Systems with Variable Temperature Feedback, *Nucl. Sci. Eng.*, **37:** 19 (1969).
35. C. N. Kelber, L. C. Just, and N. F. Morehouse, Jr., The Solution of Many Region Reactor Kinetics Problems on an Analog Computer, *Nucl. Sci. Eng.*, **11:** 285 (1961).
36. K. J. Chock, S. Kaplan, S. G. Margolis, and C. M. Lane, Analog Studies of Xenon Oscillations; The Effect of Coolant Recirculation on Spatial Stability, USAEC Report WAPD-T-1781, Westinghouse Electric Corp., Bettis Atomic Power Laboratory, 1965; see also *Trans. Amer. Nucl. Soc.*, **8**(1): (June 1965).
37. R. M. Pearce and R. E. Roth, A G-20 Program for Studying Xenon Spatial Oscillations and Applications to CANDU, Canadian Report AECL-1803, 1963.
38. S. Henley and R. Margan, Turbo—A Two-Dimensional Few-Group Depletion Code for the IBM-7090, USAEC Report WCAP-6059, Westinghouse Electric Corp., Atomic Power Division.
39. W. R. Cadwell, PDQ-7 Reference Manual, USAEC Report WAPD-TM-678, Westinghouse Electric Corp., Bettis Atomic Power Laboratory, 1967.
40. J. V. Wilson, User's Manual for MAPLE SYRUP, Report ORNL-TM-2471, Oak Ridge National Laboratory (to be published).
41. H. A. Hassan, Babcock & Wilcox Co., personal communication, 1970.
42. F. B. Skogen and A. M. McFarlane, Xenon-Induced Spatial Instabilities in Three-Dimensions, USAEC Report WCAP-3680-22, Westinghouse Electric Corp., Atomic Power Division, 1969.
43. W. M. Stacey, Jr., Space–Time Reactor Kinetics Development at KAPL, in Proceedings of the Conference on Industrial Needs and Academic Research in Reactor Kinetics, USAEC Report BNL-50117, Brookhaven National Laboratory, 1968; see also *Trans. Amer. Nucl. Soc.*, **11**(1): 226 (June 1968).
44. R. Kern, W. C. Coppersmith, and Z. R. Rosztoczy, Three-Dimensional Method for Design Studies of Xenon Induced Spatial Oscillations, *Trans. Amer. Nucl. Soc.*, **12**(1): 239 (June 1969).
45. R. Kern, D. C. Wright, W. C. Coppersmith, and Z. R. Rosztoczy, CEXE—A Three-Dimensional Nodal Method for the Analysis of Xenon Oscillations and Control, USAEC Report CEND-3932-1, Combustion Engineering, Inc., 1969.
46. B. H. Cherry, P. Buck, and A. D. Krumbein, Analysis of Xenon Transients in Large Pressurized Water Reactors with the XENOLUX Program, *Trans. Amer. Nucl. Soc.*, **12**(1): 299 (June 1969); also, personal communication from P. Buck, United Nuclear Corp., 1970.
47. W. Shinoda and S. Mitake, A Three-Dimensional Analysis of Xenon Induced Oscillations in Boiling Water Cooled Reactors, *Nucl. Sci. Eng.*, **36:** 372 (1969); see also FILE-6, A Three-Dimensional Xenon Dynamics Code, Japanese Report JAERI-Memo-3023, 1968.
48. R. R. Lee, Combustion Engineering, Inc., personal communication, 1970.
49. S. Kaplan, Synthesis Methods in Reactor Analysis, *Advan. Nucl. Sci. Technol.*, **3:** 233 (1965).
50. E. L. Wachspress, Variational Methods and Neutron Flux Synthesis, in Proceedings of Conference on the Effective Use of Computers in the Nuclear Industry, April 21–23, 1969, Knoxville, Tenn., USAEC Report CONF-690401, p. 271, 1969.
51. J. W. Stewart and J. C. Robinson, A Modal Synthesis Solution of the Xenon Transient Problem, *Trans. Amer. Nucl. Soc.*, **12**(2): 760 (November 1969); also, paper submitted to *Nucl. Sci. Eng.*
52. B. Davison, Correction for Non-Zero Time Step in the Numerical Simulation of Spatial Oscillations of Xenon in a Nuclear Reactor, Canadian Report AECL-1292, 1961.
53. W. M. Barss, Digital Simulation of Xenon Instability in Reactors, Canadian Report AECL-1226, 1961.
54. R. R. Lee, Multidimensional Effects in the Analysis of Xenon Spatial Stability, *Trans. Amer. Nucl. Soc.*, **12**(2): 760 (November 1969).
55. Westinghouse Electric Corp., Bettis Atomic Power Laboratory, Pressurized Water Reactor (PWR) Project, Technical Progress Reports, USAEC Report WAPD-MRP Series.
56. Westinghouse Electric Corp., Bettis Atomic Power Laboratory, Pressurized Water Reactor (PWR) Project, Technical Progress Report for the Period June 24, 1962, to August 23, 1962, USAEC Report WAPD-MRP-99, 1962.
57. D. Rawle, V. Rajagopal, C. G. Poncelet, R. J. Johnson, and J. R. Himmelwright, Spatial Xenon Stability Measurements on the Connecticut Yankee Reactor, *Trans. Amer. Nucl. Soc.*, **12**(2): 766 (November 1969).
58. C. G. Poncelet and A. M. Christie, Space-Dependent Reactor Transfer Function and Spatial Stability, *Trans. Amer. Nucl. Soc.*, **12**(2): 764 (November 1969).
59. R. L. Crowther, N. Eickelpasch, and R. A. Hanvelt, Spatial Xenon Tests in the Gundremmingen Reactor, presented at Conference on Reactor Operating Experience, San Juan, P. R., 1969.
60. R. L Crowther, General Electric Company, personal communication, 1970.
61. W. E. Graves, Experience with Xenon Oscillations, *Trans. Amer. Nucl. Soc.*, **12**(2): 644 (November 1969).

62. S. V. Topp and R. P. Germann, Xenon Oscillation Experiments in a Production Reactor, *Trans. Amer. Nucl. Soc.*, **12**(2): 765 (November 1969); paper of same title submitted to *Nucl. Sci. Eng.*
63. W. E. Graves, Savannah River Laboratory, personal communication, 1970.
64. R. L. Crowther, D. L. Fischer, R. O. Niemi, and J. E. Wood, Reactor Kinetic Effects of Significance to Large Boiling Water Reactor Design and Operation, in Proceedings of the Brookhaven Conference on Industrial Needs and Academic Research in Reactor Kinetics, USAEC Report BNL-50117, Brookhaven National Laboratory, 1968.
65. C. G. Poncelet, Solution of Multigroup Space–Time Diffusion Equations, in Proceedings of the International Conference on Reactor Mathematics and Computations, Mexico City, 1967.
66. R. Kern, M. Bonaca, Z. R. Rosztoczy, and W. C. Coppersmith, Xenon Oscillation Studies for the Pickering Reactor, USAEC Report CEND-3932-2, Combustion Engineering, Inc., 1969.
67. R. L. Crowther, Non-Linear Xenon Effects in Boiling Water Reactors, *Trans. Amer. Nucl. Soc.*, **11**(2): 570 (November 1968).
68. L. E. Strawbridge, E. C. Allard, and C. P. Bhalla, Xenon-Induced Core Instabilities, USAEC Report WCAP-3269-48, Westinghouse Electric Corp., Atomic Power Division, 1965.
69. Westinghouse Electric Corp., Atomic Power Division, Control of Xenon Instabilities in Large PWR's, USAEC Reports WCAP-3680-1 to WCAP-3680-10 (1966–1969).
70. S. G. Margolis, Operator Induced Xenon Oscillation, USAEC Report WAPD-BT-29, Westinghouse Electric Corp., Bettis Atomic Power Laboratory, 1963; see also *Trans. Amer. Nucl. Soc.*, **7**(1): 220 (June 1964).
71. J. N. Grace, Recent Progress in Reactor Kinetics at the Bettis Laboratory, in *Reactor Kinetics and Control*, Tucson, Ariz., March 25–27, 1964, Lynn E. Weaver (Coordinator), AEC Symposium Series, No. 2 (TID-7662), 1964.
72. W. Shimoda and S. Mitake, Three-Dimensional Dynamic Behavior of a Reactor Zonal Control, *Trans. Amer. Nucl. Soc.*, **12**(2): 761 (November 1969).
73. P. K. Doshi, F. R. Poetschat, H. A. Hassan, and W. A. Wittkopf, Simulated Three-Dimensional Control of Xenon Oscillations, *Trans. Amer. Nucl. Soc.*, **12**(2): 763 (November 1969).
74. R. F. Barry, Westinghouse Electric Corp., personal communication, 1970.
75. F. B. Skogen and A. F. McFarlane, Control Procedures for Xenon-Induced X-Y Instabilities in Large Pressurized Water Reactors, USAEC Report WCAP-3680-21, Westinghouse Electric Corp., Nuclear Energy Systems, 1969.
76. A. M. Christie et al., Control of Xenon Instabilities in Large Pressurized Water Reactors, USAEC Report WCAP-3680-23, Westinghouse Electric Corp., Atomic Power Division, 1969.
77. A. M. Christie and C. G. Poncelet, Optimal Control of Xenon Oscillations, *Trans. Amer. Nucl. Soc.*, **12**(2): 764 (November 1969).
78. O. A. Trojan, Analysis of Spatial Flux Control in Heavy-Water Reactors, *Trans. Amer. Nucl. Soc.*, **11**(2): 571 (November 1968).
79. D. M. Wiberg, Optimal Control of Nuclear Reactor Systems, *Advan. Contr. Syst.*, **5**: 301 (1967).
80. D. M. Wiberg, Controllability of the Spatial Flux Shape, *Nucl. Sci. Eng.*, **27**: 600 (1967).
81. W. M. Stacey, Jr., Control of Xenon Spatial Oscillations, *Nucl. Sci. Eng.*, **38**: 229 (1969).
82. W. M. Stacey, Jr., Optimal Control of Xenon-Power Spatial Transients, *Nucl. Sci. Eng.*, **33**: 162 (1968).
83. W. I. Neef, Galahad: Code for Optimizing Control of Xenon Transients with Dynamic Programming, USAEC Report GA-9166, Gulf General Atomic Incorporated, 1969.
84. P. S. Lacy and E. D. Kendrick, Xenon-Transient Calculations in Large Light-Water Reactors, *Reactor Fuel-Process. Technol.*, **12**(1): 10 (Winter 1968–1969).

The Emergency Core-Cooling Problem in LMFBR's

By Ira Charak*

Abstract: *The problems associated with emergency core-cooling systems (ECCS's) in liquid-metal-cooled fast breeder reactors (LMFBR's), including the requirement to keep the core submerged at all times, are generally discussed. Specific observations are made on solutions incorporated in all the major existing fast reactors. On the basis of claims made by the designers, design criteria for the respective ECCS's are inferred. It is concluded that emergency core cooling by natural convection is more feasible in loop-type LMFBR's than in pool-type LMFBR's. However, the requirement that the core remain submerged for a variety of assumed violations of the coolant boundary is felt to be more easily fulfilled in a pool-type LMFBR.*

INTRODUCTION

General Remarks

The liquid-metal-cooled fast breeder reactor (LMFBR) is currently receiving the greatest worldwide attention of any single power-reactor concept in the development stage. This is especially true in the United States, where the total USAEC operating-expense budget request for high-gain breeder reactors in fiscal year 1969 was $90.6 million, of which $82 million was earmarked for the LMFBR program.[1]

The total USAEC program for the orderly development of the LMFBR concept to the point where it is commercially acceptable is contained in the LMFBR Program Plan.[2] One of the earliest Program Plan tasks undertaken was the performance of 1000-MW(e) LMFBR design studies by five contractors. These studies were to be a continuation and extension of the four 1000-MW(e) design studies completed in 1964.[3-6] Argonne National Laboratory (ANL) was assigned the responsibility of managing these five contracts and performing the necessary technical evaluations of the work. Preliminary plant descriptions of each of the five designs were presented at the 1968 International Conference on Sodium Technology and Large Fast Reactor Design.[7]

Evaluations of the five reference concepts revealed a great variability in philosophy and design in connection with the emergency core-cooling systems (ECCS's) provided by each of the contractors to cope with different kinds of normal and abnormal plant operations. This realization stimulated an interest in reviewing the ECCS's for those LMFBR's for which sufficient information was available in the open literature. The purpose of this paper, therefore, is twofold: (1) to compile information on, and critically review, LMFBR ECCS designs currently in use, including the means provided for preventing uncovering of the core, and (2) to summarize the design criteria for those LMFBR ECCS's.

The subject of ECCS's for water reactors has been extensively treated;[8,9] however, it may be instructive to examine some of the conditions associated with emergency cooling of an LMFBR core. Conditions to be considered are unique compared with those related to emergency cooling of a water-reactor core. First, the specific power of a typical LMFBR commercial design could be 10 times that of a typical light-water reactor. This means that a loss of coolant in an LMFBR leading to fuel-element insulation, or vapor blanketing, will result in a rate-of-rise of fuel temperature for the LMFBR approximately 10 times that for the water reactor, assuming the same fuel specific heat in both reactors and no scram.

*Reactor Analysis and Safety Division, Argonne National Laboratory, Argonne, Ill.

Another factor that disallows uncovering the LMFBR core is that the temperature margin between operating and melting conditions is much lower for the LMFBR cladding than for the water-reactor cladding. One reason for this is that the normal cladding operating temperature in an LMFBR is much higher than in water reactors; typically, the cladding temperature is about 1100–1300°F for the LMFBR compared with about 600–700°F for the water reactor. Also, the usual stainless-steel cladding of the LMFBR has a much lower melting point than the Zircaloy cladding of modern water reactors.

As far as the consequences of fuel melting in the LMFBR are concerned, the molten fuel has the potential to reassemble in a supercritical array. This stems from the fact that the fuel in an LMFBR is not normally arranged in its most reactive configuration. Gross melting and slumping of fuel can result in significant reactivity insertions and thermal-energy release and lead to significant damage to the reactor-vessel internals and perhaps to major structural components as well. The melting and rearranging of water-reactor fuel, on the other hand, generally will result in a subcritical array, particularly with a loss of coolant from the fuel region.

A final consideration is the fact that LMFBR's will contain large amounts of plutonium as the fissile material. Siting of an LMFBR may well be governed by the plutonium release following a core meltdown rather than by the dose to the thyroid resulting from the release of radioactive iodine, as is usually the case for modern water reactors. This is because the fission-product iodine inventory in a core depends on operating power. Hence an accident in a water reactor leading to iodine release will have essentially the same consequences to the thyroid as an accident in an LMFBR, all other things being equal. This factor, combined with the high toxicity of plutonium, could easily result in larger exclusion areas and low-population zones[10] for the LMFBR than for the uranium-fueled water reactor.

As a result of the preceding considerations, it is a normal design criterion that an LMFBR core be always submerged in sodium during any likely accident situation. Aside from the immediate question of core damage that would result from its becoming uncovered, the large sodium-cooled LMFBR's generally possess a positive coolant-void reactivity effect.[11] Thus a serious accident involving a loss of coolant from the core could be aggravated by positive reactivity feedbacks.

The preceding general introductory remarks are intended to lead into a specific discussion of the ECCS's for LMFBR's, including considerations of core uncovering. This paper will not address the question of ultimate decay-heat removal which might be employed to protect the containment from a molten-fuel melt-through accident (the so-called *China Syndrome*). Although it is believed that this is a potentially important issue, there has been so little design and engineering effort expended on this subject (particularly for LMFBR's) that no meaningful survey can be performed at this time.

As the water-reactor industry has settled on two basic concepts, i.e., the pressurized-water and boiling-water reactors, apparently now LMFBR purchasers will also have a choice between two basic concepts. These are the piped, or loop, concept and the submerged, or pool, concept.

The Loop Concept

The loop concept is typified by the Enrico Fermi Atomic Power Plant (EFAPP),[12] located near Detroit, Mich. (see Fig. 1). This concept is analogous to current water-reactor arrangements wherein the primary coolant is transported in loops external to the reactor vessel. Although a doubly contained vessel or a minimum-volume vault can guard against a reactor-vessel leak, this type of reactor plant usually requires some device(s), either active or passive, to prevent the siphoning of sodium from the reactor vessel through a spectrum of assumed pipe breaks external to the vessel. The major safety-related advantage of this concept relative to the pool concept is that loop elevations can be more easily made high enough to allow natural-convection emergency core cooling following a complete loss of electric power. Another advantage, although one of questionable importance at this time, is that safety-associated instrumentation may be easier to install and maintain in a loop system than in a pool system.

The Pool Concept

The pool concept is exemplified by the Experimental Breeder Reactor II (EBR-II) (Ref. 13) which is located at the National Reactor Testing Station in Idaho (see Fig. 2). This concept is characterized by the fact that the core, primary pumps, primary piping, and intermediate heat exchangers are submerged in a single tank containing the entire primary sodium inventory. The concept offers assurance that loss of primary sodium from the core and primary system is virtually incredible because all major primary sodium piping is contained within the primary tank that operates at

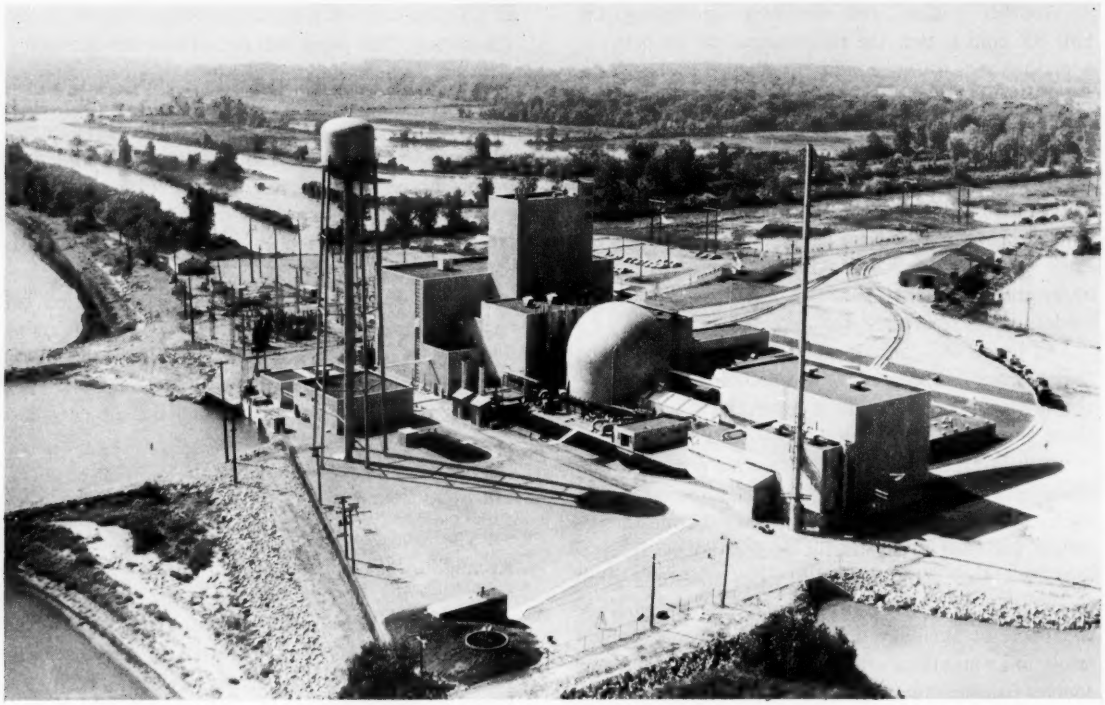

Fig. 1 Aerial view of Enrico Fermi Atomic Power Plant.

rather modest conditions of temperature and pressure. There are no subsurface penetrations of the tank wall. A second tank, or alternatively, a minimum-volume vault, is provided around the primary tank to contain any sodium leakage that might occur. This feature serves to limit to an acceptable level any loss of sodium from a primary tank leak.

An advantage of the relatively big sodium volume is the large heat sink it provides in emergency situations, e.g., if all normal heat dumps become temporarily inoperative. Also, reactor inlet-temperature transients are minimized owing to the large temperature-dilution effect of the sodium pool.

A final advantage of the large sodium reservoir, and one which will very likely be exploited in the future, is the possibility that after-heat removal might be greatly simplified, in the remote event that the core should melt through its container. The presence of sodium between the container and the cavity surrounding the primary tank, together with an appropriate core-debris collector, might solve the *China Syndrome* problem for LMFBR's. Now, of course, this potential advantage is purely conjectural.

SURVEY OF LMFBR ECCS's

Although there have been many LMFBR designs proposed in recent years (Ref. 7), in general, those designs have not progressed enough to permit a meaningful evaluation of ECCS's for those systems at this time. So the following survey of LMFBR ECCS's will be limited, with one exception, to those reactors which are in operation or nearly so.

Loop-Type LMFBR's

SEFOR.[14,15] *General Description.* The construction of the Southwest Experimental Fast Oxide Reactor (SEFOR) by the General Electric Company near Fayetteville, Ark., is complete. The main features of SEFOR relating to emergency core cooling are shown schematically in Figs. 3 and 4. The reactor primary sodium coolant loops consist of a Main Primary Loop (MPL) and an elevated Auxiliary Primary Loop (APL). The reactor vessel has a second wall, known as the safety vessel, below the MPL nozzles, so that two walls would have to fail to drain sodium from the vessel below that elevation.

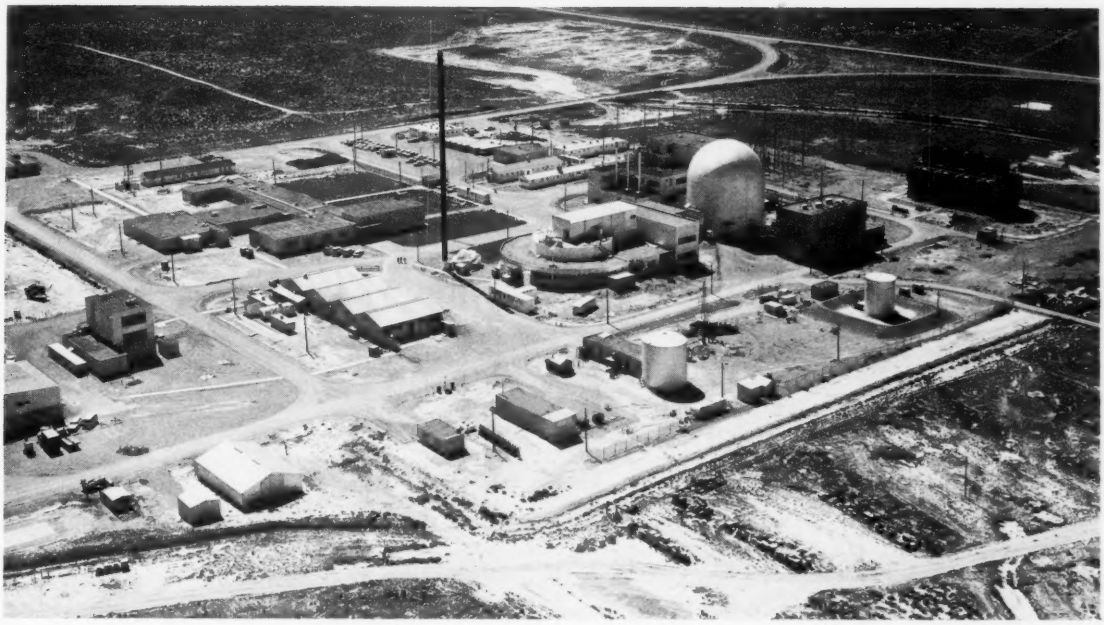

Fig. 2 Aerial view of EBR-II.

The MPL is a single piped loop with an elevated intermediate heat exchanger (IHX) to permit natural circulation of the primary sodium in the event of a loss of site electric power. One of the objectives of the APL is[14]

> Using force-circulated sodium the system must be capable of removing the decay heat in the nuclear fuel and core structure and rejecting it to the atmosphere. It must be capable of accomplishing the decay heat removal while sodium is leaking from the main primary loop and a loss of off-site power has occurred.

Both the MPL and APL consist of single-wall piping and components.

The APL is designed to remove 5% [1 MW(t)] of the design reactor power at normal coolant temperatures, but an increase in reactor outlet temperature would result in increasing the APL capacity to 12½% [2.5 MW(t)] of the reactor power. A siphon breaker and a vacuum breaker are provided in the reactor vessel to assure core cooling after a break in the MPL piping. A check valve is located in the APL reactor inlet line inside the reactor vessel to prevent the MPL pump from emptying the MPL through a break in that line.

Emergency Operation. For this reactor, emergency operation is defined here as operation arising out of a loss of primary sodium from the system. The intended operation of the SEFOR ECCS can be summarized as follows: In the event of a leak in the MPL, the sodium level in the reactor vessel will not drop below the APL reactor-vessel outlet nozzle, so that the APL remains full of sodium and can operate to remove the decay heat. In the event of a leak in the APL, the sodium level in the reactor vessel will not drop below the minimum level required to assure that the MPL reactor-vessel outlet nozzle remains submerged and that therefore the MPL can be used to remove decay heat. The ECCS operation will now be examined in detail, although qualitatively.

(1) MPL Break. If the MPL reactor-vessel outlet pipe should break at a low elevation, sodium in the reactor vessel will siphon through the outlet pipe until cover gas enters the MPL outlet nozzle and breaks the siphoning action. As can be seen from Fig. 4, the flow pattern is such that the level will drop initially to at least elevation 42.75 in., or 5.75 in. above the bottom of the APL outlet nozzle. How much lower than 42.75 in. the level drops is a function of the inertia of the fluid. In turn, this is dependent upon the break size and location, the initial cover-gas pressure, and the method of operation of the cover-gas system following the pressure reduction inside the reactor vessel caused by the sodium level change. Due to the elevation of the

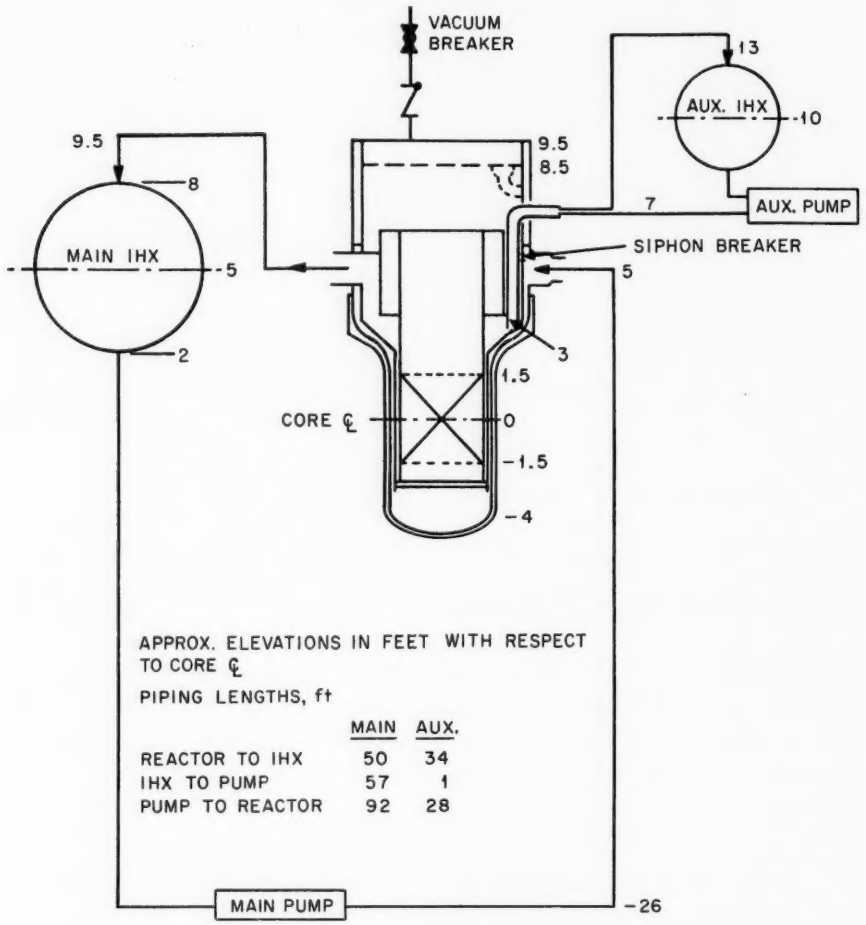

Fig. 3 Relative elevations (in feet) of SEFOR cooling system. (From Ref. 14.)

main IHX, the final level may be higher than 42.75 in., depending on whether or not any sodium remains in the riser to the IHX after flow stops. Uncovering the APL outlet nozzle would result in a complete loss of emergency core cooling due to the eventual draining of the APL.

While the MPL outlet pipe is draining, the MPL pump will continue to pump until it becomes gas-bound owing either to cavitation resulting from insufficient net positive suction head (NPSH) or simply to drawing gas into the pump suction. (The SEFOR pump is of the electromagnetic type, but the type of pump does not affect the above-mentioned conclusion.) Since there is no check valve in the MPL inlet line, the sodium therein eventually will drain out through the break and increase the speed at which the sodium level in the reactor vessel falls. This postulated leak, therefore, is essentially equivalent to a double-ended pipe failure.

A siphon breaker is provided between the reactor-vessel inlet and outlet plenums, so that siphoning action through the inlet piping (which could uncover the core) can be interrupted by cover-gas flow into the inlet nozzle through the siphon breaker. This siphon breaker is merely a hole through which sodium will bypass the core during normal operation. The size of the hole is dependent on the same factors mentioned above for determining the final level in the reactor-vessel outlet plenum. General Electric claims the siphon breaker will function for a 20-in.^{2} hole in the MPL pump-discharge line. This break area is equivalent to about one-fifth of the cross-sectional area of the

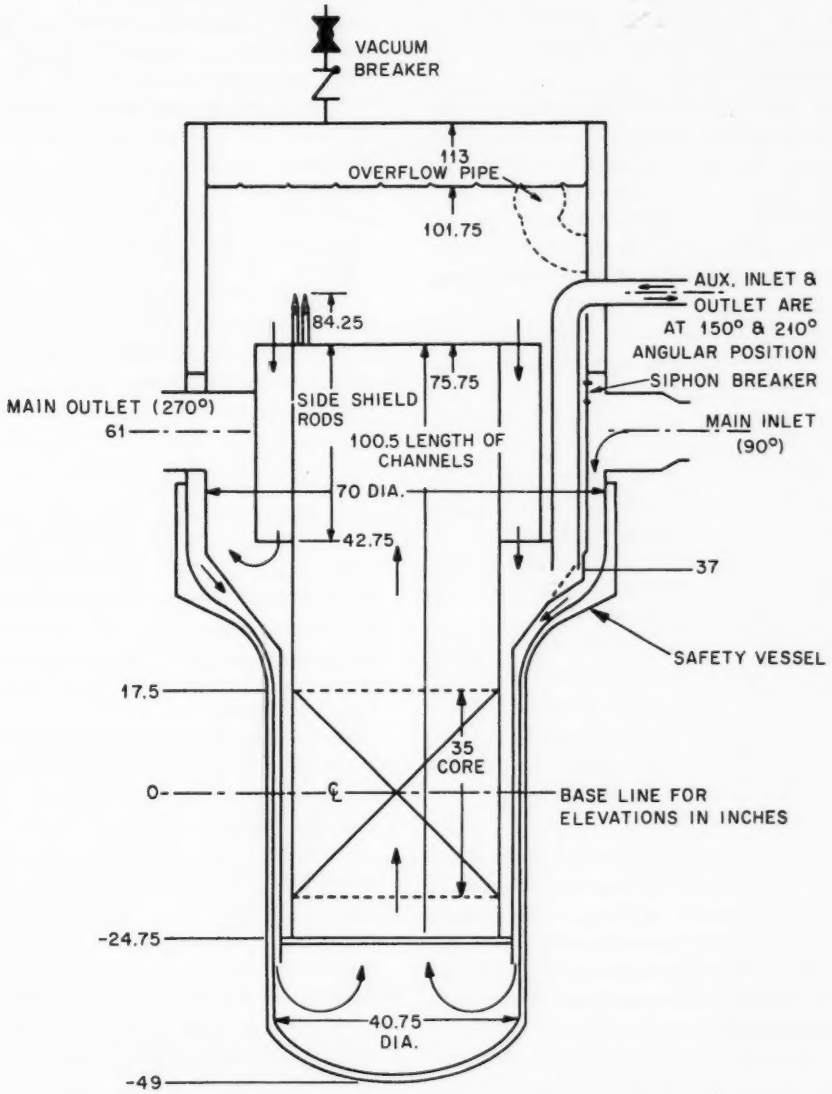

Fig. 4 SEFOR reactor-vessel elevations, inches. (From Ref. 14.)

MPL piping and is almost seven times the area of the largest service-system line connecting to the MPL. To assure that a sufficient gas volume is available to break the siphon action, General Electric has provided a vacuum breaker in the reactor-vessel head. The breaker opens when the reactor-vessel cover-gas pressure drops to below atmospheric, thereby admitting argon to the vessel from the refueling cell above.

It should be noted that after siphoning action has been interrupted in the MPL, some means must be provided to ensure communication between the outlet plenum and the inside of the core barrel and subassemblies. If such provision is not made, it would be impossible to provide sodium flow through the APL because of elevation requirements. Specifically, sodium would have to be lifted to elevation 75.75 in. (after the sodium lost has been replaced to that elevation), and this action would simply result in reverse flow of the sodium through the core and out the MPL inlet nozzle. In the interim period, before sodium is added to the

reactor vessel, the APL would very likely have been emptied. General Electric does not describe the provisions to cope with this situation.

If the MPL inlet pipe should break, sodium would be siphoned backward through the inlet line after flow reversal occurred, and the action would be similar to that described above for the outlet pipe break. The only significant difference is that the MPL pump would tend to drain the outlet line much faster than gravity alone. The same general considerations of sodium level and siphon-breaker action apply, however.

The functioning of the APL is guaranteed by assuring that, for some size MPL pipe break, the APL outlet nozzle remains submerged. Further, since this design features a pumped and elevated APL loop, assurance must be provided that the APL pump will have a sufficient NPSH during the accidents for which the APL is intended to furnish emergency core cooling. In the SEFOR design the APL can remove only about 100 kW with natural-convection flow; hence pump operation appears to be essential for this class of accident if fuel damage is to be prevented.

A desirable (though not necessarily required) feature of the SEFOR APL claimed by General Electric is that the APL is operating under normal reactor conditions, but at a reduced flow rate because the APL pump head has to buck the MPL pump head. In this manner, no delay time is incurred following a break in the MPL piping in starting the APL.

(2) APL Break. A break at the lowest elevation of the APL outlet line upstream of the APL pump will result in the sodium level in the reactor vessel dropping, by gravity assisted by cover-gas expansion, to the elevation of the break. The level may drop further if the cover-gas pressure is above atmospheric at the time the level reaches the break elevation.

If the cover-gas system tries to maintain a positive pressure in the reactor vessel, then the gas pressure could conceivably continue to lower the level below the MPL outlet nozzle. This lowering would disable the MPL and would eventually adversely affect the cooling of the core.* The MPL could be reactivated at some later time if an emergency sodium supply were available to replace the sodium lost during the accident. This situation, however, is not discussed by General Electric in the literature.

A break in the APL inlet line between the reactor vessel and the APL pump discharge is potentially more severe than the outlet line break because the APL might continue to pump the sodium in the reactor-vessel outlet plenum out through the break, and the MPL pump could pump sodium backward through the APL inlet line and out the break. These possibilities considered by General Electric are minimized by including an APL pump trip in the reactor safety system and a check valve in the APL inlet pipe part located within the reactor vessel.

SEFOR ECCS Design Criteria. On the basis of the preceding discussion, the criteria which, we feel, should be applied to a SEFOR-type ECCS can be listed. (Actual criteria employed by General Electric in the SEFOR design were not available when this was written.)

For a Break in the MPL:

1. The final sodium levels in the reactor vessel must be sufficiently high to prevent uncovering the APL outlet nozzle and the core. The final levels should be determined by considering the dynamic interaction of all systems, components, and other factors affecting the levels—such as the cover-gas system, siphon breaker, and vacuum breaker, as well as the assumed break size and location.

2. Communication must be provided between the outlet plenum and the inside of the subassemblies at the elevation of the outlet plenum after the sodium levels are stabilized.

3. The difference in elevation between the bottom of the MPL inlet nozzle and the final sodium level in the outlet plenum must be greater than the pressure drop through the core barrel under emergency operation so that sodium in the inlet plenum cannot be pumped out the MPL inlet nozzle by the APL pump.

4. Since it is impossible to provide any cover-gas pressure following an MPL break, the APL pump must operate reliably at its design point with a low suction pressure. If the APL pump is electromagnetic, as in the SEFOR design, collapse of the pump tube must be considered.

5. If system analysis shows that APL operation is desirable (or required) during normal reactor operation, the APL pump characteristic for such operation must be such that the pump characteristic during emergencies is not compromised.

For a Break in the APL:

1. Drainage of the primary sodium through the APL break must be limited so that the MPL remains full. It must be shown that the cover-gas system does not tend to keep the gas pressure constant following an

*According to Ref. 14, the cover-gas pressure might be as high as 20 psig.

APL break, or else the entire outlet plenum above the APL outlet could be emptied by the gas pressure.

2. The APL check valve should be located as close to the reactor vessel as possible, preferably inside the vessel.

For a Break in the Reactor Vessel:

1. If the safety vessel is not completely welded to the reactor vessel, the APL and MPL pump heads must not be high enough to force sodium out any opening between the reactor vessel and safety vessel.

2. If the safety vessel is completely welded to the reactor vessel so that a free sodium level forms in the annulus between the vessels with compression of the gas in the annulus, the reactor vessel should be designed to withstand the maximum (transient) collapsing pressure that obtains when the MPL pump is tripped.

Fermi.*[12,16] *General Description.* The following paragraph is an excerpt from a monthly report on the Enrico Fermi Atomic Power Plant by Power Reactor Development Company:

> The Enrico Fermi Atomic Power Plant is located about 30 miles southwest of Detroit, at Lagoona Beach, Frenchtown Township, Monroe County, Michigan. The reactor, which is a sodium cooled fast breeder reactor using uranium 10 w/o molybdenum fuel was brought to criticality for the first time on August 23, 1963. Operations at power levels less than one megawatt (thermal) were conducted from August 23, 1963 to December 28, 1965, during which period an extensive series of nuclear tests was completed. On December 29, 1965 the first step was taken in a series of tests at increasingly higher power levels intended to lead to eventual operation at the 200 megawatt (thermal) design level of the present core. On October 5, 1966, the reactor was shut down after damage occurred to one or more fuel subassemblies.

Emergency core cooling takes place through the same three main primary- and secondary-system loops used for normal power operation. No additional smaller capacity loop has been provided. To prevent loss of primary coolant, hence loss of core submergence, the entire primary piping system is secondarily contained, as shown in Figs. 5 and 6. Containment of the reactor vessel is provided by a surrounding tank, termed the primary shield tank (PST) because it also contains graphite in the annulus outside the reactor vessel as a neutron shield. The PST is sealed at the coolant-loop pipe penetrations by bellows. The top of the tank extends above the maximum sodium level and is sealed from the below-floor nitrogen atmosphere. The primary-system hot-leg piping is contained by chrome–molybdenum concentric piping that connects with carbon-steel containment enclosures for the IHX's and pump tanks. The primary-system cold-leg piping is contained by carbon-steel concentric piping. The containment piping was installed in halves, and all welds were dye-penetrant checked. The annuli of the secondary containment communicate freely with the vault atmosphere that is nitrogen.

Additional protection against loss-of-core submergence is afforded by siphon breakers (Figs. 5 and 6) connected to the high point of each pump discharge pipe. This is considered necessary since the piping connects to the reactor vessel at a point lower than the core, and some portions of the piping loop external to the shield tank are also lower than the core elevation. However, it should be noted that the siphon breakers can be considered backup safety devices since siphoning of sodium from the core would occur only if both a primary coolant pipe and its containment piping rupture at the same time. Sodium level and leak detection are provided at various places, and level detection is considered the principal means for determining leakage of sodium. The Fermi reports do not specify the magnitude of leak for which the siphon breakers provide protection.

The primary sodium pumps remain in operation at full speed unless loss of electric power occurs. Natural circulation of the primary sodium was found to be inadequate to cope with a loss-of-power accident. The primary and secondary heat-transport systems are capable of removing decay heat in this emergency by utilizing pony motors on each pump. The pony motor on one primary and secondary loop is supplied by a d-c bus, and the remaining pony motors are supplied by the 120-V a-c essential (emergency) bus.

Primary-coolant-system operation will be explained here briefly to aid further discussion of emergency cooling. Each of the Fermi primary pumps sits in a tank and takes suction as a sump pump. Sodium is pumped through the reactor core and flows by gravity from the reactor vessel through 30-in.-diameter pipes to and through the IHX's and finally back to the pump tank. Figure 5 shows this arrangement and the relative component elevations.

Emergency Operation. Any breach of the primary system and the accompanying sodium leakage necessitates emergency operation, and the location and size of the break determine the severity of the accident and the necessary mode of emergency operation. An

*The material in this section was researched by D. E. Lutz of ANL.

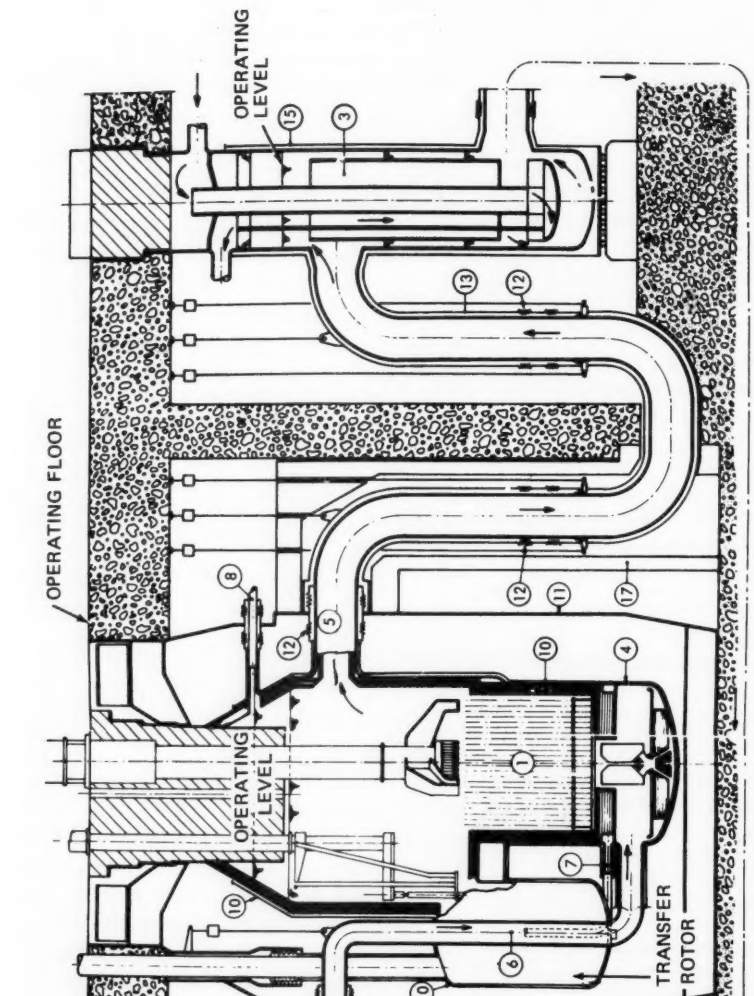

Fig. 5 Fermi primary-sodium-system elevations. (From Ref. 16.)

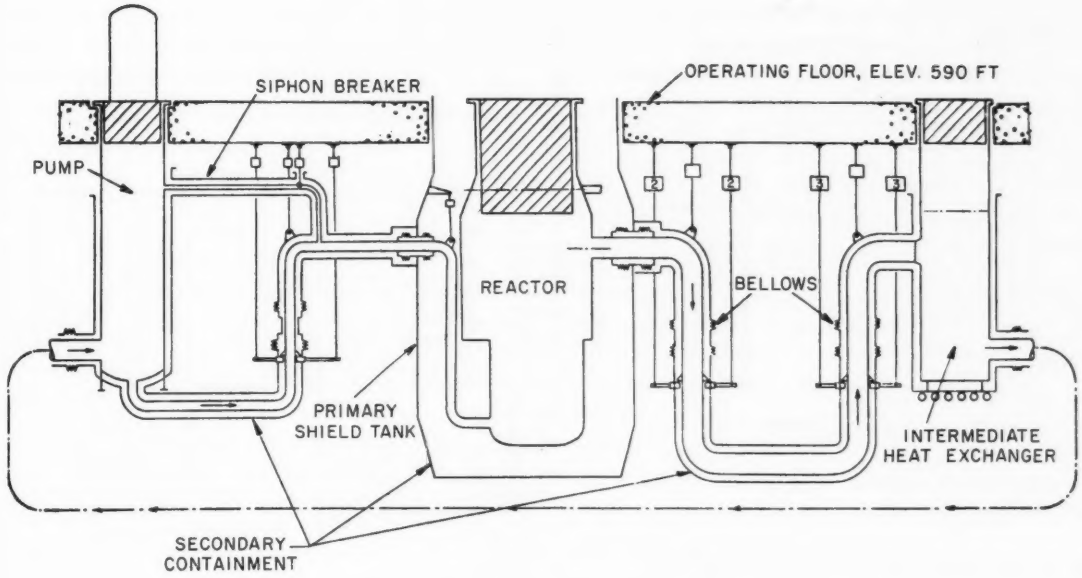

Fig. 6 Secondary containment of Fermi primary sodium system. (From Ref. 12.)

overriding concern is to prevent loss of coolant to the extent that the sodium level drops below the reactor-vessel sodium outlet nozzles, thereby preventing coolant circulation. For the Fermi plant, the critical sodium level required for circulation is arbitrarily defined as the center of the 30-in. outlet nozzles. A qualitative examination of the system vessel or pipe breaks at various locations follows:

(1) Reactor-Vessel or Outlet Piping Break Inside the PST. If a break occurs inside the PST (downstream of the core), sodium drains from the system and begins to fill the tank. The break is more serious if it occurs at or below the main coolant outlet nozzles because the PST free volume is large compared with the volume of sodium in the system above the critical sodium level. (The volume of the annuli between the primary piping and its containment is small compared with that same sodium volume.) Such a break would result in uncovering the nozzles if additional sodium were not supplied. Because of this a rather elaborate reserve sodium supply system has been provided.

The reserve sodium supply is held by the overflow and storage tanks. The system is actuated by level indicators in the reactor, pump tanks, and overflow tank, as shown in Fig. 7. The storage-tank lines are kept heated, and the tank is pressurized to permit the immediate transfer of sodium to the overflow tank when necessary. Sodium leaking into the PST is detected by leak detectors in the tank and by low-level indicators in the reactor vessel and pump tanks. The operators are then apprised of the situation and can shut down the reactor and start the overflow pumps, if they are not already running. If the leak is severe enough, the various system levels drop to a preselected elevation where the overflow pumps are automatically started. If the overflow-tank sodium is insufficient in volume to restore the system level to the critical level, a low-level alarm in the overflow tank opens the valve in the storage-tank supply line. The makeup sodium is added to the system through an IHX. During this time, sodium continues to circulate in the primary and secondary systems, and core decay heat is rejected to the steam plant.

(2) Reactor-Vessel Outlet Piping Break Outside the PST. A single pipe or tank break in this region appears to be less severe than a break inside the PST since makeup sodium would either not be required or would be quite modest owing to the small volume of the secondary-containment annulus. Also, since flow in this leg is by gravity, sodium cannot be forced out the top of the secondary containment.

(3) Primary-Pump Discharge Piping Break Inside the PST. If a break occurs in the pump discharge piping located inside the PST, the consequences, in terms of

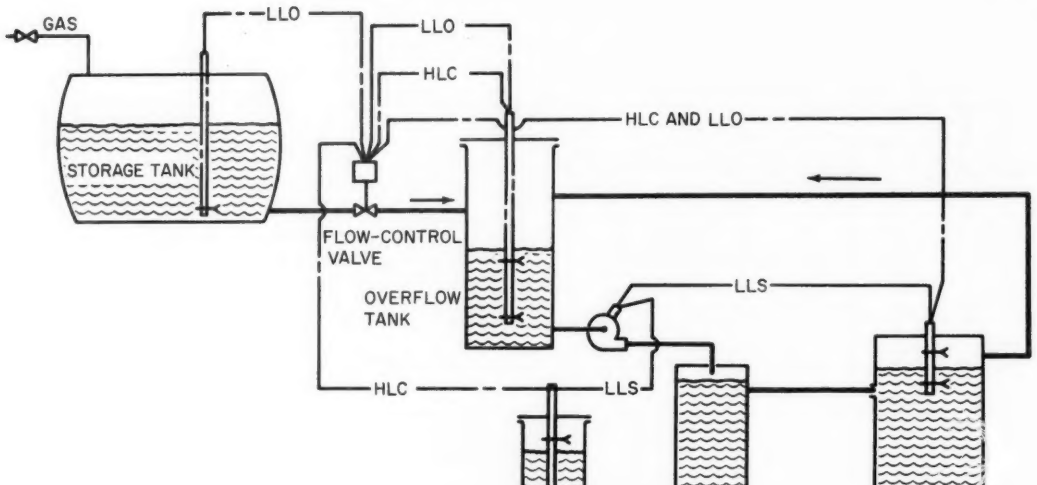

Fig. 7 Fermi reserve sodium supply system. (From Ref. 16.)

the sodium level change in the reactor vessel, are qualitatively similar to those given in (1) above. One major difference, however, should be noted. Since the three primary loops operate in parallel and have a common point at the reactor inlet plenum, an inlet line break will result in all three pumps tending to pump sodium out the break. As a result, the coolant flow through the core will be short-circuited. Assuming that the reserve sodium supply system can restore sodium to the critical level before primary-loop circulation is adversely effected, the pumping power may be provided by either the main motors or the pony motors. Detailed analysis is required to determine the best method of pump operation to cope with this accident.

(4) Primary-Pump Discharge Piping Break Outside the PST. In this case the sodium leakage is contained by the secondary containment. As in case (2) above, the small volume of the secondary-containment annulus results in a minimum makeup of sodium.

It should be noted that the secondary containment is open at the upper end approximately 23 ft from the bottom of the pump tank. This requires the primary pumps to be operated at low flow during this emergency since the full-flow discharge head of over 300 ft would cause sodium to flow rapidly out of the secondary containment at the top, and this would drain the system to the extent that circulation could not take place. As a result, the main pump motors must be tripped as soon as possible after the onset of this accident. Core cooling can then be done by circulating sodium through the primary and secondary systems under power of the pony motors.

(5) Simultaneous Break in Primary-Pump Discharge Piping and Its Secondary Containment. As noted above, the siphon breakers installed in the Fermi primary system are considered backup safety devices since they would not be required unless one would want to provide protection against a simultaneous failure of the primary-pump discharge piping and its containment piping. In this case it is considered essential to stop the siphoning of sodium backward through the core by introducing gas at the high (low-pressure) point of the siphon. The siphon breaker in the Fermi plant is simply a sodium bypass around the primary pump. As the sodium level drops in the primary piping, blanket gas from the pump tank, and ultimately from the inert-gas supply system, is introduced into the main sodium piping. This action is supposed to stop the sodium flow before the core is uncovered. However, it is important to note that, unless the normal means of circulating sodium are available, core damage is expected to occur even if the core remains covered with sodium.[12] Hence, for this accident, the best that can be hoped for is a time delay

before extensive damage occurs to the core. As noted above, the size of the simultaneous break for which the siphon breakers are effective has not been specified.

(6) Simultaneous Break in Reactor-Vessel Outlet Piping and Its Secondary Containment. For this accident, siphon breakers are not required since sodium flow out the break would terminate when the outlet nozzles become uncovered. Reverse flow through the inlet piping is prevented by check valves in each primary pump. Even if the check valves leak, the siphon breakers will act to stop any backflow through the primary-pump discharge piping. Again, as in case (5) above, core damage will likely result following this accident.

Fermi ECCS Design Criteria. On the basis of the above discussion, the criteria which, we feel, should be applied to a Fermi-type ECCS will be listed. (Firsthand knowledge of all the actual criteria employed in this design is not available at this writing.)

For a Break in the Reactor Vessel or Outlet Piping Inside the PST:

1. The final sodium level in the PST should not be allowed to drop below the critical level to allow sodium to flow over the tube-bundle shroud of the IHX. This shroud is shown in Fig. 5. This criterion requires that the level in the PST be maintained slightly higher than the reactor-vessel outlet nozzles by the addition of makeup sodium.

2. The rate at which makeup sodium is added to the system and the makeup requirements depend upon the location and magnitude of the leak as well as the PST free volume. The makeup sodium system must be activated soon enough after the break, and sodium addition must be rapid enough, to avoid disrupting coolant circulation.

3. The PST must be designed to withstand the temperature transient caused by the leaking sodium and makeup sodium.

For a Break in the Reactor-Vessel Outlet Piping Outside the PST:

1. The secondary containment must be designed to withstand a one-event thermal transient arising from a hot-sodium leak.

2. The space inside the guard piping must be small enough to keep the sodium level inside the reactor vessel above the sodium outlet nozzles.

For a Break in the Primary-Pump Discharge Piping Inside the PST:

1. The primary pumps must be shut down and placed on pony-motor operation; or, alternatively, the PST must withstand the full-flow pump discharge pressure, and the seal at the top of the PST must be maintained. This latter approach would be required to preserve the function of the PST as a secondary containment and simultaneously force-cool the core. If this philosophy is employed, the makeup-sodium-system volume must be increased over that required to simply achieve the critical level on a static basis; or the primary pumps could drain the outlet piping and simply fill the PST with sodium.

2. If pony-motor operation of the primary pumps is employed, the pump characteristic under these conditions must take account of the sodium levels and gas pressures in both the reactor vessel and PST.

For a Break in the Primary-Pump Discharge Piping Outside the PST:

1. The secondary containment must be designed to withstand a one-event thermal transient arising from a hot-sodium leak.

2. The space inside the guard piping must be small enough to keep the sodium level inside the reactor vessel above the sodium outlet nozzles.

3. The primary pump must be shut down and placed on pony-motor drive immediately to prevent pumping sodium over the top of the secondary containment.

4. The pump head developed under pony-motor operation must be less than that required to pump sodium over the top of the secondary containment.

For a Simultaneous Break in the Primary-Pump Discharge Piping and Its Secondary Containment:

1. The breaks must be defined in sufficient detail to permit siphon-breaker design.

2. Sufficient blanket-gas supply must be ensured to guarantee siphon-breaker functioning.

For a Simultaneous Break in Reactor-Vessel Outlet Piping and Its Secondary Containment:

Either the primary-pump check valves must not leak sodium, or the siphon breakers must be designed to cope with this accident as well as case (5) above.

BN-350.[17,18] *General Description.* The Russian reactor BN-350 is a 1000-MW(t) LMFBR that has the dual purpose of producing electricity and fresh water. It is now under construction and "completion of the facility and plant startup are scheduled for 1968–69."[17]

The heat-transport system is shown in Fig. 8. Heat is removed in five of six identical circuits (one circuit is on standby). Each circuit consists of a sodium-to-sodium IHX and a sodium-heated steam generator. The

reactor vessel and part of the primary piping are surrounded by a second wall, with the interspace filled with argon. Gate valves are located at the juncture of the double-walled pipe and the single-walled pipe that comprises the remainder of the primary loop. The volume of the argon-filled interspace is such that a leak in the inner pipe (or reactor vessel) would not lead to an unacceptable change in sodium level in the vessel or primary equipment.

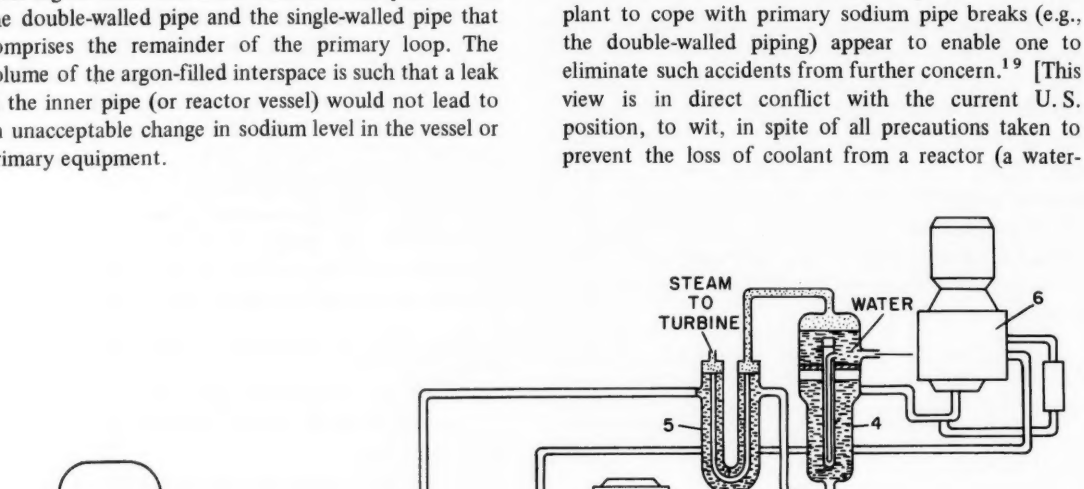

Fig. 8 The BN-350 primary sodium system. (Redrawn from Ref. 19.)

The design is such that the sodium volume change following reactor scram is not so great that the reactor outlet nozzles are uncovered. This ensures that flow can be maintained following a scram. Natural circulation of the primary sodium is enhanced by elevating the IHX with respect to the core and by orienting the IHX in a horizontal plane so that the relative elevations of core and IHX do not change under transient conditions.

Emergency Operation. Since there is no system in the BN-350 plant that can be identified as an ECCS, the primary loops will be considered as the ECCS in abnormal situations. The Russians consider the worst emergency for this reactor (and for their other fast reactors as well) to be a loss of pumping power. Although it is argued that pipe failures cannot be dismissed from consideration, the provisions in the plant to cope with primary sodium pipe breaks (e.g., the double-walled piping) appear to enable one to eliminate such accidents from further concern.[19] [This view is in direct conflict with the current U. S. position, to wit, in spite of all precautions taken to prevent the loss of coolant from a reactor (a water-cooled one as well as an LMFBR), the designer is usually required to consider the consequences of such an accident and therefore to provide containment, to protect the public.]

Analysis of the loss-of-power accident uncovered two problems:[18] (1) during the transition to natural-circulation flow (neglecting inertia of rotating equipment), reactor cooling was inadequate and would lead initially to unacceptably high sodium temperatures; and (2) using the joint inertia of the pump and its power supply to extend the flow coastdown time resulted in rapid system overcooling and excessive thermal stresses in the outlet piping and IHX. Subsequent calculations indicated that the pump inertia

alone would be adequate to prolong the flow coastdown enough to prevent excessive temperatures and that, at the same time, thermal stresses in components would be reduced to insignificant levels. Hence the power supply is disconnected from the pump on loss of electric power. The ultimate flow by natural circulation is about 5 to 6% of normal,[18] which seems more than adequate for long-term heat removal by this mechanism.

The details of emergency operation following a break in a single-walled primary-system component are not discussed. However, it is obvious that the BN-350 must rely on shutoff valve operation to stem the flow of sodium out of a break by isolating the faulty loop. Since each of the six primary loops is contained in its own hermetically sealed, nitrogen-filled cubicle, the faulty loop probably can be readily identified.

From Fig. 8, there is apparently no backup to the shutoff valve in the outlet line. The check valve in the inlet line may be considered a backup for the shutoff valve in that line. The functional requirements of the shutoff valves are not given in the literature.

BN-350 ECCS Design Criteria. If one places reliance on a double-walled system to prevent the loss of sodium from the system (as is apparently done in the BN-350 design), then one must address the question of failure in a single-walled component and the subsequent ECCS operation. In the case of the BN-350 design, we feel the following criteria should apply:

1. The shutoff-valve functional requirements should be delineated in detail. As a minimum, it must be shown that sodium lost from the system from the time of the break inception until the valve is completely shut is not enough to lower the level in the vessel to the point that continued cooling cannot be guaranteed.

2. In view of the fact that the shutoff valves cannot be tested at will without disrupting the reactor operation, it is essential that some means of assuring valve operation under emergency conditions be provided. This criterion might be satisfied, e.g., by an extensive preoperational testing program in which the probability of valve failure can be obtained with good statistics and can be shown to be acceptably small.

3. It must be shown that under no circumstances can the shutoff valves in each primary loop be closed simultaneously.

4. A backup to the outlet shutoff valve should be provided. This backup should be totally independent (i.e., mechanically, electrically, pneumatically) of the first valve.

5. Since the sixth loop is stagnant during reactor operation, its startup (inadvertent or intentional) must be examined from the standpoint of thermal-shocking the reactor vessel, core support, etc.

BOR.[18,19] *General Description.* The BOR is a 60-MW(t) reactor designed as a test bed for the development of high-performance fuels for the future large [>1000 MW(e)] Russian LMFBR's. A schematic drawing of the BOR cooling systems is shown in Fig. 9. Two equal-capacity [30 MW(t)] cooling circuits are used for normal power operation. Each circuit consists of a primary sodium loop, a secondary sodium loop, and a water–steam loop. Each water–steam loop uses a different type of steam generator—one loop has a once-through type and the other a natural-circulation type. An air-blast heat exchanger can be connected to either secondary sodium loop to dissipate up to 30 MW(t) with the respective steam generator out of service.

The natural-circulation steam generator is provided with an emergency cooling condenser for heat dissipation under loss-of-power conditions. The required auxiliaries as well as the primary sodium pumps are furnished with an emergency d-c battery power supply.

The considerations of pipe failure previously discussed for the BN-350 reactor apply equally to the BOR. One difference appears to be the elimination of the check valve in the reactor inlet line in favor of a second gate valve. There is still only one valve in the outlet line.

Emergency Operation. As previously noted, the loss-of-power accident is considered the worst accident for which active protective measures must be provided. Unlike the BN-350, the system layout precludes adequate natural-circulation flow of primary sodium in a loss-of-power accident. It was therefore necessary to provide a battery backup for emergency operation of the primary pumps. (One may infer that the pumps are provided with d-c pony motors.) The batteries are sized for 1 hr of pump operation at 25% rated speed (presumably also 25% rated flow). Since natural circulation can remove 2½% of the nominal reactor power, 1 hr of battery operation should be more than adequate to provide sufficient core cooling before natural circulation can be safely employed.

Under conditions of loss of power, the ultimate heat sink is the cooling water for the emergency cooling condenser (see Fig. 9). This condenser is provided in the natural-circulation steam-generator loop, which has a greater water holdup than the once-through steam generator. Since the once-through

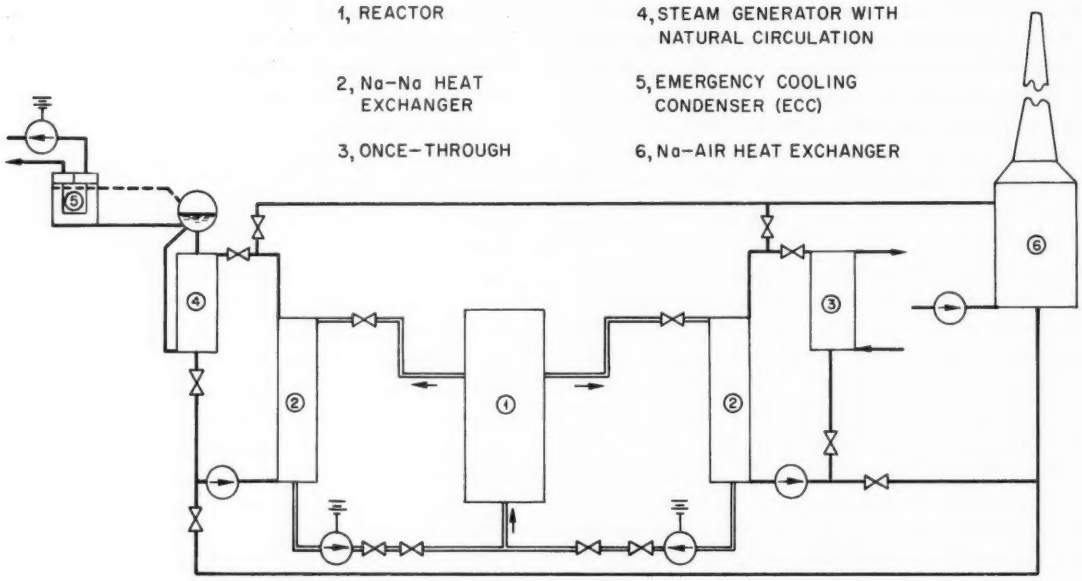

Fig. 9 The BOR primary sodium system. (Redrawn from Ref. 19.)

steam generator is dried out during the power outage, that cooling circuit is not a part of the ECCS. Both the cooling-water pump and the recirculating-water pump are powered by the emergency batteries. If power is not restored before the batteries are spent, the air-blast heat exchanger is connected to one of the secondary sodium loops and the reactor decay heat can be dumped to the atmosphere by natural circulation of both sodium loops and the air loop.

BOR ECCS Design Criteria:

1. With respect to the question of pipe breaks, Criteria 1 through 4 for the BN-350 reactor apply to the BOR as well.

2. Since the BOR ECCS depends for its operation upon actuation of valves, the probability and consequences of malfunctioning of any of those valves should be considered in the system design.

3. Since there is normally no sodium flow through the air-blast heat exchanger, it must be designed for appropriate thermal shocks under ECCS operation. Also, if the emergency cooling condenser is not on hot standby, it too must be designed with consideration of thermal stresses.

4. All emergency battery supplies to the vital equipment of the ECCS must be designed to operate long enough to allow natural circulation to cool the core effectively. All systems must be designed to cope with the thermal transients that might accompany the transition from forced circulation using the battery supply to natural convection.

FARET.[20] *General Description.* The Fast Reactor Test Facility (FARET) was a 50-MW(t) sodium-cooled reactor designed as a test bed for commercial LMFBR fuel development and also as a facility in which fast reactor safety experiments could be performed in closed in-pile loops. The facility was designed by ANL with the assistance of the Bechtel Corp. as architect–engineer. Although the project was cancelled prior to start of construction, the detailed design and preliminary safety-analysis report (PSAR) had been completed, resulting in an extensive amount of information on emergency core-cooling problems and their intended solutions. Furthermore, the PSAR had been approved by regulatory groups, including the AEC's Division of Reactor Licensing (DRL) and the Advisory Committee on Reactor Safeguards (ACRS).

The essential features and hydraulic profile of the FARET cooling systems are shown in Fig. 10. Two cooling systems provided are: a Main Cooling System (MCS) and an Auxiliary Cooling System (ACS). The MCS dissipates up to 50 MW(t) and consists of a main primary sodium loop (MPL), a sodium-to-sodium IHX, a main secondary sodium loop, and a secondary sodium-to-air forced convection heat exchanger.

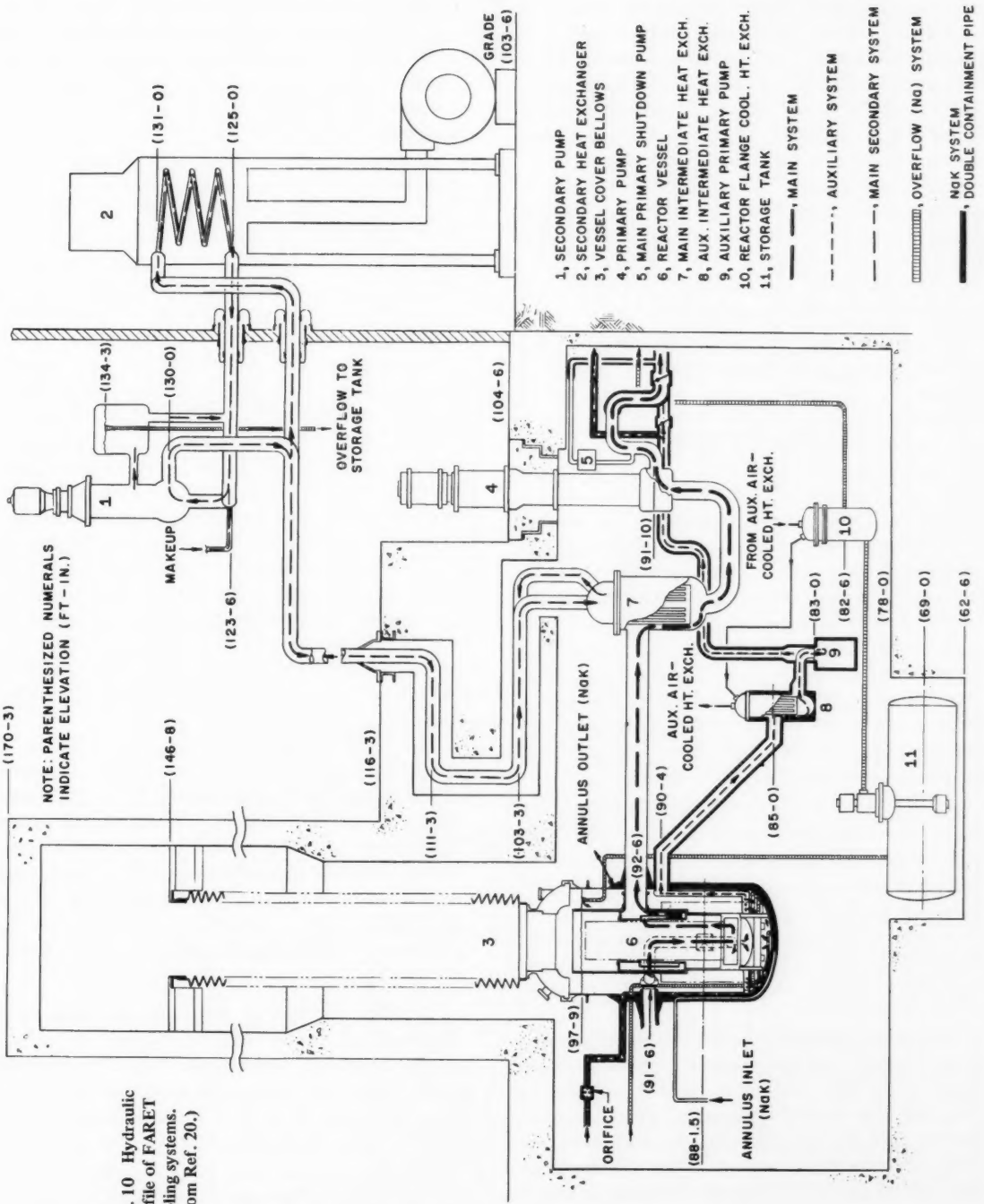

Fig. 10 Hydraulic profile of FARET cooling systems. (From Ref. 20.)

The ACS is designed to remove 1 MW(t) of decay heat under emergency conditions. The ACS consists of an auxiliary primary sodium loop (APL), a sodium-to-sodium IHX, a secondary sodium loop, and a secondary sodium-to-air natural-convection heat exchanger. The entire APL and all portions of the MPL common to the APL are surrounded by guard piping to prevent the loss of sodium in the event of a pipe or component rupture in those areas. The reactor vessel (Fig. 11) is also doubly contained. The annuli between the sodium piping and the guard system are all interconnected and filled with NaK. Leakage of primary sodium into the NaK annulus system (or vice versa) is detected as a level change in the NaK expansion tank.

The normal operating mode [50 MW(t)] of the cooling systems is as follows: Primary sodium is pumped by the main primary pump (4)* to the reactor-vessel inlet at elevation 91 ft 6 in. The flow is split and channeled into two downcomers that enter the high-pressure plenum inside the core support structure. A portion of the flow bypasses the core through the low-pressure plenum. The primary purpose of the bypass flow is to reduce the core outlet sodium temperature before the sodium leaves the vessel, so that high core temperatures can be achieved and the main sodium-containing systems can be designed for a substantially lower temperature. This bypass flow rejoins the core outlet flow in a mixing chamber (item 14 of Fig. 11) from which the sodium leaves the vessel at elevation 92 ft 6 in. and flows by gravity to the shell side of the IHX. The sodium then returns to the pump suction, and the cycle is repeated.

A main primary shutdown pump (5) is connected across the main-primary-pump discharge pipe. This pump is sized to provide enough flow to remove the decay heat after a loss of power to the main pump. The shutdown pump, always operating, is connected to a floating battery supply of enough capacity to provide forced circulation until natural-convection cooling in the MPL can be safely employed to remove decay heat.

Emergency Operation. Early in the FARET design, it was decided to provide a system to cope with a gross failure of the MPL resulting in a loss of coolant from that loop. The ACS is designed to remove the core decay heat in such an eventuality. As noted above, the entire APL is doubly contained so that a failure of the APL sodium pipe will not result in an excessive loss of primary sodium to the NaK annulus system, provided the main primary pump is tripped. Since all primary sodium piping systems (including the APL) are designed to resist large earthquake-induced loads, as well as all normal steady-state and transient forces, the likelihood of a simultaneous failure of both walls of a double-walled system is considered to be so low as to be dismissed from further consideration.

During normal [50 MW(t)] operation, the APL circulates a small amount of sodium through an orifice to the reactor vessel, bypassing the core. The APL electromagnetic pump head is too low to overcome the MPL pump head that closes the check valve in the APL. The bypass sodium flow results in the APL being constantly available on standby for emergency operation, with the sodium at elevated temperature to avoid thermal shocks. The APL pump has two separate voltage supplies; on standby operation low voltage is supplied to the pump. When APL full-flow operation is required, the winding is automatically energized by a high-voltage supply. As the MPL sodium flow diminishes and the APL flow accelerates, the APL check valve eventually opens, and the APL provides coolant to the core through the MPL inlet line. The sodium flows into the high-pressure plenum and through the core. From the mixing chamber the flow enters the core bypass region via the same holes through which the normal core bypass flow formerly entered the mixing chamber. The sodium then enters the ACS outlet line by means of a ring header located near the ACS outlet nozzle.†

The ACS is sized to remove only 1 MW(t) at normal temperatures because of the large heat capacity of the sodium in the core bypass region. The initial decay-heat load [~3 MW(t)] can be absorbed by the bypass sodium with a nominal temperature increase, thereby resulting in a substantial cost saving for the ACS.‡ The kinds of accidents that were considered in the FARET PSAR and actually protected against in the preliminary design are described in the following paragraphs.

(1) MPL Outlet Pipe Break. In the event of a massive failure of the MPL outlet pipe, the sodium level in the primary system would drop to the elevation of the bypass inlet holes in the outlet mixing chamber. The level cannot be lowered further since the mixing chamber will communicate with the cover gas as the

*Numbers in parentheses correspond to those in Fig. 10.

†The location of the header in Figs. 10 and 11 is shown at the bottom of the reactor vessel, but this is incorrect.

‡This feature would be unacceptable in a power reactor owing to the excessive outlet temperature degradation with no commensurate benefit.

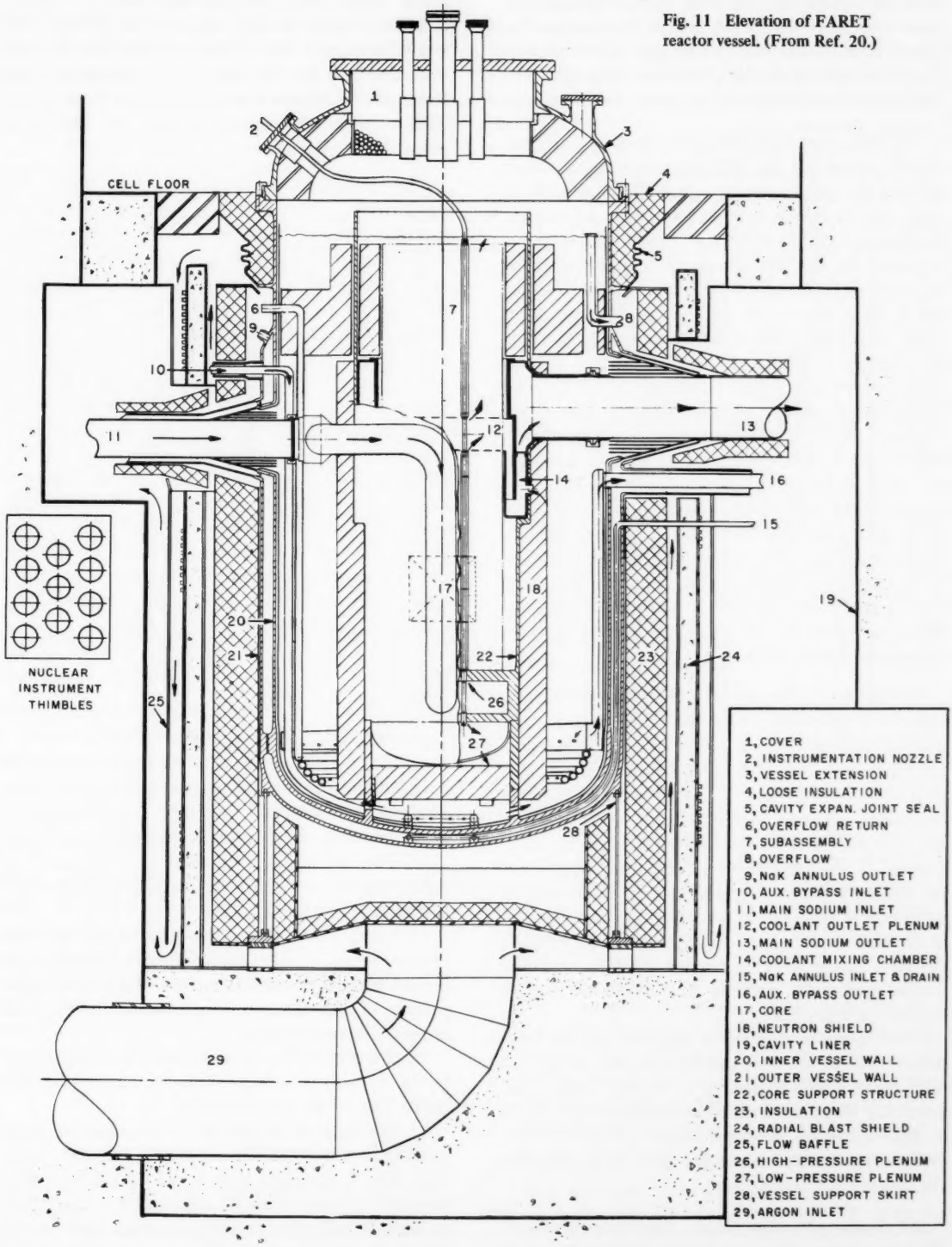

Fig. 11 Elevation of FARET reactor vessel. (From Ref. 20.)

holes are uncovered, and there is no other path for sodium to enter the outlet nozzle. Reverse (double-ended) flow through the broken pipe is prevented by the check valve in the MPL inlet line. The APL then functions as described above to remove the decay heat.

(2) MPL Inlet Line Break. A rupture in a single-walled portion of the MPL inlet line will result in draining the loop by means of the MPL pump until the outlet line is empty or the pump begins to cavitate. Siphoning of sodium backward through the inlet line is prevented by the MPL check valve. In addition, the minimum elevation of the MPL inlet (pump discharge) line is above the top of the core, so that even if the check valve were not to function, siphoning would proceed only until that minimum elevation is reached. (Note that the check valve is located entirely within a double-walled section of pipe. Hence a leak downstream of the valve is tantamount to a rupture of both pipes in the double-walled section.) The APL functions as described above to remove the decay heat. The portion of the MPL which is essential to the operation of the APL is entirely doubly contained, as previously noted; in addition, the MPL is itself doubly contained to an elevation above which the available APL pump head is insufficient to pump sodium, in the event the MPL check valve did not function to prevent backflow through the broken pipe.

(3) Doubly Contained MPL Inlet Line Break. This situation is much less severe than case (2) above since loss of sodium will be limited by the differential pressure between the MPL and the NaK annulus system at the point of the leak. Tripping of the MPL pump eventually will result in reversing the leakage, so that the flow will be from the NaK system into the MPL. Cooling of the core can be accomplished with either the MPL or APL since the pressure drop across the leak eventually is nullified by balancing the static pressure in the NaK annulus system against that in the MPL. (If the MPL pumps were not tripped, the MPL would be drained eventually, and the APL would be used to remove the decay heat.)

One safety precaution is required for this leak, however. Since the NaK guard piping will see the full MPL pump discharge pressure (~85 psig), there is the possibility that the reactor vessel would be subjected to a large collapsing pressure. Hence restrictions (i.e., orifices) are installed where the MPL guard pipe joins the vessel NaK annulus.

(4) Single APL Pipe Break. The consequences of this type of pipe failure are similar to those of case (3) above. A qualitative difference arises owing to the low pressure at which the APL operates. This low pressure results in either a flow of NaK into the APL or a low flow of sodium into the NaK system, depending on the leak location. Ultimate pressure balance between the APL and the NaK system allows core cooling to proceed as in (3) above.

(5) Flange-Cooling-System Inlet Pipe Break. The flange-cooling system (FCS) is provided essentially to furnish continuous purification of the primary sodium and to cool the hot sodium that rises inside the reactor vessel outside the core support cylinder. Sodium enters the FCS via an overflow in the reactor vessel and is returned to the vessel by a pump. The return sodium is piped to a header in the bottom of the vessel (see item 6, Fig. 11) from which point it joins the core bypass sodium. The header location would permit siphoning the vessel if the return line were broken at a low elevation or if the FCS pump were to stop pumping. Therefore a siphon breaker (not shown in Fig. 11) is installed at the high point of the inlet line near the cover-gas–sodium interface. This siphon breaker is simply a bypass through which a portion of the FCS return is pumped. If a rupture occurs in the return line, the sodium level in the vessel will drop until cover gas enters the siphon breaker and stops the backward flow. Core cooling is not affected by this pipe failure, unless the siphon breaker should not function.

FARET ECCS Design Criteria:

1. The double-walled ACS primary loop must be designed and built to the highest standards so that a simultaneous failure of both fluid containers due to any foreseeable event can be discounted as incredible.
2. The MPL check valve constitutes an engineered safety feature and must be reasonably tight under low-pressure conditions.
3. Means must be provided to ensure that the reactor vessel is not pressurized excessively from outside because of either a rupture of a double-walled portion of the MPL or a malfunction of the NaK annulus cover-gas system.
4. The FCS siphon breaker must be designed and tested to assure its functioning in the event of a malfunction in the FCS return line.
5. The ACS check valve must open under low-head conditions when ACS functioning is required. Since that valve is normally kept closed by the high MPL pressure, it must open to allow ACS sodium flow through the core. The possibility of check-valve bearing failure must be considered.

DFR.[21] *General Description.* The Dounreay Fast Reactor (DFR) is a 15-MW(e) [60-MW(t)]* LMFBR located in Northern Scotland. Although the DFR produces electricity, a main purpose is to provide a fast-neutron facility for the development of fast reactor fuels and structural materials. The DFR uses a 70/30 NaK alloy coolant instead of pure sodium to minimize potential operating problems arising from the high melting point of the latter. The cooling systems are by no means optimized since the emphasis was placed on using the limited liquid-metal technology existing in the United Kingdom in the early 1950's. As a result, the design employs twenty-four 4-in. primary coolant loops with no penetrations, e.g., for valves. Each primary loop contains an electromagnetic pump, again avoiding piping penetrations that would be required for mechanical pump shafts. The heat is dissipated to secondary NaK loops through 12 IHX's, each secondary loop taking flow from two primary loops. The secondary NaK then flows, in turn, through a superheater, evaporator, and preheater, thereby generating the required steam for the turbogenerator. A sketch of one primary coolant circuit is shown in Fig. 12.

The entire primary system is doubly contained. The reactor vessel is surrounded by a leak jacket, and all the primary piping is contained within a 6-in. guard pipe. The IHX's consist simply of coils of a pipe-within-a-pipe, with the primary sodium flowing through the inner pipe. The outer pipe then serves as the secondary containment for the primary sodium. Each primary pump operates inside a steel pressure vessel, which essentially provides double containment for the pump tube. The argon atmosphere inside the leak jackets is sealed from the vault atmosphere outside the leak jackets, and positive NaK containment is thereby assured in the event of a leak in the primary system. A recent leak in the DFR coolant system demonstrated the capability of the secondary containment to perform its intended function.[24]

A novel feature of the DFR is the downflow of coolant through the core. This scheme was selected for several reasons; however, the potential hazard during flow reversal following a complete loss of pumping power was also recognized by the designers.

Emergency Operation. The provision of leak jackets around all the primary coolant pipework and the reactor vessel appears to preclude consideration of a loss-of-coolant accident.† A contingency that has been considered, however, is the total loss of all electric power to the reactor facility. Although there is a diesel generator to provide power for each of the 12 coolant circuits (apparently the diesels provide normal as well as emergency power) and 6 standby units, the designers provided a "thermal-siphon" heat exchanger at the top of each IHX (see Fig. 13). The secondary fluid is the NaK eutectic (22/78) to help prevent accidental freezing of the coolant in the winter. The secondary lines from 6 primary-loop "thermal siphons" are connected to a single inlet and outlet header that lead to a natural-draft NaK-to-air heat exchanger located in a stack outside the containment. Thus there are four loops available to remove decay heat without electric power. The four loops are sized to dump 1.8 MW of heat, which is the power level of the core 30 min after shutting down from 60-MW operation.

Detailed calculations of the temperature transient after such an accident are not given. However, it is stated[21] that "during this (30-min) period, the coolant outlet temperature from the core will have risen to a maximum of 465°C." It is difficult to see how the peak NaK outlet temperature can rise only 115°C above the normal core outlet temperature of 350°C, particularly considering the following: (1) flow coast-down must be rapid (order of seconds), especially since there is no rotational inertia supplied to the coolant from mechanical pumps, and (2) when flow reversal occurs, the power level probably is closer to 3.6 MW (6% of normal) than to 1.8 MW.

This suspicion is supported somewhat by a curve[21] showing a peak *average* coolant temperature of 440°C for the loss-of-all-pumps accident starting from a reactor power of 60 MW(t). This would give an outlet temperature of 700°C, assuming the inlet temperature equaled the secondary NaK cold-leg temperature at steady state of 180°C. An outlet temperature of only 465°C for the same average temperature would require an inlet of 415°C, or a core ΔT of only 50°C, one-third of the full-flow, full-power value. The same curve shows fuel-element failure for this transient. In the absence of calculational details in the literature, the conclusion is that the efficacy of the "thermal siphon"

*As late as 1961 the power of DFR was given as 60 MW(t) in the core and 12 MW(t) in the blanket, for a total of 72 MW(t) (Ref. 22). In 1964 (and subsequently), the *total* power was reported as 60 MW(t) (Ref. 23). The latter appears to be the correct figure, although no intermediate reference identifying this change has been found.

†Note that there is no safety-analysis report for DFR available in the open literature. Consequently this writer is limited to reporting either what is actually written or what can be inferred from the literature.

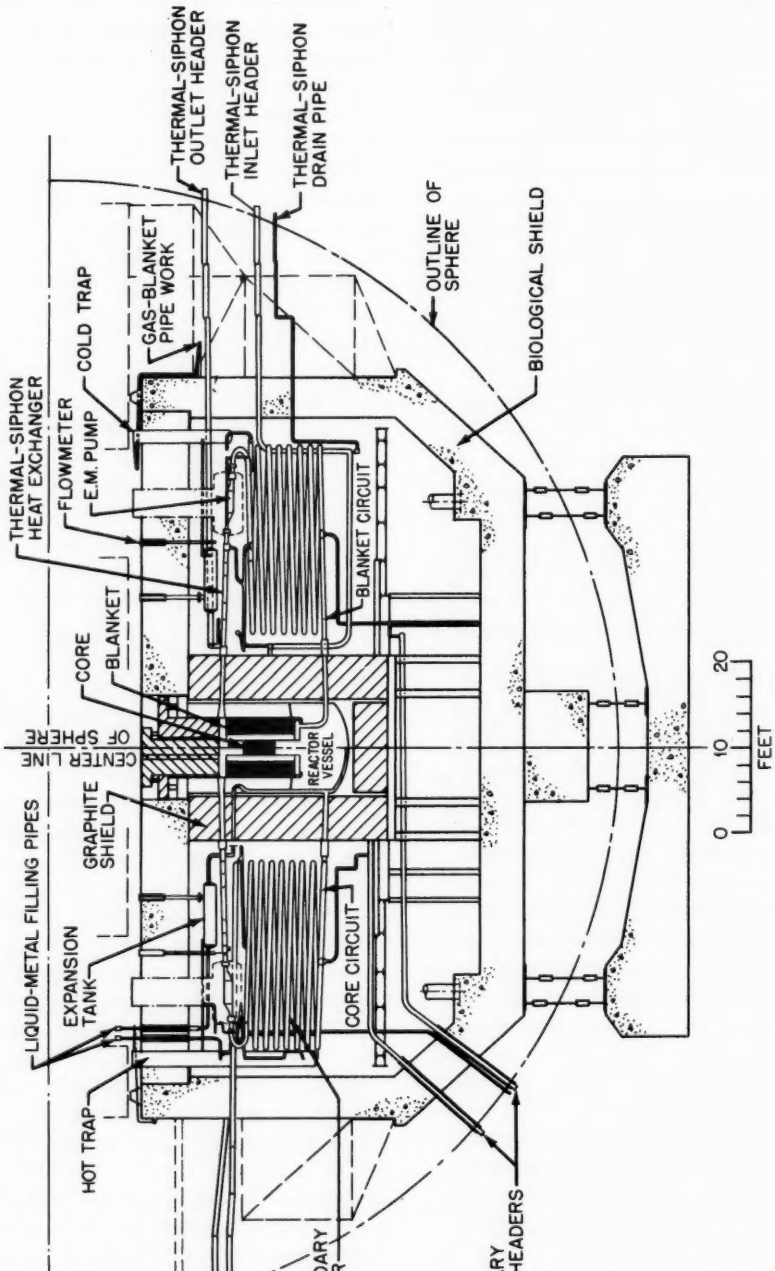

Fig. 12 DFR primary-circuit pipework. (From Ref. 21.)

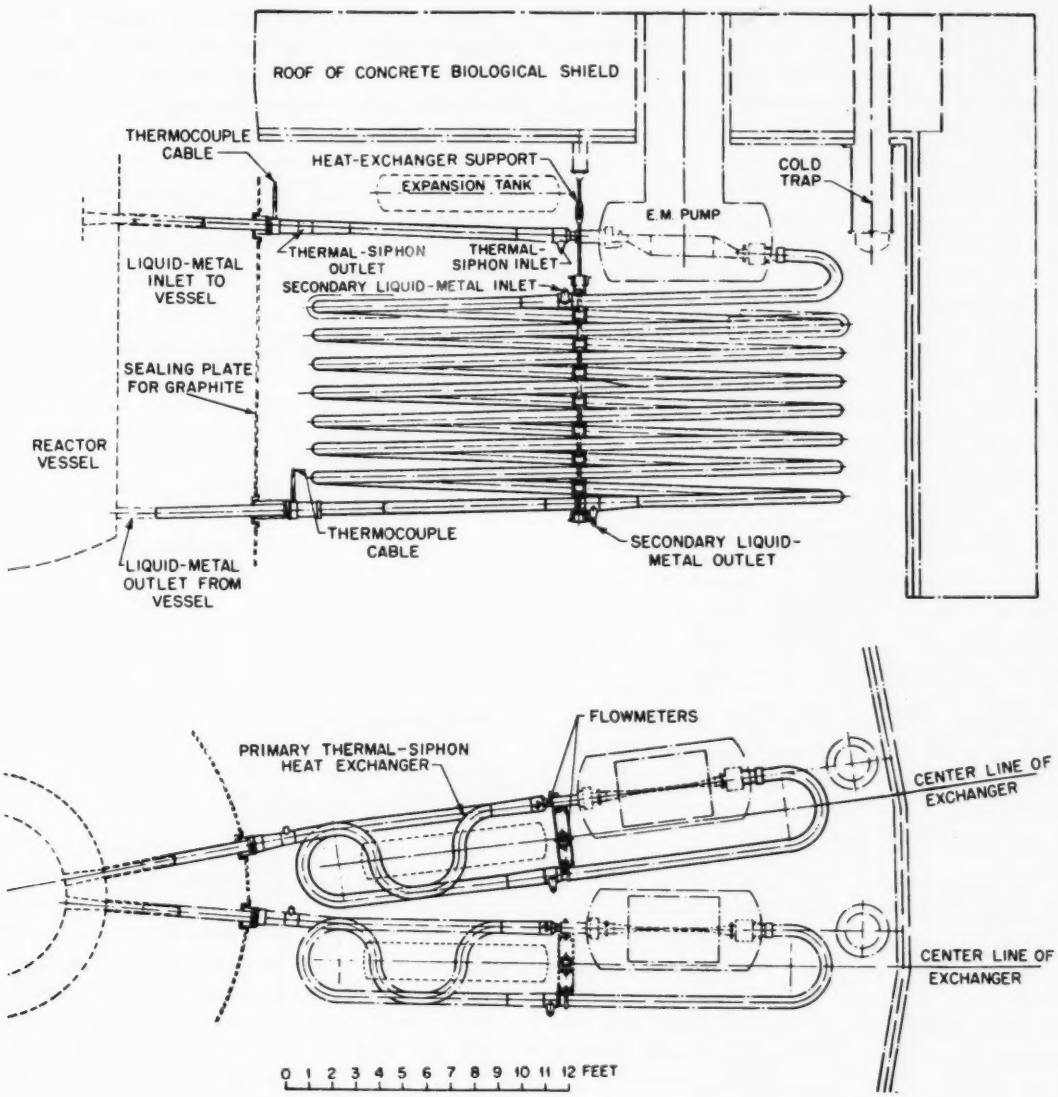

Fig. 13 Arrangement of DFR thermal-siphon system. (From Ref. 21.)

to prevent core damage after a complete loss of electric power is questionable.

Rapsodie.[25-27] *General Description.* Rapsodie is a 20-MW(t) sodium-cooled fast reactor located at the Cadarache Center of the Commissariat à l'Énergie Atomique (CEA) in southeastern France. Its primary purpose is to provide a fast-neutron environment in which to irradiate LMFBR fuel and cladding materials. Operation of Rapsodie has been so successful that its power was raised to 24 MW(t), and a program is under way to further increase its power level to 30–40 MW(t) (Ref. 28).

The 20 MW of heat is removed in two identical 10-MW circuits, each of which consists of an IHX, a secondary sodium* loop and a sodium–air secondary

*Reference 26 gives NaK as the secondary coolant, but later sources, including Ref. 27, indicate that sodium is used.

heat exchanger. The systems associated with the primary coolant loops are shown schematically in Fig. 14. All the primary sodium piping and the reactor vessel are doubly contained, with the interspace apparently sealed from the reactor-vessel cavity atmosphere. This interspace is filled with nitrogen that can serve to both preheat the system and remove decay heat in an emergency situation. In addition, the envelope of the reactor vessel is surrounded by a safety vessel, so that in the unlikely event of a failure of both the reactor vessel and its envelope, the sodium can be contained at a level high enough to ensure continued circulation through the primary loops.[26]

Decay heat can be safely dissipated by natural circulation of the primary sodium. However, to avoid the impact of the transition from forced to natural circulation on the experimental program, emergency power is supplied to the pumps by diesel-generator sets, which are further backed up by batteries.[27]

Emergency Operation. For the Rapsodie reactor, prime consideration was given to coping with primary sodium leaks from various parts of the system. The double-containment aspects of the system design were previously discussed.

Accidental draining of sodium is precluded by requiring all drains to be intentionally primed. Furthermore, drain lines are valved and plugged with frozen sodium. Certain drain lines must be specially installed for draining operations.

(1) Reactor Vessel or Pipe Failure. The failure of any single wall of the primary coolant system will not result in a loss of sodium due to the protection of the containment envelope around the vessel, piping, and components. The space inside the envelope is of a minimum volume and compartmented to limit the sodium-level reduction in the vessel. Sodium circulation in the primary system essentially is unaffected.

(2) Simultaneous Failure of Primary Coolant System and Guard Envelope Inside the Safety Vessel. All sodium piping penetrates the safety vessel at an elevation well above the top of the core. Hence, although the actual reactor-vessel inlet is at the bottom of the vessel, a simultaneous failure of a pipe (or the reactor vessel) and its envelope anywhere inside the safety vessel will not result in an excessive loss of sodium level inside the reactor vessel.

It is stated that a 55-m^3 (~14,000 gal) "flooding tank" can provide makeup sodium to the reactor vessel,[27] but there is insufficient detail to determine the circumstances that require such makeup. It is possible that the earlier comment regarding the final sodium level following a double failure of the reactor vessel and its envelope (i.e., that the outlet pipes still provide a path for the sodium) was optimistic and that a reserve sodium supply was required to compensate for the loss of sodium to the safety vessel. (See the comments on the Fermi reserve sodium supply above.) Presumably, circulation can be maintained in the primary loops as long as the sodium level can be kept above the reactor-vessel outlet nozzles.

(3) Simultaneous Failure of Reactor-Vessel Outlet Piping and Its Envelope Outside the Safety Vessel. In this case, sodium would flow out the broken pipe until the outlet nozzles were uncovered. Reverse flow by gravity through the inlet piping is prevented by check valves that are incorporated in the primary pumps.[26]

Since circulation of coolant is prevented by the double break, decay heat can be removed by forced circulation of nitrogen between the reactor vessel and its envelope. The core is cooled by internal natural convection of sodium. It is admitted, however, that such a situation would result in very high sodium temperatures at the core outlet for a decay heat of 350 kW,[27] only about one-third of the full-power, short-cooling-time value. Quite possibly core damage would result. This problem obviously would be aggravated if Rapsodie achieves higher power than 20 MW(t).

(4) Simultaneous Failure of Reactor-Vessel Inlet Piping and Its Envelope Outside the Safety Vessel. For the case where a double failure of the inlet piping and its envelope occurs outside the safety vessel, a siphon breaker prevents the siphoning of sodium through the broken section to a level below the elevation of the core. Details of the siphon breaker are not given, but one can infer that the system is very similar to the Fermi siphon breaker (see Fermi description above). As in case (3) above, the "last-ditch" cooling of the reactor vessel by nitrogen could result in core damage.

Rapsodie ECCS Design Criteria. After reading the above description of the Rapsodie ECCS, one must be struck by the similarity between the Rapsodie and Fermi primary systems. In fact, if one substitutes the words "primary shield tank" (PST) of Fermi for "safety vessel" of Rapsodie, the differences in the two reactors become almost indistinguishable. Only two significant differences are readily apparent: (1) In Fermi the reactor vessel and piping inside the PST are single-walled, but in Rapsodie those components inside the safety vessel are double-walled. (2) The interspace

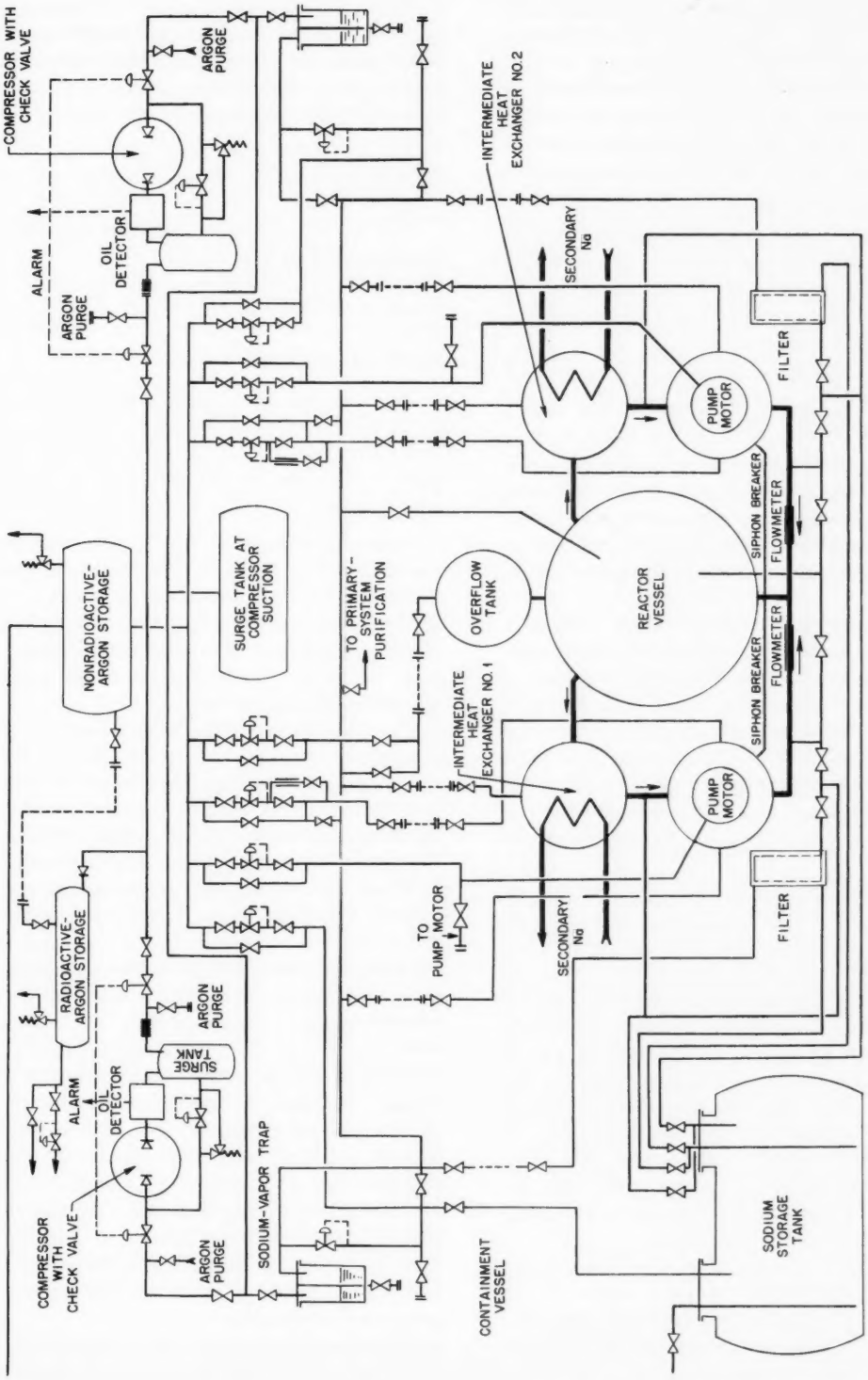

Fig. 14 Rapsodie primary coolant circuits. (From John G. Yevick (Ed.), *Fast Reactor Technology: Plant Design*, The M.I.T. Press, Cambridge, Mass., 1966.)

of the Fermi guard piping is vented to the vault atmosphere, whereas in Rapsodie that space appears to be part of a closed-loop nitrogen system.

As a result of these considerations, one would expect to establish similar ECCS design criteria for Rapsodie and Fermi, and indeed such is the case, as will be seen below.

For a Failure of the Reactor Vessel or Pipe:

1. The double envelope must be designed to withstand a one-event thermal transient arising from a hot-sodium leak. In addition, for a break in the inlet piping, the double envelope must withstand the full primary-pump discharge pressure.

2. The space inside the guard piping must be small enough to keep the sodium level inside the reactor vessel above the sodium outlet nozzles.

For a Simultaneous Failure of Primary Coolant System and Guard Envelope Inside the Safety Vessel:

1. The final sodium level in the safety vessel should not be allowed to drop below that level required to maintain sodium flow out the reactor-vessel outlet nozzles.

2. The rate at which makeup sodium is added to the system and the makeup requirements depend upon the location and magnitude of the leak as well as the safety-vessel free volume. The makeup sodium system must be activated soon enough after the break, and sodium addition must be rapid enough, to avoid disrupting coolant circulation.

3. The safety vessel must be designed to withstand the temperature transient caused by the leaking sodium.

4. For an inlet pipe break, the primary pumps must be shut down or, alternatively, the safety vessel must withstand the full-flow pump discharge pressure and the seal at the top of the safety vessel must be maintained. This latter approach would be required to preserve the function of the safety vessel as a tertiary containment and simultaneously force-cool the core. If this philosophy is employed, depending upon the free volume of the safety vessel, the makeup-sodium-system volume may have to be increased over that required to simply achieve the proper sodium level on a static basis, otherwise the primary pumps might drain the outlet piping and simply fill the safety vessel with sodium.

5. If reduced-flow operation of the primary pumps (e.g., by using the battery power) is employed, the pump characteristic under these conditions must take account of the sodium levels and gas pressures in both the reactor and safety vessels.

For a Simultaneous Failure of Reactor-Vessel Outlet Piping and Its Envelope Outside the Safety Vessel: Either the primary-pump check valves must not leak sodium, or the siphon breakers must be designed to cope with this accident as well as case (4) above.

For a Simultaneous Failure of the Reactor-Vessel Inlet Piping and Its Envelope Outside the Safety Vessel:

1. The failures must be defined in sufficient detail to permit siphon-breaker design.

2. Sufficient blanket-gas supply must be ensured to guarantee siphon-breaker functioning.

Pool-Type LMFBR's

The only pool-type LMFBR currently in operation is the EBR-II, although three other large pool-type reactors are in various stages of construction around the world.[29-31] Therefore the discussion of ECCS's for pool-type LMFBR's will be limited to the EBR-II.

General Description. The Experimental Breeder Reactor II (EBR-II) is a 20-MW(e) [62.5 MW(t)] LMFBR located at the National Reactor Testing Station near Idaho Falls, Idaho. As noted above, the EBR-II typifies that class of LMFBR called "pool type," and in fact, the EBR-II was the first LMFBR to utilize this concept.

A schematic view of the EBR-II primary tank and heat-transfer systems is shown in Fig. 15. The two primary pumps (centrifugal mechanical), as well as the single IHX, are submerged in the primary tank containing essentially all the primary sodium (~90,000 gal). The pumps take suction from the primary tank that is, in effect, the primary-sodium-system cold leg. The sodium is pumped into the reactor vessel, through the core and blanket subassemblies, and to the shell side of the IHX, from where it is discharged into the primary tank. The cycle is then repeated. The heat from the primary coolant is transferred to an intermediate sodium system on the tube side of the IHX, and the intermediate sodium is then used to raise steam for the turbine to complete the heat-transport cycle.

The primary coolant loop is provided with an auxiliary d-c electromagnetic pump in the pipe between the reactor-vessel outlet and the IHX. This pump is powered by a rectifier which also charges a floating battery bank. Upon loss of electric power to the facility, the battery bank supplies the power to the auxiliary pump for a period of time sufficient to prevent core overheating.

Calculations have shown that, in the unlikely event of a simultaneous loss of utility power and emergency

(battery) power to the auxiliary pump, the core would overheat compared with its normal operating temperature,* but the higher temperatures would be acceptable.[13] This is a direct consequence of the limited distance available between the core and the IHX, which ultimately limits the flow rate because of natural convection. In principle, this distance could be made large enough to provide adequate natural circulation, but economics would probably work against lengthening the primary tank solely for this purpose.

The normal mode of decay-heat removal requires the use of the steam system. However, since the auxiliaries (i.e., boiler feed pump, condenser cooling-water pump, etc.) are not furnished with an emergency power supply, an electric-power outage requires an alternate means of dissipating the decay heat. The means employed in EBR-II are two identical shutdown coolers that are immersed in the primary sodium. These coolers are of the bayonet type in which the eutectic NaK alloy is circulated by natural convection to an air cooler in which the air is also circulated by natural convection. Hence no electric power is required to operate the shutdown coolers. Heat is transferred to the NaK by the sodium in the primary tank. The heated NaK flows upward where the heat is ultimately removed in the air cooler.

Note that in a loss-of-power situation, the hot primary coolant is dumped into the primary tank through the IHX, but since the secondary system is essentially inoperative, the sodium leaving the IHX is still at the reactor outlet temperature. If no means (i.e., the shutdown coolers) were provided to remove that heat, the primary sodium temperature would increase, but with a large time constant due to the large bulk-heat capacity of the primary sodium.

Emergency Operation. As noted earlier, the pool-type LMFBR is unique in its ability to retain sodium under a variety of abnormal situations. As long as the core is covered and means exist to remove decay heat, serious core damage usually can be prevented for a wide spectrum of accidents.

There are only two ways in which sodium can be lost from the primary tank. The first is through a leak in the tank itself. However, an outer tank surrounds the primary tank, and any sodium leakage would be contained therein at an elevation high enough to ensure continued sodium flow through the core. This outer tank is analogous to the guard vessels employed around the reactor vessels of loop-type LMFBR's, as noted above.

The second way in which sodium could conceivably be drained from the tank is through the sodium cleanup system. As shown in Fig. 15, the suction line for the cleanup pump dips into the primary tank well below the sodium level. The purification equipment is at an elevation below the sodium level in the primary tank. In the event of a pipe leak at the purification equipment, sodium could be siphoned from the primary tank. This possibility was eliminated, however, by providing a siphon breaker in the cleanup system.† The cleanup system includes a surge tank in which the sodium level is raised by a vacuum pump. The sodium flows from the surge tank to the rest of the cleanup system and is returned to the primary tank by the cleanup pump. An equalizing line from the primary-tank cover gas enters the surge tank above the sodium level. Two valves in series in that line are normally closed. The valves open upon detection of a sodium leak in the purification cell; then the primary cover gas flows to the surge tank and thereby breaks the vacuum and interrupts the siphon action. The sodium in the surge-tank suction line runs back into the primary tank.

Leaks are detected by contact probes on the floor of the purification cell and by a radiation-monitoring device in the cell ventilation system. Any of these devices will automatically operate the siphon-breaker valves and will shut down the purification system if a leak is detected.

EBR-II ECCS Design Criteria:

1. Forced-circulation cooling of the core should be provided, with the emergency pump powered by an uninterrupted power supply.

2. A guard tank (or steel-lined cavity) should be placed around the primary tank and designed for the appropriate thermal transient to be expected in event of a leak in the primary tank. The guard tank should have a volume such that the sodium level in the primary tank does not fall to an unsafe elevation if the primary tank should leak.

3. There should be no penetrations of the primary tank at elevations lower than the minimum elevation required for maintaining core submergence and core cooling.

4. To cope with the possible siphoning of the primary tank through a break in an auxiliary system

*This conclusion would probably hold also for more advanced oxide-fueled pool-type LMFBR's.

†The following description is different from that given in Ref. 13; the latter is no longer valid due to extensive system modifications.

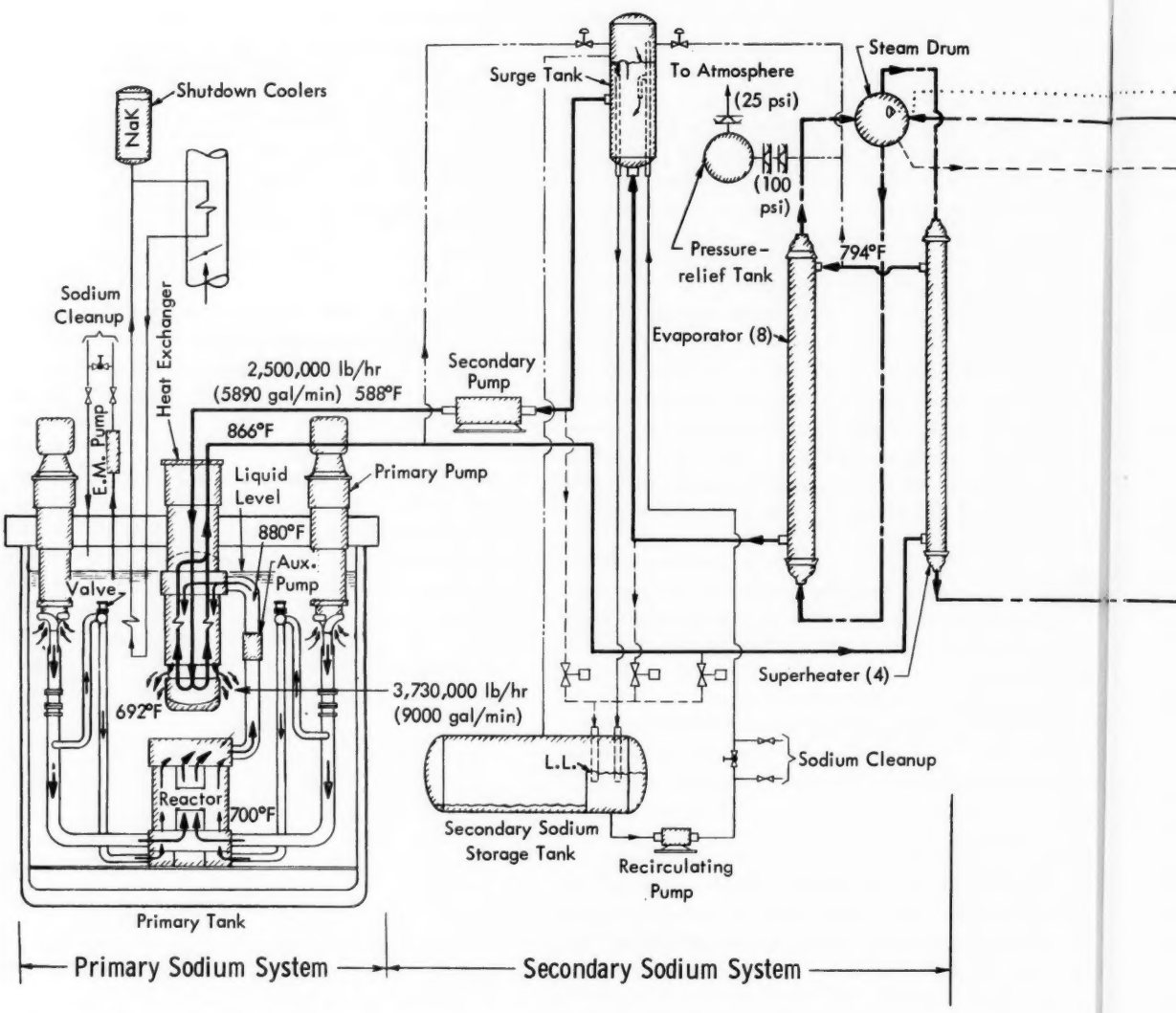

Fig. 15 EBR-II cooling systems. (From Ref. 13.)

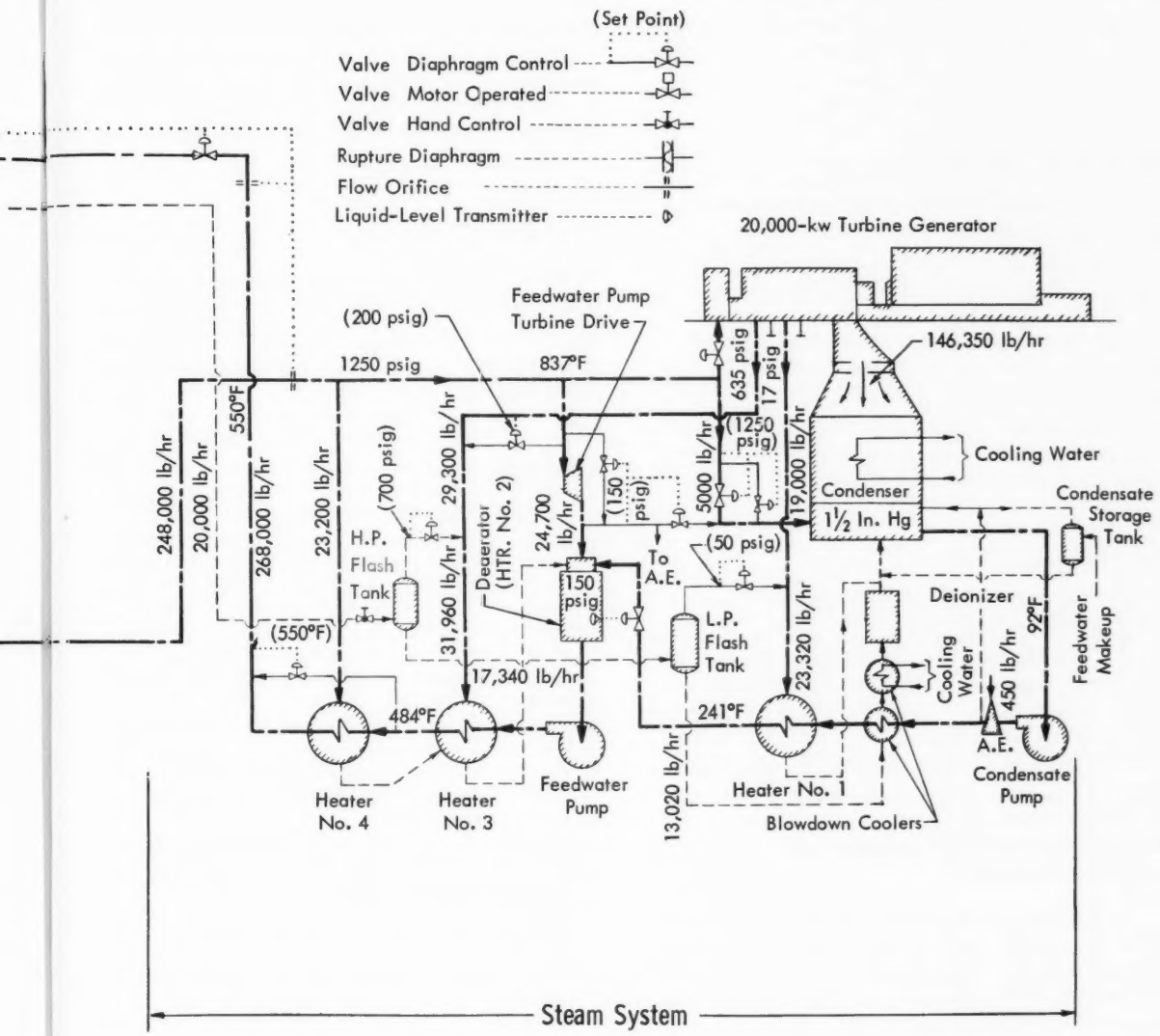
(Set Point)
Valve Diaphragm Control
Valve Motor Operated
Valve Hand Control
Rupture Diaphragm
Flow Orifice
Liquid-Level Transmitter
20,000-kw Turbine Generator
Feedwater Pump Turbine Drive
(200 psig)
1250 psig
837°F
635 psig
17 psig
146,350 lb/hr
(1250 psig)
19,000 lb/hr
Cooling Water
Condenser
1½ In. Hg
Condensate Storage Tank
5000 lb/hr
(150 psig)
(50 psig)
To A.E.
248,000 lb/hr
20,000 lb/hr
268,000 lb/hr
550°F
23,200 lb/hr
29,300 lb/hr
(700 psig)
H.P. Flash Tank
Deaerator (HTR. No. 2)
24,700 lb/hr
150 psig
31,960 lb/hr
(550°F)
17,340 lb/hr
L.P. Flash Tank
23,320 lb/hr
Deionizer
Cooling Water
450 lb/hr
92°F
Feedwater Makeup
484°F
241°F
A.E. Condensate Pump
Heater No. 4
Heater No. 3
Feedwater Pump
13,020 lb/hr
Heater No. 1
Blowdown Coolers
Steam System

requires that appropriate antisiphon protection be provided.

CONCLUSIONS AND SUMMARY

On the basis of the preceding discussions, one can come to a few main conclusions regarding actual solutions to the LMFBR emergency core-cooling problem. These can be summarized as follows:

For Loop-Type LMFBR's

1. Most reactors employ some form of secondary containment for primary sodium systems.
2. Emergency core cooling (assuming there is no loss of sodium) usually takes the form of natural circulation.
3. Some positive means usually are provided to prevent excessive loss of sodium from the primary system because of assumed leaks.
4. A hypothesized loss-of-coolant accident generally requires positive action with respect to pump operation, valve closure, etc., so that the consequences are not worse than they are calculated to be.

For Pool-Type LMFBR's

1. Some form of double containment of the primary tank is required.
2. The probability of a loss of coolant can be made vanishingly small—if penetrations of the primary tank below the sodium level are avoided and if dip tubes in the sodium either terminate at a safe minimum sodium level or are otherwise prevented from siphoning sodium from the tank.
3. Natural circulation of coolant is limited, and some reliable means of providing forced circulation seems to be required.*

In summary, it appears that, as long as sodium loss from an LMFBR can be prevented, reliable core-cooling methods seem possible, regardless of the primary-system design. However, the specter of a loss-of-coolant accident may be ever with us. If that is, in fact, the case, then future large LMFBR's may well be of the pool type to provide maximum assurance that a loss of coolant can be prevented by reliable, passive means.

In this regard, it is interesting to note that the only large LMFBR's currently under construction around the world are of the pool type.[29-31] It can be inferred that the designers of those systems are willing to attack the difficult engineering problems peculiar to large pool reactors to achieve a high degree of coolant boundary integrity. One may conjecture that future purchasers of LMFBR's will favor the pool-type system from the safety standpoint.

*In a recent design study, the General Electric Company concluded that natural circulation was feasible in its pool-type reactor.[32] However, that conclusion was based on quasi-steady-state calculations. The critical period, in terms of peak cladding temperatures, is during the transition from forced convection to natural circulation. The temperatures during this transient were not calculated.

ACKNOWLEDGMENTS

This work was performed under the auspices of the U. S. Atomic Energy Commission. The helpful discussions with T. R. Bump, D. E. Lutz, and O. S. Seim, all of Argonne National Laboratory, are gratefully acknowledged.

REFERENCES

1. *Nucl. News*, **11**(3): 6 (March 1968).
2. Liquid Metal Fast Breeder Reactor (LMFBR) Program Plan, USAEC Report WASH-1101 through WASH-1110 (10 Vols.), LMFBR Program Office, Argonne National Laboratory, August 1968.
3. Large Fast Reactor Design Study, Final Report, USAEC Report ACNP-64503, Allis-Chalmers, Atomic Power Development Associates, and Babcock & Wilcox Co., January 1964.
4. Liquid Metal Fast Breeder Design Study, USAEC Report CEND-200, Combustion Engineering, Inc., January 1964.
5. M. J. McNelly, Liquid Metal Fast Breeder Reactor Design Study, USAEC Report GEAP-4418, General Electric Company, January 1964.
6. R. B. Sieck (Comp.), Liquid Metal Fast Breeder Reactor Design Study, USAEC Report WCAP-3251-1, Westinghouse Electric Corp., January 1964.
7. Proceedings of the International Conference on Sodium Technology and Large Fast Reactor Design, Nov. 7–9, 1968. Part II. Sessions on Large Fast Reactor Design, USAEC Report ANL-7520 (Pt. II), Argonne National Laboratory.
8. Emergency Core Cooling, Report of Advisory Task Force on Power Reactor Emergency Cooling, USAEC Report TID-24226, 1967. (Free from AECW.)
9. C. G. Lawson, Emergency Core-Cooling Systems for Light-Water-Cooled Power Reactors, USAEC Report ORNL-NSIC-24, Oak Ridge National Laboratory, October 1968.
10. *Code of Federal Regulations*, Title 10, Part 100, Reactor Site Criteria.
11. Proceedings of the Conference on Safety, Fuels, and Core Design in Large Fast Power Reactors, October 11–14, 1965, USAEC Report ANL-7120, Argonne National Laboratory.

12. Enrico Fermi Atomic Power Plant, Revised License Application, Part B. Technical Information and Hazards Summary Report, Vols. 1–6, USAEC file No. NP-10458, Power Reactor Development Co., July 1961.
13. L. J. Koch et al., Hazard Summary Report, Experimental Breeder Reactor II (EBR-II), USAEC Report ANL-5719, May 1957, and USAEC Report 5719(Addendum), June 1962, Argonne National Laboratory.
14. SEFOR—Facility Description and Safety Analysis Report (available from Clearinghouse for Federal Scientific and Technical Information).
15. G. Billuris, K. Hikido, E. E. Olich, and A. B. Reynolds, SEFOR Plant Design, in Proceedings of the National Topical Meeting on Fast Reactors, San Francisco, April 1967, Report ANS-101 (CONF-670413), p. 5-1, American Nuclear Society.
16. N. T. Peters, Development of the Primary System for the Enrico Fermi Atomic Power Plant, USAEC Report APDA-308, Atomic Power Development Associates, Inc., June 1968.
17. A. I. Leipunskii et al., Nuclear Power Plant BN-350, in Proceedings of the National Topical Meeting on Fast Reactor Technology, Detroit, Apr. 26–28, 1965, Report ANS-100(Suppl.), p. 15, American Nuclear Society.
18. A. I. Leipunskii et al., The BN-350 and BOR Fast Reactors, in *Proceedings of the London Conference on Fast Breeder Reactors,* May 17–19, 1966, p. 243, British Nuclear Energy Society, 1967.
19. A. A. Pineskii et al., The Coolant System Safety of the Reactors BN-350 and BOR, in *Proceedings of the International Conference on the Safety of Fast Reactors,* Aix-en-Provence, Sept. 19–22, 1967, p. VI-4-1, Commissariat à l'Énergie Atomique.
20. J. D. Geier (Ed.), Fast Reactor Test Facility (FARET), USAEC Report ANL-7168, Vols. I and II, Argonne National Laboratory, April 1966.
21. *Proceedings of the Symposium on the Dounreay Fast Reactor,* Dec. 7, 1960, Institution of Mechanical Engineers, London, 1961, USAEC file No. NP-10685.
22. J. L. Phillips and A. G. Frame, The Dounreay Fast Breeder Reactor Experiment, in *Power Reactor Experiments,* Symposium Proceedings, Vienna, 1961, p. 295, International Atomic Energy Agency, 1962 (STI/PUB/51).
23. J. L. Phillips, Achievement of Full Power Operation of the DFR, *Nucl. Eng.*, 9: 10 (1964).
24. R. R. Mathews and K. J. Henry, Location and Repair of a Leak in the Dounreay Fast Reactor Primary Circuit, *J. Brit. Nucl. Energy Soc.*, 8(3): 168-177 (July 1969).
25. Myriam Aberdam and Gilbert Gros, Liquid Metal Reactor Cooling Systems, USAEC Report EURFNR-42F (translation of Report CEA-Bib-49), February 1965.
26. C. P. Zaleski and L. Vautrey, Le Reacteur Rapide Surregenerateur Rapsodie (The Fast Breeder Reactor, Rapsodie), French Report CEA-2193, a paper presented at the Vienna Power Reactor Experiments Meeting, Oct. 23–27, 1961; also USAEC Report AEC-tr-6310, November 1963. (Sections of this report pertinent to the present paper were translated by Argonne National Laboratory and are available from the Laboratory as ANL-Trans-740).
27. J. Fournier, J. Ladet, and I. Puig, Safety Examination of the Rapsodie Reactor, in *Proceedings of the International Conference on the Safety of Fast Reactors,* Aix-en-Provence, Sept. 19–22, 1967, p. VI-9-1, Commissariat à l'Énergie Atomique.
28. G. Gajac et al., Rapsodie's First Year of Operation, in Proceedings of the International Conference on Sodium Technology and Large Fast Reactor Design, Nov. 7–9, 1968. Part II. Sessions on Large Fast Reactor Design, USAEC Report ANL-7520(Pt. II), Argonne National Laboratory.
29. A. G. Frame, Status of the UKAEA's Prototype Fast Reactor, in Proceedings of the National Topical Meeting on Fast Reactors, San Francisco, April 1967, Report ANS-101 (CONF-670413), p. 6-15, American Nuclear Society.
30. R. Carle et al., The Phenix Reactor, in Proceedings of the National Topical Meeting on Fast Reactors, San Francisco, April 1967, Report ANS-101 (CONF-670413), p. 3-39, American Nuclear Society.
31. A. I. Leipunskii et al., The Atomic Power Station BN-600, in Seventh World Power Conference, August 20–24, 1968, Moscow, Paper 191, Sec. C, translated as Report JPRS-46747 (CONF-680829-6), Oct. 25, 1968.
32. Methods, System Optimization, and Safety Studies for a 1000-MW(e) Sodium-Cooled Fast Reactor, Task III and V Report of 1000-MW(e) LMFBR Follow-On Work, USAEC Report GEAP-5710, General Electric Company, February 1969.

Intergranular Corrosion Cracking of Type 304 Stainless Steel in Water-Cooled Reactors

By C. F. Cheng*

Abstract: *Nuclear pressure vessels, primary piping, core components, and fuel-element cladding are subject to cyclic thermal and mechanical stresses due to the high pressure and temperature of the coolant or of the fuel. When 304 stainless steel is used as material for these parts, potential intergranular corrosion failures due to the combined action of corrosion and low cyclic stress or high static stress need critical evaluation. This article reviews 304 stainless steel with respect to: (1) the instances of service failure other than chloride or caustic cracking in water-cooled reactors, (2) the various corrosion studies on intergranular cracking, and (3) the proposed mechanisms of intergranular corrosion cracking.*

Nuclear pressure vessels, primary piping, core components, and fuel-element cladding are subject to cyclic thermal and mechanical stresses due to the high pressure and temperature of the coolant or of the fuel. When 304 stainless steel is used as material for these parts, potential intergranular corrosion failures due to the combined action of corrosion and low cyclic stress or high static stress need critical evaluation. Numerous instances of such intergranular corrosion cracking of austenitic stainless steel (304 and 304L) have been observed in U. S. nuclear reactors.

In boiling-water reactors, service failures have been reported in a variety of components, including fuel-element cladding,[1,2] preheater pipes,[3] and vessel liners.[4] In pressurized-water reactors, failures of fuel-element cladding[5] and outlet nozzles[6] have been reported. These failures have occurred in both metallurgical conditions—sensitized and solution annealed. The mode of cracking is exclusively intergranular. However, none of the cracking instances are associated with either chloride or caustic solution.

This article discusses austenitic stainless steel with respect to:

1. Instances of the above-mentioned failures.
2. Various corrosion studies on intergranular cracking.
3. Proposed mechanisms of intergranular corrosion.

INSTANCES OF SERVICE FAILURE

Instances of intergranular corrosion cracking of austenitic stainless steel (304 and 304L) in water-cooled-reactor service are briefly discussed below:

Boiling-Water Reactors (BWR's)

In BWR's the primary coolant is high-purity water at a temperature of about 286°C. The water normally operates at neutral *p*H (~7) with a resistivity of approximately 1 MΩ-cm total solids from 1 to 10 ppM, chloride of about 0.02 ppM, and oxygen from radiolytic decomposition up to 0.3 ppM in the water and from 10 to 20 ppM in the steam.[5] In-service intergranular fractures have been reported in two BWR's, one at the Vallecitos Nuclear Center in Pleasanton, Calif., and the other at the Dresden Nuclear Power Station, Morris, Ill.

Vallecitos Boiling-Water Reactor (VBWR). Rods of 304 stainless-steel tubing with outside diameters and

*Materials Science Division, Argonne National Laboratory, Argonne, Ill. 60439.

wall thicknesses ranging from 0.914 to 1.07 cm (0.360 to 0.420 in.) and from 0.051 to 0.013 cm (0.020 to 0.005 in.), respectively, were tested as fuel-element cladding in the VBWR.[7] About 40 out of the 900 rods exhibited intergranular failures in 500 to 1000 hr. However, no carbide precipitate could be seen at the grain boundaries by means of either light or electron microscopy. The cracking patterns varied with the initial condition of the tubing. Cracks in the cold-worked tubing were mostly longitudinal, whereas those in the annealed condition were mostly circumferential. A statistical analysis of the failure-rate data indicated the following:

1. There was no significant difference in failure rate between solution-annealed and cold-worked cladding.
2. The failure rate of "collapsed cladding" was significantly higher than for "freestanding cladding" (indicating the influence of cyclic stress).
3. Fuel rods that operate at high surface heat fluxes [e.g., >95 W/cm^2 or 3×10^5 Btu/(hr)(ft^2)] showed an increased failure rate over fuel rods that operate at lower heat fluxes.

Dresden 1 Boiling-Water Reactor (Dresden 1 BWR). Type 304 stainless-steel fuel-element cladding exhibited longitudinal intergranular cracking in the Dresden 1 BWR.[8] The tubing used was commercially annealed and then cold rolled to 1.242 cm (0.489 in.) in outside diameter. The tubing ranged from 0.025 to 0.043 in. in wall thickness. The cladding was subject to an average exposure of 95 W/cm^2 [3×10^5 Btu/(hr)(ft^2)] peak heat flux. The conclusion was that, since the cladding was "nonfreestanding" and the failure occurred only at the highest heat-flux region, stress was a strong contributor to the cracking mechanism. Fluence was not a factor, since simulated ex-reactor tests showed similar failure phenomena for other 18 wt.% Cr–8 wt.% Ni austenitics as well. Furthermore, studies conducted by Hazelton et al.[9] on UO_2 fuel rods clad with 304 stainless steel showed that irradiation produced only slight structural changes in the cladding at similar fluences, but no increase in susceptibility to intergranular corrosion (as indicated by posttest exposure to acidified copper sulfate solution). Irradiation exposures ranged from 1.7×10^{20} to 9.8×10^{20} cm^2 (>1 MeV).

Preheated pipes of small diameter (6 in. or less) also suffered weld defects and leaking cracks in the Dresden 1 BWR.[3] The coolant leaks that occurred in 304 stainless-steel tubing (schedule 80) were circumferentially oriented cracks. The typical crack lengths were from 2 to 4 in. These cracks initiated at the inner surface of the pipe in the counterbored fit-up region adjacent to the welds. Metallographic examination revealed the mode of cracking to be exclusively intergranular. The microstructure surrounding the cracks showed grain-boundary carbide precipitation during welding. The cracking was restricted to the heat-affected zones of the pipe base metal.

The crack propagation initiated from a single gamma (γ) austenite phase of base metal of 304 stainless steel and arrested at the two-phase austenite plus delta ferrite ($\gamma + \delta$) weldment of 308 stainless steel. However, no indication of cracking was observed in any of the large-diameter (greater than 6 in.) piping. Welding of the small-diameter piping was done with a high heat input and a low number of passes, and welding of the large-diameter piping was done with a low heat input and multiple passes. The latter procedure produced less carbide precipitation than the former.

Elk River BWR. Intergranular corrosion cracks at three locations were observed in the primary-system piping in the Elk River BWR.* Type 304 stainless-steel piping was sensitized at a temperature of 621°C (1150°F) for 4 to 10 hr prior to welding onto the field run pipe. The cracks were located at (1) the nozzle safe end in the upper liquid-level line, (2) the core-spray safe end, and (3) a steam nozzle, after 41 thermal cycles of operation. These areas were exposed to stagnant steam and/or droplets of steam condensate. In each case the cracks were in the vicinity of weld deposits, but they did not initiate at the heat-affected zone. The oxygen in the steam phase is estimated at 10 to 20 ppM. The magnitude of the stress was not known.

La Crosse BWR. The 304 stainless-steel transition piece in the schedule 80 feedwater pipeline of the La Crosse BWR also exhibited intergranular corrosion cracking after some service.† The transition piece had been sensitized at 621°C (1150°F) prior to its attachment to the pipeline and later was exposed to the stagnant water (<5 ppM oxygen). The cracks were located between the thermal sleeve and the pipe. The magnitude of the stress was reported to be well above yield strength.

Nine Mile Point BWR. Intergranular fracture was observed at the core-spray safe ends connected to the

*H. C. Burghard et al., Special Report on SWRI Project No. 07-1599-02, February 1969.

†Allis Chalmers Mfg. Co., USAEC Document No. 1155-16, October 1968.

Nine Mile Point BWR after 11 thermal cycles of operation.* Type 304 stainless-steel safe ends had been sensitized at 621°C (1150°F) for 10 hr prior to welding onto the safeguard spray system located outside the reactor. The crack was adjacent to the thermal sleeve and exposed to the stagnant water (<5 ppM oxygen). The calculated stress after installation was estimated to be well above the yield strength and severalfold higher than the originally designed stress (14,000 psi). Details in the failure analysis are still being worked out by General Electric and Battelle–Northwest.

Pressurized-Water Reactors (PWR). In PWR's the primary coolant is also high-purity water. The *p*H of the coolant at room temperature is maintained in the range 9 to 10.5 by the addition of lithium or ammonium hydroxide. In addition, hydrogen is added to suppress the oxygen formed from radiolytic dissociation of water. Intergranular cladding failure of austenitic stainless steel in both sensitized and solution-annealed conditions has been reported in PWR service.

PWR Test Loops. One experiment conducted in the Engineering Test Reactor (ETR) loop was prematurely terminated as a result of the release of excessive fission products.[10] It was determined that a pump failure and subsequent loss of coolant were responsible for the severe thermal conditions that cracked a fuel-rod cladding to produce the "fission break." The fuel rods had operated for 76 days in 600°F lithiated water at *p*H 10 and at peak surface heat flux of 93 W/cm^2 [296,000 Btu/(hr)(ft^2)]. The UO_2 pellets were clad in 304L stainless-steel tubing with a diameter of 0.820 cm (0.332 in.).

The stretch-formed fuel rod with 0.038-cm (15-mil) wall tubing suffered intergranular cracking, whereas the freestanding fuel rod with 0.053-cm (21-mil) wall was only dimensionally distorted. The severe thermal condition also changed the cladding from a solution-annealed to a sensitized structure. The cladding failure of the stretch-formed fuel rod was attributed to stress rupture in conjunction with hydrogen under the severe thermal conditions. The hydrogen was generated by the reaction of the UO_2 fuel and water.

Knolls Atomic Power Laboratory (KAPL) reported intergranular cracking of vacuum-annealed 304L stainless-steel cladding on poison elements used in test PWR's.[5,11] The failure occurred during irradiation in 600°F ammoniated water at *p*H 10 when the cladding was stressed in excess of the yield point. The hydrogen content of the irradiated cladding increased from 4 to 6 ppM to 8 to 14 ppM in 700 effective full-power hours. Stress-rupture cracking aided by hydrogen was indicated.

Savannah River Reactor. Intergranular stress-corrosion cracking was detected in two 304 stainless-steel nozzles in the high-purity heavy-water moderator of a reactor at the Savannah River Laboratory.[6,12] The cracks propagated from surface intergranular attack at sensitized grain boundaries. The attack was the result of acid ($HF–HNO_3$) pickling during initial fabrication of the nozzles. Cracking was attributed to chlorides, although the bulk water contained only 0.01 to 0.03 ppM chloride. Fluoride contamination is more likely. Recent studies[13] show that fluoride ions with a concentration below 1 ppM in bulk water can result in intergranular cracking at the crevices of sensitized 304 stainless steel (see the sections on "Fluoride-Contaminated Water" and "Water Plus 100 ppM Oxygen").

CORROSION STUDIES ON INTERGRANULAR CRACKING

The failures mentioned earlier under "Instances of Service Failure" are associated with one of the following two conditions:

1. Impurities in aqueous solution.
2. Embrittlement and irradiation effects.

Laboratory studies on intergranular corrosion cracking under these conditions are reviewed below.

Impurities in Aqueous Solutions

Nitric–Dichromate Solution. Sensitization is not a prerequisite for intergranular corrosion of 304 stainless steel. Nonsensitized steel will also corrode intergranularly when exposed to certain chemical environments. Accelerated corrosion of nonsensitized stainless steel during exposure to boiling nitric acid was reported as early as 1952 by DeLong[14] and later by Shirley and Truman.[15] These workers attributed this accelerated corrosion to the presence of chromium ions that had been dissolved from the test specimens. Others[16,17] have shown that dissolved chromium in nitric acid can accelerate intergranular attack only when the chromium is at the highest oxidation state, Cr^{6+}.

Nucleonics Week*, **11(11): (Mar. 19, 1970); **11**(14): (Apr. 9, 1970); **11**(19): (May 14, 1970).

It was not until 1959, however, that Streicher[18] reported that the accelerated corrosion of nonsensitized stainless steel in nitric–dichromate solutions resulted in preferential grain-boundary attack. In addition to Cr^{6+}, the ions Mn^{7+} (MnO_4^-), Ce^{4+}, and Fe^{3+} have been found to activate intergranular corrosion of nonsensitized stainless steel in nitric acid solutions.[18,19] The kinetics of intergranular corrosion of nonsensitized stainless steel in nitric–dichromate solutions have been studied with respect to several environmental variables. Various workers have shown that the rate of intergranular attack increases with corresponding increases in HNO_3 concentration, Cr^{6+} concentration, solution temperature, or specimen stress level.

Metallurgical variables that have been studied to date include: (1) grain size of austenitic stainless steel, (2) cold work, (3) surface treatment, (4) alloy composition, and (5) heat-treatment in nitric–dichromate solutions. Coriou et al.[19] and Armijo[20] have studied the effects of grain size and cold work. They reported that the rate of intergranular penetration increases as the grain size increases and decreases with an increase of cold work. The effects of these variables are small; for example, a tenfold increase in grain size will result in only a twofold increase in intergranular corrosion rate. Similarly, a 50% reduction in thickness (by rolling) will produce only a twofold decrease in corrosion rate.

Warzee and Berge[21] have found that superficial cold work reduces the rate of intergranular corrosion. This surface working is effective in reducing the corrosion of both sensitized and nonsensitized alloys. Armijo[22] found that high-purity Fe–Cr–Ni alloys (14 wt.% Cr–14 wt.% Ni–balance Fe) are immune to intergranular corrosion. The addition of impurities such as C, N, O, Mn, and S does not promote intergranular corrosion susceptibility of a nonsensitized high-purity Fe–Cr–Ni alloy. However, the addition of silicon and phosphorus will promote severe susceptibility. Furthermore, the removal of silicon and phosphorus from austenitic alloys of commercial purity decreases susceptibility to intergranular corrosion by a factor of 6 to 8.

The effect of heat-treatment has been extensively evaluated by Aust[23] to support the solute segregation theory (see the section on "Mechanisms of Intergranular Corrosion Cracking"). He reported that 304 stainless-steel specimens quenched from high temperatures (1300°C) were more susceptible to intergranular corrosion than specimens quenched from temperatures between 1200 and 900°C. Also, specimens stabilized at 800 to 900°C were more resistant to attack than solution-annealed specimens quenched at 1050°C.

Water Plus 100 ppM $FeCl_3$. Pickett et al.[24] have reported several solutions that produce intergranular cracking of nonsensitized stainless steel. These included water solutions of $FeCl_3$, $FeCl_2$, $CuCl_2$, CrO_3, and NaOH at a temperature of 345°C. In these solutions, cracking has been observed only on stressed specimens. It was found that the type of intergranular cracking produced in 100 ppM iron chloride–water closely resembled the in-reactor cracking in appearance and occurred over the same range of temperatures.

Fluoride-Contaminated Water. Recent laboratory tests[13] have shown that 304 stainless steel is susceptible to intergranular fluoride ion (F^-) attack in neutral or alkaline water solutions. Extensive metallographic study of the corroded specimens demonstrated that F^- attack was purely intergranular and was limited to specimens with heavily sensitized structures. Neither the solution-annealed material nor the heat-affected zone adjacent to weldment produced any trace of F^- attack under the same testing conditions. The attack was consistently less severe on sensitized material of finer grain size and/or lower carbon content.

Specimens of other materials appeared to be completely resistant to F^- attack after a sensitizing heat-treatment at 1150°F (621°C) for 10 to 24 hr. These include: Inconel 600, Incoloy 800, fine-grain 304L stainless steel, fine-grain 347 stainless steel, and austeno-ferritic weld deposits or castings. Attack occurred at room temperature and was more rapid at 82°C (180°F).

Data are not yet sufficient to define the F^- concentration necessary for attack to occur. However, in a number of tests at 180°F, concentrations less than 1 ppM F^- in bulk solution caused slight attack in crevices. A very high concentration (4 wt.% NaF) was not corrosive. The rate and mode of F^- attack was not affected by the amount of Cl^- in the corrosive solution over a range from about 15 ppM to less than 30 ppB. With respect to possible mechanistic interpretation, the following patterns are significant:

1. Cracking occurs at room temperature.
2. Wide changes in the *p*H have no effect (*p*H range tested 4.70 to 9.45).
3. Very high F^- concentrations stop cracking.
4. Intergranular attack *without* stress occurs with an air-formed oxide; whereas, intergranular attack on an oxide-free surface occurs only *with* stress (except in crevices).

Water Plus 100 ppM Oxygen. General Electric Company at Vallecitos used a bellows-loading system to study the intergranular cracking of austenitic stainless steel in water containing 100 ppM oxygen at a temperature[25,26] of 289°C (554°F). The tensile specimen was stressed by adjusting the load to 0.2% offset yield strength (at 289°C). The materials used in this study include: 304 stainless steel (0.07 C), 304L stainless steel (0.02 C), 304 + Si (0.07 C, 4.1 Si), nickel-doped 304 + Si (0.06 C, 4.0 Si, 14.3 Ni), U. S. Steel 18-18-2 (0.06 C, 1.92 Si), Uranus S (0.02 C, 4.2 Si, 13.9 Ni, 17.6 Cr), and Uranus-50 (0.05 C, 0.51 Si, 7.9 Ni, 20.3 Cr).

Three heat-treatments were employed:

1. Solution annealed at 1095°C (2000°F) and water quenched.
2. Sensitized 24 hr at 595°C (1090°F) in vacuo and furnace cooled.
3. As welded.

No evidence of localized attack was found after 300 hr of exposure, when tested in the solution-annealed condition. In the sensitized condition, only those austenitic alloys (e.g., 304 stainless steel, nickel-doped 304 + Si, and U. S. Steel 18-18-2) with continuous sheet-type carbides in the grain boundaries exhibited cracking in 17 to 23 hr. In the 300-hr test, no failures were shown by other austenitic alloys (e.g., 304L stainless steel and Uranus S) that were relatively free of continuous sheet-type carbides in the grain boundaries or duplex-structure alloys (austenite + ferrite—e.g., 304 stainless steel + Si and Uranus-50) with no carbide precipitation in the austenite grain boundaries.

To explore further the intergranular stress-corrosion behavior of sensitized austenitic alloys of varying carbon content, a series of carbon-doped, high-purity alloy (18 wt.% Cr–9 wt.% Ni), with from 0.02 to 0.15 wt.% carbon, was likewise tested in the sensitized condition. The time-to-failure decreased rapidly when the carbon content exceeded 0.03 wt.%. In addition, sensitization behavior of welded heavy-plate section of 304 and 304L stainless steel was evaluated. The welds were made on 0.5-in.-thick plates (6 by 6 in.) by using a shielded argon-arc process employing three passes at high heat input with 308 stainless-steel filler material. Tensile specimens were then cut from the plate welds that had the weld bead in the middle of the gauge section. Duplicate specimens of a 304 stainless-steel weld failed in 40 and 45 hr, and corresponding specimens of a 304L stainless-steel weld survived in similar stress-corrosion tests for the entire period of 300 hr.

Metallographic examination revealed the intergranular cracking occurred through a region of heavy carbides 0.25 in. from the 304 stainless-steel weld bead. The 308 stainless-steel weld displayed no cracking, nor was carbide precipitation visible, as in the case of the 304L stainless-steel weld bead.

The following conclusions may be drawn from the above work:

1. Solution-annealed material with no plastic deformation (other than that associated with stressing to yield point) showed no evidence of intergranular stress corrosion after exposure to 289°C water + 100 ppM O_2.

2. Sensitized austenitic materials ($C \leq 0.03$ wt.%) do not exhibit intergranular stress corrosion in the above environment.

3. Addition of silicon to the austenitic alloy is of no benefit if the carbon content is sufficiently large to cause carbide precipitation during sensitization.

4. Duplex alloys (ferrite + austenite) appear to be immune to intergranular stress corrosion even after a heat-treatment that would normally result in sensitization in austenitic materials. This immunity is independent of the nature of the ferrite stabilizer employed.

Recently, Wilde[27] evaluated kinetics of crack initiation of sensitized 304 stainless steel. He observed:

1. The induction time (T_N) for cracking increases markedly when applied stress decreases from 30,000 to 20,000 psi.

2. Cracking appears to nucleate in the plastically deformed area of the surface.

In addition, surface pickling with HNO_3–HF on 304 stainless steel after sensitization [at 621°C (1150°F) for 12 hr] lowers the cracking period from 5 to 10 times compared with corresponding sensitized specimens without HNO_3–HF pickling. It should be pointed out that this surface treatment may be related to F^- attack.[13] However, crevices produced at the grain boundary by pickling is not a likely factor in the absence of F^-. For example, Armijo[25] pickled solution-annealed a specimen of 304 stainless steel in a boiling nitrate–chromate solution to produce deep (~0.015 cm), uniform, intergranular corrosion at the specimen surface. The specimen was then washed in boiling water, and no stress-corrosion failure occurred in the 289°C water + 100 ppM oxygen test.

Irradiation Embrittlement

Hydrogen and helium, which can embrittle austenitic stainless steel, are known to be present in nuclear reactors. Hydrogen is generated from radiolytic dissociation of water in thermal-flux reactors. Hydrogen is also produced by transmutations in (n,p) reactions in the matrix elements (iron, nickel, and chromium) of austenitic stainless steel. Similarly, helium is formed by transmutations in residual boron and in the (n,α) reaction in the matrix elements. Helium is currently considered a major cause of irradiation embrittlement in fast breeder reactors but not in water-cooled reactors. In the latter case the operating temperature is too low for grain-boundary shearing. For this reason, only hydrogen embrittlement will be discussed.

Hydrogen Embrittlement. Whiteman and Troiano[28,29] showed that thin sections of cathodically hydrogenated austenitic stainless steel suffered a significant loss of ductility in analogy with well-characterized hydrogen embrittlement of ferritic steel. A similar result was observed by Cheng[11] and by Vennett and Ansell[30] on 304L stainless steel when tested in a high-pressure hydrogen atmosphere.

MECHANISMS OF INTERGRANULAR CORROSION CRACKING

It can be shown that, in virtually all known cases of intergranular brittleness, the brittleness is associated with the presence of some impurity. Presumably, the impurity is present in the narrow grain-boundary interface in much higher concentration than the mean composition of the metal would indicate.[31] For many years there has been qualitative evidence for segregation of solutes to grain boundaries. This evidence was reviewed by Inman and Tipler[32] in 1963 and by Westbrook[33] in 1964.

In the past year or so, two new quantitative techniques to study the structure and composition of the grain boundaries have emerged. Marcus and Palmberg[34] used Auger electron spectrometry to study antimony segregation at the intergranular fracture surface of embrittled AISI-3340 steel. Brenner et al.[31,35] are using field ionization atom probes to explore atomic structure at a grain boundary and to identify the individual atoms in that structure.

Solute-Segregation Theory

In nitric–dichromate solution, Aust[36] postulated that chemical concentration differences exist between grains and grain boundaries, i.e., impurity segregation at boundaries. These chemical differences provide the driving force for localized attack. It is this impurity segregation that can lead to accelerated dissolution of grain boundaries when the alloy is exposed to a suitable corrodent.

Thus a rather simple model for intergranular corrosion is shown schematically in Fig. 1. It was

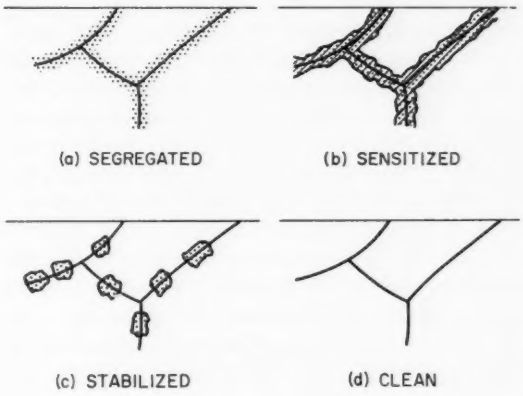

Fig. 1 Schematic illustration of the model proposed for intergranular corrosion.[37]

proposed[37] that the intergranular corrosion of austenitic stainless steel is associated with the presence of continuous grain-boundary paths of either solute-segregated (e.g., phosphorus) or second-phase (carbide) regions. For 304 stainless steel in the solution-treated condition (i.e., quenched from 1050 to about 1300°C), the solute segregation at the grain boundaries provides a narrow continuous path for attack by the corrosion solution, as shown in Fig. 1*a*. If the austenitic stainless steel is quenched from 600°C (or from the sensitization heat-treatment range of 500 to 700°C), continuous carbides or second-phase regions are formed at the grain boundaries, Fig. 1*b*, thereby producing a wide continuous path for classical intergranular corrosion in the sensitized condition.

In material heat-treated and quenched from 800 to 900°C, isolated carbides may incorporate solute impurities drained from the grain-boundary region. This latter heat-treatment (i.e., quench from 800 to 900°C) should then reduce the intergranular corrosion rate, since a discontinuous penetration path for the corrosion medium is now present at the grain boundaries (Fig. 1*c*). In addition, the reduced corrosion rate should remain unchanged even after subsequent 150 hr

sensitization at 650°C. The reason is that carbide precipitation at 850°C should reduce the carbon supersaturation sufficiently to prevent further nucleation of the carbide at the lower temperature of 650°C, despite the decrease in the solubility of the carbon at the lower temperature. Also, on the basis of this model, a low corrosion rate would be expected for a high-purity material having relatively clean or segregation-free grain boundaries, as shown in Fig. 1*d*. The results of the Aust et al.[36,38] investigation in nitric–chromate solution clearly supported this model.

According to the chromium-depletion theory, the beneficial effect of a stabilization heat-treatment (800 to 900°C) on corrosion of austenitic stainless steel is due to the diffusion of chromium into the chromium-depleted areas adjacent to the precipitated carbides. However, as was shown previously, when 304 stainless steel is slowly cooled from 1300 to 900°C, held for 1 hr at 900°C, and quenched, a high rate of intergranular attack is still observed. In other words, at the same annealing temperature and time where chromium diffusion is thought to remove chromium-depleted regions, there is poor corrosion resistance, which is due to the observed continuous carbides present at the grain boundaries.[39] This result is in agreement with the Aust model[37] but not with the chromium-depletion theory.

One of the important problems remaining was to determine the *identity* and *state* of the solute segregation that was involved in the intergranular corrosion of solution-treated and quenched austenitic stainless steel. The fact that some type of solute segregation is responsible is indicated by the work of Chaudron,[40] who found that high-purity stainless steel is immune to grain-boundary corrosion in boiling nitric–dichromate solutions. The recent results by Hanneman and Aust[38] have suggested that the mechanism of nonequilibrium solute segregation induced by excess vacancies may also be responsible for intergranular corrosion of solution-treated and quenched austenitic stainless steel. For example, both excess grain-boundary hardening (Fig. 2) and intergranular corrosion are observed in solution-treated 304 stainless steel.

However, when a high-purity austenitic stainless steel containing no excess grain-boundary hardening[41] is tested, there is no evidence of intergranular corro-

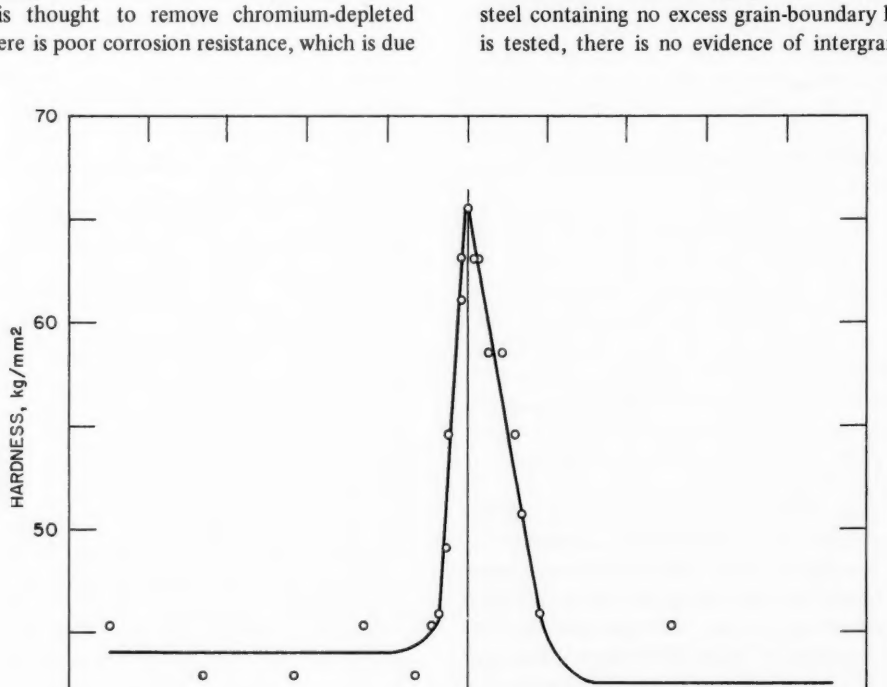

Fig. 2 Hardness–distance profile near a grain boundary in solution-treated 304 austenitic stainless steel (1-g load, 5-sec loading time).[41]

sion.[22] In addition, it is found[22] that a solute such as phosphorus (0.01 to 0.1 wt.%) promotes susceptibility to intergranular corrosion of solution-treated high-purity austenitic stainless steel in nitric–dichromate solutions, whereas carbon (up to 0.1 wt.%) has little effect (Fig. 3). The boundary hardening is found with carbon additions, except in the highest-carbon alloy tested. Electron-microscopy examination revealed the presence of carbide at the grain boundary.[38]

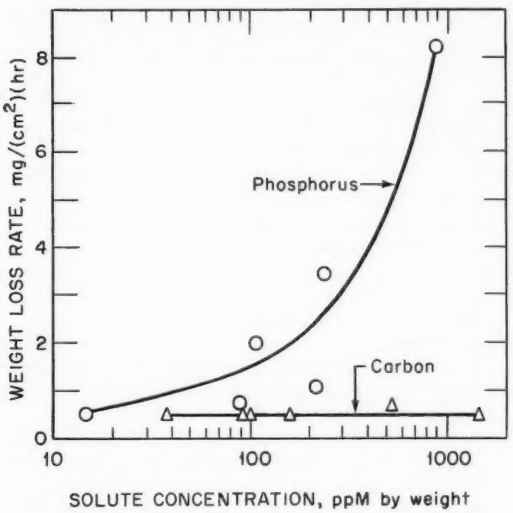

Fig. 3 Effect of phosphorus or carbon additions on the corrosion resistance of solution-treated high-purity austenitic stainless steel (14 wt.% Cr, 14 wt.% Ni, balance Fe) in boiling nitric–dichromate solution.[22]

Finally, the solute-segregation theory of intergranular corrosion of austenitic stainless steel is useful in analyzing the service failures in water-cooled reactors (see the section on "Instances of Service Failure") and in aqueous solution tests (mentioned earlier under "Corrosion Studies on Intergranular Cracking"). The only differences among these corrodents are rate of intergranular attack. In the case of duplex alloys (ferrite + austenite) in water + 100 ppM oxygen tests (see the section on "Fluoride-Contaminated Water"), it has been reported[42] that the carbon precipitates at the ferrite/austenite boundaries and reduces the availability of carbon for precipitation at the austenite/austenite boundaries. Thus the latter boundaries probably have "stabilized" or "segregated" structures rather than "sensitized" structures.

Hydrogen-Induced Transformation

The mechanism of hydrogen embrittlement in austenitic stainless steel due to a hydrogen-induced transformation was recently elucidated by Whiteman[29] and by Holzworth and Louthan.[43] Cathodic hydrogenation of austenitic stainless steel led to partial transformation of the γ (fcc) austenitic lattice to the martensitic phases, α' (bcc) and ϵ (hcp). The latter phases were the same as those formed by cold-working hydrogen-free austenite at very low temperatures. Whiteman further showed that absorption of hydrogen led both to internal strain, induced by an expansion of the γ (fcc) lattice, and to a significant lowering of the stacking-fault energy (related to the activation-energy barrier inhibiting phase transformation). As a consequence the martensitic transformation was induced even in normally stable 310 stainless steel (20% Ni, 25% Cr), which normally does not undergo a strain-induced martensitic transformation even at –4°K.

Benson et al.[44] have further shown that brittle intergranular fracture occurs along martensitic platelets formed in the presence of hydrogen atmosphere. These results indicate that the presence of hydrogen causes embrittlement and initiates microcracks at the strain-induced martensitic platelets in the steel.

CONCLUSIONS

Nuclear pressure vessels, primary piping, core components, and fuel-element cladding are subject to cyclic thermal and mechanical stresses due to the high pressure and temperature of the coolant or of the fuel. When 304 stainless steel is used as material for these parts in water-cooled reactors, instances of intergranular corrosion failure due to the combined action of corrosion and low cyclic stress or high static stress occasionally have been observed.

Sensitization is not a prerequisite for intergranular corrosion of 304 stainless steel. Under certain conditions, solution-annealed 304 stainless steel will behave the same. This is evidenced by the service failures in water-cooled reactors and by test results in laboratory corrosion studies.

On the basis of the solute-segregation theory, Aust[41] postulated that intergranular corrosion of austenitic stainless steel is associated with localized attack on the impurities segregated at the grain boundaries. This is the reason that a sensitized condition, which has a wide continuous path of either solute-segregated (e.g., phosphorus) or second-phase (carbide) regions, is more susceptible to intergranular

corrosion cracking than a solution-annealed condition with a narrow continuous path of segregates. Similarly, a stabilized condition with a discontinuous path of isolated carbide is expected to be even less susceptible to intergranular corrosion cracking. A high-purity material that has relatively clean or segregation-free grain boundaries is immune to such cracking.

The presence of hydrogen can cause embrittlement and also initiates microcracks at the strain-induced martensitic platelets in 304 stainless steel.

The intergranular corrosion failures of 304 stainless steel in water-cooled reactors may be related to (1) selective chemical attack of impurities segregated at grain boundaries or (2) hydrogen embrittlement, or both.

REFERENCES

1. W. H. Arlt and S. R. Vandenberg, Fuel Failure Examinations and Analysis in the High Power Density Program, USAEC Report GEAP-4360, General Electric Company, Sept. 16, 1963.
2. C. N. Spalaris, Finding a Corrosion-Resistant Cladding for Superheater Fuels, *Nucleonics,* **21**(9): 41 (September 1963).
3. J. P. Higgins, The General Electric Report, *Nucl. News,* **11**(11): 37 (November 1968).
4. N. Balai, C. R. Sutton, E. A. Wimunc, and R. F. Jones, Inspection, Evaluation, and Operation of the EBWR Reactor Vessel, USAEC Report ANL-7117, Argonne National Laboratory, November 1965.
5. T. J. Pashos, Stainless Steels and Related Alloys for Use in Water, in Reactor Technology, Selected Reviews, TID-8540, p. 223, USAEC Report 1964.
6. S. R. Rideout, Stress Corrosion Cracking of Type 304 Stainless Steel in High Purity Water, USAEC Report DPSPU-62-30-26, Savannah River Laboratory, March 1963.
7. R. N. Duncan et al., Stainless-Steel-Clad Fuel Rod Failures, *Nucl. Appl.,* **1**(5): 413 (October 1965).
8. S. Naymark and C. N. Spalaris, Oxide Fuel Fabrication and Performance, in *Proceedings of the Third International Conference on the Peaceful Uses of Atomic Energy, Geneva, 1964,* Vol. 11, p. 425, United Nations, New York, 1965.
9. W. S. Hazelton, C. J. Kubit, and D. R. McClintock, A Study of Structural Changes and Corrosion Susceptibility of Irradiated 304 Stainless Steel, *Trans. Amer. Nucl. Soc.,* **6**(2): 388 (November 1963).
10. D. C. Bullington, Yankee Irradiation Program, Summary Report, Part I. Yankee In-Pile Loop Irradiation Test, USAEC Report YAEC-182, Westinghouse Electric Corp., January 1962.
11. C. F. Cheng, Corrosion Aspects of Iron, Austenitic Stainless Steel, and Inconel in High Temperature Water, *Corrosion,* **20**(11): 341t-349t (November 1964) and unpublished data.
12. W. E. Berry, Some Facts About Stress Corrosion of Austenitic Stainless Steels in Reactor Systems, *Reactor Mater.,* **7**(1): 1 (Spring 1964).
13. C. T. Ward, D. L. Mathis, and R. W. Staehle, Intergranular Attack of Sensitized Austenitic Stainless Steel by Water Containing Fluoride Ions, *Corrosion,* **25:** 394 (1969).
14. W. B. DeLong, Symposium on Evaluation Tests for Stainless Steel—Testing Multiple Specimens of Stainless Steels in Modified Boiling Nitric Acid Test, American Society for Testing and Materials, Special Technical Publication No. 93, p. 211, 1949.
15. H. T. Shirley and J. E. Truman, Some Factors Affecting the Resistance of Austenitic Chromium–Nickel Steels to Attack by Hot Concentrated Nitric Acid, *J. Iron Steel Inst.,* **171:** 354 (1952).
16. A. B. McIntosh, Corrosion Problems in Nuclear Power Production, *Chemistry and Industry,* p. 687 (June 1957).
17. J. E. Truman, Factors Affecting the Testing of Stainless Steels in Boiling Concentrated Nitric Acid, *J. Appl. Chem.,* **4:** 273 (May 1954).
18. M. A. Streicher, General and Intergranular Corrosion of Austenitic Stainless Steels in Acids, *J. Electrochem. Soc.,* **106:** 161 (March 1959).
19. H. Coriou et al., Influence des Ions Chrome sur la Corrosion Intergranulaire D'aciers Inoxydables Austenitiques en Milieu Nitrique, *Colloque de Metallurgy IV,* p. 75, Presses Universitaires de France, Paris, 1961.
20. J. S. Armijo, Intergranular Corrosion of Nonsensitized Austenitic Stainless Steels—1. Environmental Variables, *Corrosion,* **21:** 235 (July 1965).
21. M. Warzee and P. Berge, L'influence du Traitement de Surface sur la Corrosion Intergranular des Aciers Inoxydables du Type 18/10 dan L'acide Nitrique Contenant du Chrome Hexavalent, *Compt. Rend.,* **259:** 144 (1964).
22. J. S. Armijo, Intergranular Corrosion of Nonsensitized Austenitic Stainless Steel, *Corrosion,* **24:** 24 (June 1968).
23. K. T. Aust, Intergranular Corrosion of Austenitic Stainless Steels, *Trans. Met. Soc. AIME,* **245:** 2124 (October 1969).
24. A. E. Pickett et al., Development of Test To Simulate Intergranular Cracking of Nonsensitized Stainless Steel in Water Reactor Environment, *Nucl. Appl.,* **1**(5): 453 (October 1965).
25. J. S. Armijo, Intergranular Stress Corrosion Cracking of Austenitic Stainless Steels in Oxygenated High Temperature Water, *Corrosion,* **24:** 319 (October 1968).
26. Jersey Central Power and Light Co., Reactor Vessel Repair Program—Oyster Creek Nuclear Power Plant No. 1, USAEC Docket No. 50-219, Amendment No. 37, April 1968.
27. R. E. Wilde, Technique for Studying the Kinetics of Intergranular Crack Nucleation on AISI Type 304 Stainless Steel in Oxygenated Water at 289°C, *Corrosion,* **25:** 359 (September 1969).
28. M. B. Whiteman, Ph.D. Thesis, The Influence of Hydrogen on Metastable FCC Alloys, Case Institute of Technology, 1965.
29. M. B. Whiteman and A. R. Troiano, Hydrogen Embrittlement of Austenitic Stainless Steel, *Corrosion,* **21:** 53 (February 1965).
30. R. M. Vennett and G. S. Ansell, Effect of High-Pressure Hydrogen upon the Tensile Properties and Fracture Behavior of 304L Stainless Steel, *ASM, Trans. Quart.,* **60:** 242 (1967).
31. J. R. Low, Impurities, Interfaces and Brittle Fracture, *Trans. Met. Soc. AIME,* **245:** 2481-2494 (December 1969).

32. M. C. Inman and H. R. Tipler, Interfacial Energy and Composition in Metals and Alloys, *Met. Rev.*, **8:** 105 (1963).
33. J. H. Westbrook, Segregation at Grain Boundaries, *Met. Rev.*, **9:** 415 (1964).
34. H. Marcus and P. W. Palmberg, Auger Fracture Surface Analysis of a Temper Embrittled 3340 Steel, *Trans. Met. Soc. AIME*, **245:** 1664 (July 1969).
35. S. S. Brenner and J. Y. McKinney, On the Ionization State of Field Evaporated Atoms as Measured in the Film-Atom Probe, *Appl. Phys. Lett.*, **13:** 29 (July 1968).
36. K. T. Aust, Intergranular Corrosion of Austenitic Stainless Steels, *Trans. Met. Soc. AIME*, **245:** 2117 (October 1969).
37. K. T. Aust, J. S. Armijo, and J. H. Westbrook, Heat Treatment and Corrosion Resistance of Austenitic Type 304 Stainless Steel, *ASM, Trans. Quart.*, **59:** 544 (September 1966).
38. R. E. Hanneman and K. T. Aust, Solute Clustering and Intergranular Corrosion, *Scr. Met.*, **2:** 235 (1968).
39. K. T. Aust, J. S. Armijo, E. F. Koch, and J. H. Westbrook, Intergranular Corrosion and Electron Microscopic Studies of Austenitic Stainless Steels, *ASM, Trans. Quart.*, **60:** 360 (March 1967).
40. G. Chaudron, Corrosion of Steels, Quarterly Report No. 6, October 1, 1963–December 31, 1963, USAEC Report EURAEC-976, United States–Euratom Joint Research and Development Program.
41. K. T. Aust, J. S. Armijo, E. F. Koch, and J. H. Westbrook, Intergranular Corrosion and Mechanical Properties of Austenitic Stainless Steels, *ASM, Trans. Quart.*, **61:** 270 (March 1968).
42. *Metals Handbook, Vol. 1, Properties and Selection of Metals*, 8th ed., p. 435, American Society for Metals, 1961.
43. M. L. Holzworth and M. R. Louthan Jr., Hydrogen-Induced Phase Transformations in Type 304 Stainless Steels, *Corrosion*, **24:** 110 (April 1968).
44. R. B. Benson Jr., R. K. Dann, and L. W. Roberts, Jr., Hydrogen Embrittlement of Stainless Steel, *Trans. Met. Soc. Aime*, **242:** 2199 (October 1968).

AEC Critical Review Series

Available for $3.00 each from the Clearinghouse for Federal Scientific and Technical Information, National Bureau of Standards, U. S. Department of Commerce, Springfield, Virginia 22151

SOURCES OF TRITIUM AND ITS BEHAVIOR UPON RELEASE TO THE ENVIRONMENT (TID-24635), December 1968, **D. G. Jacobs,** Oak Ridge National Laboratory.

Projects the production and accumulation of tritium in an expanding nuclear power economy and evaluates the impact of increased tritium production on local and worldwide populations.

REACTOR-NOISE ANALYSIS IN THE TIME DOMAIN (TID-24512), April 1969, **Nicola Pacilio,** Argonne National Laboratory and Comitato Nazionale per l'Energia Nucleare.

Discusses methods of reactor-noise analysis, their uses, limitations, and potentialities and examines the possibilities of using current chambers to extend time-analysis methods to non-zero-power systems.

PLUME RISE (TID-25075), November 1969, **G. A. Briggs,** Environmental Science Services Administration.

Provides an in-depth evaluation of plume-rise formulas and an overall view of the literature. The author develops and compares a simple theoretical model and makes clear recommendations on the basis of all the available data.

ATMOSPHERIC TRANSPORT PROCESSES, Part 1: Energy Transfers and Transformations (TID-24868), December 1969, **Elmar R. Reiter,** Colorado State University.

Deals with the properties of the atmosphere that are capable of transporting atmospheric characteristics, e.g., chemical constituents and dynamic properties.

Nuclear Science Abstracts

The U. S. Atomic Energy Commission, Division of Technical Information, publishes *Nuclear Science Abstracts (NSA)*, a semimonthly journal containing abstracts of the literature of nuclear science and engineering.

NSA covers (1) research reports of the U. S. Atomic Energy Commission and its contractors; (2) research reports of government agencies, universities, and industrial research organizations on a worldwide basis; and (3) translations, patents, books, and articles appearing in technical and scientific journals.

Complete indexes covering subject, author, source, and report number are included in each issue. These indexes are cumulated and sold separately.

Availability of NSA

SALE *NSA* is available on subscription from the Superintendent of Documents, U. S. Government Printing Office, Washington, D. C. 20402, at $42.00 per year for the semimonthly abstract issues and $38.00 per year for the cumulated-index issues. Subscriptions are postpaid within the United States, Canada, Mexico, and all Central and South American countries, except Argentina, Brazil, Guyana, French Guiana, Surinam, and British Honduras. Subscribers in these Central and South American countries, and in all other countries throughout the world, should remit $52.50 per year for subscriptions to semimonthly abstract issues and $47.50 per year for the cumulated-index issues. The single-copy price for the abstract issues is $1.75 postpaid, with this exception: Add one-fourth of $1.75 for mailing to the countries to which the $52.50 subscription rate applies.

EXCHANGE *NSA* is also available on an exchange basis to universities, research institutions, industrial firms, and publishers of scientific information. Inquiries should be directed to the Division of Technical Information Extension, U. S. Atomic Energy Commission, P. O. Box 62, Oak Ridge, Tennessee 37830.

TECHNICAL PROGRESS REVIEWS may be purchased from Superintendent of Documents, U. S. Government Printing Office, Washington, D. C. 20402. *Nuclear Safety* at $3.50 per year (six issues) for each subscription or $0.60 per issue; *Reactor Technology* at $3.00 per year (four issues) for each subscription or $0.75 per issue; *Isotopes and Radiation Technology* at $2.50 per year (four issues) or $0.70 per issue. The use of the order form below will facilitate the handling of your order.

POSTAGE AND REMITTANCE: Postpaid within the United States, Canada, Mexico, and all Central and South American countries except Argentina, Brazil, Guyana, French Guiana, Surinam, and British Honduras. For these Central and South American countries and all other countries: add, for each annual subscription, $1.00 for *Nuclear Safety* and $0.75 for each of the other journals; for single issues, add one-fourth of the single-issue price. Payment should be by check, money order, or document coupons, and MUST accompany order. Remittances from foreign countries should be made by international money order or draft on an American bank payable to the Superintendent of Documents or by UNESCO book coupons.

order form

SUPERINTENDENT OF DOCUMENTS
U. S. GOVERNMENT PRINTING OFFICE
WASHINGTON, D. C. 20402

Please send — 1, 2, or 3 years

- ☐ Isotopes and Radiation Technology _____
- ☐ Nuclear Safety _____
- ☐ Reactor Technology _____

Enclosed: document coupons ☐ check ☐ money order ☐

Charge: Superintendent of Documents No._____

SUPERINTENDENT OF DOCUMENTS
U. S. GOVERNMENT PRINTING OFFICE
WASHINGTON, D. C. 20402

(Print clearly)

_____
Name

_____
Street

_____
City, State, ZIP Code